7.   PHYSICAL & APPLIED CHEMISTRY

7.1. Lectures

L01 SELF-AGGREGATION OF HUMIC AND FULVIC ACIDS STUDIED ON IHSS STANDARDS

MARTIN DRASTÍK, ANNA ČTVRTNÍČKOVÁ and JIŘÍ KUČERÍK

Institute of Physical and Applied Chemistry, Faculty of Chemistry, Brno University of Technology, Purkyňova 118, 612 00 Brno, Czech Republic,
xcdrastik@fch.vutbr.cz

Introduction

Humic substances (HS) are ubiquitous and also the most occurring organic matter on the Earth. Due to their high heterogeneity and chemical character they tend to self-aggregate forming various molecular organisations. Despite an intensive research, the mechanisms and ways of aggregation are still not precisely known.

According to the solubility under acidic or alkaline conditions, HS are traditionally divided into three groups: humin, the insoluble fraction; humic acids (HA), the fraction soluble under alkaline but not acidic conditions (generally pH<2); and fulvic acids (FA), the fraction soluble under all pH conditions. FA may be regarded as associations of small hydrophilic molecules in which there are enough acidic functional groups to keep the fulvic clusters dispersed in solution at any pH. On the other hand, humic acids consist of associations of predominantly hydrophobic compounds which are stabilised at neutral pH by hydrophobic dispersive forces (van der Waals, $\pi-\pi$ and CH$-\pi$ bondings). Their conformations grow progressively in size when intermolecular hydrogen bondings are increasingly formed at lower values of pH, until they flocculate[1].

In 1961 Kononova introduced the concept that HS are comprised of system of polymers[2]. Piccolo, unlike foregoing theory, claims that humic constituents are supramolecular associations of relatively small heterogeneous molecules held together by weak interactions (van der Waals, $\pi-\pi$, CH$-\pi$ interactions and H-bonds)[3].

In this work the thermodynamic stability of HS standards obtained from the International Humic Substance Society (IHSS) at various concentrations was studied. In our case, the high resolution ultrasonic spectroscopy (HRUS) was the method of choice. Since in HRUS the mechanical type of waves is involved, it can succeed where classical optical methods are limited by the nature of the sample (e.g. sample concentration, pH, purity of sample, etc.). This non-destructive method has already been applied to monitor phase and thermal transitions, hydrations, coagulations and other conformational changes of various biomolecules including humic substances and proved itself as a powerful tool in colloidal chemistry due to its sensitivity (resolution down to 10–5 %) and broad possibilities of application[4,5].

Applied waves probe the elastic characteristics of materials. Compression caused by the ultrasonic wave decreases the distances between the sample molecules which then respond *via* intermolecular repulsions and, *vice versa*, the decompression probes the attractive forces. As the result, the ultrasonic velocity parameter is extremely sensitive to molecular organization and intermolecular interactions in samples.

Experimental

IHSS standards of humic acids (Suwanee River 1S101H, Leonardite 1S104H) and fulvic acids (Suwanee River 2S101F, Pahokee Peat 2S103F) were measured. Sodium salts of HA samples were prepared using following procedure. HA standard was dissolved in distilled water and the pH value was adjusted with 0.1M NaOH to 7. The sodium humate solution was freeze-dried and homogenised. FA standards were simply dissolved in distilled water.

To monitor the ultrasonic velocity, HRUS 102 device (Ultrasonic-Scientific, Dublin, Ireland) was employed. HRUS consists of two independent quartz cells which secures that complications caused by changing of water compressibility and density during non-isothermal regime are no longer significant. Cell 1 serves as a sample cell and cell 2 as a reference. Both cells are tempered by a water bath. All measurements were set up at 25.00 ± 0.02 °C, under constant stirring (600 rpm) and at ultrasound frequency of approximately 5,480 kHz. Samples were dissolved in distilled water to desired concentrations (0.01; 0.1; 1; 4 g dm^{-3}). Cell 1 was loaded up by 1 ml of a sample whereas cell 2 by 1 ml of distilled water. Temperature regime was as follows: step 1 – from 25 °C to 90 °C for 3 hours, back to 5 °C for 4 hours, step 2 – from 5 °C to 90 °C for 4 hours and back to 5 °C for 4 hours, step 3 – from 5 °C to 90 °C for 4 hours and back to 25 °C for 3 hours. The first heating cycle was used to ensure that humic samples have the same "thermal history" and that are completely dissolved. The second heating cycle was used to monitor the changes in humic solutions induced by heat, while the third one served as the reproducibility control of the experiment. During the temperature programs the ultrasonic velocity (U) was measured in both cells. The results were expressed as a difference of measured values between cell 1 and cell 2, i.e. U12.

Results

As the records from second and third step gave very similar results, we can assume that only physical and no chemical changes occurred.

HA sample of concentration 4 g dm^{-3} (Fig. 1.) showed practically monotonous decrease of U12. At this concentration, aggregates with hydrophilic surface are present. This surface is surrounded by water shall that is due to the smaller compressibility more supportive for ultrasonic wave propagation than bulk water. With increasing temperature the relative static permittivity of water decreases which leads to the fact
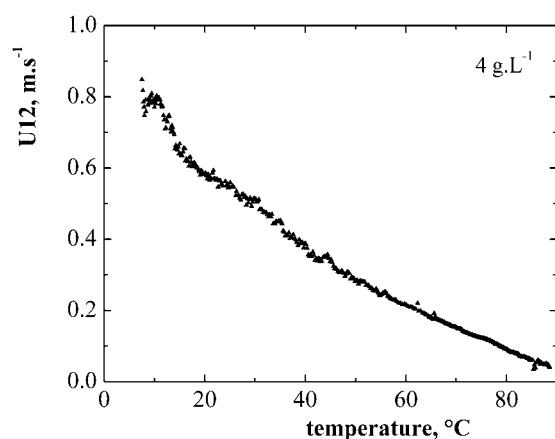
Fig. 1.   **Difference of ultrasonic velocity (U12) as a function of temperature, Suwanee River 1S101H, 4 g dm⁻³**

that the hydration shell is weakened and U12 decreases. Furthermore, at higher temperatures the hydrophobicity of some amphiphilic headgroups increases which results in additional weakening of aggregate protecting hydration shell.

Diluting the sample solution (Fig. 2.), HA assemblies tend to form aggregates with a bit more hydrophobic exterior. The water shell is not so rigid and with increasing temperature is collapsing which results in disruption of humic aggregates. This destabilisations and consequent reaggregation can be observed as a wave-like shape of the curve.
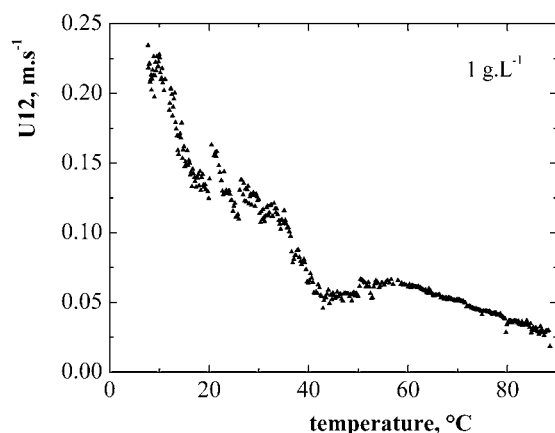

Fig. 2.   **Difference of ultrasonic velocity (U12) as a function of temperature, Suwanee River 1S101H, 1 g dm⁻³**

It is in line with recent statement given in ref.[6] where has been demonstrated that diluting of humates is associated with decreasing in the number of relatively stable H-bonds and humic molecules are loosely bound by hydrophobic interactions such as $CH-\pi$, $\pi-\pi$ interactions or van der Waals forces[6].

Further diluting of the sample solution (i.e. under concentration of 1 g dm⁻³) leads to formation of aggregates with

predominantly hydrophobic exterior. At some concentration, the nature of prevailing interactions holding together humic assemblies is dramatically changed. The disintegration of big aggregates into small ones or even single molecules is associated with the increase of number of water molecules in the hydration shells. With increasing temperature, the relative static permittivity of water decreases which is supportive to hydrophobic hydration. In total this leads to U12 increase (Fig. 3.).
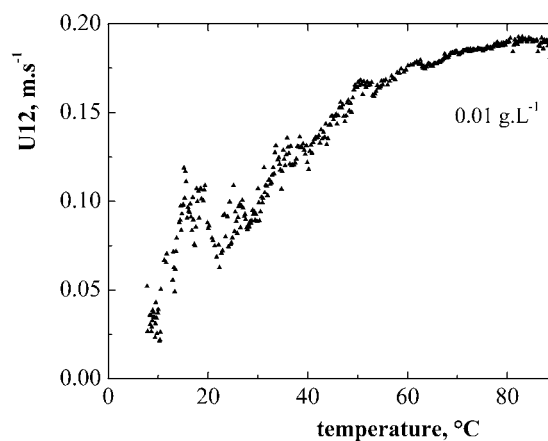

Fig. 3.   **Difference of ultrasonic velocity (U12) as a function of temperature, Suwanee River 1S101H, 0.01 g dm⁻³**

Furthermore, the basic chemical composition (elemental analysis and carbon distribution in functional groups as revealed by liquid state ^{13}C NMR) was compared with the slope of ultrasonic velocity decrease of standards at concentration of 4 g dm⁻³ as measured by HRUS. The slope was observed steeper in line: Leonardite HA, Suwannee River HA, Pahokee Peat FA and Suwannee River FA.

As can be seen in Table I, basic chemical composition does not show clear correlation with the slope of ultrasonic velocity decrease. On the other hand, carbon distribution
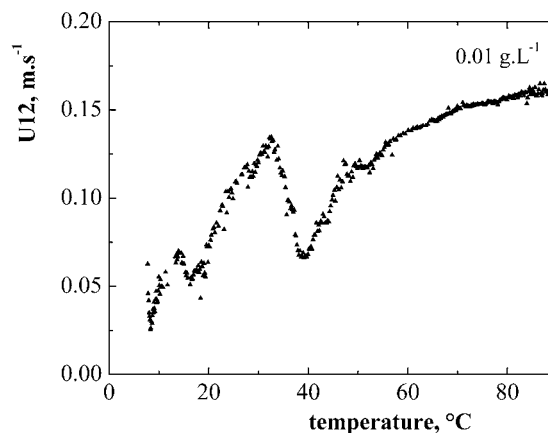

Fig. 4.   **Difference of ultrasonic velocity (U12) as a function of temperature, Leonardite 1S104H, 0.01 g dm⁻³**

Table I
Elemental analysis of HA and FA standards (C. C – Carboxyl Carbon, Ar. C – Aromatic Carbon, Al. C – Aliphatic Carbon)

[%]	Leonardite HA	Suwannee River HA	Pahokee Peat HA	Suwannee River FA
C	63.8	52.6	51.3	52.5
H	3.7	4.4	3.5	4.3
O	31.3	42.5	43.3	42.2
N	1.2	1.2	2.3	0.7
C. C	15	19	28	20
Ar. C	58	37	34	24
Al. C	14	21	20	33

in functional groups, namely aromatic and aliphatic carbon content, can be regarded as potential indicator of the slope of ultrasonic velocity decrease. Anyway, these inferences are based on only four samples measurements thus another records are in need.

Conclusions

Results obtained by high resolution ultrasonic spectroscopy revealed differences in ultrasonic records for all samples. At the same concentration, all samples showed similar trends, nevertheless, easily distinguishable differences were observed (compare Fig. 3. with Fig. 4.). Observed differences may be explained by differences in the samples origin.

Furthermore, diluted samples brought completely different records in compare with the concentrated ones. That was attributed to the fact that at high concentrations the humic aggregates are stabilised mainly by H-bonds but at low concentrations the aggregates and/or single molecules are loosely bound predominantly via hydrophobic interactions. Elemental composition did not show clear correlation with HRUS measurements. On the other hand, slope of ultrasonic velocity decrease seemed to purvey information about carbon distribution in functional groups.

REFERENCES
1. Piccolo A.: Adv. Agron *75*, 57 (2002).
2. Kononova M. M.: *Soil organic matter. Its nature, its role in soil formation and in soil fertility.* Pergamon press, New York 1961.
3. Piccolo A.: Soil Sci *166*, 810 (2001).
4. Buckin V., Kudryashov E., Morrissey S.: Int. Labmate *27*, 23 (2002).
5. Kučerík J., Šmejkalová D., Čechlovská H., Pekař M.: Org. Geochem. *38*, 2098 (2007).
6. Conte P., Piccolo A.: Dev Soil Sci *28*, 409 (2002).

L02 ROBUST NONLINEAR CONTROL OF A SEPARATION COLUMN FOR ^{13}C ENRICHMENT BY CRYOGENIC DISTILLATION OF CARBON MONOXIDE

EVA-HENRIETTA DULF[a], CLEMENT FESTILA[a] and FRANCISC V. DULF[b]

[a]Technical University of Cluj-Napoca, Faculty of Automation and Computer Science, 400020 Cluj-Napoca, C. Daicoviciu Str., 15 Romania,
[b]University of Agricultural Sciences and Veterinary Medicine, Food Quality Control Department, 3–5 Mănăştur Str., Cluj-Napoca, Romania,
Eva.Dulf@aut.utcluj.ro

Introduction

Isotope separation columns are characterized by complex nonlinearities. Furthermore, such processes are subject to external disturbances, which are difficult to model. The controller synthesis problem for such processes is extremely challenging and has been an active area of research for the past two decades.

One approach that has proved popular is the input/output (I/O) linearization approach. In this multi-loop design methodology, Fig. 1., a coordinate transformation is utilized that results in a linear relation between the inputs and outputs (inner loop controller design). Then, an external linear controller is designed for this linear system to enforce desired performance and stability characteristics (outer loop controller design). The performance of this controller largely depends on the availability of an accurate model that leads to exact cancellation of nonlinear terms via the coordinate transformation. However, due to uncertainty and disturbance this is seldom the case and often leads to poor performance.
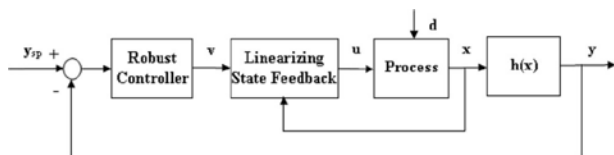

Fig. 1. **Multi-loop robust controller design for nonlinear processes**

In principle, once the nonlinearities are canceled (or inverted), the outer-loop can be designed to impose any desired stable dynamics on the closed loop. The nonlinear model will very likely represent only an approximation of the actual plant. In addition to the modeling uncertainty, there is uncertainty in the model parameters especially in process systems. The controller in the outer loop must be designed not only for nominal stability and performance but for robustness in face of uncertainty in the model and the environment. This robustness issue can be addressed in two alternative approaches. The first approach is to consider the effect of the uncertainty in the nonlinear model and use nonlinear techniques to account for the uncertainty[1]. The second approach[2] is to consider the effect of uncertainty as a perturbation to the I/O linear model and use linear robust control techniques to account for this uncertainty.

Robust Nonlinear Control: the Linearization Approach

The first problem is to systematically design a state feedback for performance and robustness for I/O linearizable systems with parametric uncertainty. In particular, we use a multi-model approach to design a robust controller for the uncertain nonlinear system. In this multi-model approach, the state matrices are written as affine functions of the uncertain parameters and a controller is designed so that stability and performance specifications are met for all members in this polytopic family of models.

Consider the following state space model of a single input single-output (SISO) nonlinear system with parametric uncertainty

$$\dot{x} = f(x, \theta) + g(x)u$$
$$y = h(x) \qquad , \qquad (1)$$

where $x \in \Re^n$ is the state, $u \in \Re$ the control input, $u \in \Re$ the measured output, and θ is a vector of uncertain parameters that takes values in a compact set $\Theta \subset \Re^p$ $\theta \in \Theta$ we assume that f and g are smooth vector fields on , and $\Re^n$ a smooth real vector valued function. The objective is to design a controller such that the closed loop system is stable and certain performance objectives, e.g. tracking, disturbance rejection, etc., are satisfied for all $\theta \in \Theta$. To solve this problem we propose a multi-loop design approach. The inner-loop uses state-feedback to linearize the nominal process dynamics in the input-output sense. In the presence of uncertainties, these methods do not give perfectly linear models. Perturbations appear in the canonical form, as nonlinear functions, due to the presence of uncertainties. For the use of linear robust control techniques these nonlinearities have to be linearized. Standard Jacobi linearization of these nonlinear perturbations around the steady states can be used for this purpose. We note that this is different from the Jacobi linearization of the original nonlinear system. Only the perturbations arising due to uncertainties are linearized but not the whole model. The outer-loop controller is a robust controller that guarantees performance despite uncertainty in the model. The H_∞ objective in the robust controller design is to cancel the e!ect of worst-case disturbances (the nonlinear perturbations) and the H_2 objective is to obtain the optimal LQG control. This linear robust control problem can be solved via multi-objective optimization techniques such as mixed H_2/H_∞ synthesis with pole placement constraints. This technique can be used for robust design when the linear fractional representation of the plant is affne in θ. The multi-model H_2/H_∞ state-feedback synthesis places the poles such that the system has good performance for all values of θ. This problem is represented in Fig. 2., where w contains all external disturbances, e.g. d, and Z_2 and Z_∞ contains the relevant errors signals that we want to maintain small with respect to the 2-norm (average) and ∞-

norm (worst case), respectively. The generalized plant $G(\theta)$ represents the plant model together with performance and normalization weights and is affine in θ.
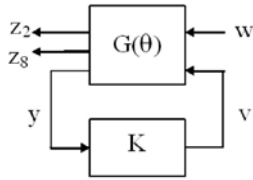

Fig. 2.   **Multi-model H_2/H_∞ synthesis problem**

The objective is to finnd a stabilizing controller *K* such that

$$a\left\|T_{Z_\infty w}\right\|_\infty + b\left\|T_{Z_2 w}\right\|_2 \tag{2}$$

is minimized, for all $\theta \in \Theta$, where $T_{Z_\infty w}$ and $T_{Z_2 w}$ are linear operators mapping *w* to Z_∞ and *w* to Z_2, respectively, and *a*, *b* are positive numbers representing the trade-off between the H_2/H_∞ objectives.

The multi-objective synthesis problem for an uncertain state-space realization can be solved using linear matrix inequalities (LMI). First, the uncertain state-space model is represented as a polytopic family of systems where the state-space matrices are affne functions of the uncertain parameters, i.e. of the form

$$A(\theta) = A_0 + \theta_1 A_1 + \ldots + \theta_k A_k + \ldots \theta_p A_p, \tag{3}$$

where, *p* is number of uncertain parameters. Then, multi-objective problem (2) is solved by LMI using the following theorem.

Theorem 1. (Khargonekar & Rotea, 1991). Given a polytopic family of LTI systems, of the form

$$\dot{z} = A(\theta)z + B_1(\theta)d + B_2(\theta)v \tag{4}$$

$$Z_\infty = C_1 z + D_{11}d + D_{12}v \tag{5}$$

$$Z_2 = C_2 z + D_{22}v \tag{6}$$

The state feedback $v = Kz$ that robustly stabilizes the above system and minimizes the performance objective is given by $K = YX^{-1}$, where $\times$ and Y are obtained by solving the following LMI formulation of the multi-objective state feedback synthesis problem:

Minimize $a\gamma^2 + b$ Trace(Q) over Y, X, Q and γ^2 satisfying

$$\begin{pmatrix} A_k X + X A_k^T + B_{2k}Y + Y^T B_{2k}^T & B_{1k} & XC_1^T + Y^T D_{12}^T \\ B_{1k}^T & -I & D_{11}^T \\ C_1 X + D_{12}Y & D_{11} & -\gamma^2 I \end{pmatrix} \tag{7}$$

$$\begin{pmatrix} Q & C_2 X + D_{22}Y \\ XC_2^T + Y^T D_{22}^T & X \end{pmatrix} > 0 \tag{8}$$

$$\text{Trace}(Q) < v_0^2 \tag{9}$$

$$\gamma < \gamma_0^2 \tag{10}$$

$$f_D < 0 \tag{11}$$

where A_k, B_{1k}, B_{2k} are coefficients in the polytopic representation (as shown in (3)) of the parameter dependent state matrices A, B_1, B_2, respectively, γ and v are upper bounds on the H_∞ and H_2 norms, respectively, and f_D specifies the pole placement constraints.

Robust Nonlinear Control: Nonlinear Technique

This second approach of robust nonlinear control considers the process dynamics of the form

$$\dot{x} = f(x, \bar{u}) + \sigma(x)\dot{d} \tag{12}$$

(1) and a cost criterion L(x, u). We choose a disturbance attenuation constant, γ, and look for a nonlinear feedback control $u^*(x)$ such that[2]

$$\int_0^T L(x(t), u^*(x(t)))dt \leq \gamma^2 \int_0^T |d(t)|^2 dt + D(x) \tag{13}$$

for some function of initial condition D(x) for all $d \in L_2(0, T)$, $T < \infty$. Ideally one would like γ to be nearly as small as possible. Considering the control problem as a differential game with dynamics (12), the payoff and value are given by:

$$P(x, u, d, T) = \int_0^T L(x(t), \varphi[w](t)) - \gamma^2|d(t)|^2 dt \tag{14}$$

$$\overline{W}(x) = \inf_{\phi \in \Phi} \sup_{d \in D} \sup_{T < \infty} P(x, \phi[d], d) \tag{15}$$

If one obtains an optimal feedback control $u^*(x)$ for the game, then

$$\overline{W}(x) = \sup_{d \in D} \sup_{T < \infty} \int_0^T L(x(t), u^*(x(t))) - \gamma^2|d(t)|^2 \tag{16}$$

which implied that (13) is satisfied.

The Isaac equation corresponding to (14) is:

$$0 = \inf_{u \in U} \sup_{d \in \Re^a} \left\{ [f(x, u) + \sigma(x)d]^T \nabla D + L(x, u) - \gamma^2 |d|^2 \right\} =$$
$$= \inf_{u \in U} \left\{ f^T(x, u)\nabla D + L(x, u) \right\} + \frac{1}{4\gamma^2}\nabla D^T \sigma(x)\sigma^T(x)\nabla D = \tag{17}$$
$$= H(x, \nabla D)$$

which is a first-order partial differential equation.

The Isotope Separation

The stable isotopes, species of any element with different number of neutrons in nucleus, exhibit today a large field of applications: research laboratories, medicine, chemical industry, etc. For each element, the natural distribution

of the isotope concentration is very well established, but in applications are necessary chemical compounds based on isotopes with higher concentration. Small differences in physical – chemical properties developed a broad range of isotope enrichment ("isotope separation") methods, technologies and equipments. For instance, by carbon, the ^{12}C and ^{13}C components have a concentration ratio of 98.9 at.%/1.1 at.%.
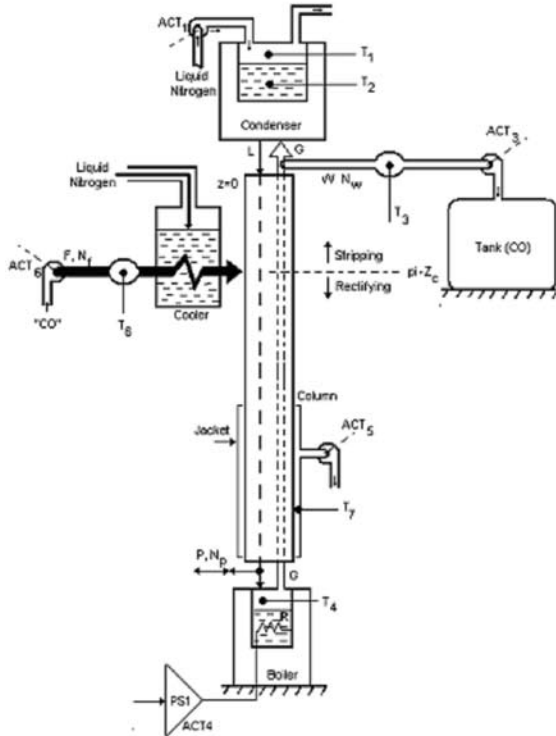

Fig. 3. **Simplified scheme of the isotope separation column**

The Mathematical Model of the Isotope Separation Column

Considering the above presented isotope separation column, the objective is to keep the ^{13}C isotope transfer rate ($\dot{c}$) constant by manipulating the level of N_2 in condenser (h_c) and the voltage on boiler resistor (U_B). The disturbance is the vacuum pressure in the jacket of the column (p_{vac}). Using the

physical equations for the hydrodynamic internal process, the system can be modeles as[3,4,5]

$$\dot{c} = k_{11}(\theta_B - \theta_C) - k_{12}(\theta_B + \theta_C)^2 - k_{13}p_{vac}^2 \quad (17)$$

$$\dot{\theta}_B = -\frac{\theta_B}{T_B} + k_{21}U_B^2 + k_{22}p_{vac}^4 \quad (18)$$

$$\dot{\theta}_C = -\frac{\theta_C}{T_C} + k_{31}h_c^{1/2} \quad (19)$$

where θ_B is the temperature in the boiler zone, θ_C is the temperature in the condenser zone, T_B and T_C are the boiler and condenser time constants and k_{11}, k_{12}, k_{13}, k_{21}, k_{22}, k_{31} are specific constants. Choosing

$$\begin{aligned} x_1 &= c \\ x_2 &= \theta_B \\ x_3 &= \theta_C \end{aligned} \quad (20)$$

as state variables

$$\begin{aligned} m_1 &= U_B \\ m_2 &= h_C \end{aligned} \quad (21)$$

as manipulated variables and

$$d_1 = p_{vac} \quad (22)$$

as disturbance, the obtained LTI model is:

$$\begin{cases} \dot{x}_1 = k_{11}x_2 - k_{12}x_3 - k_{12}x_2^2 - k_{12}x_3^2 - \\ \qquad - 2k_1k_2x_2x_3 - k_{13}d_1^2 \\ \dot{x}_2 = -\frac{1}{T_B}x_2 + k_{21}m_1^2 + k_{22}d_1^4 \\ \dot{x}_3 = -\frac{1}{T_C}x_3 + k_{31}m_2^{1/2} \\ y = x_1 \end{cases} \quad (23)$$

It is an uncertainty in the parameter k_{11} which $k_{11} = \hat{k}_{11} + c_{11}\theta$, $|\theta| < 1$ $\hat{k}_{11}$ the nominal value of k_{11} and c_{11} is a scaling constant representing the magnitude of the uncertainty.

Using this multi-model, it can be design the robust controller as described in previous sections.

Conclusions

Two design procedures were developed for the ^{13}C isotope separation column control: one design is based on I/O linearization and multi-objective H_2/H_∞ synthesis and the second one uses nonlinear techniques. The first approach combines the advantages of I/O linearization and linear robust control techniques to guarantee performance for the nonlinear system with uncertainty. The main advantage of the method is that does not require restrictive matching conditions to be satisfied. With the second approach was obtained a true, global, nonlinear H_∞ controller.

The cryogenic isotope separation technology for ^{13}C is based on the vapor difference of ^{13}CO compared to ^{12}CO at very low temperature (about $-192\ °C$). The isotope separation column is represented in Fig. 3. If the liquid and gaseous phases of the carbon monoxide coexist in the separation column, concentration of ^{13}CO rises in the liquid phase and ^{12}CO accumulates in the gaseous phase. In the isotope separation column a permanent ascendend gas flow and a descendent liquid flow arrises. The liquid phase is vaporized in te column base by an electric "boiler" and the vapor phase is condensed on the wall of the vessel cooled by liquid nitrogen.

REFERENCES

1. Kolavennu S., Palanki S., Cockburn J. C.: Chem. Eng. Sci. *55*, 1583 (2000).
2. Elisante E., Rangaiah G. P., Palanki S.,: Chemical Engineering Science, *59*, 977 (2004).
3. Gligan M., Dulf E., Unguresan M. L., Festila C.,: *Proceedings of International IEEE-TTTC International Conference on Automation, Quality and Testing, Robotics AQTR 2006 (THETA 15)*, p. 155. Cluj-Napoca, 2006.
4. Dulf E. H., Unguresan L. M., Gligan M., Festila C.: *Proceedings of International IEEE-TTTC International Conference on Automation, Quality and Testing, Robotics AQTR 2006 (THETA 15)*, p. 159. Cluj-Napoca, 2006.
5. Dulf E. H., Dulf F., Festila C., Baldea A., Gligan M.: *The fifth Conference Isotopic and Molecular Processes*. Cluj-Napoca, Romania, 2007.

L04　PREDICTION OF THE ACETIC AND FORMIC ACID FORMATION IN THE PAPER DURING THE ACCELERATED AGEING BY THE CHANGE OF OPTICAL PROPERTIES

MICHAL JABLONSKÝ[a], KATARINA HROBOŇOVÁ[b] and RADOVAN TIŇO[a]

[a]Department of Chemical Technology of Wood, Pulp and Paper,
[b]Department of Analytical Chemistry, Faculty of Chemical and Food Technology, Slovak University of Technology in Bratislava, Radlinskeho 9, 812 37 Bratislava, Slovak Republic,
michal.jablonsky@stuba.sk

Introduction

The deterioration of paper as it ages is a serious problem for archival and library communities throughout the world[1]. The most important chemical reactions that occurs during the ageing of paper is the acid-catalyzed hydrolysis of cellulose in paper fibers[2–4] and oxidation of cellulose by oxygen.[2,5–7] The natural ageing processes in the paper lead to the formation of several low molecular weight compounds. Organic acids are spontaneously generated in the natural ageing of all cellulose–based papers, including alkaline papers. Easily detectable concentrations of formic (methanoic), acetic (ethanoic), lactic, glycolic, oxalic and a few others also unidentified acids accumulate within a few months of manufacture in paper stored under ambient conditions[8]. In another work Shahani[9] analyzed papers aged naturally and accelerated by ageing for carbohydrate species using ion chromatography and aliphatic acids such as formic and acetic, which we have discovered to form in surprisingly abundant concentrations, by capillary electrophoresis. In earlier works, which showed us that acidic degradation products tend to accumulate inside polyester encapsulations and other enclosures, and thereby hasten the ageing of the paper[10,11]. To stop the degradation and save millions of the books that are stored in archives different technologies of deacidification and fibre strengthening were invented[12] and considerable efforts have been devoted to find a new additives such as scavengers of free radicals, natural and synthetic compounds, inorganic compounds, solvent and improved original technologies of deacidification.[13–15]

The advantage of the optical methods in the visible part of the spectra consists in their non destructive character. Visually evaluated colour information are widely used in common praxis and in everyday life for grading, production control, sate, decisions of consumers, aesthetic and economical value evaluation, in utilisation, renovation and recycling of lignocellulosic materials and products. The objectively measured quantitative colour information are antropomorphous in nature (human-like, understandable and sometimes or to some extent proportional to the human perception).[16–19]

Experimental

Raw material

Commercial groundwood newsprint paper (grammage 45 g m^{-2}, liquor pH: 4.5–5.0) containing mechanically bleached, groundwood (55 %), bleached sulphite pulp (20 %), catch trash fibres (15 %) and clay (10 %) was used in all experiments.

Accelerated Ageing at 98 °C

Paper were conditioned for 24 hours at T = 23 ± 1 °C, RH = 50 ± 2 % by the norm TAPPI T 402 om-93. Twenty papers (sheets of paper in size A4 format) were put into PET/Al/PE bag which was subsequently completely sealed off. This bag was put into another PET/Al/PE bag which was also completely sealed off and was again put into third (final) sealed PET/Al/PE bag. Finally sample sheets were in the package consisting of three sealed bags put one in another. The bags with samples were put into the thermostat for 0, 1, 2, 3, 5, 7, 10, 15, 20, 30 and 60 days at temperature 98 ± 2 °C.

High Performance Ion-Exchange Chromatography

Approximately 2 g of the paper were accurately weighed and 15 ml of water (Millipore) was added. The mixture was mixed during 2 hour and filtered through 0.45 µm filter. Amount of 20 µl filtrate was injected into the analytical column. The used HPLC system consists of a DeltaChrom SDS 030 isocratic pump, a 7125 Rheodyne injector with a 20 µl injection loop, a thermostat Model LCT 5100, a Knauer variable wavelength detector (set at 210 nm), and CSW32 software for peak identification and integration.

Chromatographic separations of acids were performed with column Polymer IEX H-form (250 × 8 mm I.D., 8 µm). The mobile phase consisted of 9 mmol dm^{-3} sulphuric acid. The column temperature was 20 °C and the flow rate of the mobile phase was 0.8 ml min^{-1}. Formic and acetic acid were detected with spectrophotometric detection at 210 nm. The retention times were 9.7 ± 0.2 min. for formic acid and 10.7 ± 0.1 min. for acetic acid. The identification of the acids in water extract of paper was based on comparison of their retention factors (formic acid k = 1.21 ± 0.03, acetic acid k = 1.44 ± 0.03).

Calibration curves were constructed by performing a regression linear analysis of the peak area versus the concentration of acids. Based on a four-point calibration, a linear response (r = 0.99) was observed from the limit of determination to 20 mg ml^{-1} of studied acids. The limits of detection, defined as the lowest sample concentration, which can be detected (signal-to-noise ratio of 3 : 1) were 10.7 µg ml^{-1} for formic acid and 18.4 µg ml^{-1} for acetic acid. The limits of determination, defined as the lowest sample concentration, which can be quantitatively determined with suitable precision and accuracy (signal-to-noise ratio of 10 : 1) were 42.8 µg ml^{-1} for formic acid and 92.2 µg ml^{-1} for acetic acid.

O p t i c a l   P r o p e r t i e s

Changes in colour of paper surfaces due to ageing were measured using a colour measuring system ELREPHO DATACOLOR 2000. Brightness (B), yellowness (Ys), CIE-Lab L^*, a^*, b^* and ΔE parameters were measured at five spots on each specimen and average value was calculated. The precision in the optical properties determinations brightness are estimated to be less than ± 0.05 units. The Kubelka–Munk coefficient (k/s) describing the number of chromophores present in the paper was determined on the basis of experimental values for brightness[20].

Results

On the Fig. 1. are shown correlations between each pair of variables. Fig. 1 shows Pearson product moment correlations between each pair of variables. These correlation coefficients range between -1 and $+1$ and measure the strength of the linear relationship between the variables. The second number in each location of the Fig. 1. is a p-value which tests the statistical significance of the estimated correlations. P-values below 0.05 indicate statistically significant non-zero correlations at the 95% confidence level.

The most evident signs of paper are yellowing and loss of mechanical strength[21]. During the ageing of paper, decreases the lightness, brightness, but on the other side increases redness and b^* coordinate, yellowness (Ys), total colour difference, Kubelka-Munk coefficient and also increases content of acetic and formic acid in paper. In modern papers the decrease of brightness is about 13–15 %, in historic papers is 3–16 %[22]. In our paper the initial value of brightness was 66.20 % ISO and after 60 days of ageing was decrease of brightness about 78 %.
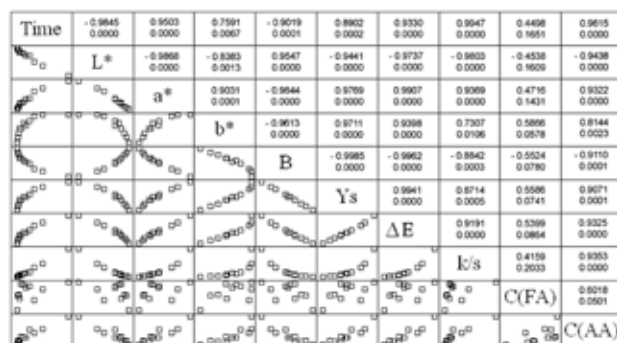

Fig. 1. **Scatter plot for Pearson product moment correlations between each pair of variables**

The acidic products formed during the accelerated ageing accumulate inside the paper and inter-sheet spaces of the books or archival files and it results in enhanced degradation[23]. On the basis of evaluation of carboxylic acids content (formic and acetic acid) was noted unambiguous increase of acetic acid concentration during the accelerated ageing and moderate increase of formic acid concentration. During the accelerated ageing was increased concentration of acetic acid from 0.361 on the value 4.798 mg g^{-1} of paper (after 60 days).

The content of formic acid during the accelerated ageing increases from 0.185 to 0.868 mg g^{-1} of paper (after 60 days). All chemical reactions causing paper degradation are also responsible for the creation of chromophores, especially thermal oxidations and photo–Oxidations. Other reactions such as condensation, cross linking and dehydration due to heat and strongly acid environment, also produce coloured chemical compounds[23,24]. In principle, simple acid hydrolysis does not affect colour, but low-molecular-weight products are more prone to oxidation and colour formation than cellulose chains[23]. The yellowing of paper during the ageing procedure is attributed to the presence of chromophores formed by the degradation of paper components (cellulose, hemicellulose, lignin)[25,26]. The formation of macromolecular hydroperoxides in the cellulose backbone was evidenced previously in the research on paper ageing and the significant role of the produced radical species was postulated[25,26].

Correlations between optical properties and all other characteristics were mostly strong. Fig. 1. demonstrates that a few outliers did not drive the lack of correlation. It was seen earlier that a good correlation exists between C(AA) and time of accelerated ageing (r = 0.9615) and to a lesser extent between C(AA) and L^* (–0.9438), k/s (0.9353), ΔE (0.9325), a^* (0.9322), B (–0.9110) and Ys (0.9071).

Whereas the values for C(FA) are poorly correlated with the optical properties and time of accelerated ageing and C(AA). The correlation between content of formic acid and all other characteristics was evaluated (r < 0.61). The weak correlation were between time of accelerated ageing at 98 °C and b^* coordinate (0.7591) and between b^* coordinate and k/s (0.7307).

We tried to achieve a quantitative linear correlation between optical properties of ageing paper and a property related to extent of degradation formation of acetic and formic acid in paper, respectively. For our multiple regression models, we have used the model set containing samples aged in the time interval from 0–60 days at 98 °C. The output shows the results of fitting a multiple linear regression model to describe the relationship between content of acetic acid (C(AA)) or formic acid (C(FA)) and 8 independent variables. The equation of the fitted model is

$$C(AA) = -23.5965 + 0.239192T + 0.354993L^* - 0.925779a^* - 1.82714b^* - 0.311187B + 2.17738Ys - 2.7564\Delta E + 0.850291k/s$$

Since the p-value is less than 0.01, there is a statistically significant relationship between the variables at the 99 % confidence level. The R^2 parameter indicates that the model as fitted explains 99.88 % of the variability in C(AA). By the method forward selection was evaluated new multiple linear regression model are presented Table I. The R^2 parameter indicates that the model as fitted explains 96.70 % of the variability in C(AA).

The equation of the fitted model for concentration of formic acid and optical properties and time of accelerated ageing is:

$$C(FA) = -70.4895 + 0.0640916T + 0.667981L^* - 0.836883a^* - 2.84595b^* + 0.234988B + 1.19121Ys + 1.29359\Delta E - 10.578k/s$$

Table I
Parameters and estimates of fitting of linear multiple regression model for concentration of acetic acid

Dependent variable: C(AA)			
Parameter	Estimate	Standard error	p-value
Constant	1.0985	0.1303	0.0000
Time	0.2119	0.0448	0.0015
k/s	–3.6854	1.1477	0.0124
$R^2 = 0.967$			

Since the p-value is greater or equal to 0.10, there is not a statistically significant relationship between the variables at the 90% or higher confidence level. The R^2 indicates that the model as fitted explains 92.95 % of the variability in C(FA). By the method forward selection was evaluated new multiple linear regression model which is presented in Table II. The R^2 parameter indicates that the model as fitted explains 34.4 % of the variability in C(FA).

Table II
Parameters and estimates of fitting of linear multiple regression model for concentration of formic acid

Dependent variable: C(AA)			
Parameter	Estimate	Standard error	p-value
Constant	0.2990	0.1648	0.1031
b*	0.0209	0.0096	0.0578
$R^2 = 0.344$			

As was mentioned before, optical properties are physical properties which are often monitored by the conservators for the indication of chemical changes[27]. From this paper is obvious that brightness decreases during the ageing, probably because of formation of chromophore in cellulose, hemicellulose and lignin, and then it increases. In this work was confirmed that formation of acetic acid in paper depends on the time of accelerated ageing and on number of chromophores present in the paper which can be described by the Kubelka-Munk coefficient. The correlation between time of accelerated ageing, Kubelka-Munk coefficient and formation of acetic acid is strongly significant. Correlation between optical properties and time of accelerated ageing according to formation of formic acid is weak significant.

In this work was also confirmed that low-molecular product such as acetic acid have coherence with the colour information which is consequence of the accelerated ageing. Paper properties are interdependent[27] hence the change of optical properties relates with the change of chemical properties and fragility of pulp fibers during the accelerated ageing.

Conclusions

The aim of the work was to quantify the failure of acetic and formic acid estimation by optical parameters in models of ageing papers at 98 °C from 0 to 60 days. The results presented in the paper has shown that multiple linear regression model describes the relationship between acetic acid content and independent variables as time of accelerated ageing (T) and coefficient of Kubelka-Munk (k/s). The equation of the fitted model is C(AA) = 1.0985 + 0.2119T – 3.6854k/s.

The R^2 parameter indicates that the model as fitted explains 96.70 % of the variability in acetic acid content. For formic acid content the equation of the fitted model is C(FA) = 0.299 + 0.0209b*. The R^2 parameter indicates that the model as fitted explains 34.40 % of the variability in formic acid content.

Low-molecular product such as acetic acid, have coherence with the colour information which is consequence of the accelerated ageing. Formation of acetic acid in the paper depends on the time of accelerated ageing and on number of chromophores in the paper.

REFERENCES

1. Carter A. C.: Journal Chem. Edu. *73*, 1160 (1996).
2. Unsworth J., Mitchell F.: IEEE Trans. Electr. Insul. *25*, 737 (1990).
3. Bayer M., Lind A., Koch H., Fischer J.: J. Pulp Paper Sci. *25*, 47 (1999).
4. Margutti S., Conio G., Calvini P., Pedemonte E.: Restaurator *22*, 67 (2001).
5. Malesic J., Kolar J., Strlic M.: *Proceedings of the Int. Conference Chemical Technology of Wood, Pulp and Paper*, p. 382 Bratislava 2003.
6. Strlic M., Selih V. S., Kolar J.: *Proceedings of the Int. Conference Chemical Technology of Wood, Pulp and Paper*, p.385, Bratislava 2003.
7. Trnkova M., Bukovsky V.: *Proceedings of the Int. Conference Chemical Technology of Wood, Pulp and Paper*, p.444, Bratislava 2003.
8. Shahani C. J., Harrison G.: *Works of Art on Paper, Books, Documents and Photographs: Techniques and Conservation.* London 2002.
9. Shahani C. J.: *Preservation Research and Testing Division, Library of Congress.* Washington. DC.
10. Shahani C. J., Hengemihle F. H., Weberg N., in: *Amer. Chem. Soc. Symposium Series 410, S. Historic Textiles and Paper Materials II: Conservation and Characterization, American Chemical Society* (Zeronian H., Needles L.eds.), p.63, Washington DC 1989.

11. Shahani C. J.: *ASTM Workshop on the Effects of Aging on Printing and Writing Papers*, ASTM. Philadelphia PA (1994).
12. Proniewicz L. M., Paluszkiewicz C., Wesenucha-Birczynska A., Majcherczyk H., Baranski A., Konieczna A.: J. Molec. Struc. *596*, 163 (2001).
13. Cedzova M., Vrska M., Szeiffova G.: Chem. Listy *99*, 442 (2005).
14. Cedzova M., Gallova I., Katuscak S.: Restaurator *27*, 35 (2006).
15. Cedzova M., Katuscak S.: Papir Celuloza *61*, 10 (2006).
16. Katuscak S.: Drev. Vysk. *24*, 33 (1984).
17. Katuscak S., Katuscakova G.: Holzforschung *41*, 315 (1987).
18. Kucera L. J., Katuscak S.: Holz-Farbe–Gestaítung, Lignum, Zurich, 43 (1992).
19. Katuscak S., Kucera L. J.: Wood Research *45*, 9 (2000).
20. Dence, C.W., Reeve D.W.: *Pulp bleaching. Principles and practice.* Tappi Press, Atlanta 1996.
21. Vives J. M. G., Escoda J. R. M., Guerra R. A., Hernandez L. A.: Restaurator *22*, 187 (2001).
22. Bukovský M.: Restaurator *20*, 77 (1999).
23. Baranski A., Lagan J. M., Lojewski T.: *Ageing and stabilisation of paper*, p.93 Ljubljana 2005.
24. Sjostrom E.: *Wood Chemistry.* Academic Press 2, New York 1993.
25. Havlinova B., Babiakova D., Brezova V., Durovic M., Novotna M., Belanyi F.: Dyes Pigm. *54*, 173 (2002).
26. Carter H.A.: J. Chem. Educ. *73*, 1068 (1996).
27. Van Der Reyden D.: JAIC *31*, 117 (1992).

L05 EFFECT OF STABILISATION OF PAPER WITH PIPERIDINE-BASED ANTIOXIDANT ON RECOGNISABILITY OF PRINTED BLACK CHARACTERS

JANA KAZÍKOVÁ, ATTILA SZITÁS, KATARÍNA VIZÁROVÁ, MICHAL JABLONSKÝ, FRANTIŠEK POVAŽANEC, SOŇA KIRSCHNEROVÁ and SVETOZÁR KATUŠČÁK

Institute of Polymer Materials, Department of Chemical Technology of Wood,Pulp and Paper, Slovak University of Technology in Bratislava, Radlinského 9, 812 37, Bratislava, Slovak Republic,
jana.kazikova@stuba.sk

Introduction

It is well-known that the visibility, recognisability and readability of any document depend on the contrast between text characters and background[1,2,3]. The question is – how to quantify, measure objectively and predict the visibility of characters of text and more generally of any information in a document. Objective method enabling to predict human-like, or antropomorphous visibility and recognisability of letters of characters on paper would be of great importance. If available, such method could be widely used in paper quality control, process development and optimizing, recycling and promoting of recycled papers, in optimizing stabilisation, deacidification, modification of properties, coating, encapsulation, paper splitting and other conservation technologies, measurement of effects of ageing and conservation processes of old books and archive documents; and last but not least, to improve the communication between papermaking and printing industry and their customers. In spite of this key importance, no generally accepted method is available at the time being.

Optical properties of both paper and the printed, written, drawn or painted characters change at processes of production, ageing, recycling, conservation[4–7] and utilization. These processes influence both the visibility and recognisability of characters on the paper. The question is how. How to measure the changes of the recognisability of character objectivelly and simultaneously via human-like manner to be able to predict the changes of antropomorphous visibility, recognisability, and readability? How to objectivise and predict human-like readable and perceived information content changes caused by processes of treating the paper documents?

Visibility or legibility of a letter, or a character or an information in a document is the property expressing the ability to be seen by human eye more or less quickly, correctly, distinctly from a certain distance. It is determined and influenced by several factors, generally comprising objective properties of documents (colour contrast, light intensity, character`s font face, size...) as well as subjective quality of human eye, illumination, geometry and other objective factors.

Recognisability of a character of information in a document is closely related to visibility, and could be defined as a measure of extractability of its exact meaning.

Readability – the quality of a document expressing the ability to be understood by a human observer or intelligent optical device (CCD camera, OCR scanner.) correctly.

The semantic hierarchy of the above mentioned terms from the viewpoint of their complexity is: visibility > recognisability > readability*;* It means, readability includes both the visibility of characters and their recognisability. Present conservation platforms and substances for mass conservation deacidification can change mechanical, chemical and optical properties and their stability and therefore also the visibility and recognisability of black letter or characters studied in this work.

The work was aimed at determining the effect of thermally induced accelerated ageing on antropomorphous recognisability and documenting application options of developed algorithm for quantifying an effect of a selected piperidine-based antioxidant on a change in the recognisability and its stability.

Experimental

Wood-containing paper with the grammage 45 g m^{-2}, surface pH: 5.6, consisting of 55 % of the mechanically bleached groundwood, 20 % of the bleached sulphate pulp, 15 % of the recovered fibres and 10 % of clay was used in experiments. The test paper was modified by 0.5% wt. solution of a piperidine-based antioxidant DAO3 in hexamethyl-disiloxane.

The used untreated paper had the following optical parameters: $L^*_B = 84.817$; $a^*_B = -0.666$; $b^*_B = 3.763$.

The white paper used for calibration (2) between subjective psychometrically measured recognisability and objective parameters, and as white reference point in Figs. 1. and 2., with the R/R$_0$ = 1, was white office paper Maestro Standard (Mondi Business Paper SCP, a.s.) with the following CIE colour parameters: $L^* = 95.52$; $a^* = 1.98$; $b^* = -3.64$.

The paper samples were exposed to the thermally-induced accelerated ageing following the ASTM D 6819-02 standard, in a thermostat up to 15 days at temperature 98 ± 1 °C, then air-conditioned according to the ISO 187 standard at temperature 23 ± 1 °C and the relative humidity RH = 50 ± 1 %.

The CIE total colour difference ΔE_{C-B} between the text character characters (L^*_C, a^*_C, b^*_C) and its background (L^*_B, a^*_B, b^*_B,) was calculated using the following equation:

$$\Delta E_{C-B} = \sqrt{(L^*_C - L^*_B)^2 + (a^*_C - a^*_B)^2 + (b^*_C - b^*_B)^2} \quad (1)$$

where

ΔE_{C-B} – the optical contrast as expressed through total colour difference in the CIE L^*, a^*, b^* system between a printed character/letter and its background.

$L^*_C = 28.915$; $a^*_C = 0.555$; $b^*_C = -0.56$ – the optical parameters of the printed characters or letters in the model test documents used for the experiments.

The subjectively perceived recognisability (R) was calculated[8] using the optical contrast expressed by total colour difference (ΔE_{C-B}) between black character (C) and white paper (B) by the following mathematical equation:

$$ R = \left(1 - \left(\frac{\Delta E_{C-B} - 62.56}{62.56} \right)^2 \right)^{0.42} \tag{2} $$

Relationships between the relative recognisability R/R_0 and ΔE_{C-B} were plotted, where:

R – recognisability of a black character (C) printed on modified or unmodified, aged or unaged paper background (B).

R_0 – recognisability of the black character printed on white calibration paper with the $L^* = 95.5$; $a^* = 1.98$; $b^* = -3.64$.

Results

Currently it is generally accepted that the visibility, recognisability and readability of any document depends on the contrast between text characters and the background1. This hypothesis was tested and the obtained results are shown in Figs. 1. and 2. as dashed lines (2). The paper samples were subjected to accelerated ageing, which changed the paper lightness (L^*), and the optical contrast ΔE_{C-B} between a printed character and the paper, as well as the relative recognisability (R/R_0). The relationship between the relative recognisability (R/R_0), the optical contrast (ΔE_{C-B}) and the paper lightness (L^*_B) is shown in Fig. 1. The relative recognisability of characters R/R0 has been related to the recognisability of the same black letters /characters on white calibration paper with the following optical parameters: $L^*_B = 95.52$; $a^*_B = 1.98$; $b^*_B = -3.64$.

In Fig. 1., also the visualisation of the effect of the constant decrease of a certain optical contrast $\Delta(\Delta E^*_{C-B}) = 5$ – can be seen, caused through a 15 days ageing of paper on the human-like recognisability of black letters on a typical white paper ($L^*_B = 85$), middle light ($L^*_B = 45$) and dark paper ($L^*_B = 34$); Fig. 1. represents also a difference between the relative recognisability based on so far accepted conceptions on a dependence of recognisability on optical contrast (line 1) and actually perceived recognisability[8] based on our psychometric measurements (line 2). According to the mentioned so far accepted conceptions, visibility, recognisability and readability of any document depends on the contrast between text characters and background1. Following the accelerated ageing (for 15 days at 98 ± 1 °C), the optical contrast ΔE_{C-B} between character and background decreased by $\Delta(\Delta E^*_{C-B}) = -8.3\%$. Stemming from a simplified linear conception on dependence on the optical contrast, the character recognisability should decrease in the same extent, i.e. by $\Delta R/R_0 = -8.0\%$. Based on our measurements of calibration between subjective and objective evaluation using eq. (2) we calculated that the actually perceived/ antropomorphous change of recognisability kept almost identical in a lighter part of document.
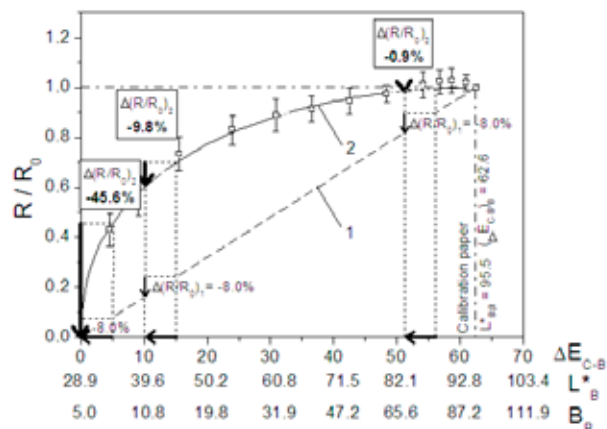

Fig. 1.   **Visualisation of the effect of the constant decrease of the optical contrast $\Delta(\Delta E^*_{C-B}) = -5$ through the ageing of unmodified paper on the human-like recognisability of black letters on a typical white paper ($L^* = 85$), middle light ($L^* = 45$) and dark paper ($L^* = 34$); The relationship between the visually estimated relative recognisability index (R/R_0), and both the printed black character-paper optical contrast (ΔE_{C-B}) and the paper lightness (L^*_B); 1 – function based on the assumption of equivalency of the subjective relative recognisability and the optical contrast 2 – function according to equation (1); $\Delta R/R_0$ [%] = a relative decrease in recognisability related to the recognisability of the characters possessing the same black intensity colour in calibration paper with $L^*_B = 95.52$; $a^*_B = 1.98$; $b^*_B = -3.64$; Non-modified sample had the optical parameters: $L^*_B = 84.817$; $a^*_B = -0.666$; $b^*_B = 3.763$**

It follows from Fig. 1 that the hypothesis on dependence of visibility and recognisability on the optical contrast is not valid for white papers ranging from $L^* = 80$ to 95, i.e. for papers being the most important for the productiom, recycling and use of white, recycled paper for graphic and newprints usage, or other papers for printed documents production.

It can be seen in Fig. 1. that while in a light part of unmodified document or in light paper (from $L^*_B = 85$ to $L^*_B = 76$ and an optical contrast decrease by $\Delta(\Delta E^*_{C-B}) = -5$ units) the decrease in lightness does not cause any significant decrease in document characters visibility, the identical decrease of paper lightness and optical contrast (from $L^*_B = 45$ to $L^*_B = 40$ and $\Delta(\Delta E^*_{C-B}) = -5$ units, respectively) in a middle part leads to multiply decrease in recognisability (by $\Delta R/R_0 = -9.8$ %) and in document dark part with the lightness of $L^*_B = 34$ the same darkening means 45.6% loss of information ($R/R_0 = 0$).

What is the effect of antioxidant on human predicted change of visibility and recognisability?

We anticipated that the antioxidant could decelerate the paper ageing and yellowing during the ageing which, in turn, should lead to a change in the human predicted recognisability of characters in document. In Fig. 2., dependences of optical contrast and recognisability are shown for modified document with $L^*_B = 84.582$; $a^*_B = -0.586$; $b^*_B = 4.139$.
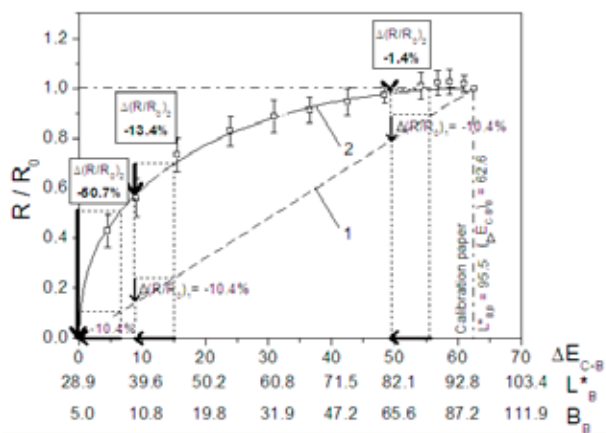
Fig. 2. **Visualisation of the effect of the constant decrease of the optical contrast $\Delta(\Delta E^*_{C-B}) = -6.5$ through the ageing of paper modified with the antioxidant DAO3 on the human-like recognisability of black letters on typical white paper ($L^* = 85$), middle light ($L^* = 45$) and dark paper ($L^* = 36$); The relationship between the recognisability index (R/R_0), the optical contrast (ΔE_{C-B}) and the paper lightness (L^*_B)**

Fig. 2. demonstrates the effect of ageing to a change in optical properties and recognisability of the paper modified by the used antioxidant. Comparing to Fig. 1. it is obvious that the effect of the antioxidant for recognisability is not significant. Using eq. (2) we came to a conclusion that antropomorphous change of recognisability in light document is −1.4 %. It is 7.4 times less than at recognisability according to so far accepted knowledge. The effect of the antioxidant thus lies in a mild decrease of antropomorphous recognisability after 15-days ageing.

What is the situation concerning a dark part of the document or dark documents from dark papers? If the ageing and antioxidant caused the same change of optical contrast, i.e. change in ΔE_{C-B} by 6.5 units, the actual human-perceived recognisability decreases due to the ageing by 13.4 %. As given by Fig. 2., a change in ΔE_{C-B} by 6.5 units from 15 to 8.5.

Conclusions

Generally it is believed that the visibility and recognisability of a document depend on optical contrast between the characters and the paper backround. The aim of this work was to test this hypothesis and to quantify the effect of accelerated ageing and paper modification with piperidine-based antioxidant on the visibility and recognisability of the black characters on paper.

It has been estimated that the hypothesis of a dependence of recognisability on the optical contrast failed – in very wide range of white papers. The dependence of recognisability is negligible in white paper documents. The less the recognisability of characters depends on the white papers the more meaningfull is the dependence in middle light paper documents and critically in dark paper documents.

The used antioxidant of piperidine type did not have meaningfull effect on paper stabilisation, neither against the changes of the paper optical properties nor the changes antropomorphous visibility and recognisability of printed information in a document caused by ageing.

REFERENCES

1. Pescio S., de Mattiello M., Álvarez R.: *Proceedings of the Interim Meeting of the International Colour Association,* p. 47, Porto Alegre 2004.
2. Eperjesi F., Fowler C. W., Kempster A. J.: Ophthalmic and Physiological Optics *15,* 561 (1995).
3. Rubin G. S., Legge G. E.: Vis Res, *29*, 79 (1988).
4. Barrow, W. J., Sproull, R. C.:, Science *129*, 3356 (1959).
5. Malesic J., Kolar J., Strlic M.: *Proceedings of the Int. Conference Chemical Technology of Wood, Pulp and Paper*, p. 382-384, Bratislava 2003.
6. Strlic M., Selih V. S., Kolar J.: *Proceedings of the Int. Conference Chemical Technology of Wood, Pulp and Paper*, p. 385, Bratislava 2003..
7. Trnková M., Bukovský V.: *Proceedings of the Int. Conference Chemical Technology of Wood, Pulp and Paper*, p. 444, Bratislava 2003.
8. Szitas A., Jablonský M., Katuščák S.: Chem. listy *99*, 2008.

L06 ROLE OF AROMATICITY IN HUMIC SUBSTANCES DEGRADATION KINETICS USING NON-ARRHENIUS TEMPERATURE FUNCTIONS

JIŘÍ KISLINGER[a], FRANTIŠEK NOVÁK[b] and JIŘÍ KUČERÍK[a]

[a]*Institute of Physical and Applied Chemistry, Faculty of Chemistry, Brno University of Technology, Purkyňova 118, 612 00 Brno, Czech Republic,*
[b]*Institute of Soil Biology, Biology Centre of the Academy of Sciences of the Czech Republic, Na Sádkách 7, 370 05 České Budějovice, Czech Republic,*
xckislinger@fch.vutbr.cz

Introduction

The problem of global warming has been uncovered a long time ago. The attention of scientists and researchers in many fields is focused on possible reduction of greenhouse gases increase to the atmosphere. Such process requires principal understanding of carbon (C) stabilization in soils because the amount of organic matter stored in soils represents one of the largest reservoirs of organic carbon on the global scale. Unfortunately, the mechanisms for carbon stabilization in soils are still not perfectly clear and thus the maximal potential for C stabilization in soils remains unascertained[1].

Some important soil qualities, such as fertility or stability are directly related to its organic matter presence. Many functions of soil organic matter (SOM) are due to its stable fraction, the humified materials, and to its balance with the labile fractions. Altogether it affects, directly or indirectly, many physical, chemical and biological properties that control soil productivity and resistance to degradation. Changes in the quantity and quality of SOM and its equilibrium level depend on the interaction of several factors. As SOM enters and resides in soil, it is subjected to fundamental processes that alter its composition and quantity. These are e.g. humification, aggregation, translocation, erosion, leaching and mineralization[2]. Other changes in SOM content are related to changes in microbial biomass turnover because they reflect the balance between rates of microbial organic matter accumulation and degradation. However, SOM as a whole responds less quickly to changing soil conditions than microbial biomass. Therefore, the nature of the organic matter itself, rather than its concentration, may be more sensitive indicator of the changes in soil quality[3].

The main fraction of organic matter contained in soils, peats, sediments, low-rank coals and natural waters consists of humic substances (HS), which comprise a complex mixture of both aromatic and aliphatic moieties, having a large number of functional groups. Chemical and structural characteristics of HS are known to be better predictors of the rate of SOM turnover than SOM content itself[4].

Processes in condensed phase are extensively studied by thermoanalytical methods. Mechanisms of these processes are very often unknown or too complicated to be characterized by simple kinetic model. To describe their kinetics, of which we speak, the methods based on the single-step approximation are often used, either the model-free or model-fitting ones. It is generally recognized that the rate of the processes in condensed phase is a function of temperature (T) and conversion (α). The rate of the complex multi-step condensed-state process can be formally described as

$$\frac{d\alpha}{dt} = k(T)f(\alpha), \tag{1}$$

where $k(T)$ is temperature function and $f(\alpha)$ conversion function. The temperature function in (1) is mostly considered to be the rate constant and the conversion function is considered to reflect the mechanism of the process[5,6]. With only for few exceptions, the temperature function is expressed by the well-known Arrhenius equation:

$$k(T) = A\exp[-\frac{E}{RT}], \tag{2}$$

where A and E are considered the pre-exponential factor and the activation energy, respectively, T is the absolute temperature and R stands for the gas constant. It has been justified that, since $k(T)$ is not the rate constant and E cannot be mechanistically interpreted in the term of free energy barrier, there is no reason to be confined to the Arrhenius relationship and use of two non-Arrhenius temperature functions was suggested:

$$k(T) = AT^m \tag{3}$$

$$k(T) = Ae^{DT}, \tag{4}$$

where m and D are adjustable parameters[7]. The evaluation is carried out at fixed conversion. The isoconversional predictive procedure is huge and has already been successfully employed also in studying HS[8].

Experimental

Humic samples were extracted according to International Humic Substances Society (IHSS) procedures. They included:

- fulvic acid FA1, (B horizon of Spodo-Dystric Cambisol, mountain spruce forest, Boubín, Bohemian Forest, CZ), aromaticty: 29.0 %
- humic acid HA1, (Of horizon of Spodo-Dystric Cambisol, mountain spruce forest, Boubín, Bohemian Forest, CZ), aromaticty: 30.2 %
- humic acid HA2 (Of horizon of Podzol, mountain spruce forest, Trojmezí, Bohemian Forest, CZ), aromaticty: 46.5 %
- humic acid HA3 (Oxyhumolite lignite, Bílina mine, North Bohemia, CZ), aromaticity: 61.0 %

The aromaticity of samples was determined by ^{13}C LS NMR analysis. Thermogravimetric analyses of all samples in the dynamic air atmosphere (25 ml min^{-1}) were performed

using TA Instruments TGA Q 5000 IR. Approximately 2–3 mg of each sample were measured in open crucible at 7 different heating rates (0.5–15 K min⁻¹) from room temperature up to 600 °C.

The aim of this study lies in assessment of the stability of humic substances with different aromaticity degrees using two distinct equations, (3) and (4), as temperature functions. Such computed conversion times (having a meaning of stability – the higher the conversion time the higher the stability) serve for elucidation of role of aromaticity during the humic substances degradation.

Results

The thermogravimetric records (Fig. 1., TG) showed two or more steps of weight losses, the first one clearly attributable to loss of water (Fig. 1., part I), whereas others to degradation of organic molecules present in the humic matter (Fig. 1., part II). The latter steps were used to assess the stability of examined samples. Both the beginning as well as the end of such steps was verified by the first derivative of the TG curve (Fig. 1., DTG).
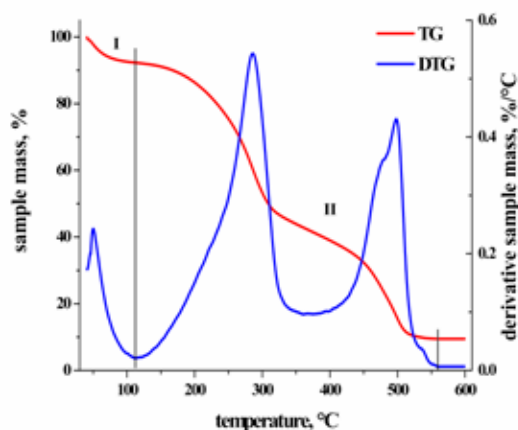
Fig. 1. **TG and DTG record of FA1, heating rate: 10 K min⁻¹**

The mass losses obtained at different heating rates were recalculated to conversion intervals (0–100 %). From this interval, several conversions were selected and for those the stabilities for 25 °C were calculated using the mathematical apparatus of integral isoconversional method at linear heating with two non-Arrhenius temperature functions. Values of conversion times served for comparison between samples with different aromatic degrees. Relative stabilities (RS) were determined as a ratio of conversion times for each conversion over the whole interval. The conversion time of sample FA1 being always the denominator (and thus the reference) because of its lowest aromatic degree. Such approach is usually used in evaluation of de-/stabilizing effect of various additives in many materials. In these cases the RS is called the protection factor with the value 1 having crucial meaning.[9] For our purposes the absolute values of RS are not of key relevance.

The induction periods (i.e. conversion times at 0% con-

version) of all samples regarding both temperature functions are summarized in Table I. Comparing the humic acids, it is obvious that the higher the aromaticity the higher the stability of the sample. The fulvic acid shows higher stability than its humic analogue having almost the same aromatic C content. This can be caused by the presence of structurally different aliphatic parts, more energy demanding for degradation than in HA1. Comparison of FA1 with HAs having the aromatic C content much higher shows that the previously described dependence is abided.

The comparison of stability curves in Figs. 2. and 3. implies the fact that both temperature functions are suitable for evaluation of thermo-oxidative stability of humic matter

Table I
Induction periods for 25 °C using both functions

Sample	IP using Eq. 3 [yrs]	IP using Eq. 4 [yrs]
FA1	0.166	0.067
HA1	0.064	0.030
HA2	0.275	0.107
HA3	1.651	0.429

because the patterns are much likely similar. A major difference can be seen in the values of RS, which is axiomatic considering the diverse temperature functions. But as stated above, if these values serve only for comparison between samples there is no reason to take the absolute values into account.
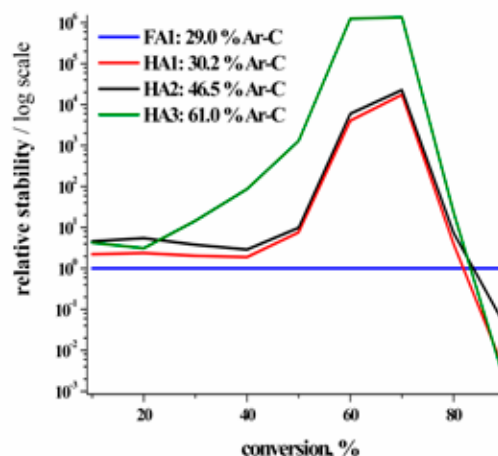

Fig. 2. **Relative stability curves of humic samples, Eq. (3)**

It is generally accepted that degradation proceeds from labile parts of humified matter to stable constituents represented by aromatic and heterocyclic cores. As suggested elsewhere[10], humic molecules tend to recombine and therefore the introduction of new, more stable molecules is probable.

Sample with the lowest aromaticity degree (FA1) has been selected as a reference and all other samples are compared to that one. It shows very low initial and also progressing
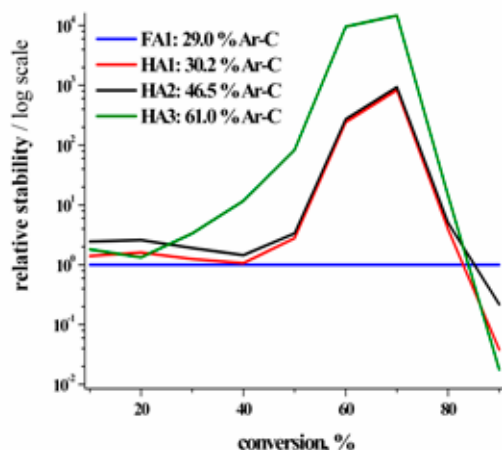
Fig. 3.   **Relative stability curves of humic samples, Eq. (4)**

stability during the degradation process, meaning that first the high amount of aliphatic parts degrade. The RS of all other samples show from 70 % of conversion steep decrease indicating the presence of original or newly ocurring aromatic moieties in FA1. Stability of this sample is at the end of the degradation process the greatest of all. HA1 is of same origin as FA1 differing only in the soil horizon and in higher aromaticty, of course. Their stability progress is up to 40 % more or less the same. The stability differs from higher conversion, which can be explained by higher content of aromatic C in sample HA1 and also by distinct types of present aromatic molecules when comparing fulvic to humic acid. Although the aromaticty of sample HA2 is much larger when compared to HA1, their conversion patterns as well as stability values are very similar. Both of the samples are of soil origin, suggesting presence of analogous molecules. Slighter difference can be observed from 80 % of conversion. The explanation can lie in the fact that in HA2 very stable aromatic constituents are present and their degradation occurs in the last stage. Sample HA3 displays different shape of stability curve from the very beginning. Its stability increases until the conversion of 70 % is reached but then it decreases and at the end of the degradation process the stability is the lowest of all examined samples. A presence of absolutely different aromatic and ali-

phatic molecules in comparison with other samples is highly probable because of its origin. Aromatic molecules in lignitic humic acids are supposed to possess more extensive condensation. Thus the stability from 30 to 70 % exhibits extremely high values. The end of the degradation process shows utterly opposite progress than that of sample FA1 with the lowest aromatic C content.

Conclusions

Summarizing all the results, it can be seen that the aromaticity itself is not the absolute indicator of stability of humic materials and their origin has to be taken into account. But it can be helpful in assessment of soil organic matter depletion and help in development of remediation and soil restoration techniques. Moreover, the discovery of the right temperature function and approximation could contribute to modelling of C flux in natural systems.

REFERENCES

1. v. Lützow M., Kögel-Knaber I., Ekschmitt K., Matzner E., Guggenberger G., Marschner B., Flessa H.: Eur. J. Soil Sci. *57*, 426 (2006).
2. Dick W. A., Gregorich E. G., in: *Managing Soil Quality: Challenges in Modern*, CABI Publishing, Oxon 2004.
3. Dell'Abate M. T., Benedetti A., Brookes P. C.: J. Sep. Sci. *26*, 433 (2003).
4. Hayes M. H. B., MacCarthy P., Malcolm R. C., Swift, R. S.: *Humic Substances II. In Search of Structure.* Wiley, New York 1989.
5. Šimon P.: J. Therm. Anal. Cal. *88*, 709 (2007).
6. Šimon P.: J. Therm. Anal. Cal. *82*, 651 (2005).
7. Šimon P.: J. Therm. Anal. Cal. *79*, 703 (2005).
8. Válková D., Kislinger J., Pekař M., Kučerík J.: J. Therm. Anal. Cal. *89*, 957 (2007).
9. Cibulková Z., Šimon P., Lehocký P., Balko J.: Polym. Degrad. Stabil. *87*, 479 (2005).
10. Kučerík J., Kamenářová D., Válková D., Pekař M., Kislinger J.: J. Therm. Anal. Cal. *84*, 715 (2006).

L07 NMR SPECTROSCOPY OF MINOR COMPOUNDS IN WINE A COMPARISON OF DIFFERENT PRE-CONCENTRATION METHODS

MILAN MAZUR, KATARÍNA FURDÍKOVÁ, MICHAL KALIŇÁK, MARIÁN VALKO, VLADIMÍR ŽÚBOR and NAĎA PRÓNAYOVÁ

Faculty of Chemical and Food Technology, Slovak Technical University, Radlinského 9, 812 37 Bratislava, Slovak Republic,
milan.mazur@stuba.sk

Introduction

The certification of the origin and geographical indications of food products has aroused increasing interest due to the introduction of European regulations for protection of agricultural products in the common market.[1–6]

Wine is a complex mixture of several hundred compounds present at different concentrations. The dominant ones are water, ethanol, glycerol, sugars, organic acids and various ions. Besides water, ethanol and glycerol, the other compounds like aliphatic and aromatic alcohols, amino acids and phenolic compounds are present at much lower concentrations[5]. Chemical analysis of complex mixtures like wine is becoming more important due to general endeavour to achieve adequate production quality. For wines particularly, differentiation according to wine variety, geographical origin and the year of production is of importance also in authenticity determination.[1–3]

High-resolution NMR spectroscopy has an outstanding position in the field of chemical analysis of food products because it is non-destructive, selective, and capable of simultaneous detection of many low molecular mass components in complex wine mixture[5]. The sample preparation for NMR spectroscopy is relatively simple and less time consuming. Another advantage of NMR spectroscopy is the possibility of detecting the magnetic resonance of different nuclei present in a molecule in different electronic and spatial environments. ^{1}H and ^{13}C NMR spectroscopy can successfully be used for detection of sugars, organic acids, anthocyans and amino acids present in wine as well as differences in their composition originating from different geographical area and can be used as a fingerprint for the monitoring of European wines.[5–10] Unfortunately, the weak signals of the minor compounds in NMR spectra are overlapped by the signals of other compounds present and especially by the dominant signals of water, ethanol and glycerol. For example, the amino acids are normally present in wine only at very low concentrations (in the range of 1–150 $mg\,dm^{-3}$) and therefore various techniques for the pre-concentration of the wine samples are needed.[8–10]

This contribution describes the comparison of three methods of sample preparation namely vacuum concentration, freeze-drying and argon-flow concentration with the results obtained from untreated wine for characterization of minor compounds in Slovak Chardonnay white wine by ^{1}H NMR spectroscopy.

Experimental

Apparatus

All ^{1}H NMR spectra were recorded on a Varian INOVA 600 MHz NMR spectrometer, which is located at Faculty of Chemical and Food Technology (Department of NMR and mass spectrometry, Bratislava, Slovakia), with a 5.00 mm indirect detection pulsed field gradient probe operating at 600 MHz for ^{1}H nuclei. The temperature during all experiments was 25 °C.

Chemicals

Deuterium oxide (99.9 %) was purchased from Aldrich and it contained 0.05% sodium 3-(trimethylsilyl)propionate $-2,2,3,3,-d_4$ (TSP) that served as an internal standard for chemical shift 0.0 ppm).

Sample preparation

Chardonnay white wine (Small Carpathian wine-growing region, Slovakia, vintage 2005) was selected for all NMR experiments. Four different groups of wine samples were prepared as follows:
- Wine samples were not pre-concentrated. In this direct analysis of wine samples 0.5 ml of wine was mixed with 0.1 ml D_2O for NMR field/frequency lock.
- Wine samples were pre-concentrated by vacuum-distillation. 5 ml of wine was pre-concentrated by vacuum distillation using rotary evaporation unit for 6 hours. The concentrate was dissolved in 1 ml of D_2O and 0.6 ml was used for measurement.
- Wine samples were pre-concentrated by freeze-drying. Again 5 ml of wine was frozen in liquid nitrogen and freeze-dried for 20 hours. The lyophylisate was dissolved in 1 ml of D_2O and 0.6 ml was used for measurement.
- Wine samples were pre-concentrated under argon-flow. Again, 5 ml of wine was dried under argon-flow for 2 hours until there was no further liquid in the sample. The dried sample film was dissolved in 1 ml of D_2O and 0.6 ml was used for measurement.

After the freeze and argon-flow- drying, close attention should be given to minimise the contamination of the dried sample with atmospheric humidity.[4,6–9] The pH values of all prepared samples were found in the interval of 3–4.

Measurement

^{1}H NMR spectra were acquired in 5 ml NMR tubes with and without the suppression of strong signals by presaturation. For suppression of large water signal the presaturation pulses (Varian pulse sequence PRESAT) were applied to irradiate the water signal at 4.80 ppm.

Results

It is known that ^{1}H NMR resonances of amino acids together with signals of succinic acid, glycol and buthylene glycol can be used to differentiate wines according to the wine variety, geographical origin and year of production.[3,5–10] In the present paper a different technique of the pre-concentration of the Chardonnay white wine has been investigated.

Fig. 1. shows the ^{1}H NMR spectra of the wine sample that was directly analyzed without any pre-concentration. The signal assignment in ^{1}H NMR spectra of wine samples was done according to literature[5–10] as follows: valine at 1.05 ppm, butylene glycol at 1.13 ppm, ethanol (CH₃) at 1.17 ppm, lactic acid 1.35 ppm, alanine at 1.49 ppm, isoleucine at 2.01 ppm, acetic acid/acetates at 2.04 ppm, proline at 2.34 ppm, malic acid at 2.63 and 2.82 ppm, succinic acid/succinates at 2.66 ppm, lysine at 3.04 ppm, citruline at 3.13 ppm, arginine at 3.26 ppm, ethanol (CH₂) at 3.64 ppm, glycerol (CH₂) at 3.62 ppm, glycerol (CH) at 3.76 ppm, tartaric acid at 4.79 ppm and water at 4.80 ppm.
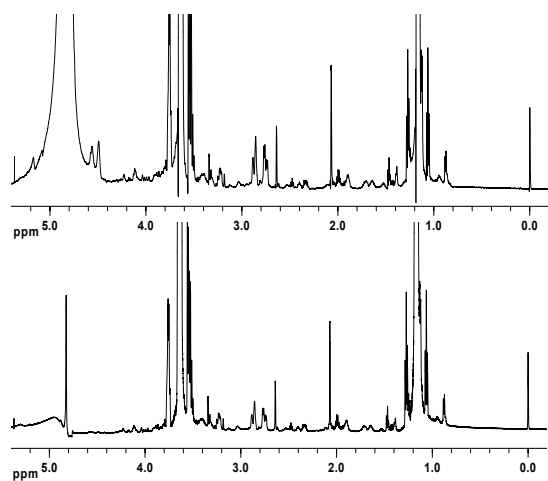
Fig. 1. Part of 1H NMR spectra of white wine (Chardonnay, Small Carpathian wine-growing region, Slovakia, 2005). Spectra were acquired: (a) without suppression of strong signals, (b) with suppression of water signal by presaturation. Wine samples were not pre-concentrated (direct analysis of wine samples). For assignment of selected signals of amino acids see text

It is obvious that ^{1}H NMR spectra of wine are very crowded and many signals are overlapping (see Fig. 1.). Because of the different concentration levels of the particular compounds the signal intensities can vary by the factor of 20 or more. Therefore the small signals of minor compounds are overlapped by the signals of dominant compounds (water, ethanol and glycerol) and the correct assignment is very problematic. In accord with literature data[5–10], the region of the spectrum between 0.5–2.5 ppm contains the signals from many species including ethanol, acetic acid and acetates. Strong signal of ethanol at 1.17 ppm shows overlapping and it causes difficulties in the assignment of this region. Between 2.5–5.5 ppm the spectrum shows signals related to the principal organic acids present in wine (malic,

sucinic, lactic and tartaric). However the tails of the dominant frequencies of ethanol at 3.64 ppm and glycerol at 3.62 and 3.76 ppm obscure the weak signals in the vicinity of the strong ones. This causes problems with the assignment of ^{1}H signals in the region between 3.6–4.8 ppm, in which the signals of (CH₂) protons of amino acids and the signals of sugars are expected[7,9].

Successful suppression of intense signals improves the clarity of the spectrum and the signal to noise ratio. With the increasing amplification of the vertical scale the baseline near the strong signals is strongly affected by their tails in the spectrum without suppression, whereas in the case of suppression their influence on the surrounding is significantly reduced. Nevertheless, when using the signal suppression techniques we have to be aware that some information from the spectra close to the suppressed signals may be lost[9], because suppression causes "holes in the spectrum". The penalty is not significant considering the extra amount of information obtained.

It is common to use some kind of pre-concentration technique in the preparation procedure[4,6-9]. Most prevalent techniques are vacuum-distillation using rotary evaporation unit, lyophilization and drying under nitrogen-flow. Concentrated samples are obtained that contain not only the compounds of interest but also some portion of major constituents that may cause the signal shifting and/or line broadening[9].
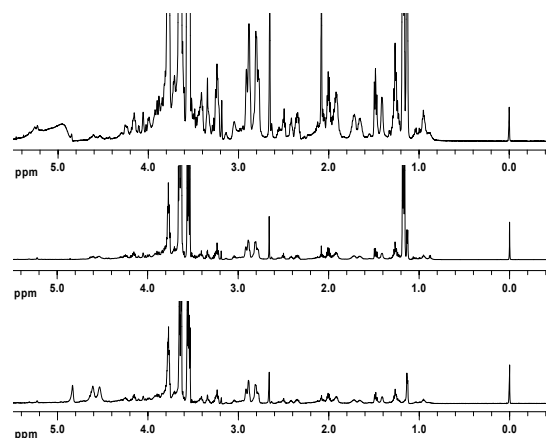

Fig. 2. Part of 1H NMR spectra of white wine (Chardonnay, Small Carpathian wine-growing region, Slovakia, 2005). Spectra were acquired with suppression of water signal by presaturation. Wine samples were pre-concentrated: (a) by vacuum-distillation, (b) by freeze-drying, (c) under argon-flow. For assignment of selected signals of amino acids see text

Fig. 2. shows ^{1}H NMR spectra of Chardonnay wine samples, which were pre-concentrated by (a) vacuum-distillation, (b) freeze-drying and (c) argon-flow. The water signal (at 4.80 ppm) was suppressed by presaturation. The ^{1}H spectra of wine samples pre-concentrated by vacuum-distillation and freeze-drying (Fig. 2.a and b) still show signals at 1.17 and 3.64 ppm that demonstrate a low quantity of ethanol remained in these samples. This is in accordance with litera-

ture data.[6–10] Differences in signal intensity were also observed especially for compounds such as acetic acids and acetates at 2.04 ppm when compared to the ^{1}H spectrum of wine without pre-concentration (see Fig. 1.). The drying of Chardonnay wine by argon-flow revealed compounds between 1.0–1.5 ppm in the ^{1}H NMR spectrum (Fig. 2.c). It is clear that the ethanol signals were diminished in the spectrum of such pre-concentrated sample. As shown in literature[7], this allows the determination of butylene glycol and alanine at 1.13 and 1.49 ppm. The presence of significant resonance of lactic acid at 1.35 ppm (due to malolatic fermentation) makes difficulties to assign alanine signals. Between 2.0–3.4 ppm peaks from organic acids, arginine and proline are also observed in the ^{1}H NMR spectrum of the Chardonnay wine samples pre-concentrated by argon-flow. The 3.5–4.0 ppm region of the spectrum still shows a strong contribution of the glycerol. Then the spectral distinction of carbohydrate is extremely difficult due to peak overlap[7].

As cited in the literature[6–10], even after more than two days of freeze-drying some water and ethanol remained in the lyophylisate. Because prolonged drying is not acceptable for a procedure that should required as little time as possible, the limit ca 20 hours is a good compromise between acceptable time of sample preparation and losing sensitivity in NMR measurement. The conditions of vacuum-distillation and mainly during freeze-drying are not easily controlled and the temperature and pressure must be well monitored in order to reach a good state of reproducibility[7,9]. In vacuum-distillation, freeze-drying and argon-flow-drying it is not possible to make quantitative analysis of the volatile compounds due to their evaporation[7,9]. In complex mixture such as wine, care should be taken to pH, which may influence considerably the chemical shifts[9]. Attention should also be paid to the concentration of paramagnetic species in the wine samples.

Conclusions

High field NMR spectroscopy has been shown to be a promising method for the non-destructive analysis of minor components in wine. However, the direct analysis of minor compounds such as amino acids in wine samples by ^{1}H NMR is limited by overlapping of their weak signals by strong signals of dominant compounds (water, ethanol and glycerol).

In the wine samples pre-concentrated by vacuum-distillation (for 6 hours) a low quantity of water and ethanol, but relative high glycerol concentration still remained in the sample. The same is true for the freeze-dried samples and additionally this process is relatively long (about 20 hours) and its reproducibility is affected by many factors. Diminution of the ethanol signal was observed in ^{1}H NMR spectra of the wine samples, which were dried under argon-flow. Unfortunately, a relative high quantity of glycerol is still present in the sample even using this technique. The argon-flow drying shows advantages in the identification of compounds present as minor constituents and it is less time consuming (ca 2 hours).

REFERENCES

1. Košir I. J., Kocjančič M., Ogrinc N., Kidrič J.: Anal. Chim. Acta *429*, 195 (2001).
2. Ogrinc N., Košir I. J., Kociancič M., Kidrič J.: J. Agric. Food Chem. *49*, 1432 (2001).
3. Ogrinc N., Košir I. J., Spangenberg J.E., M., Kidrič J.: Anal. Bioanal. Chem. *376*, 424 (2003).
4. Košir I. J., Lapornik B., Andrašek S., Wondra A. G., Vrhovšek U., Kidrič J.: Anal. Chim. Acta *512*, 277 (2004).
5. Košir I. J., Kidrič J.: Anal. Chim. Acta *458*, 77 (2002).
6. Brescia M. A., Caldaroda V., De Giglio A., Banedetti D., Fanizzi F. P., Sacco A.: Anal. Chim. Acta *458*, 177 (2002).
7. Amaral F. M., Caro M. S. B.: Food Chem. *93*, 507, (2005).
8. Košir I. J., Kidrič J.: Analusis *26*, 7797 (1998).
9. Košir I. J., Kidrič J.: J. Agric. Food Chem. *49*, 50 (2001).
10. Brescia M. A., Košir I. J., Caldaroda V., Kidrič J., Sacco A.: J. Agric. Food Chem. *51*, 21 (2003).

L08 HYDROPHOBIZATION OF PAPER BY VAPOURS IN N₂ PLASMA AT ATMOSPHERIC PRESSURE

MILAN MIKULA, ZUZANA JAKUBÍKOVÁ and VIERA JANČOVIČOVÁ

Faculty of Chemical and Food Technology STU, Radlinského 9, 812 37 Bratislava, Slovak Republic,
milan.mikula@stuba.sk

Introduction

Increasing demands for new materials and solutions in printing and packaging industry cause continuous innovation in a growing market. Paper and cellulosic materials are still promising candidates for flexible materials provided suitable properties including barrier ones such as water repellence and grease resistance[1]. Other demands are focused in restoring of naturally aged papers, documents and books in archives heritage to save and stabilize them[2].

Surface modification like hydrophobization, strengthening or stabilization of paper/cellulose can be achieved by standard coatings or also by several chemical vapours deposition (CVD) techniques[1–4] mostly enhanced by plasma (PECVD) or using plasma polymerization. Plasma deposited films have several advantages: compact layers are pinhole-free, chemically inert, insoluble, mechanically tough, thermally stable and coherent and highly adherent to variety of substrates[1]. However, often thin inhomogeneous and discontinuous (island type) coatings are produced by plasma assisted deposition or grafting. Despite of just the top surface modification the surface energy is changed considerably[3,4].

Low-pressure plasma treatment is not convenient to treat common paper, because of the vacuum problems and long and expensive process. So, the atmospheric pressure discharges are preferentially used, particularly the corona discharge and several types of dielectric barrier discharges (DBD).[4–6] Next advantages of atmospheric discharges are a high effectivity of free radical, metastables and excimers creation and the ability of high rate and large scale of technological treatment. The energy of the plasma breaks the molecular bonds on the surface of the substrate. The broken bonds then recombine with the free radicals from the plasma bulk to form additional functional groups on the film surface, where grafting, polymerization or crosslinking can occur. In the presence of oxygen, the high speed oxidation occurs, that results in high surface energy, polarity, wettability, but also in degradation[6]. Under special conditions plasma etching can be applied to cleaning or even to thinning the paper. Thinning the cellulose it can convert to a low energy hydrophobic surface[7]. However, hydrophobization is mostly made by fluorinating thin layer, e.g. with fluorotrimethylsilane[3], CF_4, SF_6 or C_4F_8.[1–4]

Also organosilicon compounds (particularly hexamethyldisiloxane HMDSO) are used to achieve hydrophobization of paper/cellulose[3,5,8], where the presence of a crosslinked macromolecular structure, based on $Si-O-Si$ and $Si-O-C$ linkages was detected. Implanted functional groups (as $-Si(CH_3)_x$) at the surface layers of the paper substrates are chemically linked mainly to the lignin component on the paper[3]. Water absorption of papers was significantly reduced (from hundreds to tens $g\,m^{-2}$ of water) and the contact angle increased from $<15\,°$ to $>120\,°$ while the strength properties and brightness of the papers remained practically unaffected.

Plasma has been already used in the restoration of naturally aged paper, focusing on sterilization, cleaning and deacidifying books as well, by using alkaline plasma (nitrogen, ammonia) and strengthening them by a grafting and coating by a plasma polymerization[2,9].

In this work, we investigate the hydrophobization of different papers by vapours of HMDSO and 3 carbohydrates activated in N₂ plasma at atmospheric pressure in 2 manners.
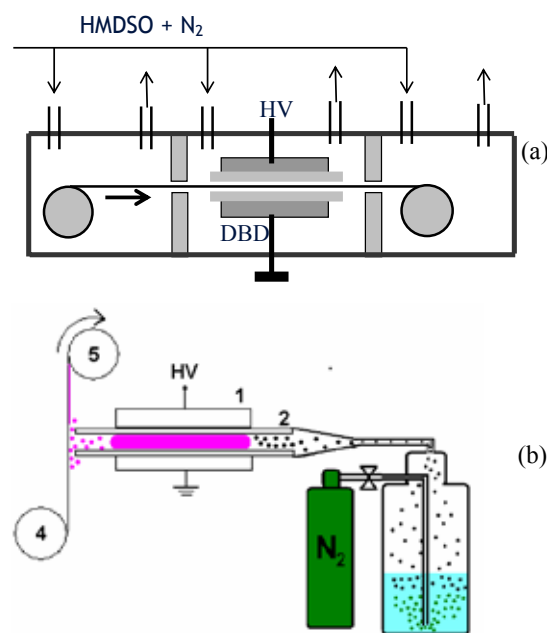

Fig. 1. **Paper treatment inside DBD (a) and in down-stream after-DBD (b) plasma**

Experimental

- Two techniques of plasma treatment of papers were used. *(i)* The volume dielectric barrier discharge (DBD, 15 kV, 5 kHz) in standard configuration (Fig. 1.a), where the treated paper is going directly through the plasma of the mixture of N₂ and vapours, everything inside the air protective chamber ("inside-DBD" regime). *(ii)* The plasma mixture of N₂ and vapours is created in DBD and is blown onto the untreated paper passing 2 mm near the jet in common air atmosphere (Fig. 1.b, "after- DBD" regime).
- Three different paper sheets were used as substrates: cellulosic Whatman (standard filter paper, No. 1001-917, England, 90 $g\,m^{-2}$, thickness 280 mm), newsprint paper (NP, simulating acidic papers from 19–20th century,

45 g m^{-2}, Vetrni, Czech. Rep.) and common office copy paper (CP, woodfree, white, 80 g m^{-2}, Europapier)
- 4 different monomers: hexamethyldisiloxane (HMDSO), n-heptane, cyclohexane and toluene were used as vapours in a mixture with nitrogen created by percolating of nitrogen through the bottle of liquid monomer.
- Paper properties were characterized by 5 ml water drop imbibition using CCD camera (SEE software 6.1, MU Brno, Czech.Rep.,) by FTIR spectroscopy (Excalibur, FTS 3000 MX, Digilab, USA, resolution 4 cm^{-1}) with total reflection (ATR) technique (25 reflections KRS-5 crystal, 45 °), and by water adsorption measurement using classical McBain balances with quartz spiral (1,230 mm g^{-1}).
- Aging stability of the modified paper was tested by artificial accelerated thermal aging according new method of Begin-Kaminska (5 days in closed bottle at 100 °C, RH 50%)[10]

Results

The papers treated in mixture plasma of nitrogen and vapours exhibited hydrophobic character as was evident from icreasing water contact angles up to 120 ° already in short exposition times Table I. However, when the water drop imbibition occurs the contact angle is not relevant parameter because of non stable drop. The changes to hydrophobic character can be better evaluated by imbibition (soaking) kinetics (Fig. 2.).

Table I
Contact angles [°] of water drop at initial and plasma treated paper surfaces, after-DBD, 60 J cm^{-2}

Papers	Initiale surface	Pure N$_2$	HMDSO	n-heptane	Cyclo-hexane	Toluene
Whatm.	n*	n*	122	90	110	105
NP	65	85	119	100	106	105
CP	85	75	120	102	105	110

n* – nonmeasurable

The flow rate of N$_2$ through the liquid monomer (HMDSO) was optimized to a value of 3.8 dm^3 min^{-1} for standard inside-DBD regime and 6.8 dm^3 min^{-1} for after-DBD regime.

Drops volumes for soaking experiments were round 5 ml and the volume of spherical cap, *V*, was calculated from the sessile drop radius *r* and height *h* and contact angle q:

$$V = \pi h^2(3r-h)/3 \qquad h = r(1-\cos\theta) \qquad (1)$$

The rate of imbibition (in ml s^{-1}) was calculated from the slope of imbibition kinetics (Fig. 3.), where some minimum was achieved for inside-DBD. It is caused by creation/degradation balance inside the plasma. Stronger hydrophobization was achieved by after-DBD, however it is less effective energetically (10 times higher exposition) than inside-DBD,
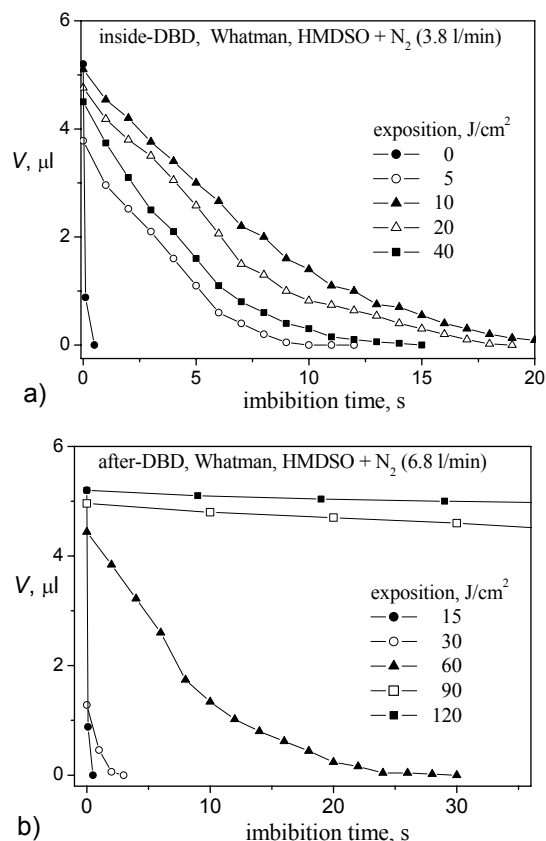

a)

b)

Fig. 2. **Time evolution of sessile water drop volume for Whatman and HMDSO and different expositions, for inside-DBD (a) and after-DBD (b) regimes**
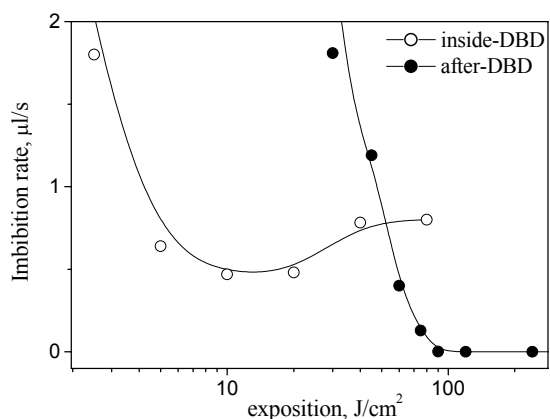

Fig. 3. **Exposition dependence of imbibition rates for Whatman treated inside-DBD and in after-DBD (N$_2$/HMDSO)**

and some problems could be in physical bonding of coating to the paper. So, the exposition was optimized to 10 J cm^{-2} for inside-DBD and to 80 J cm^{-2} for after-DBD.

Other three monomers (n-heptane, cyclohexane and toluene) were applied to treat papers just in optimized exposition doses. The level of hydrophobization correlates with reverse rate of imbibition, that is the imbibition time of 1 ml,
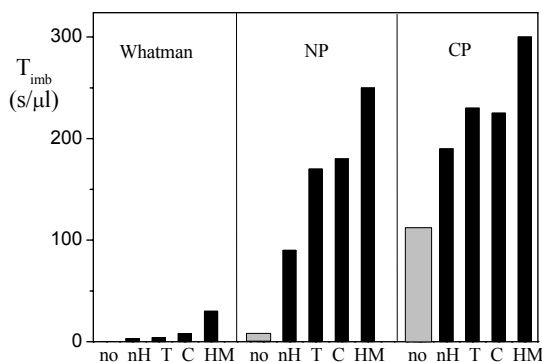
Fig. 4. **Water drop imbibition time for different vapours and treated papers in after-DBD (no – initial paper, nH – n-heptane, T – toluene, C – cyclohexane, HM – HMDSO)**
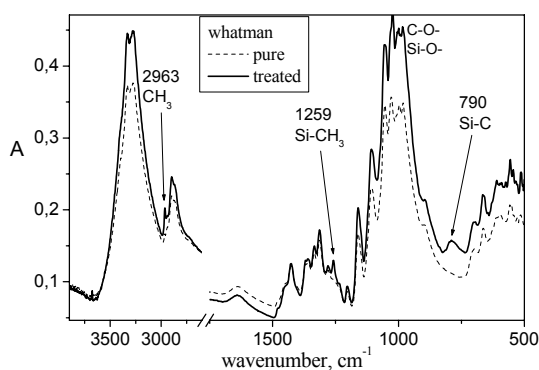

Fig. 5. **25-reflection ATR-KRS-5 IR spectra of pure and modified Whatman (after-DBD, HMDSO, 6.8 dm^3 min^{-1})**

T_{imb} [s ml^{-1}]. Calculated T_{imb} from experimental data of imbibition kinetics are shown in Fig. 4. for all vapours and substrate materials used.

The level of hydrophobization is very different for different papers, because of big differences of initial materials including wetting and roughness. The hydrophobization is most effective in case of newsprint paper (NP) and generally using HMDSO. However, the data dispersion is very high (up to 30 %), because of materials inhomogenity, DBD instabilities and inhomogenities and droplet soaking errors.

The changes of absorption IR spectra (surface ATR technique) of treated paper surfaces were generally very small. It means that very thin surface layer of paper is affected or very thin deposited layer is created, considering paper porosity. In the most successful case of HMDSO, some new functional groups are readable in FTIR spectra, Fig. 5.

The hydrophobized papers exhibited interesting performance after artificial aging. Namely in the case of inside-DBD and at long time expositions the aging causes considerable increase of hydrophobic character, probably because of recombination (and crosslinking) of long live free radicals created in plasma during long exposition.

Despite of noticeable hydrophobization in soaking process, adsorption properties of papers hydrophobized in both

manners were changed just a little, Fig. 6. The adsorption was performed at 25 °C, however, it is not typical isotherm, because of relatively quick increase of RH (1 % min^{-1}).

If slower increase were applied (0.1 % min^{-1} – equilibrium regime), the curves were nearly identical with the non-treated Whatman paper. It means that the long-term water sorption maintained unchanged, while the penetration rate was lowered due to hydrophobic surface.

It indicates that the paper porosity did not changed practically with the hydrophobization processes. Probably, the hydrophobic coating is very fine, discontinual, with an island-like character, and the thickness of coating as well as the islands dimensions are in nanometer scale.
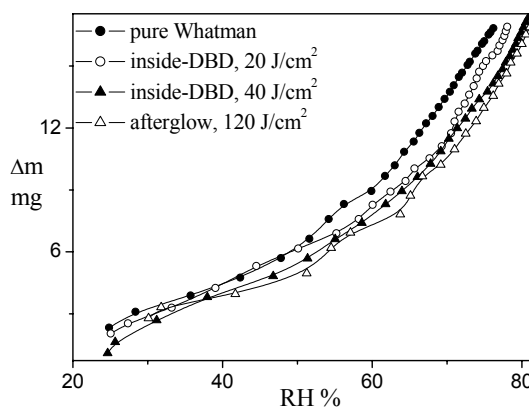

Fig. 6. **Adsorption kinetics of modified papers at 25 °C (RH increase rate: 1 % min^{-1}, samples weight: 180 mg)**

Conclusions

Different papers were continuously modified/hydrophobized by dielectric barrier discharge (DBD), inside DBD and down stream (after-DBD), using nitrogen as working gas with four organic vapors (including hexamethyldisiloxane, HMDSO). Modified papers were characterized by water imbibition (soaking), sorption and penetration kinetics and by absorption FTIR spectroscopy (surface sensitive ATR techniques).

The levels of hydrophobization of papers are very different for different papers and vapours, because of big differences of initial materials including wetting and roughness. The hydrophobization was the most effective using HMDSO and good noticeable for newsprint paper (NP) and Whatman. However, the data errors were very high (30 %) due to paper surface inhomogenities and instabilities of DBD that ought to be more controlled.

REFERENCES

1. Vaswani S.: Dissertation, Georgia Inst.of Technol., USA 2005.

2. Vohrer U., Trick I., Bernhard J., Oehr C., Brunner H.: Surface and Coatings Technol. *142*, 1069 (2001).

3. Navarro F., Davalos F., Denes F., Cruz L. E., Young R. A., Ramos J.: Cellulose *10***,** 411 (2003).

4. Kloc P., Sťahel P., Buršíková V., Brablec A., Navrátil Z., Šíra M., Janča J.: Czech. J. Phys. *56***,** 1345 (2006).

5. Trunec D., Navrátil Z., Sťahel P., Zajíčková L., Buršíková V., Cech J.: J. Phys. D: Appl. Phys. *37***,** 2112 (2004).

6. Mikula M., Jakubíková Z., Zahoranová A.: J. Adhesion Sci. Technol. *17,* 2097 (2003).

7. Sapieha S., Wertheimer M. R.: *Application of plasma microtoming in paper science. Proc. of Int. Paper Physics Conf.*, Kailua Kona, USA (1991)

8 Šíra M., Trunec D., Sťahel P., Buršíková V., Franta D.: Czech. J. Phys. *56*, 1377 (2006).

9 Havermans J.: Abbey Newsletter *19*, 1 (1996).

10 Bégin P. L., Kaminska E.: Restaurator *23*, 89 (2002).

L09 FLUORESCENCE STUDY OF POLYSACCHARIDE IN DILUTE AQUEOUS SOLUTION

FILIP MRAVEC[a,b], TEREZA HALASOVÁ[b], MILOSLAV PEKAŘ[b] and VLADIMÍR VELEBNÝ[a]

[a]*CPN Ltd, Dolní Dobrouč 401, 561 02 Dolní Dobrouč, Czech Republic,*
[b]*IPAC FCH BUT, Purkyňova 118, 612 00 Brno, Czech Republic,*
mravec@fch.vutbr.cz

Introduction

During the last ten years, hyaluronan molecule rises in his importance. Due to its high biocompatibility and its common presence in the extracellular matrix of tissues, hyaluronan is gaining popularity as a biomaterial scaffold in tissue engineering research. Its modification can fortify hyaluronan's unique properties and opens a new fields for application this polysaccharide.

One of the most sensitive, progressive, and modern methods successfully used in investigation of polymer surfactant, is fluorescence spectroscopy. Widely used fluorescence probe method looks useful in our research; because of it contains additional information about investigated system – micellar properties, polarity, fluidity, dimensions.

We hope we are able to contribute with our results to clarification-complicated relations in this interesting system.

Experimental

Sodium hyaluronate and its derivatives (Fig. 1.) were obtained from CPN Ltd. (Dolní Dobrouč, Czech Republic). Details on the synthesis of derivatives have been published elsewhere[1]. Hyaluronate was of the molecular weight around 500 kg mol^{-1}.

All derivatives have the molecular weight around 500 kg mol^{-1}, and their substitution degrees were in the range from 10 to 70 %. Substitution degree is defined as the ratio of the mol of substituents per mol of the disaccharide unit, e.g. SD 100 % means one alkyl chain per each disaccharide unit in the hyaluronate chain. All the molecular parameters were determined and provided by the producer. The molecular weights were determined by SEC-MALLS and the substitution degree is defined from the ^{1}H NMR spectra[1]. The hyaluronate samples were dissolved in doubly distilled water
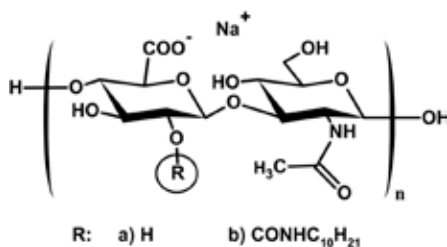
to the concentration 5 g dm^{-3}. This stock solution was stabilized by addition of sodium azide (p.a., Lachema) in final concentration 10^{-3} mol dm^{-3}.

The stock solution of pyrene (purchased from Fluka, GmbH; *for fluorescence grade*) was prepared in acetone. Probe stock solution was introduced into a vial and acetone was evaporated. The concentration of the probe in final samples was set to 5×10^{-6} mol dm^{-3}. The stock solution of HA or hHA was introduced into the vial with the probe, diluted to the desired concentration, and the resulting solution was sonicated for 4 hours and stored during next 20 hours. The fluorescence emission spectra were monitored with a luminiscence spectrophotometer (AMINCO-Bowman, Series 2) at 293.15 ± 0.1 K. The excitation and emission slit widths were set to 4 nm, and the excitation wavelength was 335 nm.

The experimental data, i.e. the pyrene I_1/I_3 ratio (y) dependency on concentration (x), were evaluated using non-linear fitting with Boltzman's curve containing four parameters – the maximum (a), the minimum (b), the inflex point (x_0), and the width of the step change (Δx) (Equation 1).

$$y = \frac{a-b}{1+e^{x_0-x/\Delta x}} + b \qquad (1)$$

The stock solution of acridine orange (AO, purchased from Sigma-Aldrich, Co.; hydrochloride hydrate) was prepared in distilled water. Probe stock solution was introduced into after addition of HA or hHA stock solutions. The concentration of the probe in final samples was set to 5×10^{-6} mol dm^{-3}. The resulting solution was simiraly treated as pyrene's samples. The fluorescence emission spectra were monitored with a luminiscence spectrophotometer (AMINCO-Bowman, Series 2) at 293.15 ± 0.1 K. The excitation and emission slit widths were set to 4 nm, and the excitation wavelength was 492 nm.

Acridine orange is a much-studied member of a class of cationic dyes whose planar molecules aggregate in aqueous solution to cause concentration-dependent spectral changes (metachromasy).[Y] Direct evidence for the aggregation of AO has been obtained from proton chemical shifts. The concentration dependence of changes in the visible absorption spectrum of dilute AO solutions is consistent with dimerization equilibrium. The emission spectrum of AO in aqueous
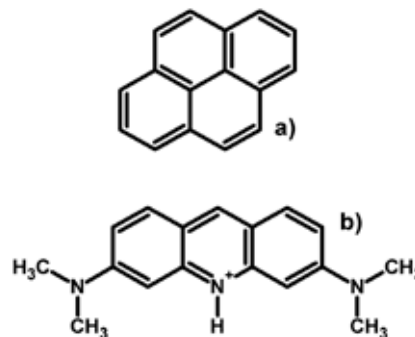

Fig. 1. **Schematic structure of the sodium hyaluronate (a) and its C$_{10}$ alkyl-derivative (b)**

Fig. 2. **Schematic structure of the pyrene (a) and protonated form of the acridine orange (b)**

solution has a maximum at 532 nm. In the highest concentration range a new weak emission band at 630 nm is occurs. This band is related to the forbidden H-type aggregate transition. Formation of aggregates (dimers) leads to the decreasing o the fluorescence intensity.[Z]

Results
Pyrene and AO in Native Hyaluronan

Existence of hydrophobic patch, resulted from secondary structure of the hyaluronan molecule in aqueous solution, allow hyaluronan's chains aggregate to form helical structures.[X] Dissociated carboxylic groups from the *D*-Glucuronic sub-unit in aqueous solutions make hyaluronan's chain possible to interact via electrostatic interaction with a cationic species.

First measurements have been focused on possible aggregation behavior of native hyaluronan in aqueous solution. Molecular weight 500 kg mol^{-1} was selected to investigate its concentration dependencies in the presence of pyrene and acridine orange. Fig. 3. shows obtained results. It is obvious that the polarity index, ranges only from 1.40 to 1.42 through a wide concentration range. Value of the polarity index in this concentration range can be taken as constant and invariant on the hyaluronan concentration. So, from the hydrophobic polarity probe point of view no aggregation behavior was observed in these solutions and in this concentration range. Hyaluronan molecule is also known as extremely hydrophilic specie, thus it organizes water molecules around the chain resulted in water barrier. This barrier looks to be insuperable for the pyrene.
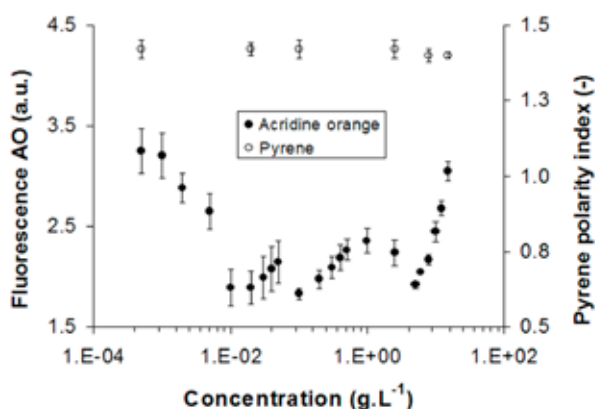

Fig. 3.   **Dependencies of the pyrene polarity index and the fluorescence intensity of the acridine orange on the concentration of the native hyaluronan in aqueous solution. Hyaluronan molecular weight was 500 kg mol^{-1}**

On the other hand, electrostatic interaction between AO and hyaluronan gives interesting results. First decreasing of the AO fluorescence can be ascribed to the AO dimer formation on the HA chain. This dependency has two minimums. First, correspond to the equal point 1 mol of the AO dimer

per 1 mol of the COO$^-$ group. Second minimum corresponds to the range of the physiological concentration of the hyaluronan. In concentration around 1 g dm^{-3} a polymer domain overlay is occurs. This phenomenon will take a part in next investigation.

Pyrene in Alkyl Modified Hyaluronan

Results with hydrophobized hyaluronans, obtained for D30/30 a 1,470/30, are presented in Fig. 4. For good lucidity, concentration values are plotted in dimension g dm^{-3}. The CAC value for lower molecular weight looks to be lower than for higher molecular weight. After the conversion of the concentration dimension from "g dm^{-3}" to "10^{-6} mol dm^{-3}" the CAC value for 1.470 kg mol^{-1} (1.667 × 10^{-6} mol dm^{-3}) is 25-times smaller than for 30 kg mol^{-1} (0.068 10^{-6} mol dm^{-3}).
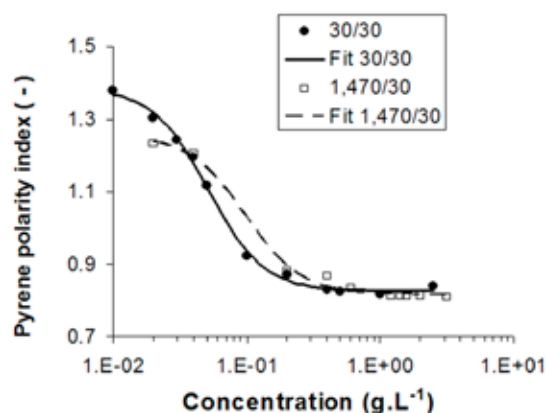

Fig. 4.   **Pyrene polarity index in hydrophobized hyaluronan aqueous solution. Derivatives were in the same degree of substitution 30 % and in different molecular weights, 1.470 (□) and 30 kg mol^{-1} (●)**

Aguiar and co-workers[5] suggested a condition to select the CAC value from the pyrene polarity index. If the $x_0/\Delta x$ (cf. Eq. (1)) is less than 10, the CAC point is determined by the *x*-coordinate of the inflex point x_0. All of hyaluronan derivatives used in this study passed this the "less than 10-condition".

Aggregate process of the modified hyaluronan was also studied through the electrostatic interaction with AO. Aim of this study was find out if alkyl chains association has an image in processes, which can influence Stern bilayer around polyectrolyte's surface.

Fig. 5. shows comparison of the pyrene polarity index and fluorescence intensity of the AO dependencies on the concentration of the modified hyaluronan. AO dependency shows after first decreasing an area with stable values of the fluorescence intensity. This plateau is followed with next decreasing of the fluorescence intensity. According to a prediction the decreasing of the AO fluorescence is caused only by the dimer formation, in concentration range, starts near CAC point, the hyaluronan's aggregate formation cause
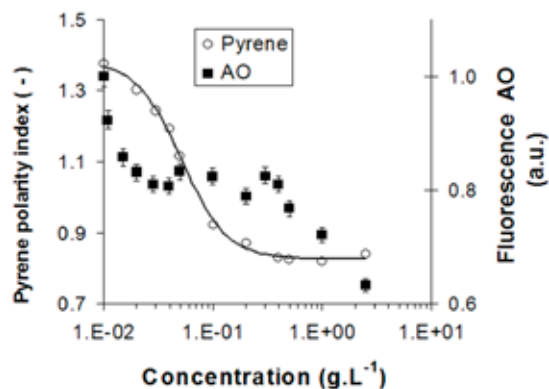
Fig. 5. **Comparison of the pyrene polarity index (○) and fluorescence intensity of the AO dependencies (■) on the concentration of the modified hyaluronan (1.470/30)**

that newly added carboxylics group are inaccessible for AO molecules. We predicted intermolecular formation process of these aggregate types.

Conclusions

The hyaluronan alkyl derivatives, with different molecular weights and same degree of substitution, show surfactant-like aggregation behavior in aqueous solutions. Their critical aggregation concentration was comparable in dimensions $g\,dm^{-3}$. Acridine orange can be used to determine aggregation process via electrostatic interaction with the modified hyaluronan.

Aggregation properties of sodium hyaluronate (HA) in molecular weight 500 kg mol^{-1} were studied by fluorescence methods. Interactions with hydrophobic fluorescence probe pyrene showed hydrophobically-modified analogues of sodium hyaluronate, as suitable systems for drug delivery applications. Properties of hydrophobic core were studied with polarity and viscosity fluorescence probes.

Interaction with hydrophilic probe acridine orange can help to understand native hyaluronate's self-aggregation behavior in aqueous environment. Depolymerization of dye-aggregates, evidenced by fluorescence intensity, showed an abrupt change in physiological concentration region (~ 1 g dm^{-3}). Acridine orange can be also used to determine aggregation process via electrostatic interaction with the modified hyaluronan.

REFERENCES
1. Mlčochová P., Bystrický S., Steiner B., Machová E., Velebný V., Krčmář M.: Biopolymers *82*, 74 (2006).
2. De S., Girigoswami A.: J. Coll. Int. Sci. *271*, 485 (2004).
3. Wang F., Yang J., Wu X., Wang X., Feng L., Jia Z., Guo C.: J. Coll. Int. Sci. *298*, 757 (2006).
4. Scott J. E., Heatley F.: Biomacromolecules *3*, 547 (2002).
5. Aguiar J., Carpena P., Molina-Bolívar J. A., Ruiz C. C.: J. Colloid Interface Sci. *258*, 116 (2003).

L10　SPIN-TRAPPING INVESTIGATION OF RADICAL INTERMEDIATES GENERATED FROM PHENOLS SPECIFIC BEHAVIOR OF *PARA*-METHYL PHENOLS

LADISLAV OMELKA, PETR MAJZLÍK, RENATA SUPERATOVÁ and PETRA HOLUBCOVÁ

Brno University of Technology, Faculty of Chemistry, Institute of Physical and Applied Chemistry, Purkyňova 118, 612 00 Brno, Czech Republic
omelka@fch.vutbr.cz

Introduction

The formation of phenoxyl radicals is the predominating process occurring by the oxidation of monohydric phenols using different agents (PbO_2, MnO_2, $RO_2^\bullet$). Their stability substantially depends on the substitution in the *ortho* position. Very high stability is the typical feature of the phenoxyl radicals derived from 2,6-di-alkyl substituted phenols, especially those with bulky *tert*-butyl substituent (sterically hindered phenols). Monohydric phenols with 2,6-dialkyl substituents containing α–CH bond, as well as phenols with unsubstituted or partially substituted *ortho* position (sterically unhindered phenols) provide by the oxidation the unstable phenoxyl radicals, which can be detected only using special EPR technique, *e.g.* flow[1] or spin trapping method[2]. It was found that the addition of sterically unhindered phenoxyl radicals to aromatic nitroso spin-traps (nitrosobenzene, nitrosodurene) proceeds in the *ortho* position and leads to two different types of nitroxyl radicals (1).

(1)
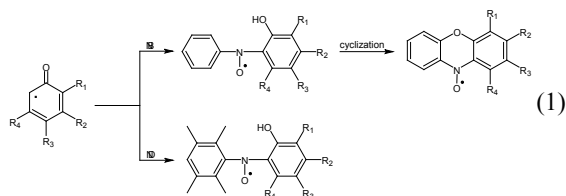
Although the generation of phenoxyl radicals, resulting from the abstraction of phenolic hydrogen atom plays an important role during the oxidation, the tendency towards the abstraction of hydrogen atom from methyl group in *para* methyl substituted phenols was also observed. The benzyl radicals formed were detected by spin-trapping technique using nitroso spin-traps[2,3]. The recombination products of benzyl radicals proved by the analysis of reaction mixture of oxidized 2,6-di-*tert*-butyl-4-methylphenol also support this mechanism, although there are also another theories interpreting their formation. To understand the specific behavior of *para* methyl group in substituted phenols in more detail, the oxidation of the series of phenols having this structure was investigated using spin-trapping method.
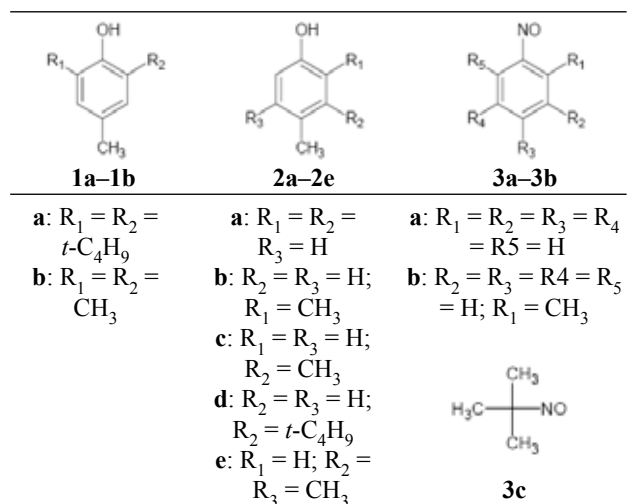
Experimental

All chemicals (phenols, nitroso compounds, *tert*.-butyl-hydroperoxide, PbO_2) were commercially available and were used without further purification. Toluene of analytical grade purity (Sigma) was used as the solvent in all experiments.

The oxidation of phenols in the presence of nitroso compounds was performed according to the following procedure: In 5×10^{-2}M toluene solution of the phenol the corresponding amount of nitroso compounds was dissolved, to adjust the molar ratio phenol : nitroso compound = 1 : 1. To 2 ml of this solution 150 mg PbO_2 were added under stirring. The stirring was regularly stopped in 30 min. interval and after the sedimentation of solid phase 0.3 ml of the reaction mixture were placed into the EPR tube. To obtain the high quality EPR spectra, the solution in the tube was bubbled with nitrogen for 30 sec.

Results

Hydrogen abstraction from *para*-methyl group was investigated within the series of different substituted phenols **1 – 2** in the presence of substituted nitroso compounds **3a – 3c**.

1a–1b	2a–2e	3a–3b
a: $R_1 = R_2 = t\text{-}C_4H_9$	**a**: $R_1 = R_2 = R_3 = H$	**a**: $R_1 = R_2 = R_3 = R_4 = R5 = H$
b: $R_1 = R_2 = CH_3$	**b**: $R_2 = R_3 = H$; $R_1 = CH_3$	**b**: $R_2 = R_3 = R4 = R_5 = H$; $R_1 = CH_3$
	c: $R_1 = R_3 = H$; $R_2 = CH_3$	
	d: $R_2 = R_3 = H$; $R_2 = t\text{-}C_4H_9$	
	e: $R_1 = H$; $R_2 = R_3 = CH_3$	**3c**

The oxidation of **1a** ($R_1 = R_2 = tert$.butyl) in the presence of nitrosobenzene (NB, **3a**) affords the mixture of radical products, where the corresponding phenoxyl radicals **4** ($a_H(CH_3) = 1.094$ mT, $a_H(m) = 0.155$ mT) together with benzyl radicals **5,** indirectly detected through the adducts **6** ($X = C_6H_5$; $a_N(NO) = 1.049$ mT, $a_H(CH_2) = 0.565$ mT, $a_H(o,p) = 0.273$ mT, $a_H(m) = 0.092$ mT)) prevail (2).

(2)
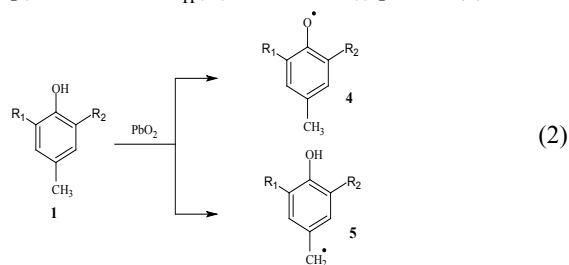
EPR parameters of **6** are similar to those observed by spin trapping of **5** with 3,5-di-*tert*.butyl-nitrosobenzene[3].

The concentration ratio between these two radicals depends on the experimental conditions and by the surplus of phenol over spin trap the pure EPR spectrum of the benzyl adduct

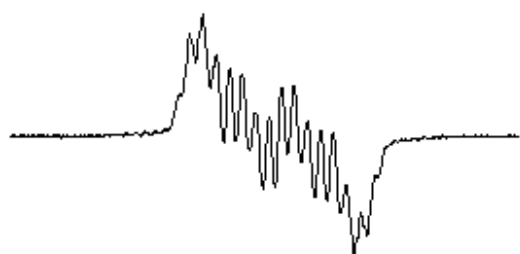Fig. 1.   **Experimental EPR spectra of nitroxyl radical 6 prepared from 2,6-di-tert-butyl-4-methylphenol 1a**

Fig. 2.   **Experimental EPR spectra of phenoxyl radical 8 prepared from 2,6-di-tert-butyl-4-methylphenol 1a**

can be observed (Fig. 1.).

Nevertheless, it was found that further changes in EPR spectra occur with time. One hour after the preparation of the sample the spectrum outlined in Fig. 1.b was detected. The g-value (g ≈ 2.0045) points out that the secondary phenoxyl radicals are formed in the consecutive steps of the oxidation. This statement is also supported by the splitting constant of two protons ($a_H = 0.15$ mT), which is the typical value of *meta* protons in phenoxyls. Other dominating splitting constants proved by the simulation of the experimental EPR spectra were attributed to one hydrogen and one nitrogen atom (Table I). Based on these experimental facts it is evident that the secondary phenoxyl radicals result from the
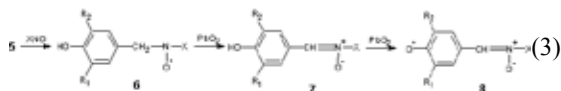
transformation of the benzyl adduct (3).

Moreover, the number of interacting nuclei suggests that the *para* position in secondary phenoxyls has the structure of the nitrone fragment $-CH = N^+O^- - C_6H_5$, which originates from the conversion of the nitroxyl moiety $-CH_2 - NO^{\bullet} - C_6H_5$. This implies that the nitrone **7** (X = C_6H_5) is the intermediate product, which is consequently oxidized to phenoxyl radical **8** (Fig. 2.). In the framework of further experiments the number of nitroso compounds was expanded. Besides nitro-

sobenzene other substituted derivatives X–NO (**3b**, **3c**) were studied. The analysis of EPR spectra proves that the above mentioned reaction route is valid, except for **3c**, in all cases under study.

On the other side, neither the adduct **6** nor the phenoxyl radical **8** was observed using 2-methyl-2-nitrosopropane **3c** (X = *tert.*-C_4H_9). Instead of them, only the nitroxyl radical X–NO–X (a_N(NO) = 1.555 mT) was detected, as a product of the decomposition of *tert.*-C_4H_9–NO on the surface of PbO_2. This fact is surprising, because the EPR parameters of the phenoxyl radical **8** (X = *tert.*-C_4H_9, Table I) produced by the oxidation of the nitrone **7** (prepared by reaction of 3,5-di-*tert*-butyl-4-hydroxybenzaldehyde with *N-tert*-butyl-hydroxylamine) using benzoyloxy radicals, are reported in the

Table I
EPR parameters of phenoxyl radicals 8 prepared by the oxidation of 2,6-di-tert-butyl-4-methylphenol 1a with PbO_2 in toluene solution in the presence of nitroso compounds (**3a–3c**)

X	aH(3.5) [mT]	aH(CH) [mT]	a(N) [mT]	a(X) [mT]
	0.150	0.290	0.510	0.090 (3H)
	0.150	0.280	0.490	–
	0.170 (1H) 0.150 (1H)	0.260	0.505	–

literature[4].

The experimental results obtained by PbO_2 oxidation of the sterically hindered 2,6-di-*tert*-butyl-4-methylphenol (**1a**) in toluene solution in the presence of different nitroso compounds X–NO initiated further investigation in this field. The tendency towards the liberation of one hydrogen atom from *para* methyl group was studied also with the methylated phenol (**1b**) and mono-, di- and tri- alkyl substituted phenols **2a–2e**. When 2,4,6-trimethylphenol (**1b**) was subjected to the oxidation, immediately after the addition of PbO_2 to the toluene solution of **1b** and nitrosobenzene the high concentration of benzyl adduct **6** ($R_1 = R_2 = CH_3$) was observed. Its EPR signal is stable for more then 24 hours without being overlapped by the signal of another radical. This fact seemingly points out that the suggested reaction route for **1a** (1), based on the conversion of benzyl adduct to nitrone **7** and consecutively to phenoxyl radical **8**, is not valid in this case. However, this effect can also be satisfactorily interpreted as a result of a substantially lower stability of 2,6-dimethyl-4R phenoxyl radicals in comparison with those derived from 2,6-di-*tert*.butyl-4R- phenols. The presence of nitrone **7** ($R_1 = R_2 = CH_3$) in reaction mixture was directly proved by the experiment, where *tert*.butylhydroperoxide was added to the reaction mixture 24 hours after the preparation of the adduct **6**. The high concentration of nitroxyl radical **9** with the

splitting constants (a_N(NO) = 1.049 mT, a_H(CH) = 0.175 mT, a_H(*o,p*) = 0.273 mT, a_H(*m*) = 0.092 mT) was observed in this
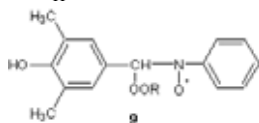
case.

The EPR parameters well agree with the published data for $RO_2^\bullet$ adducts with phenyl-*N*-phenyl nitrone[5]. The EPR signal undergoes further changes with time, which presumes the succesive degradation of hydrogen atom in nitrone fragment by peroxyl radicals.

Similarly as with **1a**, the simultaneous generation of corresponding phenoxyl and benzyl radicals is also expected in the course of the oxidation of sterically unhindered phenols **2a**–**2e** using PbO_2. In contrast to **1a**, the primary phenoxyl radical cannot be directly detected by EPR method due to their unstability. Nevertheless, by the application of spin trapping technique, they can be observed in the form of spin adducts. Due to the tendency towards the abstraction of hydrogen atom from *para* methyl substituent, the benzyl radicals

also react with nitroso spin traps and the generated adducts mostly dominate in the EPR spectrum. These EPR parameters do not substantialy differ from those observed in the case of **1a**, **1b**.

REFERENCES

1. Stone T. J., Waters W. A.: J. Chem. Soc. 213 (1964).
2. Omelka L.,Kováčová J.: Magn. Reson. Chem. *32*, 525 (1994).
3. Zhuzhgov E. I., Bazhin N. M.,Terpugova M. P.,Tsvetkov Y. D. Bull.: Acad. Sci. USSR (English translation) *23*, 2438 (1974).
4. Pacifici J. G., Browning H. L.: J. Am. Chem. Soc. *92*, 5231 (1970).
5. Cholvad V., Staško A., Tkáč A., Buchachenko A. L., Malík L.: Coll. Czech. Chem. Commun. 46, 823 (1981).

L11 VORTEX-FRACTAL-RING STRUCTURE OF MOLECULE

PAVEL OŠMERA

Brno University of Technology, Faculty of Mechanical Engineering, Technicka 2, 616 69 Brno, Czech Republic,
osmera@fme.vutbr.cz

Introduction

Most of our knowledge of the electronic structure of atoms has been obtained by the study of the light given out by atoms when they are exited. The light that is emitted by atoms of given substance can be refracted or diffracted into a distinctive pattern of lines of certain frequencies and create the line spectrum of the atom. The careful study of line spectra began about 1880. The regularity is evident in the spectrum of the hydrogen atom. The interpretation of the spectrum of hydrogen was not achieved until 1913. In that year the Danish physicist Niels Bohr successfully applied the quantum theory to this problem and created a model of hydrogen. Bohr also discovered a method of calculation of the energy of the stationary states of the hydrogen atom, with use of Planck's constant *h*. Later in 1923 it was recognized that Bohr's formulation of the theory of the electronic structure of atoms to be improved and extended. The Bohr theory did not give correct values for the energy levels of helium atom or the hydrogen molecule-ion, H_2^+, or of any other atom with more than one electron or any molecule. During the two-year period 1924 to 1926 the Bohr description of electron orbits in atoms was replaced by the greatly improved description of wave mechanics, which is still in use and seems to be satisfactory[1].

The discovery[1] by de Broglie in 1924 that an electron moving with velocity *v* has a wavelength $\lambda = h/mev$. The theory of quantum mechanics was developed in 1925 by the German physicist Werner Heisenberg. An equivalent theory, called wave mechanics, was independently developed early in 1926 by Austrian physicist Ervin Schroedinger. Important contribution to the theory were also made by the English physicist Paul Adrien Maurice Dirac. The most probable distance of the electron from the nucleus is thus just the Bohr radius r_o; the electron is, however, not restricted to this distance. The electron is not to be thought of as going around the nucleus, but rather as going in and out, in varying directions, so as to make the electron distribution spherically symmetrical[1].

This paper is an attempt to attain a new and profound model of the nature's structure using vortex, fractal and ring structures. Scientists try to explain some phenomena in Nature that have not been explained so far. The aim of this paper is the vortex-fractal modeling of vortex-ring fractal structure of atoms, molecules, and a creation of elements in the Mendeleev's periodic table with vortex-ring particles which is not in contradiction to the known laws of nature.

Electron with Vortex-Fractal-Ring Structure

The discovery of the electron was a landmark in physics and led to great technological advances. The electron emission is the process when negative charges in the form of electron, escape for example from the hot filament. Streams of electrons moving at high speed are called cathode rays or electron rays. The rays are deflected by a magnetic field too. If the N pole of a magnet is brought up to the neck of the tube, the rays move upwards, using Fleming's left-hand rule. The ratio of the charge *q* of an electron *e* to its mass m_e is called its specific charge and can be found from experiments in which cathode rays are deflected by electric and magnetic fields. It was first done by J. J. Thomson in 1897 using a deflection-type tube. His work is regarded as proving the existence of the electron as a negatively charged particle of very small mass and not, as some scientists thought a form of electromagnetic radiation like light.

Electron is defined as a fundamental particle of matter, with negative electric charge, which populates the outer region of atoms.

The electrical force decreases inversely with the square of distance between charges. This relationship is called Coulomb's law. There are two kinds of "matter", which we can call positive and negative. Like kinds repel each other, while unlike kinds attract – unlike gravity, where only attraction occurs[2]. When charges are moving the electrical forces depend also on the motion of charges in a complicated way[2,3,4].

Fractals seem to be very powerful in describing natural objects on all scales. Fractal dimensions and fractal measures are crucial parameters for such description. Many natural objects have self-similarity or partial-self-similarity of the whole object and its part[5].

The structure of the electron in Fig. 1 presents the electron as "pure" ring fractal structure. Electrons ^0e (or *e*) in the electron ray ^0r hold together by photon's vortex structure ^0f (a pair of vortices).[6–20] Generally, in the fractal structure of
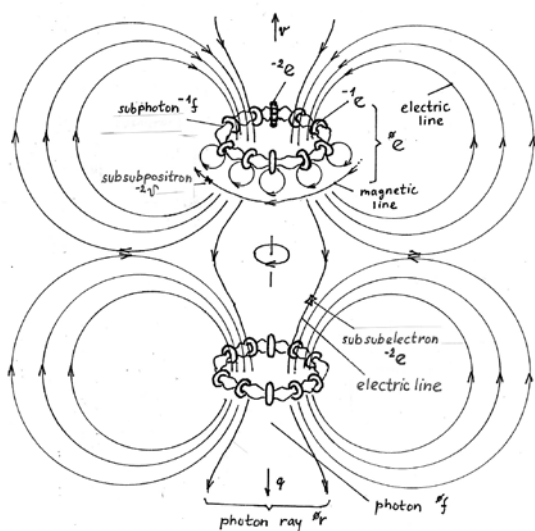

Fig. 1. **The vortex-fractal structure of the electron ray with two electrons[19]**

the electron, the number *n* defines the level of substructure $^n e$. The name osmeron we derived from the name "Osmera" of Egyptian deity with 4 pairs of gods as primary creative forces (from a chaos beginning). Osmerons are too small that is why have unmeasurable size and mass. Osmerons on osmeron's trajectory creates an osmeron ray.

We know that the apparent mass of a particle changes by $1/\sqrt{(1 - v^2/c^2)}$. Does its charge do something similar? No charges are always the same, moving or not[4]. If the charge of a particle depended on the speed of the particle carrying it, in the heated block the charge of the electrons and protons would no longer balance. A block would become charged when heated. If the charge on an electron charged with speed, the net charge in piece of material would be charged in a chemical reaction. Even a very small dependence of charge on speed would give enormous fields from the simplest chemical reactions. No such effect has been observed[3,4], and we conclude that the electric charge of a single particle is independent of its state of motion.

For a calculation[9,23] of the fractal-ring electron structure we will use the structure that is shown in Fig. 1. and Fig. 2. In the ring electron structure (see Fig. 2.) the subelectrons e_o rotate with a velocity v_e and subsubelectrons e_1 with a velocity v_o. The radius of the electron is R_e and a radius of axes of subelectrons e_o is r_e. A rough estimation of number of subrings is N and number of subsubring is N^2. They are determined in the electron structure by the mass m_p of the proton structure[17].

Let us calculate properties of the electron with a vortex-fractal theory[6–20]. This requires that subelectrons are accelerated towards the center of the electron ring. The amount of the acceleration force F_a has to be in balance with two coulomb forces F_o. A whole force of attraction F_A can be calculated by Ampere's law:
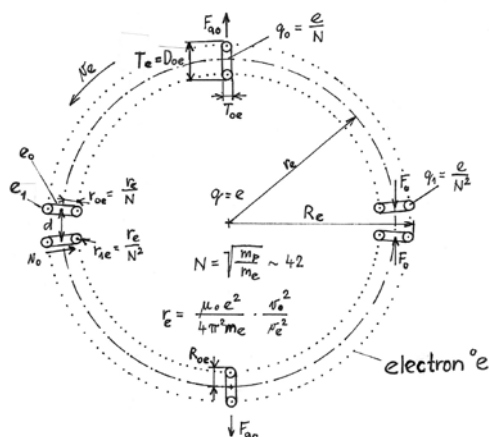

Fig. 2.　**The fractal-ring structure of the electron[17]**

$$F_a = F_A \qquad (2.1)$$

The fundamental physical law for an acceleration force F_a for mass *m* with velocity *v* and distance *r* is :

$$F_a \approx m \frac{v^2}{r} \qquad (2.2)$$

The mass m_{oe} of the subelectron e_o for the fractal structure of the electron is:

$$m_{oe} = \frac{m_e}{N} \qquad (2.3)$$

where N is number of subelectrons. To cover creation of the proton structure and the electron structure from the same very small rings (N^2 subsubelectrons e_1)[17,22]:

$$N = \sqrt{\frac{m_p}{m_e}} \approx 42 = 2 \cdot 3 \cdot 7 \qquad (2.4)$$

where m_p is the mass of the proton and me is the mass of the electron. From the fractal structure of the electron on Fig.2:

$$F_e = F_{ao} \cdot \frac{2}{\pi} \cdot \frac{N}{2} = \frac{m_e v_e^2}{N r_e} \cdot \frac{2}{\pi} \cdot \frac{N}{2} \qquad (2.5)$$

The average value of forces F_{ao} for *N/2* subelectrons is on Fig.3. Their average value *2/π* was calculated following way:

$$\int_0^\pi \sin x\, dx = 2 \qquad (2.6)$$

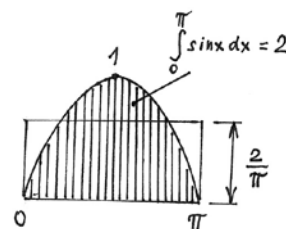$$\frac{\int_0^\pi \sin x\, dx}{\pi} = \frac{2}{\pi} \qquad (2.7)$$

Fig. 3.　**Average value of the acceleration force F_{ao}**

The fundamental physical law for attraction force F_A (Amper's law) between two wires with a current *I*, a length *l*, a distance *d*, and a permeability μ_o of vacuum:

$$F_A \approx \frac{\mu_o}{2\pi} I^2 \frac{l}{d} \qquad (2.8)$$

Electric charges *q1* in the subring *e1* create the current *I*:

$$I = \frac{dQ}{dt} = \frac{q_1 N}{T} \qquad (2.9)$$

$$2\pi r_{oe} = v_o T \qquad (2.10)$$

$$q_1 = \frac{e}{N^2} \tag{2.11}$$

$$I = \frac{\frac{e}{N^2} N}{T} = \frac{e}{NT} = \frac{ev_e}{N2\pi r_{oe}} = \frac{ev_e}{N2\pi \frac{r_e}{N}} = \frac{ev_e}{2\pi r_e} \tag{2.12}$$

$$d = \frac{2\pi r_e}{N} \tag{2.13}$$

Equation (2.12) and (2.13) we use in (2.8):

$$F_e = F_A = 2F_o = 2\frac{\mu_o}{2\pi}\frac{e^2 v_e^2}{4\pi^2 r_e^2}\frac{2\pi \frac{r_e}{N}}{\frac{2\pi r_e}{N}} \tag{2.14}$$

From (2.5) and (2.14):

$$\frac{m_e v_e^2}{N} \frac{2}{r_e} \frac{N}{\pi} \frac{1}{2} = 2\frac{\mu_o}{2\pi}\frac{e^2 v_e^2}{4\pi^2 r_e^2}\frac{2\pi \frac{r_e}{N}}{\frac{2\pi r_e}{N}} \tag{2.15}$$

and the radius *re* of the electron (in Fig. 2) is :

$$r_e = \frac{\mu_o e^2}{4\pi^2 m_e}\cdot\frac{v_e^2}{v_e^2} \tag{2.16}$$

If velocities of rings and subrings are:

$$v_o = v_e \approx c \tag{2.17}$$

then

$$r_e = \frac{\mu_o e^2}{4\pi^2 m_e} \approx 0.89\times10^{-15}\,\text{m} \tag{2.18}$$

We can now calculate the size of the electron with the fractal geometry on Fig. 4. Full calculation is in reference[17,19]. But it is only for the free and quite electron. The size of the electron in the hydrogen atom is not constant[19] (see Fig. 8.).

Energy E_o of the quite electron ^0e, which has velocity $v=0$ and quite mass m_{eo}, can be calculated[17] from kinetic energy of their subelectrons ^{-1}e with velocity v_{-1} (v_e), subsubelectrons ^{-2}e with velocity v_{-2} (v_o), subsubsubelectrons ^{-3}e with velocity v_{-3}, subsubsubsubelectrons ^{-4}e with velocity v_{-4}:

If velocities of substructures are:

$$v = v_e = 0 \ ,$$

$$v_o = v_{-3} \approx \frac{c}{\sqrt{2}} \ , \tag{2.19}$$

$$v_{-4} \approx c \ ,$$

their inner kinetic energy is:

$$E_o = \frac{1}{2}\frac{m_{e0}}{N^2}v_o^2 N^2 + \frac{1}{2}\frac{m_{e0}}{N^3}v_{-3}^2 N^3 + \frac{1}{2}\frac{m_{e0}}{N^4}v_{-4}^2 N^4 \approx m_{e0}c^2 \tag{2.20}$$

$$E_o \approx m_{e0}c^2 \tag{2.21}$$

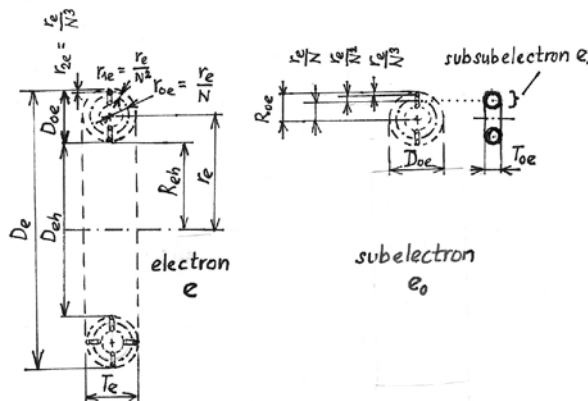This result is in coincidence with the well-known Einstein equation (2.21).

Fig. 4.　**Geometry of the electron and the subelectron[16]**

The Model of Hydrogen with Levitating Electron

The hydrogen atom can have the electron on left side or on right side (see Fig. 9.a, 9.b), thus the difference in exponents must be 2 then exp = 4. The attractive force F_+ is Coulomb's force. A distance between the electron an the proton is r :

$$F = F_+ - F_- = \frac{e^2}{4\pi\varepsilon_o}\left(\frac{1}{r^2} - \frac{A}{r^{exp}}\right) = \frac{e^2}{4\pi\varepsilon_o}\frac{1}{r^2} - \frac{e^2}{4\pi\varepsilon_o}\frac{r_o^2}{r^4} \tag{3.1}$$

For Bohr distance $r_B = r_o \approx 5.29\times10^{-11}\,\text{m}$ [18] is the resulting force $F = 0$.

$$A = r_0^2 \tag{3.2}$$

$$F = F_+ - F_- = \frac{e^2}{4\pi\varepsilon_o}\left(\frac{1}{r^2} - \frac{r_o^2}{r^4}\right) \tag{3.3}$$
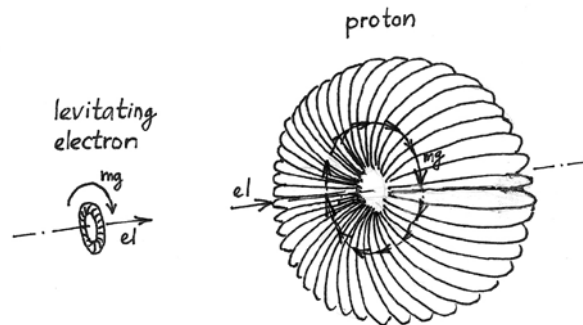

Fig. 5.　**The levitating electron in the field of the proton[18]**

Let us use equation (3.3) as a postulate for next calculations. To find the distance where F has maximum (see Fig. 3.):

$$\frac{dF}{dr} = \frac{e^2}{4\pi\varepsilon_o}\left[-\frac{2}{r^3} - \left(-\frac{4r_o^2}{r^5}\right)\right] = \frac{e^2}{2\pi\varepsilon_o r^3}\left(-1 + \frac{2r_o^2}{r^2}\right) \quad (3.4)$$

for r_o:

$$\frac{dF}{dr} = \frac{e^2}{4\pi\varepsilon_o r_e^3} = K_o \quad (3.5)$$

It is line k_o in Fig. 6

$$\frac{dF}{dr} = \frac{e^2}{2\pi\varepsilon_o r^3}\left(-1 + \frac{2r_o^2}{r^2}\right) = 0 \quad (3.6)$$

and solution is $r_{1,2} = \pm\sqrt{2}r_o$ for F_{max}. Energy E of the electron in the distance r:

$$E = \int \frac{e^2}{4\pi\varepsilon_o}\left(\frac{1}{r^2} - \frac{r_o^2}{r^4}\right)dr = \frac{e^2}{4\pi\varepsilon_o}\int\left(\frac{1}{r^2} - \frac{r_o^2}{r^4}\right)dr = \frac{e^2}{2\pi\varepsilon_o r}\left(-1 + \frac{2r_o^2}{r^2}\right)(3.7)$$

The graph of E is on Fig. 7. Energy E_o which must be added to the electron to be free:

$$E_o = \frac{e^2}{4\pi\varepsilon_o}\int_{r_o}^{\infty}\left(\frac{1}{r^2} - \frac{r_o^2}{r^4}\right)dr = \frac{e^2}{4\pi\varepsilon_o}\left[-\frac{1}{r} + \frac{r_o^2}{3r^3}\right]_{r_o}^{\infty} = \frac{e^2}{4\pi\varepsilon_o}\left(\frac{1}{r} - \frac{r_o^2}{3r^3}\right)(3.8)$$

For $E_o = 0$

$$r_{Eo} = \pm\frac{r_o}{\sqrt{3}} \approx \pm 3.05 \times 10^{-11}\,\text{m} \quad (3.9)$$

For r_o is E_o:

$$E_o = \frac{e^2}{4\pi\varepsilon_o}\left(\frac{1}{r_o} - \frac{r_o^2}{3r_o^3}\right) = \frac{e^2}{4\pi\varepsilon_o}\frac{1}{r_o}\frac{2}{3} = \frac{e^2}{6\pi\varepsilon_o}\frac{1}{r_o} \approx 18.13\,\text{eV} \quad (3.10)$$

$$E_o = \frac{e^2}{4\pi\varepsilon_o}\frac{1}{r_o}\frac{2}{3} \approx 27.2\frac{2}{3}\,eV \approx 18.13\,eV \quad (3.11)$$

We can calculate frequency f_o and period T_o of oscillation of the electron in the hydrogen atom around r_o if we insert K_o defined in equation (3.5) into (3.12):

$$f_o = \frac{1}{2\pi}\sqrt{\frac{K_o}{m_e}} \approx 9.3 \times 10^{14}\,\text{Hz} \quad (3.12)$$

$$T_o = \frac{1}{f_o} \approx 1.075 \times 10^{-15}\,\text{s} \quad (3.13)$$

To calculate quantum model of hydrogen we use radius r_e (2.16):

$$r_e = \frac{\mu_o e^2}{4\pi^2 m_e}\frac{v_o^2}{v_e^2} \quad (3.14)$$

$$2\pi r_e = 2\pi\frac{\mu_o e^2}{4\pi^2 m_e}\frac{v_o^2}{v_e^2} \quad (3.15)$$

We assume that[19]:

$$v_o^2 = \frac{c^2}{2} = \frac{1}{2\varepsilon_o\mu_o} \quad (3.16)$$

Subelectrons are on the orbit with the radius r_e. On this circle have to be n half-waves $\lambda/2 = h/2m_e v$ (n is quantum number):

$$2\pi r_e = 2\pi\frac{\mu_o e^2}{4\pi^2 m_e}\frac{v_o^2}{\overline{v}_e^2} = \frac{\mu_o e^2}{4\pi m_e}\frac{c^2}{\overline{v}_e^2} = \quad (3.17)$$

$$\frac{e^2}{4\pi\varepsilon_o m_e}\frac{1}{\overline{v}_e^2} = n\frac{\lambda}{2} = n\frac{1}{2}\frac{h}{m_e \overline{v}_e}$$

$$\frac{e^2}{2\pi\varepsilon_o}\frac{1}{\overline{v}_e} = nh \quad (3.18)$$

where $\overline{v}_e$ ($\overline{v}_{-1}$) is mean velocity of the subelectron ^{-1}e.

Kinetic energy[19] of the electron with mean velocity $\overline{v}$ is transformed into kinetic energy of subelectrons in 4 substruktures ($v_e, v_{-2}, v_{-3}, v_{-4}$):

$$\frac{1}{2}m_e\overline{v}_e^2 = \frac{1}{4}\frac{1}{2}m_e\overline{v}^2 \quad (3.19)$$

$$\overline{v}_e = \frac{1}{2}\overline{v} = \frac{1}{2}\frac{2}{\pi}v_m = \frac{v_m}{\pi} \quad (3.20)$$

where v_m is a maximum velocity of the electron, when the electron has the distance r_o and has minimum energy E_{min}:

$$\frac{e^2}{2\pi\varepsilon_o}\frac{\pi}{v_m} = nh \quad (3.21)$$

$$v_m = \frac{1}{n}\frac{e^2}{2\varepsilon_o h} \quad (3.22)$$

$$E_e = \frac{1}{2}m_e v_m^2 = \frac{1}{n^2}\frac{m_e e^4}{8\varepsilon_o^2 h^2} \quad (3.23)$$

For quantum number $n = 1$

$$E_{e0} = \frac{m_e e^4}{8\varepsilon_o^2 h^2} \approx 13.6\,eV \quad (3.24)$$

$$E_{e0} = E_o\frac{3}{4} = \frac{e^2}{6\pi\varepsilon_o}\frac{1}{r_o}\frac{3}{4} = \frac{e^2}{8\pi\varepsilon_o}\frac{1}{r_o} \approx 13.6\,eV \quad (3.25)$$

$$E_{e0} = \frac{m_e e^4}{8\varepsilon_o^2 h^2} = \frac{e^2}{8\pi\varepsilon_o}\frac{1}{r_o} \quad (3.26)$$

$$r_o = \frac{\varepsilon_o h^2}{m_e e^2} \approx 5.29 \times 10^{-11}\,\text{m} \quad (3.27)$$

$$r = n^2\frac{\varepsilon_o h^2}{m_e e^2} \quad (3.28)$$

It is the same result as Bohr obtained but with quite different hydrogen model[1].

To find the size of r where $E_o = 13.6\text{eV} = E_{qo}$ in (3.24) and (2.25) we must solve cubic equation:

$$3r^3 - 6r^2 r_0 + 2r_0{}^3 = 0 \qquad (3.29)$$

The roots of equation (3.29) are:
$r_1 = 0.7223517245 r_o \sim 0.382\text{Å}$,
$r_2 = 1.792517214 r_o \sim 0.948\text{Å}$, $r_3 = -0.5148689384 r_o$

The values of r_1 and r_2 are the distances where the electron has velocity $v = 0$ (see Fig. 7.).

$$E_q = \frac{1}{n^2} E_{qo} \qquad (3.30)$$

For quantum number $n = 1$ we calculate the maximum velocity v_m from (3.22) and the couple constant α:

$$v_m = \frac{e^2}{2\varepsilon_o h} \qquad (3.31)$$

$$\frac{c}{v_m} = \frac{2\varepsilon_o hc}{e^2} = \frac{1}{\alpha} \approx 137.036 \qquad (3.32)$$
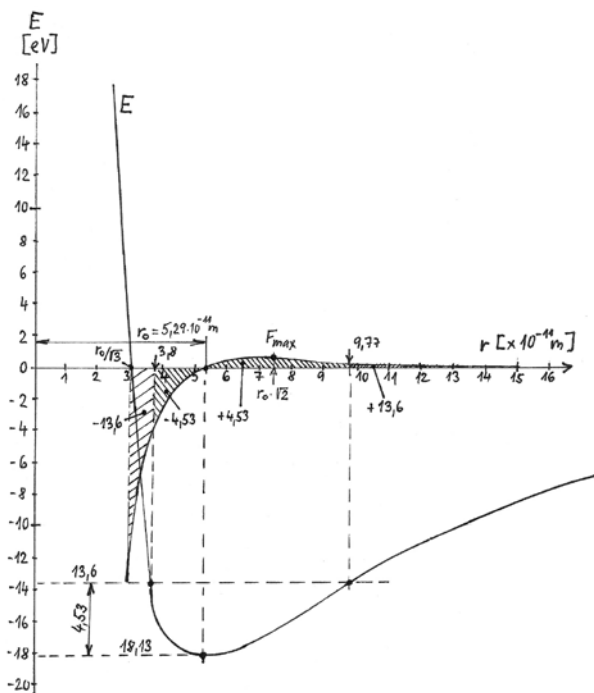
Fig. 6.   **Forces in the hydrogen atom**

In the hydrogen molecule H_2 the covalent bond has $n_e = 2$, $n_p = 1$ (see Fig. 9):

$$F = F_+ - F_- = \frac{e^2}{4\pi\varepsilon_o}\left(\frac{n_e n_p}{r^2} - \frac{r_o^2}{r^4}\right) \qquad (3.33)$$

$$F = \frac{e^2}{4\pi\varepsilon_o}\left(\frac{2}{r^2} - \frac{r_o^2}{r^4}\right) = 0 \qquad (3.34)$$

$$r_c = \pm\frac{r_o}{\sqrt{2}} \approx \pm 3.75\times10^{-11}\text{m} \qquad (3.35)$$

$$d_{cp} = 2r_c \approx 7.5\times10^{-11}\text{m} \qquad (3.36)$$

It is in coincidence with the distance between two protons for their covalent bond[1].

For the hydrogen molecule-ion $H_2{}^+$ is $n_e = 1$, $n_p = 1$ then d_{p+} (see Fig. 9.):

$$d_{p+} = 2r_o \approx 10.6\times10^{-11}\text{m} \qquad (3.37)$$

To calculate the size of the proton structure we use fractal-coil geometry[17] (see Fig. 7.). Results are on Fig. 9.
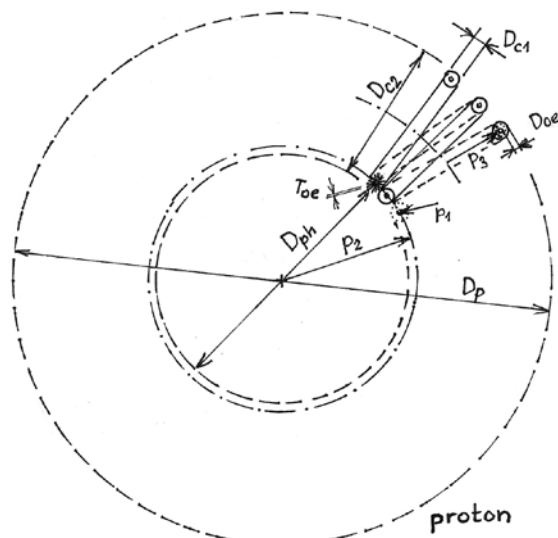

Fig. 7.   **Vortex-fractal-coil structure of the proton[18]**

The Spin of the Electron

The spin of the electron is defined as angular momentum:

$$\vec{S} = m_e(\vec{r}_e \times \vec{v}_e) \qquad (4.1)$$

For the spin[19] on axis z:

$$S_z = N\frac{m_e}{N}r_e\bar{v}_e \qquad (4.2)$$

$$r_e = \frac{e^2}{8\pi^2\varepsilon_0 m_e}\cdot\frac{1}{\bar{v}_e^2} \qquad (4.3)$$

$$\bar{v}_e = \pm\frac{v_m}{\pi} \qquad (4.4)$$

$$v_m = \frac{e^2}{2\varepsilon_0 h} \qquad (4.5)$$

$$r_e = \frac{e^2}{8\pi^2\varepsilon_0 m_e}\cdot\frac{\pi^2}{v_m^2} = \frac{e^2}{8\varepsilon_0 m_e}\cdot\frac{1}{v_m^2} = \frac{e^2}{8\varepsilon_0 m_e}\cdot\frac{4\varepsilon_0^2 h^2}{e^4} = \frac{\varepsilon_0 h^2}{2m_e e^2} \qquad (4.6)$$
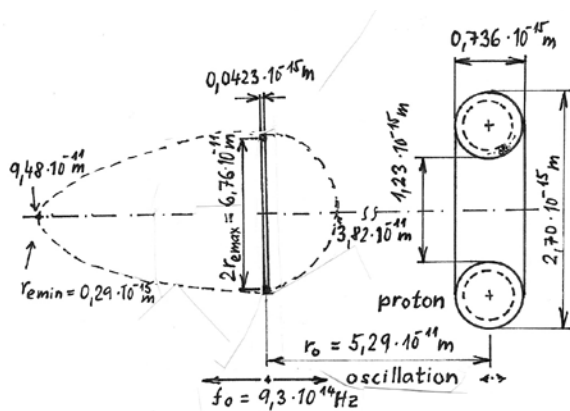
Fig. 8.   **Calculated size of the electron and the proton in the hydrogen atom (in different scales)**

$$S_z = \pm m_e \bar{v}_e r_e = \pm m_e \frac{v_m}{\pi} r_e =$$

$$= \pm m_e \frac{e^2}{2\varepsilon_0 h} \cdot \frac{1}{\pi} \cdot \frac{\varepsilon_0 h^2}{2 m_e e^2} = \pm \frac{1}{2} \cdot \frac{h}{2\pi} = \pm \frac{1}{2} \hbar = m_s \hbar \qquad (4.7)$$

$$m_s = \pm \frac{1}{2} \qquad (4.8)$$

The result in (4.7) is in coincidence with the generally equation for the spin, where m_s is spin quantum number.

Magnetic momentum M_z:

$$M_z = IS \qquad (4.9)$$

where I is an current around a surface S:

$$T = \frac{2\pi r_e}{\bar{v}_e} \qquad (4.10)$$

where T is period for calculation of I:

$$I = \pm \frac{Q}{T} = \pm \frac{\frac{e}{N} N}{\frac{2\pi r_e}{\bar{v}_e} \cdot \frac{1}{2}} = \pm \frac{e \bar{v}_e}{\pi r_e} \qquad (4.11)$$

$$S = \pi r_e^2 \qquad (4.12)$$

$$M_z = IS = \pm \frac{e \bar{v}_e}{\pi r_e} \cdot \pi r_e^2 \cdot \frac{m_s}{m_s} = \pm \frac{e}{m_e} S_z = \pm \frac{e}{m_e} \cdot \frac{1}{2} \hbar = \pm \mu_B \quad (4.13)$$

where μ_B is Bohr magneton.

The Size of the Electron in Hydrogen Atoms

For maximum velocity of the electron v_{em} we use analogy with (3.19):

$$v_{em} = \pm \frac{v_m}{2} \qquad (5.1)$$

If we insert v_m from (3.31) into (4.3) and (5.1) we receive the maximum radius of the electron:
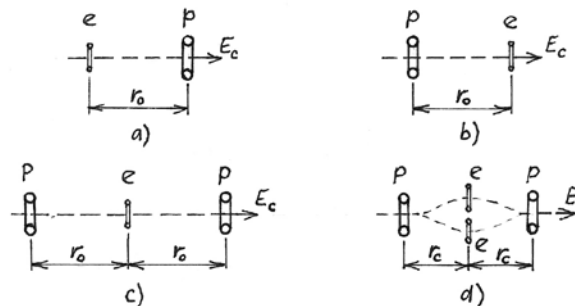

Fig. 9.   **Calculated distances between the proton and the electron. a) left side orientation of hydrogen, b) right side orientation of hydrogen, c) the hydrogen molecule-ion H_2^+, d) the hydrogen molecule H_2 with covalent bond**

$$r_{emax} = \frac{e^2}{8\pi^2 \varepsilon_0 m_e} \cdot \frac{4}{v_m^2} = \frac{2\varepsilon_0 h^2}{\pi^2 m_e e^2} = 3.38 \times 10^{-11} \text{m} \qquad (5.2)$$

For minimum radius of the electron where $v=0$:

$$2\pi r_{emin} = ND_{ee} \qquad (5.3)$$

$$r_{emin} = \frac{ND_{ee}}{2\pi} = 0.29 \times 10^{-15} \text{m} \qquad (5.4)$$

The levitating electron changes the size from very small to relatively large size[19] (see Fig. 8.).

The Structure of Molecules

Atoms combine to form a molecule. Their shared air of electrons is called a covalent bond. They occupy the same orbital with opposite spins. The H_2 molecule atoms H share electrons. Each hydrogen atom shares its electron with another hydrogen atom to gain a full outer *s* shell of 2 electrons. Covalent bonding is important in carbon compounds.

There are two simple rules how to create atom nuclei:

(i) Only two protons can be on one rotational axis

(ii) Two protons cannot be connected directly with vortex nuclear bond (only the proton with the neutron can be nuclear bond)
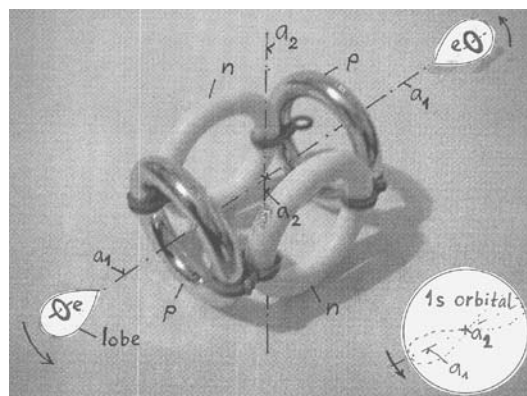

Fig. 10.   **The vortex-ring structure of the nucleus of the helium $_2^4$He (alpha particle) and its orbital 1s**

Fig. 11.　**The vortex-ring structure of the atom $_6^{12}C$ to create the benzene molecule[15] (see Fig. 12.)**

Conclusions

Our science creates terrific demands on the imagination[2]. To understand the electromagnetic field requires a high degree of imagination. The degree of imagination that is required is much more extreme than that required for some of the ancient ideas. The modern ideas are much harder to imagine. We usually use mathematical equations and rules, but we used a lot of pictures to describe very complex vortex-fractal models. There is not easy to formulate mathematical models[21,23]. We can't allow ourselves to seriously imagine things, which are obviously in contradiction to the known laws of nature. We created vortex-fractal-ring model of the electron, of the proton and hydrogen and then calculated sizes, forces, energies and covalent bonds.
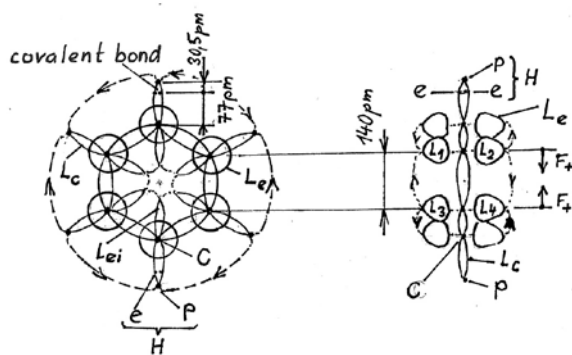

Fig. 12.　**The structure of the benzene molecule[15]**

REFERENCES

1. Pauling L.: *General Chemistry*, Dover Publication, Inc, New York, 1988
2. Feynman R.P. Leighton R.B., Sands M.: *The Feynman Lectures on Physics, volume I, II, III* Addison-Wesley publishing company, 1977
3. Feynman R.P.: *QED – The Strange Theory of Light and Matter*, Princeton University Press, 1988
4. Feynman R.P.: *The Character of Physical Law,* Penguin Books, 1992
5. Zmeskal, O., Nezadal, M., Buchnicek, M.: Chaos, Solitons and Fractals 17 (2003) 113–119
6. Ošmera, P.: *Proceedings of MENDEL 2005*, Brno, Czech Republic (2005) 1–6.
7. Ošmera, P.: *Proceedings of MENDEL 2005*, Brno, Czech Republic (2005) 7–14.
8. Ošmera, P.: *Proceedings of the 4th International Conference on Soft Computing ICSC2006,* January 27, 2006, Kunovice, Czech Republic, 111–122
9. Ošmera, P.: *Proceedings of the 4th International Conference on Soft Computing ICSC2006,* January 27, 2006, Kunovice, Czech Republic, 123–129
10. Ošmera, P.: *CD Proceedings of MENDEL 2006*, Brno, Czech Republic (2006) 12 pages
11. Ošmera, P.: *CD Proceedings of MENDEL 2006*, Brno, Czech Republic (2006) 14 pages
12. Ošmera, P.: *CD Proceedings of MENDEL 2006*, Brno, Czech Republic (2006) 10 pages
13. Ošmera, P.: *Proceedings of MENDEL 2007*, Praha, Czech Republic (2007), 105 - 110
14. Ošmera, P.: *Proceedings of MENDEL 2007*, Praha, Czech Republic (2007), 72 - 75
15. Ošmera P.: *Proceedings of World Congress on Engineering and Computer Science,* San Francisco, 2007, 152–157
16. Ošmera P.*: New Trends in Physics*, NTF 2007, Brno Czech Republic, 2007, 179–182
17. Ošmera, P.: *Proceedings of the 6th International Conference on Soft Computing ICSC2008*, January 25, Kunovice, Czech Republic, (2008) 151 - 158
18. Ošmera, P.: *Proceedings of the 6th International Conference on Soft Computing ICSC2008*, January 25, Kunovice, Czech Republic, (2008) 159 - 168
19. Ošmera P.: Evolution of nonliving Nature, Kognice VIII, Prague, Czech Republic, (2008), 179
20. Li Z., Halang W. A., Chen G.*: Integration of Fuzzy Logic and Chaos Theory;* paragraph: Osmera P: Evolution of Complexity, Springer, (2006) (ISBN: 3–540–26899–5) 527 – 578
21. Thorne, K.S.: Black Holes & Time Warps, W.W.Norton & Company, Inc., 1994
22. Gottvald, A.: *Proceedings of the 6th International Conference on Soft Computing ICSC2008*, January 25, Kunovice, Czech Republic, (2008) v tisku
23. Bouchal Z.: *New Trends in Physics*, NTF 2007, Brno Czech Republic, (2007), 3–6

L12 HYDRATION OF HYALURONAN

ALENA PRŮŠOVÁ, PETRA BURSÁKOVÁ and JIŘÍ KUČERÍK

Brno University of Technology, Faculty of Chemistry, Department of Applied and Physical Chemistry, Purkyňova 118, Brno 612 00, Czech Republic,
xcprusova@fch.vutbr.cz

Introduction

During the last decades, significant advances have been made in the development of biocompatible and biodegradable materials for biomedical applications. One of an appropriate material seems to be hyaluronic acid also known as hyaluronan (HYA). It is a naturally occurring biopolymer, which serves important biological functions in bacteria and higher animals including humans. Hyaluronan is water soluble giving viscoelastic fluids[1] and it has a considerably greater ability to trap water than other polyelectrolyte polysaccharides.

Hyaluronan is a linear unbranched, high molecular weight, polar polysaccharide of the glycosaminoglycans class. Hyaluronan is composed of repeating polyanionic disaccharide units which consists of N-acetyl-D-glucoseamine and D-glucuronic acid linked by a β 1-4 glycosidic bond. The disaccharides are linked by β 1–3 bonds to form hyaluronan chains (Fig. 1.)[2].
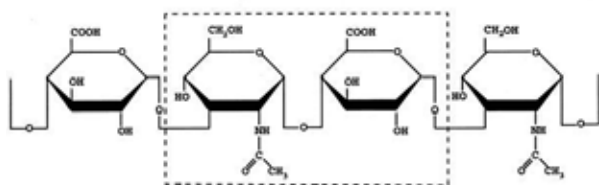

Fig. 1.　The formula of disaccharide unit of hyaluronan

The structure of water surrounding hyaluronan in the solution is affected by the the interactions between polymer and water, and thus, it exhibits different physical properties depending on their mutual distance. The aim of this work is to recognize and enumerate such hydration shells by differential scanning calorimetry (DSC), i.e. to use their different enthalpies of melting.

Experimental

S a m p l e s

Hyaluronan, isolated from Streptococcus zooepidemicus, was obtained from CPN Company (Dolní Dobrouč, Czech Republic). Five molecular weight of hyaluronan were used as follows: 100.1 kDa, 253.9 kDa, 522.1 kDa, 740 kDa and 1,390 kDa. By means of thermogravimetry (TA Instruments, Q5000IR) it was determined an equilibrium moisture content to obtain more precise results.

Low water content

Hyaluronan was placed in an aluminum pan. Excess of water was added to hyaluronan samples. Surplus water was allowed to evaporate slowly until the desired water content was obtained at room temperature. The pans were subsequently hermetically sealed and left to equilibrate at room temperature overnight. Water content (W_c) was defined as follows:

$$W_c = \frac{\text{grams of water}}{\text{grams of dry sample}} \ (\text{g/g}) \tag{1}$$

For each molecular fraction, 7 different W_c were measured.

High water content

Hyaluronan samples were dissolved in milli-Q water. The hyaluronan concentrations was 0.1 %, 0.5 %, 1 %, 1.5 %, 2 %, 2.5 %, 3 % wt. The solutions were slowly mixed by a magnetic laboratory stirrer over a period of 24 hours to obtain perfectly dissolved and homogeneous hyaluronan sample.

DSC measurement

Differential scanning calorimetry was performed using the TA Instruments DSC Q200, equipped with a cooling accessory, and TA Universal Analysis 2000 software. Samples of approximately 10 mg were placed in hermetically sealed aluminum sample pans. High water content samples were measured immediately, to avoid condensation of water on the pan lid, which can occur if the sealed samples are stored in the cold before use. Low water content samples were measured the next day after the preparation. The thermal protocols used were as follows: equilibrate at 40.0 °C; isothermal at 40.0 °C for 2 min; cooling from 40.0 °C to –90.0 °C at 3.0 °C min⁻¹; isothermal at –90.0 °C for 2.0 min; heating from –90.0 °C to 30 °C at 3.0 °C min⁻¹.

Results

LWC – Low Water Content

Representative DSC cooling and heating curves of hyaluronan are given in Fig. 2. the sample shown is 253 kDa hyaluronan with W_c 0.75. Hyaluronan hydrogels with the lowest W_c showed almost infinitesimal fusion endothermic peak on heating curves. Nearly all water molecules are present in the form of non-freezing water in this system, and a slight amount of water molecules are present in the form of freezing-bound water which caused the observed endothermic fusion peaks. For the increasing W_c can be seen a small crystallization exothermic peak, which growth wtih the increasing W_c, on cooling curve, and consequently, on the heating curve presence of overlapped endothermic fusion peaks. Enlarged peak area is caused by larger amount of freezing and freezing-bound water. The DSC data records for higher W_c look like previous DSC records plus an increasing tendency as mentioned above.

From the obtained data it can be considered that there are tree types of water which are 'free (bulk) water' which freezes as normal water it means that this water melts, crystallized around 0 °C and enthalpy of fusion is 333.56 J g⁻¹. Only the free water contributes to the observed enthalpy change. Further 'freezing-bound water' (f-b) which freezes at
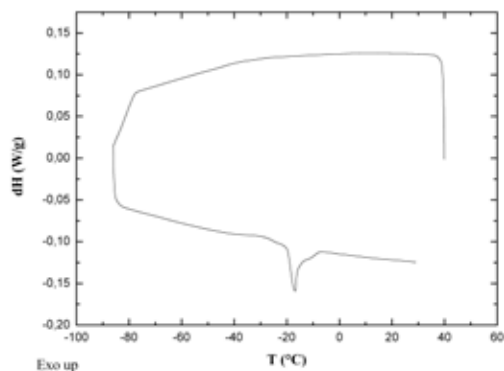
Fig. 2.   **High water content – DSC record**

lower temperature than normal water but it freezes and it also exhibits a reduced enthalpy of fusion. Finally 'non-freezing water' (n-f) which does not freeze even at low temperature which was used in this work, i.e. –90 °C.

Assuming that the weight of free water is equal to the total water weight less the non-freezing water and freezing bound water, the following expression holds:

$$\frac{\Delta H_{obs}}{g_{HYA}} = \frac{\Delta H_{free\,water}}{g_{free\,water}}\left(\frac{g_{free\,water}}{g_{HYA}}\right) + \frac{\Delta H_{f\,b\,water}}{g_{f\,b\,water}}\left(\frac{g_{f\,b\,water}}{g_{HYA}}\right) \quad (2)$$

Expressing the weight of free water in terms of total water, freezing-bound water, and non-freezing water, one can obtain:

$$\frac{\Delta H_{obs}}{g_{HYA}} = \frac{\Delta H_{free\,water}}{g_{free\,water}}\left(\frac{g_{total\,water}}{g_{HYA}}\right) +$$

$$(3)$$

$$+ \left(\frac{\Delta H_{f\,b\,water}}{g_{f\,b\,water}} - \frac{\Delta H_{free\,water}}{g_{free\,water}}\right)\left(\frac{g_{f\,b\,water}}{g_{HYA}}\right) - \frac{\Delta H_{free\,water}}{g_{free\,water}}\left(\frac{g_{n\,f\,water}}{g_{HYA}}\right)$$

The total amount of non-freezing water in hyaluronan hydrogels was determined directly from the X intercept. Table I reports the dependency of non-freezing water content to the molecular weight of hyaluronan reveals, although small, but evident trend of increasing number of non-freezing water with increasing molecular weight of hyaluronan. We hypothesize that large content of water in case of 1,390 kDa sample is caused by the tertiary structure of hyaluronan and by the mutual approaching of its chains to the closer proximity.

Table I
Weight of n-f water for different MW

MW [kDa]	n-f water [g 1g^{-1} HYA]
100.1	0.59
253.9	0.58
522.1	0.65
740.0	0.57
1,390	0.81

High Water Content

Fig. 3 shows record of a representative DSC cooling and heating curve for hyaluronan dissolved in water. In fact, there can be seen two phase transitions, first one in the above record which corresponds to the cooling phase and bellow one, which reflect processes of melting. Due to supercooling effect, the latter was used for enthalpy determination.
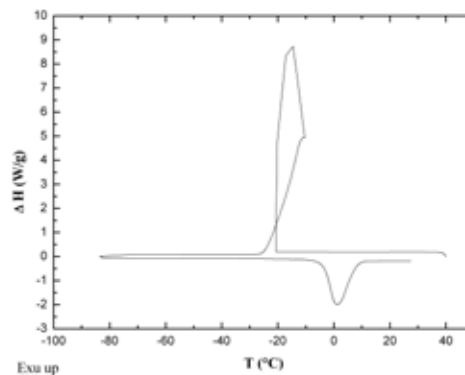

Fig. 3.   **High water content – DSC record**

After the plotting the observed enthalpy change, normalized to the polymer weight, as a function of the total water content of the sample (Fig. 4.), the melting enthalpy for the free water can be obtained from the slope. The x-intercept in (3) includes terms for both the freezing-bound water and the non-freezing water. Now one can estimate the minimum amount of freezing-bound water per gram of hyaluronan in diluted and semi-diluted solutions by combination of data obtained in this part, high water content, with the data analysis from the part concerning the determination of low water content (see Table I).
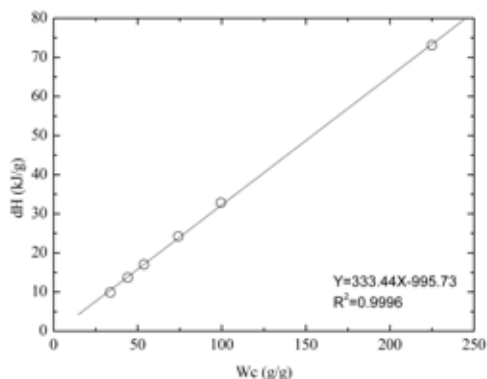

Fig. 4.   **Normalized melting enthalpy versus Wc**

The content of non-freezing water was adopted from the table reporting the low water content for specific hyaluronan molecular weight (Table I). The minimum value for the enthalpy change associated with melting of the freezing-bound water was used 312 J g^{-1} ref.[3]. The determination of freezing-bound water can be carried out as follows[4]: x-inter-

cept of dependency of normalized enthalpy change on water content (Fig. 4.). This dependecy gives a value which is equal to the following formula.

$$\frac{g_{n\,f\,water}}{g_{HYA}} + \left(1 - \frac{\Delta H_{f\,b\,water}}{g_{f\,b\,water}}\frac{g_{free\,water}}{\Delta H_{free\,water}}\right)\left(\frac{g_{f\,b\,water}}{g_{HYA}}\right) \qquad (4)$$

Table II
Weight of f-b water for different M_W

M_W [kDa]	f-b water [g 1g^{-1} HYA]
100.1	38.7
253.9	38.2
522.1	29.2
740.0	70.7
1,390	76.9

Obtained values of freezing-bound water, summarized in Table II exhibit no obvious dependency. For the first three value (100.1 kDa; 253.9 kDa; 522.1 kDa), there is decrease but for the next two values (740.0 kDa; 1,390 kDa) there is increase of the values.

Conclusions

Semi-diluted hyaluronan solutions have significantly altered freezing and melting transitions of water. The results are affected by the presence of freezing-bound and of a small amount of non-freezing water strongly bound to the polymer. Those have slightly altered thermodynamic properties which were used for the enumeration of such types of water.

REFERENCES
1. Jouon N., Rinaudo M., Milas M., Desbrieres J.: Carbohydr. Polym. *26*, 69, (1995).
2. Lapčík L.Jr., Lapčík L., De Smedt S., Demeester J., Chabreček P.: Chem. Rev. *8*, 2664, (1998).
3. Yoshida H., Hatakeyama T., Hatakeyama H.: J. Therm. Anal. *40*, 483, (1992).
4. Lui J., Cowman M.K.: J. Therm. Anal. Calor., *59*, 547, (2000).

L13 ELECTROCHEMICAL ANALYSIS OF NEW INDOLE BASED ANTIOXIDANTS

MICHAL ZALIBERA[a], PETER RAPTA[a], VLADIMÍR ŠNIRC[b] and SVORAD ŠTOLC[b]

[a]Institute of Physical Chemistry and Chemical Physics, Faculty of Chemical and Food Technology, Slovak University of Technology in Bratislava, Radlinského 9, 812 37,
[b]Institute of Experimental Pharmacology, Slovak Academy of Sciences, Dúbravská cesta 9, 841 04 Bratislava, Slovak Republic,
peter.rapta@stuba.sk

Introduction

The concept of pharmacological interventions in prevention and therapy of oxidative stress-related diseases has still not found adequate application in clinical practice. One of the potential drugs intensively investigated in this area is the synthetic pyridoindole stobadine. Numerous studies in the literature were focused on its protective properties[1]. Its beneficial effects have been observed in metabolic, cardiovascular, renal, neural and hepatic systems[2]. However, only few reports deal with the electrochemical oxidation of stobadine and its derivatives[3]. Recently new indole-derived neuroprotective drugs with improved pharmacodynamic and toxicity profiles were synthesized based on the stobadine structure[4].

In this contribution a comprehensive study of the electrochemical, antioxidant and radical scavenging properties of selected indole-derived drugs (Fig. 1.) is presented. The data from three independent methods are compared including *(i)* cyclic voltammetry in DMSO and aqueous solutions, *(ii)* EPR/spin-trapping study covering the estimation of reactive radical scavenging capacity and *(iii)* estimation of Trolox equivalent antioxidant capacity (TEAC) by monitoring of ABTS$^{\bullet+}$ cation radical and DPPH radical with UV-VIS spectroscopy, delivering information about the hydrogen/electron donating antioxidant action.

Experimental

Stobadine dihydrochloride and new stobadine derivatives SMe1EC2.HCl, SM1M3EC2.HCl, and SMe1nBuoC2.

Fig. 1.　**Investigated indole-derived drugs**

HCl were prepared in the Institute of Experimental Pharmacology, Slovak Academy of Sciences. The analytical purity grade NaCl was from Slavus Ltd. and 5,5-dimethyl-1-pyrroline-*N*-oxide (DMPO) was the product of Sigma-Aldrich. Tetrabutylammonium perchlorate (TBAP), lithium perchlorate (LiClO$_4$) puriss., both purchased from Fluka and ferrocene (p.a.,$\geq$98.0 %), dimethyl sulfoxide (DMSO) purchased from Merck were used as received. The deionized water was used for aqueous solutions.

All cyclovoltammetric experiments were performed at room temperature under argon atmosphere. A standard three-electrode arrangement of a platinum wire (in DMSO) or glassy carbon rod (in water) as working electrodes, a platinum coil as counter electrode, and a saturated calomel electrode (SCE) as a reference electrode was used. The concentration of investigated samples was 0.5 mM in water and 1.0 mM in DMSO. The electrochemical measurements were carried out with a HEKA PG 284 (Germany) potentiostat/galvanostat using the software package PotPulse 8.53.

Standard ABTS assay was used for determination of antioxidant capacity of samples. Here, 100 µl of 0.1 mM sample solution in 10% ethanol was added to 2 ml of ABTS$^{\bullet+}$ (70 µM) solution in 1 cm UV-cell and rigorously mixed. The decrease of absorbance at 730 nm was followed for 10 minutes. UV/VIS/NIR Shimadzu 3600 spectrometer (Japan) was used both in antioxidant tests and for the measurement of the UV-VIS spectra of samples (Fig. 2.). The difference in the absorbance in 10th minute relative to the reference, ΔA, and the calibration curve of Trolox (Sigma-Aldrich, Germany) was used to calculate the values of TEAC.
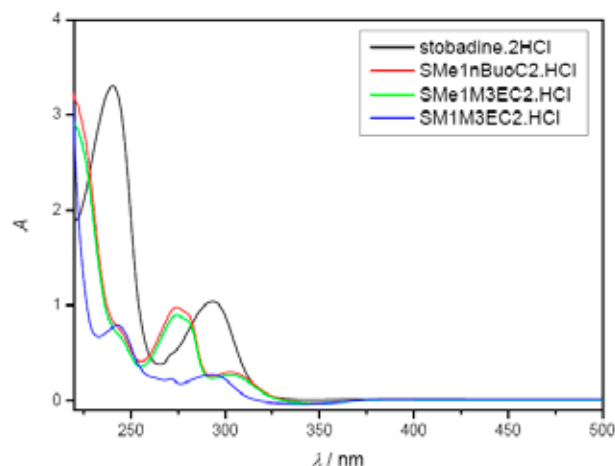

Fig. 2.　**UV-VIS spectra of freshly prepared 0.15 M NaCl aqueous solutions of investigated pyridoindoles (0.5 mM)**

Antioxidant activity determination using the free DPPH radical (95%, Aldrich, Germany) was similar to the ABTS assay. 200 µl of 0.1mM sample solution in 10% ethanol was mixed with 2 ml of 0.1mM DPPH in ethanol and decrease of absorbance at 516 nm was followed for 10 minutes.

In EPR experiments the thermal decomposition of K$_2$S$_2$O$_8$ at 333 K was used as a source of reactive radicals.

The amount of generated radicals was monitored in air employing DMPO spin trap. 200 µl 0.5mM sample aqueous solutions, 25 µl 200mM DMPO in DMSO and 25 µl 10mM $K_2S_2O_8$ in H_2O were used in the reaction mixture.

Results

Remarkable differences in redox behavior of stobadine derivatives were observed by replacing the DMSO representing a low proton donating solvent, with highly proton donating aqueous media (see Figs. 3. and 4.). Generally, in DMSO solutions complex irreversible redox behavior in the anodic part was observed (Fig. 3.). Rich cyclovoltammetric responses with several oxidation peaks were found indicating the complexity of the stobadine oxidation in non-aqueous media.

In all cases the first irreversible oxidation peak indicates a consecutive reaction of the unstable oxidation products. Simultaneously new cathodic peaks are detected on the reverse scan in the cathodic part of voltammogram. The number of new redox couples and the corresponding oxidation potentials strongly depend on the indole substitution.

Even more complex redox behavior in the potential region from 0 V to 1 V *vs.* SCE was observed in aqueous solutions compared to DMSO, indicating the participation of water and supporting electrolyte in the formation of various forms of indoles already in the initial solutions. Fig. 4. shows the cyclic voltammograms of three selected pyridoindoles in 0.15M aqueous NaCl. The first sample is stobadine as reference. The second sample represents stobadine derivatives with metoxy group (SMe-type samples) on benzene ring instead of the methyl group in the stobadine. The third SM1M3EC2.HCl sample contains additional methyl group on the benzene ring.

In all cyclic voltammograms found in water solutions one or two consecutive products were observed in the reverse
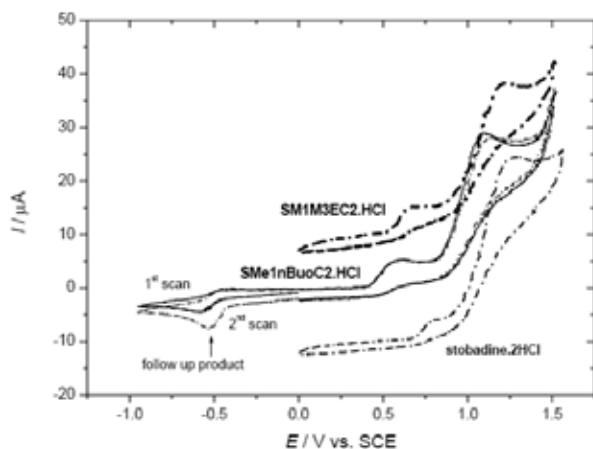

Fig. 3.   **Cyclic voltammograms obtained in the oxidation of investigated stobadine and its derivatives (freshly prepared 0.1 mM solutions) in DMSO containing 0.1 M TBAP as supporting electrolyte (two CV scans including cathodic part are shown for sample SMe1nBuoC2.HCl)**

scans for SMe type structures (Fig. 4.). One of them can be again oxidized in a reversible step. These redox peaks originate from the newly formed oxidation products as illustrated in Fig. 5.
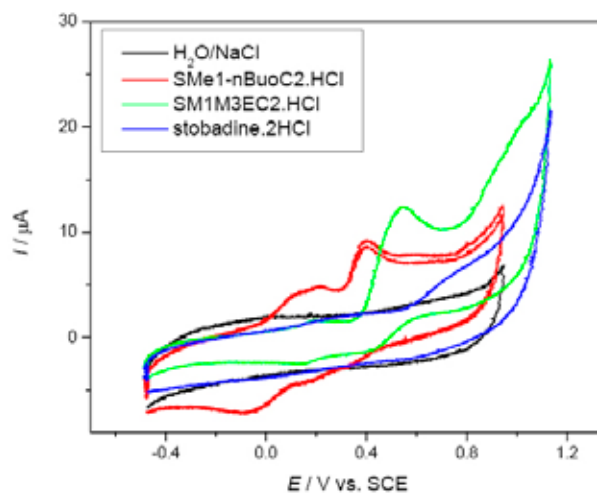

Fig. 4.   **Cyclic voltammograms obtained in the oxidation of investigated stobadine and its derivatives (freshly prepared 0.5mM solutions) in H_2O containing 0.14M NaCl using glassy carbon rod working electrode**
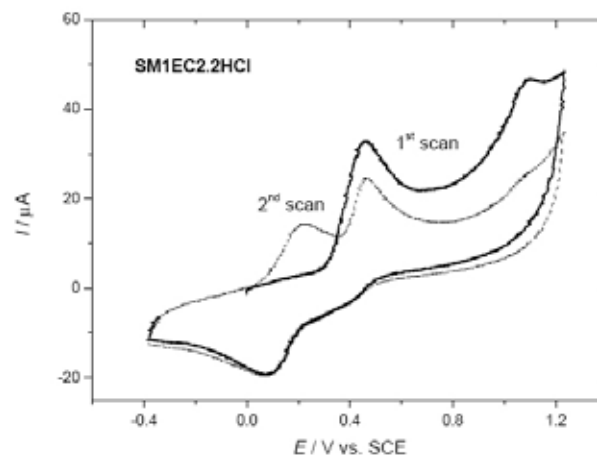

Fig. 5.   **Cyclic voltammogram (1st and 2nd scan) obtained in the oxidation of SMe1EC2.HCl in H_2O containing 0.1M LiClO4 using glassy carbon rod working electrode**

The low redox potentials of these products indicate the easiness of their oxidation and reduction. Therefore deviations in the relationship between electrochemical redox potentials and antioxidant and radical scavenging capacity of the investigated pyridoindoles are to be expected due to the differences in the reaction mechanisms in different media. Whereas the electrochemical redox potentials of secondary xidation products can clearly be separated from those of the parent compounds, when measuring antioxidant properties by various tests an overall activity of the parent compound and of its secondary oxidation and reduction products is measured.

Antioxidant capacity was determined by ABTS and DPPH tests, as well as EPR/spin trapping assay. The investigated samples can be divided into two groups based on the redox and radical scavenging behavior in aqueous solutions. Stobadine and SM1M3EC2.HCl exhibit higher oxidation potentials of follow up reaction products compared to the second group (SMe type derivatives). Standard ABTS and DPPH assays were used for determination of antioxidant capacity of samples expressed in TEAC (Fig. 6.).

As seen from Fig. 6. the best hydrogen/electron donating antioxidant action exhibits the sample SM1M3EC2.HCl. The lowest antioxidant activity was observed for stobadine. The total antioxidant capacity of samples was also compared with the radical scavenging capacity evaluated using the EPR/spin-trapping method (Fig. 7.).
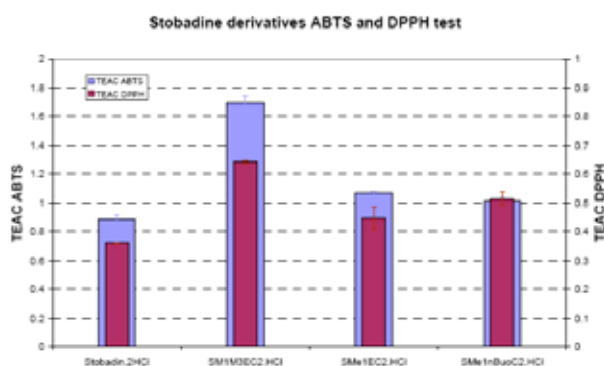

Fig. 6. **Trolox Equivalent of Antioxidant Capacity (TEAC) of the investigated pyridoindoles determined by ABTS and DPPH tests in aqueous solutions**

The thermal decomposition of $K_2S_2O_8$ in water solutions at 333 K was used as a source of reactive hydroxyl radicals. Completely different behavior in EPR test was observed for SMe type structures in water solutions as illustrated for SMe1EC2.HCl in Fig. 7. Unusual kinetic curve was observed with a strong elimination of OH radicals formed in the reaction mixture. This confirms a special role of the methoxy group on benzene ring in stobadine-derived indoles, already indicated in the cyclovoltammetric experiments, concerning antioxidant properties of these compounds.

Conclusions

Electrochemical, UV-VIS and EPR/spin trapping investigations of new prepared indole-derived drugs were performed in order to explain in more detail the redox processes of the studied compounds in relation to their antio-
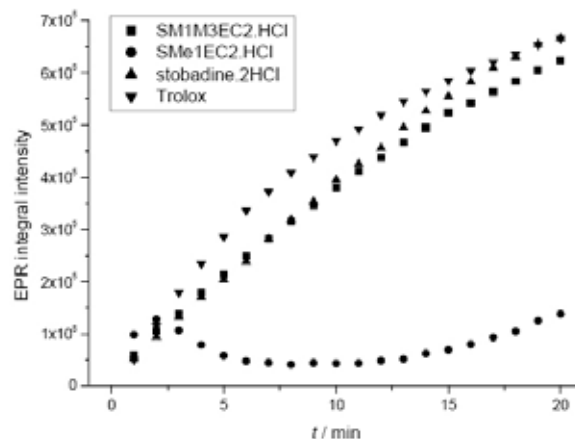

Fig. 7. **The time course of integral EPR intensities of OH-DMPO spin adducts measured indole derivatives and Trolox in EPR/spin-trapping test**

xidant and radical scavenging activity. Cyclic voltammetric and EPR studies indicate the formation of different oxidation products strongly depending on the pyridoindole substitution and on the solvent used. It can be concluded that similar to the most studied natural indole-type antioxidant melatonin (see recent review[5]), the indole metabolites that are formed due to oxidation, strongly contribute to the antioxidant and radical scavenging capacity of indole-based compounds both in aqueous and non aqueous media.

REFERENCES

1. Life Sciences 65 (1999*), A special issue from the International Symposium on Drug Action on Reactive Oxygen Species with Special Attention to Stobadine*
2. Yulek F., Or M., Ozogul C., Isik A. C., Ari N., Stefek M., Bauer V., Karasue C.: Arch. Med. Res. *38*, 503 (2007) and refs. cited therein.
3. Rapta P., Lichnerová E., Staško A., Šnirc V., Štolc S.: Chem. listy *99*, 221 (2005) and refs. cited therein.
4. Štolc S., Šnirc V., Májeková M., Gašparová Z., Gajdošíková A., Štvrtina S.: Cell. Mol. Neurobiol. 1495 (2006).
5. Reiter R. J., Tan D., Terron M. P., Flores L. J., Czarnocki Z.: Acta Biochim. Pol. *54*, 1 (2007).

L14 NEW COLLOIDAL SYSTEMS MADE OF HUMIC ACIDS

PETR SEDLÁČEK, MARTINA KLUČÁKOVÁ and PAVEL ONDRUCH

Brno University of Technology, Faculty of Chemistry, Purkyňova 464/118, 612 00 Brno
sedlacek-p@fch.vutbr.cz

Introduction

Humic acids (HA), as the most beneficial fraction of soil organic matter, responsible for natural detoxification of soils, provide outstanding sorption ability towards common groups of pollutants. This makes HA very promising in a production of soil remediation agents. Because of slightly acidic pH of underground waters, HA are naturally found in an insoluble state and form swelled material with high water content. Preparation of a gel form of humic substances therefore looks promising in the modeling of natural humic environments and also for a direct application of HA in agriculture or in industry.

Gelation of HA by the use of biopolymers represents rapidly evolving branch of humic research. Chitosan, polyelectrolyte biopolymer formed by a deacetylation of chitin, provides high potential on this field of study. It is known as a biocompatible material with such valuable properties as haemostatic and bacteriostatic function and sorption ability for both anionic and cationic pollutants.

Experimental

Controlled coagulation of alkalic (sodium) humate was applied in order to prepare a gel without any additional network forming agent. Solid humic acids, obtained by the method of alkalic extraction[1] from South-Moravian lignite were dissolved in 0.5 M sodium humate in solid-to-liquid ratio of 8 g dm^{-3}. This solution was precipitated by HCl addition up to pH below 1. Resulting hydrogel was separated by means of centrifugation (4,000 rpm) and washed in deionized water several times until removal of Cl$^-$ ions.

Mixed chitosan/HA hydrogels were obtained by a reaction between sodium humate and chitosan solution in volume ratio of 1:1. Chitosan solution was prepared by dissolution of 6.5 g of a chitosan powder (medium molecular weight, Sigma Aldrich) in 300 ml of 0.1M hydrochloric acid. pH of both solutions were adjusted to appropriate values using HCl and NaOH. After 10 minutes of continuous agitation, hydrogel was separated by either centrifugation (15 minutes, 4,000 rpm) or filtration. Hydrogel was repeatedly washed by deionized water in order to remove remaining reagents. Dry solid content of a gel was determined after drying in a laboratory oven for 5 days (at 50 °C).

For the preparation of chitosan/HA hydrogel beads, 3.3 g of chitosan flakes were dissolved in 100 ml of 5% acetic acid. This solution was slowly dropped into either 0.5M NaOH or corresponding sodium humate under continuous agitation.

In the former case, resulting chitosan beads were let to adsorb HA in the sodium humate with pH value of 8.5.

Following instruments were used for the determination of physical and chemical properties of resulting gels: Mettler Toledo 7 Easy pH-Meter, Sentron Hotline needle electrode for measurement of pH inside a gel, Hitachi U3300 UV-VIS spectrometer, Nicolet Impact 400 FT-IR spectrometer and ARG2 Rheometer from TA Instruments. Hydrogel samples were dried either via free evaporation at 25 °C or using Free-Zone 4.5 (LABCONCO) freeze dry system.

Results

Humic gel, prepared by the coagulation of sodium humate solution, represents a suitable model in order to study a pollutant transport in natural humic systems[1]. Water formed 81 % of its weight. The gel was irreversible, either freeze drying or air drying in laboratory oven provided hydrophobic humic acid powder with limited swelling ability. Main disadvantage of this gel is its high acidity (inner pH value measured by needle electrode was 1.4). Similar irreversible gel can be prepared by a precipitation of sodium humate using a solution of salt with higher valence of a cation. This method of gelation can be applied in order to mask the structural groups, responsible for the reaction between HA and metal cations (useful in diffusion experiments).

Properties of hydrogels, prepared via rection between HA and chitosan, can be dramaticaly influenced by the parameters of initial solutions (temperature, pH, ionic strength etc.). Results of an experiment, focused on the effect of initial pH showed that the highest water content of the fresh hydrogel (around 97 %) was obtained using the HA solution with the value of pH = 8.5 and chitosan solution with pH = 5.5. Also the yield of gelation (amount of a produced gel) was the highest for this way of preparation, no matter whether calculated as an amount of total gel or as an amount of dry solid content. Freeze drying of this hydrogel lead to highly porous xerogel with very fast swelling in the presence of water. Nevertheless, the structure of this xerogel was brittle; grounded or broken xerogel did not swell back into the volume of initial gel.

Another experiment determined an influence of a low-molecular electrolyte (NaCl) addition. It has been confirmed that NaCl addition causes even visually evident changes in a consistency of the gel. Small addition (~ 0.3% of the weight of mixture) increases water content of the gel, while higher addition (~ 3 %) has an opposite effect. Rheometrical measurement proved that all hydrogels show typical response of a fully cross-linked highly elastic gel; storage moduli (G') are about one order higher than the loss moduli (G'') and almost constant in a whole region of available frequencies. Addition of NaCl also affects sorption properties of gels. It was proved that isotherms for a sorption of Cu^{2+} showed typical Freundlich shape. Addition of NaCl lead to stronger binding of sorbate in a gel (during desorption experiments).

Hydrogel beads, as prepared either by reaction between chitosan solution and sodium humate or by a sorption of

humic acids on the chitosan beads, represent promissing form for industrial and agricultural application (mainly after freeze drying). Dry content of the bead is higher (~ 15% of weight). Sorption and swelling properties of this material will be taken as a focus of following experimental work.

Conclusions

This contribution introduces several preparation methods providing novel hydrogel systems made of HA. Profitable properties of resulting gels and xerogels (high swelling, sorp-tion ability, compact consistency and others) make chitosan become a material of choice for mixed biopolymer gelation of HA.

REFERENCES
1. Sedláček P., Klučáková M.: *ECCE-6, Copenhagen, Book of Abstracts* Vol. 1, p. 995. 2007.
2. Santosa S. J. et al.: Surf. Sci. *601*, 5148 (2007).
3. Ruvalcaba-Martínez A. et al.: Carbohydr. Polymer. *67*, 586 (2007).

L15　PHOTOCHEMICAL AND FREE RADICALS STUDY OF CYANOBACTERIA USING EPR SPECTROSCOPY

PAVEL STOPKA[a], BLAHOSLAV MARŠÁLEK[b] and JANA KŘÍŽOVÁ[a]

[a]*Institute of Inorganic chemistry v.v.i., Czech Academy of Science v.v.i., 25068 Husinec-Řež,*
[b]*Institute of Botany, Czech Academy of Science v.v.i., 60365 Brno, Czech Republic,*
stopka@iic.cas.cz

Introduction

We studied free radicals and their reactions in Cyanobacteria from Brno Dam on Svratka River by EPR spectroscopy. We have found free oxygen radicals on the surface of Cynobacteria. Their concentrations increase by the UV and visible light irradiation, and, in the process of their grow. By the breakdown of Cyanobacteria their concentrations falling down. These free radicals cause the health damage on the human skin and inner membranes. We have found, that some natural products cause breakdown of Cyanobacteria on the basis of their interaction with free radicals on their surface. Wheat and barley straw generate free radicals, mainly hydroxyl radicals in aqueous suspensions also. These radicals could have interaction with free radicals on Cyanobacteria to destroy it. Cynobacteria contains Fe(III) and high spin Mn(II) complexes.

Our previous experiments measured by electron paramagnetic resonance spectroscopy (EPR, ESR) proved, that actively growing cyanobacteria produce characteristic spectrum of free radicals, which may play an important role in aquatic ecosystems. Our preliminary experiments analysed by EPR also proved, that barley and wheat straw produce quite different spectrum of free radicals. Application of barley straw was published many times, but the principle remains unknown. At least on of he principle could be based on the trapping and quenching the cyanobacterial stable radicals by specific radicals produced by especially prepared natural materials. This "neutralisation" of radicals could be safe for aquatic ecosystems. We study select different natural plant materials with potential algistatic activity. Eutrophication of aquatic ecosystems and the consequent mass occurrence of harmful cyanobacterial blooms are growing problems in the entire world. Cyanobacterial blooms deteriorate water quality by toxins and odours production. Cyanobacterial toxins (microcystins, anatoxins, lipopolysacharide etc.) are known to have hepatotoxic, neurotoxic, imunotoxic, genotoxic and other adverse effects. Cyanotoxins in drinking water, fish consumption and recreational use of reservoirs represents a growing risk for human health. Besides this, cyanobacterial bloom means considerable stress for ecological stability of aquatic ecosystems, natural fish and amphibian reproduction, biodiversity of phytoplankton and zooplankton community etc. Not only toxin production is harmful, but also decrease of light intensity, pH change and excessive oxygen deple-

tion. Therefore measures to control of cyanobacterial growth are of high priority for water management. This is an actual problem in the Czech republic and many European countries For effect in shorter time algal blooms have been formerly injured by non-selective chemicals such as copper salts, but this application is no longer acceptable. Consequently there is a scope for finding of new types of algicides more selective for cyanobacteria. Except selectivity the biodegradability is the second requirement for new types of algicides. Therefore, the use of some natural agents could be acceptable and more environmental friendly way than the undesirable application of toxic algicidal chemicals. There are several references about algicidal compounds based on natural materials or extracts in the scientific literature.

Materials and Methods

Methodology for the EPR spectroscopy studies, especially *in vivo* studies was developed. The presence of free radicals on Cyanobacteria samples was measured and evaluated. The measurements of free radicals, will continue and somehypothesis regarding the content of phenolic compounds and their antioxidative capacity.

M a t e r i a l s

5,5-Dimethyl-1-pyrroline-N-oxide (DMPO) (Sigma-Aldrich) was used as a radical trapping agent for oxygen and nitrogen radicals. 2,2,6,6-Tetramethylpiperidine-1-oxyl (Tempol) (Sigma-Aldrich) was used as a reactant with antioxidative substances for determination of antioxidant activities. Calibration standards were Mn^{2+}/ZnS and Cr^{3+}/MgO (Magnettech, Berlin, Germany).

E l e c t r o n　P a r a m a g n e t i c　R e s o n a n c e　(E P R)　M e a s u r e m e n t s

EPR spectra were recorded with E-540 Spectrometer X-Band (Bruker-Biospin,Germany). The following conditions were used while recording the spectra: microwave power 20 mW, magnetic modulation amplitude 0.2 mT, attenuation 20 dB, time konstant 0.5 s, scan speed 0.3 mT min^{-1}, calibration standards Mn^{2+}/ZnS and Cr^{3+}/MgO, measurement at 25 °C. WinEPR and Bruker (Bruker-Biospin, Germany) programs were used for spectra recording, handling and evaluation. The evaluation of EPR spectra was achieved according literature Weil, Bolton and Wertz[1], program Bruker-Xepr, Origin and Data Base of free radicals[2] (NIEHS, Bethesda, Maryland, USA).

Irradiation: UV and visible light irradiation of liquid sample in EPR resonator were used in the study of effect of irradiation on free radicals generation. Samples were irradiated in the EPR resonator using mercury discharge lamp for UV light irradiation (Bruker-Biospin), and halogen lamp for visible light irradiation.

Results

Typical EPR spectrum of Cyanobacteria has been shown on Fig. 1. The spectrum contains: *(i)* broad signal of low spin

Fe(III), *(ii)* organic stable radical, singlet, g = 1.99435, near to signal of free electron g = 2.0032, *(iii)* 2nd singlet of other free radical g = 2.0801, *(iv)* sextet 1:1:1:1:1:1 of high spin complex of Mn(II). No other signals in broad range are presented. There are new signals by the UV and visible irradiation of Cyanobacteria, see Fig. 2.
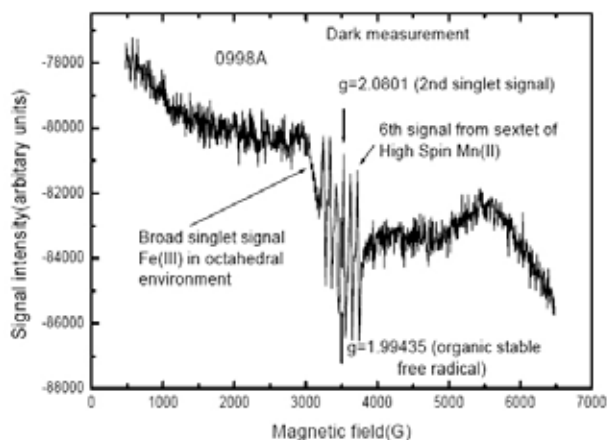

Fig. 1. **Typical EPR spectrum of aqueous suspension of Cyanobacteria (EPR X-Band, 25 °C, microwave pover 20 mW, Magnetic modulation 0.1 mT)**
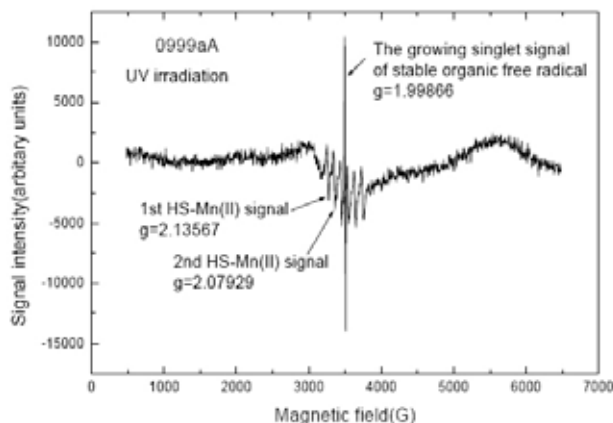

Fig. 2. **EPR spectrum of UV irradiated aqueous suspension of Cyanobacteria (EPR X-Band, 25 °C, microwave pover 20 mW, Magnetic modulation 0.1 mT)**

The generation of unstable free radicals was studied by the spin trapping method, using DMPO as a spin trap. It has been found hydroxyl and nitroxide radicals in Cyanobacteria. Their concentrations increase by the UV and visible irradiation. It has been found hydroxyl radicals and nitroxide radicals. They generate in nature and are dangered for human skin and tissue membranes: danger of irritation, inflammation, fever.

We studied effect of copper sulfate $CuSO_4$ and cyanobacteria interaction in aqueous suspensions. The new free radicals have been found: multi line spectra: their identifica-
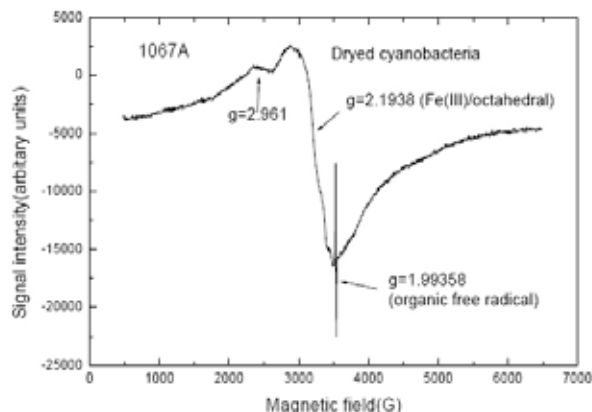

Fig. 3. **Dryed Cyanobacteria (EPR X-Band, 25 °C, microwave pover 20 mW, Magnetic modulation 0.1 mT)**

tion was not possible. We studied effect of added hydrogen peroxide H_2O_2 to aqueous suspensions of Cynobacteria. The increasing concentration of stable organic radical (g near 2) is generated, hydroxyl and nitroxide radicals. We tried to measure dry cynobacteria. We have measured this EPR spectrum.

We studied effect of straw on free radicals on cyanobacteria surfaces and their interactions.

Wheat straw show the simply EPR spectrum: singlet signal (g = 2.0031, ΔH_{pp} = 0.6619 mT = 6.619 Gauss). There is the possibility of interaction between this radical and radical from Cyanobacteria leading to the breakdown of Cyanobacteria radical.

Barley straw show the simply EPR spectrum: singlet signal (g = 2.00325, ΔH_{pp} = 0.6317 mT = 6.317 Gauss). There is the possibility of interaction between this radical and radical from Cyanobacteria leading to the breakdown of Cyanobacteria radical.

Barley straw (aqueous suspension, bubbled by air at room temperature) show the simple EPR spectrum: singlet signal (g = 2.00, ΔH_{pp} = 0.63 mT = 6.30 Gauss). This signal increases by the UV irradiation of this sample. There is the possibility of interaction between this radical and radical from Cyanobacteria leading to the breakdown of Cyanobacteria radical.

Wheat straw (aqueous suspension, bubbled by air at room temperature): no signal, noise only.

We studied these samples in aqueous suspensions at anaerobic conditions:

Wheat straw show the anisotropic EPR spectrum: ($g_{\parallel}$ = 2.39, $g_{\perp}$ = 2.01045, ΔH_{pp} = 24 mT = 240 Gauss). Probably radical with axial symmetry. There is small singlet signal in the little part of spectra: g = 1.9924, probably stable organic radical on the surface of straw. These radicals are presented in the environment of wheat straw particles.

Barley straw show the EPR spectrum: (g = 2.2331 ΔH_{pp} = 75 mT = 750 Gauss) probably low spin complex of Fe(III) and spectrum of high spin complex of Mn(II). These

radicals are presented in the environment of Barley straw particles. There is the principle of action of straw against Cyanobacteria free radicals.

Discussion

The generation of hydroxyl and nitroxide radicals on the surface of Cyanobacteria in natural waters has been found using EPR spectroscopy. These radicals could cause damage on the human skin and membranes. Their generation increase by UV and visible light irradiation. The generation of hydroxyl radicals by the breakdown of hydrogen peroxide is accelerated in the presence of Cyanobacteria. Wheat and barley straw generate free radicals, mainly hydroxyl radicals in aqueous suspensions also. These radicals could have interaction with free radicals on Cyanobacteria to destroy it. Cynobacteria contains Fe(III) and high spin Mn(II) complexes. The UV and visible light accelerate their generation and the ultimate concentration is higher. Cyanobacteria accelerate the breakdown of hydrogen peroxide and UV and visible light accelerate this effect. Wheat straw and barley straw generate free radicals which are on their surfaces and in surrounding aqueous solution. These radicals can react with free radicals located on the surface of Cyanobacteria to destroy their. Cyanobacteria (wet and dry) contain complexes of low-spin Fe (III) and high-spin Mn (II). It can play an important role for stabilization of presented unstable free radicals.

Conclusions

We have found the role of free radicals (mostly hydroxyl radicals) in ill-effects of Cyanobacteria. This result pointed to that the effect of these radicals could be eliminated by the action of straw. We have found the effect of UV and visible irradiation on the generation of hydroxyl and nitroxide radicals. Wheat straw and barley straw generate free radicals which are located on their surfaces and in surrounding aqueous solution. We have an idea to fight against Cyanobacteria using free radicals and paramagnetic metal complexes with UV and visible light irradiation.

REFERENCES

1. Weil J. A., Bolton J. R, Wertz J. E.: *Electron Paramagnetic Resonance, Elementary Theory and Practical Applications*, J.Wiley and Sons, N.York 1994.
2. Wyard S. J.: *Elektronenspinresonanz und andere spektroskopische Methoden in Biologie und Medizin*. Akademie-Verlag-Berlin 1973.
3. Stopka P., Křížová J.: Chem. listy *100*, 716 (2006).

L16 MOLECULAR ELECTRONICS: ADVANCES AND LIMITATIONS, STRATEGIES, MATERIALS, METHODS AND APPLICATIONS

MARTIN VALA and MARTIN WEITER

Brno University of Technology, Faculty of Chemistry, Purkyňova 118, Brno 612 00, Czech Republic,
vala@fch.vutbr.cz

Introduction

A molecular electronics (ME) might be defined as set of electronic behaviours in molecule-containing structures that depend upon the characteristic molecular (rather than atomic) organization of space. This behaviour is fixed at the scale of individual molecule, which is the naoscale. While the structures and devices may be macroscopic, the fundamental behavious arise at the molecular level.

Over the past several decades there have been dramatic advances toward the realization of electronic components from organic materials instead of the inorganic semiconductors. The true advencement can be achieved by utilization of the original properties of the organic materials to construct devices based on those individual features, which do not have analogies in the inorganic semiconducting physics. This is usually accomplished with the help of quantum chemical calculations, which can predict the desired properties of new materials prior to the synthesis.

The aim of this article is to introduce some of the strategies developed to take full advantage that the organic-based electronics offer. The attention is paid to solar cells, displays, and transistors representing the most developed applications. Some of them are already entering the commercial world. The last part is devoted to single molecule current switching device as the essential components of molecular memories and as good example of quantum chemistry-synthesis-device pathway used in ME research nowadays.

Materials

There is wide range of materials used in the area of ME. In the present time not only the actively performing materials (electroluminescencent, electric charge fotogenerating, etc.) but also other supporting materials are used to increase the performance of the produced devices. The materials have to cover broad range of requirements and therefore range from the low molecular weight over polymeric ones to supramolecular structures. It is therefore common strategy to tailor the properties by introducing side groups whose position, number and properties adjust the required qualities (preventing of agreagation, solubility, etc.).

However, a wide pool of posibilities exists also for the active area of the device. Many scientific groups and companies use small molecules mainly because of their intrinsic high thermal and optical stability, fatique resistance etc. On the other hand the processing usually requires thermal evaporation under vacuum which migh increase the cost of the device prepared. To increase the performance, the devices usually consists of many layeres (> 20) whose preaparation requires many precise processing steps (e.g. co-evaporation) and can increse the possibillitiy of introduction of defecst and thus might also raise the cost of such devices. Doping of these materials turned out to be a necessary strategy in order to obtain efficient devices. Examples of the materials are in Fig. 1.

The other main class of materials used consists of high molecular weight materials: polymers. The field of semiconducting polymers has it root in the 1977 discovery of the semiconducting properties of polyacetyene[1]. This breakthrough earned Alan Heeger, Alan MacDiarmid, and Hideki Shirakawa the 2000 Nobel Prize in Chemisty for "the discovery and development of conductive polymers".[2–4]

There are four specific types of semiconducting polymers:

- Filled polymers are loaded with conductive fillers, such as carbon black, graphite fiber, or metal oxide particles, and have the broadest application in electronic devices. However, they are inhomogeneous materials, which makes them hevily process-dependent and harder to reproduce.
- Ionically conducting polymers are used in such consumer electronic applications as rechargeable batteries, fuel cells, and polymer light emitting devices although their conductivity is highly sensitive to humidity.
- Conjugated polymers where delocalisation of pi-electrons allows for charge carrier conduction and is responsible for their semi-conducting properties; see Fig. 2.
- Charge-transport polymers have become the most established semiconducting organic system because of their commercial use in xerographic photoreceptors.

A special class of materials consists of molecules specially designed and synthesized to ensure a specific feature on molecular level. As an example we may mention a carotenoid-porphyrin-fullerene (C-P-C_{60}) triad. When porphyrin absorbs light, it donates electron to the fullerene and take electon form the carotenoid. This leads to charge separation (creation of C^{+}-P-C_{60}^{-}) and is analogous to the processe involved in photosysnthesis[5]. Another example will be discussed later.

Applications

Organic Solar Cells

In principle, there are four types of solar cells in terms of organic based electronics:

- Conjugated polymers based solar cells usually utilize "bulk heterojunction" between semiconducting polymer as an electron donor and low molecular weight acceptor to ensure efficient photo-induced charge generation.
- Small molecular solar cells are based on the same donor-acceptor concept but composed of low molecular weight materials and therefore require different device design and processing.

- Dye-sensitised solar cells are based on electron transfer from organic sensitizer to wide bandgap semiconductor (e.g. TiO_x) and redox reactions of mediator[6,7].
- Organic-inorganic hybrid solar cells compose of nano sized inorganic semiconductors (usually in the form of core-shell nanoparticle whose bandgap and doping levels can be easily tailored) dispersed in polymeric matrix. The charge separation occurs on the prticle-polymer interface[8]. Since our group deals with the first two types we will pay closer attention to their operational principles, material reguirements and device design and advancement.

The solar cells based on conjugated polymers in its simplest form can be acomplised as a metal-insulator-metal (MIM) diode with the metal electrodes of asymmetrical workfunction (Fig. 3.). The potential difference between electrodes have to be high enough to overcome exiciton binding energy (energy needed to dissociate Coulomb attraction of the foto-generated electon-hole pair: exciton) othervise the excitons will decay geminately (either radiatively or non-radiatively). The usually used electrodes (indium tin oxide, ITO, as the transparent high workfunction metal and Aluminium as the low workunction metal) do not fulfill this requirement sufficiently. The energy conversion efficiencies are typically 10^{-3}–10^{-1} %, too low for practical applications.[9–11] To overcome this limitation various strategies have been employed to increase the photo-induced charge carrier generation.

One of the possible pathways is to introduce p-n junction by doping. The initial experiments of Chiang et al. in 1978 with p-type and n-type polyacetylene films did not succeeded[12]. The alternative way is to use a Shotky junction between conducting polymer and metal. However, neither this approach solved the problem of inefficient charge carrier generation.[13–15]

To overcome the limitation of the photo-induced charge carrier generation, a donor/acceptor (D/A) approach has been suggested.[16–19] The most widely used concept uses semiconducting polymers as an electron donor and fulerene (C_{60}) as an electron acceptor. Analogically to the p-n junction a bi-layer device can be constructed with the D/A interface between the two layers representing the heterojunction (although the actual physical processes are different). Such device has rectifying current-voltage characteristics even for the same metal electrodes on both sides. The positions of the HOMO and LUMO energy levels have to be choosen carefully to realize charge transfer rather than energy transfer, which does not lead to the charge separation. It was shown that the charge transfer from semiconducting polymers to C_{60} occurs within 50 fs after photo-excitation.[20–22] The charge transfer is therefore more than 10^3 times faster than any other competing process.

It follows that further step for efficient photo-induced charge generation is to increase the interfacial area between the donor and acceptor. Creation of so called "bulk hetero-
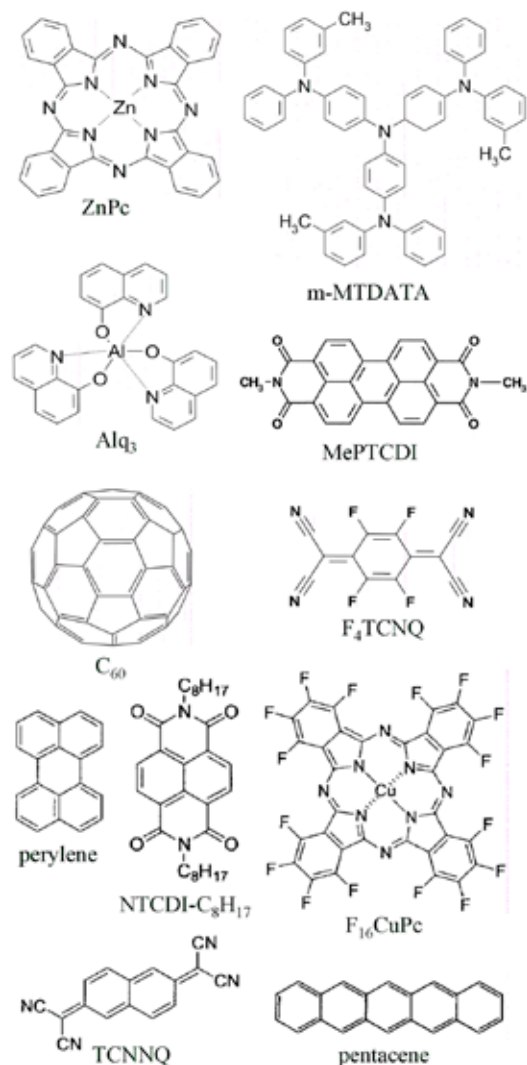

Fig. 1. **Examples of small molecular weight materials nowadays used in molecular electronics as hole transport material (zink pthalocyanine (ZnPc), tris-(phenyl–3-methyl-phenyl-amine)-triphenylamine (m-MTDATA), pentacene), electron acceptors (buckminster-fullerene (C_{60}), 2,3,5,6-tetrafluoro-7,7,8,8-tetra-cyano-quinodimethane (F_4TCNQ)) and electron transport materials (aluminium-tris-8-hydroxy-quinoline (Alq_3), m-MEPTCDI, perylene, NTCDI-C_8H_{17}, F_{16}CuPc, TCNNQ)**

junction" *via* control of the morphology of the phase separation thus have the crutial role for device efficiency[23,24]. Due to the necessity of bipolar charge transport in the bulk an interpenetrating network of D/A phase is further necessary also for equally efficient collection of charges. This approach led to increase of the solar power conversion efficiencies of around 3 %.

Although the polymer based solar cells provide promisssing concept of organic photovoltaics, the match of the absorption spectrum of the polymer with the solar spectrum is rather small and it turned out to be difficult to achieve smaller bandgap in polymers. Alternatively, small organic

dye molecules have been studied as promising materials for photovoltaic devices.[25–30] One of their advantages is their high absorption coefficient ($\sim 10^5$ cm^{-1}) with good overlap with the solar spectrum.
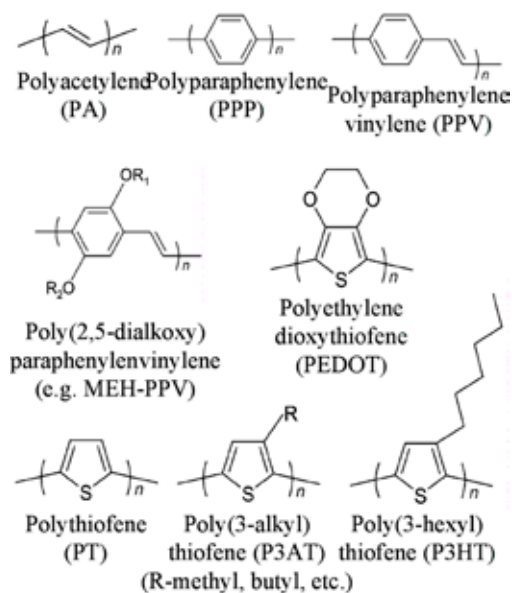

Fig. 2. **Molecular structures of a few conjugated polymers, note the bond-alternated structure responsible for the semi-conducting properties (p-type)**

The general structure of this type of solar cells is in the form of PIN (p-doped/intrinsic/n-dopoed) composed of the active layer and doped wide bandgap materials for hole and electron transport, see Fig. 4. The intrinsic layer is usualy composed of mixture of donor/acceptor molecules which create bulk heterojunction in the same way as in the case of polymer based solar cells. This approach has several advantages.

(i) The transport layers are doped in order to increase the conductivity and thus reduce the ohmic losses. *(ii)* Quenching processes at the electrode can be avoided because excitons created in the active layer cannot penetrate into the wide-gap transport layers. *(iii)* The thickness of the highly conductive spacer layers can be tuned to optimize the optical field distribution in the solar cell. *(iv)* The increased overall thickness of the devices allows higher stability and a lower probability for short cuts.

Organic Light Emitting Diodes

Since the first demonstration of efficient light emission from organic light emitting diodes (OLEDs) by the Kodak[31], the attention of following research were paid to lower operating voltages, higher efficiencies and longer lifetimes of the devices. As for the photovoltaics there are also two main clases of materials used: The polymer based LEDs mainly benefiting from the solution processing and the small molecules based LEDs with better stability and efficiency[32].
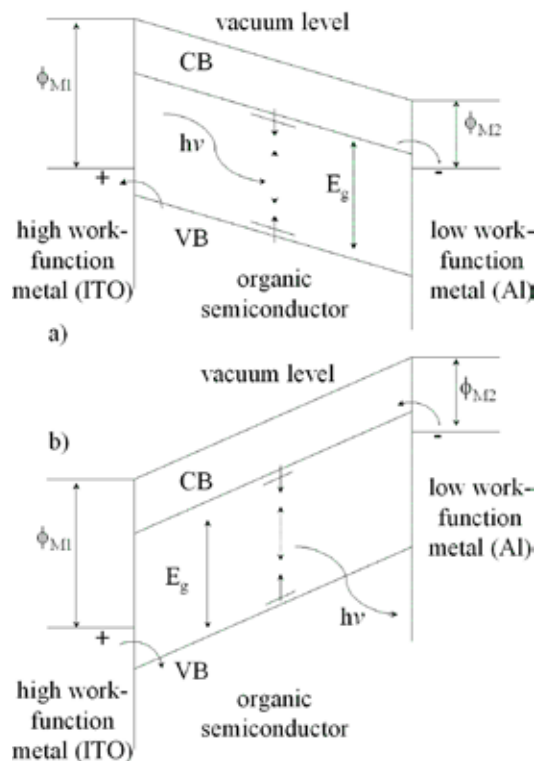

Fig. 3. **a) Charge generation in a single layer organic semiconductor device under short cut conditions (MIM structure), b) the same device under forward bias with suffitient charge injection shows light emission (electroluminiscece). VB is the valence band, CB conduction band, E$_g$ bandgap and φ workfunction**

Electroluminiscence form conjugated polymers were first reported in 1990, using poly(*p*-phenylene vinylene), PPV, as the single semiconductor layer sandwitched between metallic electrodes with different workfunctions. The MIM diode-like structure is the same as depicted for the case of single layer solar cell in Fig. 3. Under sufficient forward bias, holes from the high workfunction metal and electrons form the low workfunction metal are injected in to the thin film of organic semiconductor. Capture of oppositely charged carriers within the semiconductor can then result in photon emission.

The efficiency of the first simple LEDs based on polymers were reatively low, of the order of 10^{-4} photons generated within the device per electron injected (an internal quantum efficiency of 0.01 %)[33]. The internal quantum efficiency is defined as product of the ratio of the number of exciton formation events within the device to the number of electron flowing in the external circuit, the fraction of excitons which are formed as a singlets and the efficiency of radiative decay of these singlet excitons. In order to achieve efficient luminescence, it is therefore necessary to have good balancing of electon and hole currents, efficient capture of electons and holes within the emissive layer, strong radiative transitions

for singlet excitons, and efficient coupling of these excitons to photon states allowed in the device structure.

The electon-hole capture leads to formation of excitons. The spin wavefunction of the exciton can be either singlet or triplet. Because of the exchange energy (the difference between the singlet and triplet state) is usually large, the allowed radiative emission is from the singlet only (fluorescence). Assuming that the electon-hole capture is spin independent (Langevin model) the created excitons are in the triplet and singlet configuration in the ratio 3 : 1, therefore it is expected to loose 75 % of the electron-hole pairs. It would be therefore very attractive to use the triplet excitons. One possible approach is to introduce high-atomic-number elements with strong spin-orbit coupling to utilize the triplet luminescence (phosphorescence).[34–36] However, the triplet emission is usually red-shifted and it turned out to be rather difficult to utilize this approach for emission of green and blue colours.[34,35,37]
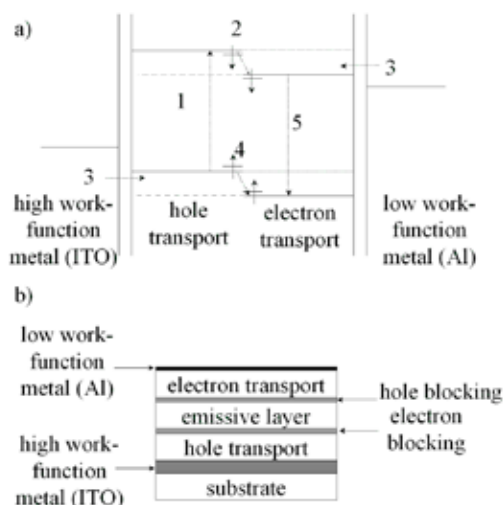

Fig. 4.   **a) Schematic diagram of a bilayer device and formation of bulk heterojunction (dotted lines) before contact of the materials is made. The charge generation process (1 – absorption, 2 – charge transfer and subsequent exciton dissociation) and light emission process (3 – charge injection, 4 – tunneling across a barrier and capture of charges and 5 – light emission), b) diagram of multilayer device configuration. Each of the layers can consist of more materials (doped) and each of the interfaces can be tailored**

Efficient electron-hole capture can be acomplished only with high density of charges in the emissive layer. Therefore great attention is paid to charge injection and transport. There exist several mechanisms that are involved for the injection of charges from metal electrodes. For diodes with large barriers either the thermionic emission or tunneling can limit the current flow. Therefore proper selection of metals used as the contact and series of pre-contact layers are employed to lower the potential barriers. Using this approach the charge injection is no more considered to limit the current flow.

Instead, the current flow is bulk-limited through the bild-up of space charge[38].

The need for balanced electron and hole current let to implementation of hole-conducting and electon-conducting layers and thus to the creation of heterojunction in the same fashion as for the solar cells, see Fig. 4. Injected charges move to the heterojunction at which they are confined by the potential barrier. Depending on the relative position of the energy position electrons or holes tunnel through this barrier and electon-hole capture lead to the electroluminescence from the respective layer. Using this approach external quantum efficiecies up to 2,5 % were obtained[39,40].

All of the principles mentioned for the polymer based LEDs are valid also for LEDs based on small molecules. In fact many of the strategies described were simultaneously or firstly discovered using this type of materials (e.g. the bilayer structures). Simirally to the solar cells the preparation technique (sublimation) offers easy way for doping and co-deposition of several materials and therefore provides additional degrees of freedom and potentially better tunability of the device performance[41]. The structures that are nowadays under study are usually composed of many layers and inter-penetrating regions with controlled thickness, level of n- or p-type doping and provides energetic barier reduction, electron or hole transport or serves as blocking layers and finaly as emissive layers with specific colour or white light emission (>20 layers). For the commercial utilization dynamic in-line deposition techniques producing efficient enough OLEDs with low operational voltages are currently under study[42].

Organic Thin-Film Transistors

Organic thin-film transistors (OTFTs) based on conjugated polymers, oligomers, or fused aromatics have been forecasted as a viable alternative to the traditional thin film transistors based on inorganic semiconductors. But because of the relatively low charge carrier mobilities (μ) in organic semiconductors OTFTs cannot rival the performance of field effect transistors based on inorganic single crystals such as Si, Ge and GaAs, which have charge carrier mobilities of three or more orders of magnitude higher[43]. Therefore, OTFTs are not suitable for high switching frequency applications. However, like in the case of photovoltaic and LED applications, OTFTs can be competitive candidates for applications requiring large area coverage, structural flexibility, low temperature processing, and especially low cost manufacturing (e.g. flat panel displays, sensors, radio-frequency identification tags (RFIDs), etc.).

Due to the weak intermolecular interaction forces, typically van der Waals with energies smaller than 10 kcal·mol^{-1}, which is close to the vibrational energy at or above RT, the upper limit of microscopic mobilities in organic molecular crystals for T = 300 K falls between 1 and 10 cm^{2}V^{-1}s^{-1} (ref.[44]). In contrast, in inorganic semiconductors such as Si, Ge and GaAs, the atoms are held together with very strong covalent bonds, which in the case of Si have energies as high as 76 kcal mol^{-1}. The charge carriers move as highly

delocalised plane waves and have a very high mobility at RT ($\mu \sim 10^3$ cm^2 V^{-1} s^{-1}).

The boundary between band transport and hopping is defined by materials having RT mobilities of the order of 1 cm^2 V^{-1} s^{-1} (ref.[44]). Thin films of highly oriented organic semiconductors, such as several members of the acene series including pentacene, have RT mobilities in this intermediate region. Furthermore, very high mobility values have been measured using time of flight (TOF) experiments (up to 400 cm^2 V^{-1} s^{-1} for holes in single crystals of naphthalene at 4.2 K[45, 46]) and field effect experiments (up to $\sim 10^5$ cm^2 V^{-1} s^{-1} for holes in single crystals of tetracene and pentacene at 1.7 K[47,48]) following a power law ($\mu \approx T^{-n}$). This gives the evidence for band-like transport in these high qualities, ultra pure single crystals. On the other hand, this behaviour is rather impossible to observe in amorphous or polycrystaline films because traps attributed to grain boundaries and other structural defects dominate transport[49]. The carrier transport takes place by hopping between localised states and carriers are scattered at every step.

Several strategies leading to increased mobilities in organic materials follow from these fundamental limits[43]. One of them is to strengthen the intermolecular interactions. Stronger interactions would lead to more rigid crystalline structures and thus it would take temperatures higher than RT to generate subtatntial scattering of charge carriers. A second way is to dramatically reduce the conduction path. If the carrier transport occurs via an array of single molecules, such as polymer chains or nanotubes the mobility is no more influenced by the grain boundary or other structural defects. Reduction of the TFT channel from micrometer to nanometer size led to mobilities of the order of 100 cm^2 V^{-1} s^{-1} in the case of carbon nanotubes[50].

Molecular Switch

This chapter deals with construction of molecular current switch based on light driven switching of on-chain charge carrier mobility investigated at our department. To describe the proposed molecular switch, we have to briefly describe origin of traps in molecular solids first, for details see[49].

According to electrostatic approach, the ionisation energy of a crystal (I_c) is related to the molecular value (I_g) by $I_c = I_g - P$. The parameter P, referred to as the polarisation energy, represents the energy of interactions between a charge carrier localised on a given lattice site and the surrounding polarizable lattice. Local decrease of I_c in an otherwise perfect crystal lattice represents a trap for moving hole. The trap can be thus created *(i)* on a host molecule with suitably low I_g, or *(ii)* by increasing of the value of the polarization energy P contrary to that in a physically perfect material. In a molecular solid build of non-polar polarizable units, e.g. polymer segments, containing a small amount of polar guest species, its dipole moment contributes to the field acting on surrounding molecules and modifies the local values of the polarization energy. Thus, the presence of polar species may result in production of local states in their vicinity; even thus they

are not necessarily trapping sites themselves. The calculations of trap parameters (depth, extension) indicate that local perturbations of the polarization energy due to the presence of a highly polar guest molecule may result in extension over several lattice constants, and hence should influence the on-chain charge carrier mobility[51].

Changing of the dipole moment of suitably chosen side groups both, chemically attached to the polymer chain via a neutral spacer or dispersed in the matrix, thus results in changing of the on-chain charge carrier mobility. Use of photochromic side groups make it possible to modulate the charge mobility by light-activated photochromic reaction.
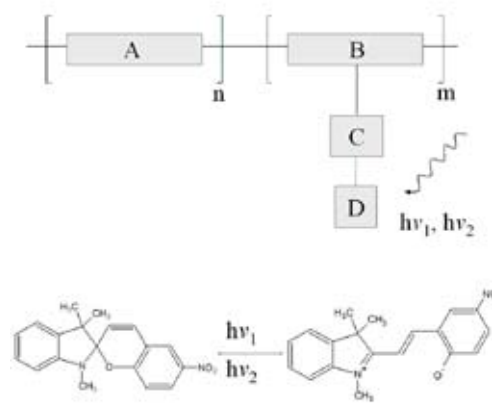

Fig. 5. **Schematic representation of light driven molecular current switch and photochromic reaction of spiropyran. The two states can be obtained using light of different wavelength (UV for the forward and VIS for the back reaction)**

The molecular current modulator is schematically demonstrated in Fig. 5. The switch consists of a molecular wire with suitable bistable side group(s). Various materials can be used to build the switch. Blocks A and B (molecular wire) can be realised by π- or σ- conjugated polymer chains as depicted in Fig. 2. The spacer C can be realised by several chemical structures, its length being easily tailored to needs resulting from e.g. model calculations. The active switching system (block D) should be selected in order to produce large dipole moment change in its two states as described above. The active moiety can be successfully realised by e.g. spiropyrans (Fig. 5.). Depending on substituents attached to their backbones, these molecules can change their dipole moment from 2–5 D to 5–13 D (theoretical calculations reveal up to 30 D)[52].

The change of the electrostatic potential due to the charge-dipole interactions shifts the transport levels. Since the position and orientations of the additive are essentially random the effect results in broadening of the distribution of transport states[53,54] and to the decrease of the charge carrier mobility[55,56,57].

In a similar way to the charge-dipole interactions resulting in mobility switching the formation of chemical traps was also demonstrated[58]. Quantum mechanical calculations

showed the possibility of the participation of the main chain electrons in the photochromic process of the side group and points to the importance of the chemical structure of the spacer. The spacer can be realised as a 'quasi-neutral' from the point of view of the charge transfer, or can freely transfer the charge. In the former case, the electrostatic contribution of the polar side groups, based on the charge-dipole interactions, is the most important factor influencing the behavior of the charges on the molecular wire. In the latter case however, the situation is more complex: the change of the chemical structure and charge redistribution on the substituent, and a charge redistribution between the molecular wire and the photochromic group may influence the ionization energy of the entire polymer segment. Such modification may results in the creation of a chemical trap on the segment.

Conclusions

Since the early times in 1970s molecular electronics went through long way from visionary (sometimes speculative) ideas over pioneering measurement of molecular-level properties to devices efficient enough enabling to start their mass production. Despite such immense development there are still many fundamental aspects that need to be answered in order to fully exploit the potential this area offers as can be seen from the examples we outlined in this article. The progress can be possible only with synergic development in many scientific areas e.g. physics, chemistry, quantum chemistry, metrology and in close cooperation of basic and applied research (science and technology).

REFERENCES

1. Chiang C. K., Fincher C. R., Park Y. W., Heeger A. J., Shirakawa H., Louis E. J., Gau S. C., MacDiarmid A. G.: Phys. Rev. Lett. *39*, 1098 (1977).
2. Heeger A. J.: Synth. Met. *125*, 23 (2002).
3. MacDiarmid A. G.: Synth. Met. *125*, 11 (2002).
4. Shirakawa H.: Synth. Met. *125*, 3 (2002).
5. Liddell P. A., Kuciauskas D., Sumida J. P., Nash B., Nguyen D., Moore A. L., Moore T. A., Gust D.: J. Am. Chem. Soc. *119*, 1400 (1997).
6. Grätzel M.: J. Photoch. Photobio. C *4*, 145 (2003).
7. Durrant J. R., Haque S. A., Palomares E.: Coordin. Chem. Rev. *248*, 1247 (2004).
8. Huynh W. U., Dittmer J. J., Teclemariam N., Milliron D. J., Alivisatos A. P., Barnham K. W.: Phys. Rev. B *67*, 115326 (2003).
9. Yu G., Zhang C., Heeger A. J.: Appl. Phys. Lett. *64*, 1540 (1994).
10. Antoniadis H., Hsieh B. R., Abkowitz M. A., Stolka M., Jenekhe S. A.: Polym. Prepr. *34*, 490. (1993).
11. Karg S., Riess W., Dyakonov V., Schwoerer M.: Synth. Met. *54*, 427 (1993).
12. Chiang C. K., Gau S. C., Fincher C. R., Park Y. W., MacDiarmid A. G., Heeger A. J.: Phys. Rev. Lett. *33*, 18 (1978).
13. Antoniadis H., Hsieh B. R., Abkowitz M. A., Stolka M., Jenekhe S. A.: Polym. Prepr. *34*, 490 (1993).
14. Antoniadis H., Hsieh B. R., Abkowitz M. A., Jenehke S. A., Stolka M.: Synth. Met. *62*, 265 (1994).
15. Rieß W., Karg S., Dyakonov V., Meier M., Schwoerer M.: J. Lumin. *60–61*, 906 (1994).
16. Sariciftci N. S., Smilowitz L., Heeger A. J., Wudl F.: Science *258*, 1474 (1992).
17. Sariciftci N. S., Braun D., Zhang C., Srdanov V., Heeger A. J., Stucky G., Wudl F.: Appl. Phys. Lett. *62*, 585 (1993).
18. Yu G., Gao J., Hummelen J. C., Wudl F., Heeger A. J.: Science *270*, 1789 (1995).
19 Halls J. J. M., Walsh C. A., Greenham N. C., Marseglia E. A., Friend R. H., Moratti S. C., Holmes A. B.: Nature *376*, 498 (1995).
20. Kraabel B., McBranch D., Sariciftci N. S., Moses D., Heeger A. J.: Mol. Cryst. Liq. Cryst. *256*, 733 (1994).
21. Kraabel B., Hummelen J. C., Vacar D., Moses D., Sariciftci N. S., Heeger A. J.: J. Chem. Phys. *104*, 4246 (1996).
22. Lanzani G., Zenz C., Cerullo G., Graupner W., Leising G., Scherf U.: Synth. Met. *111–112*, 493 (2000).
23. Brabec C. J., Shaheen S. E., Fromherz T., Padinger F., Hummelen J. C., Dhanabalan A., J. Janssen R. A., Sariciftci N. S.: Synth. Met. *121*, 1517 (2001).
24. Hoppe H., Glatzel T., Niggemann M., Schwinger W., Schaeffler F., Hinsch A., Lux-Steiner M., Sariciftci N. S.: Synth. Met. *511–512*, 287 (2006).
25. Simon J., Andre J. J.: *Molecular semiconductors*, Spring, Berlin, Heidelberg, 1985.
26. Tang C. W.: Appl. Phys. Lett., 48, 183 (1986)
27. Wöhrle D., Meissner D.: Adv. Mater. *3*, 129 (1991).
28. Petrish K., Dittmer J. J., Marseglia E. A., Friend R. H., Lux A., Rozenberg G. G., Moratiti S. C., Holmes A. B.: Sol. Energy Matter. Sol. Cells *61*, 63 (2000).
29. Debeyhu D., Männig B., Drechsel J., Leo K., Pfeiffer M.: Sol. Energy Matter. Sol. Cells *79*, 81 (2003).
30. Drechsel J., Männig B., Debeyhu D., Pfeiffer M., Leo K., Hoppe H.: Org. Electron. *5*, 175 (2004).
31. Tang C. W., VanSlyke S. A.: Appl. Phys. Lett. *51*, 913 (1987).
32. Shi J., Tang C. W.: Appl. Phys. Lett. *70*, 1665 (1997).
33. Burroughes J. H., Bradley D. D. C., Brown A. R., Marks R. N., Mackay K., Friend R. H., Burns P. L., Holmes A. B.: Nature *347*, 539 (1990).
34. Baldo M. A., O'Brien D. F., You Y., Shoustikov A., Sibley S., Thompson M. E., Forrest S. R.: Nature *395*, 151 (1998).
35. Cleave V., Yahioglu G., Le Barny P., Hwang D. H., Holmes A. B., Friend R. H., Tessler N.: Adv. Mater. *13*, 44 (2001).

36. Pfeiffer M., Forrest S. R., Zhou X., Leo K.: Org. Electron. *4*, 21 (2003).
37. Cleave V., Yahioglu G., Le Barny P., Friend R. H., Tessler N.: Adv. Matter. *11*, 285 (1999).
38. Blom P. W. M., De Jong M. J. M., Vleggar J. J. M.: App. Phys. Lett. *68*, 3308 (1996).
39. Baigent D. R., Greenham N. C., Gruner J., Marks R. N., Friend R. H., Morrati S. C., Holmes A. B.: Synth. Met. *67*, 3 (1994).
40. Becker H., Burns S. E., Friend R. H.: Phys. Rev. B *56*, 1893 (1997).
41. Pfeiffer M., Leo K., Zhou X., Huang J. S., Hofmann M., Werner A., Blochwitz-Nimoth J.: Org. Electron. *4*, 89 (2003).
42. May C., Tomita Y., Toerker M., Eritt M., Loeffler F., Amelung J., Leo K.:Current Appl. Phys. *3*, 293 (2003).
43. Dimitrakopoulos C. D., Malenfant P. R. L.:Adv. Mater. *14*, 99 (2002).
44. Pope M., Swenberg C. E.: *Electronic Processes in Organic Crystals and Ppolymers, 2nd ed.,* Oxford University Press, Oxford 1999.
45. Warta W., Stehle R., Karl N.: Appl. Phys. A *36*, 163 (1985).
46. Karl N., Marktanner J., Stehle R., Warta W.: Synth. Met. *41–43*, 2473 (1991).
47. Shön J. H., Kloc C., Batlogg B.: Org. Electron. *1*, 57 (2000).
48. Shön J. H., Kloc C., Batlogg B.: Science *288*, 2338 (2000).
49. Sworakowski J., Janus K., Nešpůrek S., Vala, M.: IEEE T. Dielect. El. In. *13*, 1001 (2006).
50. Collins P. G., Arnold M. R., Avouris P.: Science *292*, 706 (2001).
51. Nešpůrek S., Sworakowski J., Thin Solid Films *393*, 168 (2001).
52. Dürr H., Laurent H. B.: *Photochromism: Molecules and Systems, 2nd ed.,* Elsevier Science B.V., Amsterdam, 2003.
53. Toman P., Nešpůrek S., Weiter M., Vala M., Sworakowski J., Bartkowiak W., Menšík M.: Nonlinear Opt. , Quantum Opt. *36*, 289 (2007).
54. Toman P., Nešpůrek S., Weiter M., Vala M., Sworakowski J., Bartkowiak W., Menšík M.: Polym. Adv. Technol. *17*, 673 (2006).
55. Weiter M., Vala M., Zmeškal O., Nešpůrek S., Toman P.: Macromol. Symp. *247*, 318 (2007).
56. Bletz M., Pfeifer-Fukumura U., Kolb U., Baumann W.: J. Phys. Chem A *106*, 2232 (2002).
57. Vala M., Weiter M., Zmeškal O., Nešpůrek S., Toman P.: Macromol. Symp., accepted.
58. Nešpůrek S., Toman P., Sworakowski J., Thin Solid Films *438–439*, 268 (2003).

L17 MUTUAL RELATION BETWEEN FRACTAL AND STATISTICAL (RANDOM, THERMODYNAMIC) PHENOMENA IN NATURE

OLDŘICH ZMEŠKAL, MARTIN WEITER, MARTIN VALA and TOMÁŠ BŽATEK

Brno University of Technology, Faculty of Chemistry, Purkynova 118, 612 00 Brno, Czech Republic,
zmeskal@fch.vutbr.cz

Introduction

This paper deals with the unification of views on different physical and chemical fields of knowledge on natural phenomena. We put into context physical quantities defined in fractal physics, thermodynamics and statistical physics with general mathematical description by momentum of random quantities.

The mathematical tools of fractal physics enable a universal description of such phenomena as e.g. thermal radiation, conduction and convection of heat, properties of ideal and real liquids and/or gases, thermodynamic entropy of closed and open system and classic and quantum distribution functions.

This unification is not only of a theoretic importance, but enable the implementation of further modules into the HarFA application (developed by authors of this paper). The program HarFA was intended for fractal analysis of digital images, video clips, signals and numerical data sets. The new modules enable calculation of five fractal dimensions (topological, information – thermodynamic, correlative, skewness and kurtosis) which relate to corresponding moments and entropies. Thus a unification of phenomena description by different sciences is achieved.

Theoretical Backgrounds

General and Central Moments

To describe studied phenomenon, various mathematical apparatus is used in different science areas. As an example we can mention mechanics, statistical physics and physical chemistry which use general and central moments do define mean values of the respective physical qualities (e.g. position, velocity, acceleration) or their deviations form the mean values (absolute error, standard deviation, skewness, kurtosis).

Generally these moments for one variable functions can be expressed using equations (1) and (2), ref.[1].

General moments of qth order of discrete and continuous functions in real number field can be defined using the equations

$$M_q = \int_{-\infty}^{\infty} x^q f(x)\,dx \quad M_q = \sum_{i=0}^{\infty} x_i^q f(x_i) \tag{1}$$

Similarly the central moment q^{th} order of the discrete or continuous functions related to general moment of the first order (mean value μ) can be defined as

$$m_q = \int_{-\infty}^{\infty} (x-\mu)^q f(x)\,dx , \quad m_q = \sum_{i=0}^{\infty} (x_i-\mu)^q f(x_i) . \tag{2}$$

Absolute Errors

To calculate absolute values of random real quantities values of qth order defined in the final interval or in final interval of random real quantities with functional values uniformly distributed ($f(x)$ = const.) can the equation (2) written as

$$r_q = \frac{1}{l}\int_0^l |x-\mu|^q\,dx , \quad r_q = \frac{1}{n}\sum_{i=0}^{m} |x_i-\mu|^q . \tag{3}$$

The comparison of the equation (2) and (3) gives an evidence that the central moments of the even orders are in the case of uniform distribution of random quantities equal to the absolute errors of the random quantities but the odd orders differ (e.g. central moment 1st order $m_1 = 0$, r_1 is an absolute error of random value).

To compare the random samples, standardization to central moment of 2nd order (to standard deviation σ) is often employed

$$R_q = \frac{1}{l}\int_0^l \left|\frac{x-\mu}{\sigma}\right|^q\,dx , \quad R_q = \frac{1}{n}\sum_{i=0}^{m} \left|\frac{x_i-\mu}{\sigma}\right|^q , \tag{4}$$

where $\sigma = r_2^{1/2}$. A simple consideration we can derive that $R_2 = 1$, R_3 is *skewness* (standardized moment of 3rd order) and R4 is *kurtosis* (standardized moment of 4th order). These equations are used as a standard DIN EN ISO 4287/ASME *Perthometer. Surface Texture Parameters* used for surface roughness evaluation although the equations have more general character.

Entropy and Fractal Dimension

The entropy is very often used for describing of statistical processes. The Kolmogorov K-entropy is important characteristic which describes a degree of chaoticity of the system. It is well-known that: in an ordered system ($K = 0$), in a random system ($K \to \infty$) and in a chaotic (semi deterministic) system ($0 < K < \infty$).

The generalized entropy K_q can be defined like the generalized dimension. From the term of generalized entropy[3] the Renyi entropy S_q of q order implicit

$$S_q = \frac{1}{1-q}\ln\int_0^l p^q\,dx , \quad S_q = \frac{1}{1-q}\ln\sum_{i=1}^{m} p_i^q , \tag{5}$$

where p (p_i respectively) is probability of continuous (discrete) random process.

It follows form the comparison of the equations (3) and (4) that the Renyi entropy of q order is related with absolute errors of q order defined for the statistical evaluation of random samples $S_q = \ln R_q/(1-q)$ for probability (relative frequency) defined by term $p_i = (x_i - \mu)/(n\sigma)$. It is evident that for $q < 1$ will be entropy positive ($S_0 = \ln m$, so called *topological* or *Hausdorff entropy*) and for $q > 1$ will be entropy

negative already. The special case is for $q \rightarrow 1$ when the value of numerator is implicate to zero and entropy will be

numerator is implicate to zero and entropy will be

$$S_1 = \sum_{i=1}^{m} p_i \ln p_i \ \text{ or } \ S_1 = k_B \sum_{i=1}^{m} p_i \ln p_i \,, \qquad (6)$$

The left term is called *information* or *Shanon entropy*, the right one (information entropy multiplied by Boltzmann constant) as a *thermodynamic entropy*. The entropies for $q = 2$, 3 or 4 are called as *correlation*, *skewness* or *kurtosis entropy*. Fractal dimensions can be assigned to individual entropies

$$S_q = -D_q \ln r \qquad (7)$$

The dimensions for $q = 0$, 1, 2, 3 or 4 are called *topological* (*Hausdorff*) *information* (*Shanon*), *correlation*, *skewness* or *kurtosis dimension*.

Experimental

F r a c t a l   D i m e n s i o n

Statistical (e.g. thermodynamic) processes can be also understood as fractal systems. In this case the fractal algebra is used for its description. Suppose that cell with size $r = 1$ will have K states (K is so called fractal measure). The cell with dimension $r < 1$ will than have $N(r) \leq K$ states given quality according to the way the states are distributed in the cell (microstates in macrostate). The type of the distribution can be described using quantity called fractal dimension D. Relating of this number to the elementary cell unit in E-dimensional space (r^E), the density of fractal quantity $F(e)$ can be determined. Dependence of number of states $N(r)$ and density of fractal quantity $F(r)$ is defined by equations

$$N(r) = K \cdot r^D \,, \ F(r) = K \cdot r^{D-E} \,. \qquad (8)$$

To determine the fractal structure parameters for special cases of deterministic fractals analytical or numerical methods (e.g. radius or box counting method) can be used. The fractal parameters can be in these cases determined by the linear regression of dependence

$$\ln N(r) = \ln K + D \ln r = \ln K - S(r) \,, \qquad (9)$$

where $S(r)$ is so far unspecified entropy (5). This entropy can be determined from the statistical parameters (4). For $q = 0$ it yields

$$S(r) = \ln R(r) = \ln m(r) - \ln n \,. \qquad (10)$$

Comparing the equations (9) and (10) we can see that the fractal measure K is total number of states n and $m(r) = N(r)$ and is number of states having the defined qualities. Using the radius method it is related to number of black and white pixels threshold pictures in a selected area with the size of r. Using box counting methods it is related to a number of squares with the size $\varepsilon = 1/r$ with all pixels neither black

(N_{WBW}) or white (N_{WBW}), respectively. In this case it is also possible to determine numbers of squares with pixels neither black nor white (N_{BW}). Subsequently, from the (9) and (10) dependencies is possible to derive fractal measure K, fractal dimension D, entropy S and absolute error r (R respectively). All of these parameters can be derived with the help of HarFA 5.3. software developed by the authors of the contribution.

The new version of the HarFA 5.4. allows for determination of all of the statistical and fractal parameters mentioned above following from the moments of q order ($q = 0$, 1, 2, 3 or 4).

The area of surface and volumes under and above this area in % can be calculated from fractal measures

$$S_{BW} = \frac{K_{BW}}{K_{BBW} + K_{WBW} - K_{BW}} 100 \quad (\%) \,, \qquad (11)$$

$$V_B = \frac{K_{BBW} - K_{BW}}{K_{BBW} + K_{WBW} - K_{BW}} 100 \quad (\%) \,, \qquad (12)$$

$$V_W = \frac{K_{WBW} - K_{BW}}{K_{BBW} + K_{WBW} - K_{BW}} 100 \quad (\%) \,. \qquad (13)$$

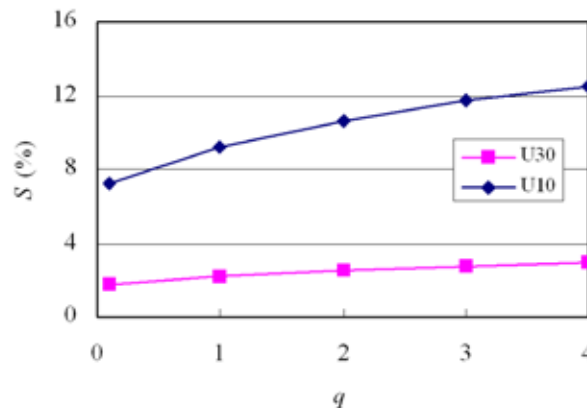Fig. 1.   **Fractal structure of the real sample surfaces (U10, U30)**

Fig. 2.   **Fractal analysis of inhomogenities of thin film layer surface for different moments of qth order**

The results of these calculations for all moments and different parts of the sample (U10, U30, see Fig. 1.) are shown

at Fig. 2. This figure shows dependence of surface size of selected part for different moments q = 0.1, 1, 2, 3 and 4.

The dependence of surface structure fractal dimensions for all these moments is at Fig. 3. We can see the decreasing fractal dimension for higher order values.
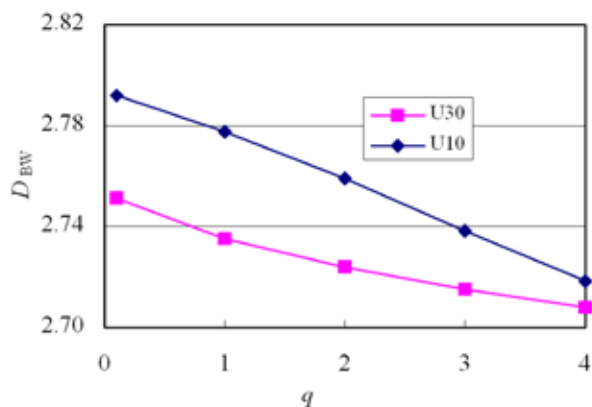

Fig. 3. **Surface structure fractal dimension of U10 and U30 samples for different moment of qth order**

Conclusions

Direct relation of the description of various physical and physical-chemical phenomenons in various science areas (statistical physics, thermodynamics, and fractal physics) is described in the contribution. It follows that the fractal analysis methods originally used to analyse threshold pictures can be easily utilized for continuous phenomenon in informatics, thermodynamics, kinetics theory of gases, etc.

REFERENCES
1. *Moment (mathematics)*, definitions in Wikipedia: http://en.wikipedia.org/wiki/Moment
2. *Perthometer. Surface Texture Parameters.* standard DIN EN ISO 4287/ASME. Göttingen: Mahr GmbH, 1999.
3. Grassberger P., Procaccia I.: Phys. Rev. Lett. *50*, 346 (1983).
4. Grassberger P.: Phys. Lett. *97*, 227 (1986).
5. Zmeskal O., Nezadal M., Buchnicek M.*:* Chaos, Solitons Fractals *17*, 113 (2003).
6. Zmeskal O., Nezadal M., Buchnicek M.: Chaos, Solitons Fractals *19*, 1013 (2004).

7.2. Posters

P01 INFLUENCE OF REGENERATED HUMIC ACIDS ON POLYVINYL ALCOHOL THERMO-OXIDATIVE STABILITY

BARBORA BAKAJOVÁ, ZOJA VLČKOVÁ and JIŘÍ KUČERÍK

Brno Univerzity of Technology ,Purkyňova 118, 612 00 Brno, Czech Republic,
xcbakajova@fch.vutbr.cz

Introduction

Transformation of coal into humic acids (HA) can be achieved by means of the oxidation process. Oxidation could be ideally considered as an inverse diagenetic process able to regenerate the molecules, which originally led to the insoluble structure of the coal. The HA produced is generally called "regenerated" humic acid (RHA) or oxyhumic acid[1]. Oxidation can be performed using many of the oxidants usually utilized in organic chemistry (HNO_3, $KMnO_4$, H_2O_2, etc.)[2].

The practical final result of the acidic treatment of the alkaline solution of humates, extracted from oxycoal, is a black, amorphous, water-insoluble regenerated HA (RHA) powder. RHA have similar characteristics and chemical behavior like the original HA, whose conversion led to coal. In fact RHA generally contain more carbon and less oxygen than HA obtained from natural environments. The major functional groups in RHA are carboxylic and phenolic groups[1].

The goal of this work is to evaluate the antioxidant or pro-oxidant efficiency of RHA as additives in polyvinylalcohol (PVA) blends.

Experimental

Line of four humic acids was obtained from South Moravian lignite and extracted by the IHSS standard alkaline method[3]. Before extraction, part of lignite sample, milled and sieved (0.2 mm) was pretreated with different oxidizing agents for 30 minutes, filtrated and washed with deionized water until agent-free.

As a reference, a HA sample was extracted from non-treated lignite. All these samples were mixed with solution of polyvinyl alcohol (PVA) (2 $g\,dm^{-3}$) to obtain, after water evaporation, final concentrations in the polymer 0.5, 2 and 5 % wt.

Thermogravimetry analysis

Thermogravimetry (TA instruments) with the dynamic air atmosphere was used for testing of PVA/RHA blends. The airflow rate was set at 25 ml per minute and the heating rates were 0.5, 1, 3, 5, 7, 10 and 15 K per minute. The measurement was carried out from room temperature to 600 °C.

As a measure of stability the induction period (IP) was determined. The thermogravimetric records showed two steps of weight loss, the first one attributable to loss of water, whereas the second one to the degradation of the polymer.

Table I
Samples of regenerated humic acids

Sample	Pretreatment agent
HA 1	–
RHA 2	5% HNO_3
RHA 3	10% HNO_3
RHA 4	20% HNO_3

The onset of the latter step corresponded to the end of IP and it was detected by the extrapolation of inclination of 1st derivative weight curve of the TG curve (DTG) for several temperature rates (Fig. 1.). The IP was determined using equations with Arrhenius temperature function (1).

$$t_i = A\exp(B/T) \tag{1}$$

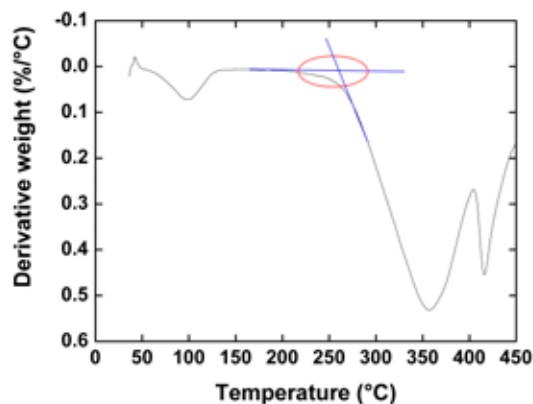t_i is a length of the induction period, A and B are adjustable kinetic parameters and T is temperature.

Fig. 1. **Onset temperature detected by the extrapolation of inclination of 1st derivative weight curve of the TG curve (DTG)**

Results

Antioxidant Efficiency of Regenerated Humic Acids

In our previous work[3] the antioxidant effect of South Moravian lignite humic acids and its ammonium salts in mixture with PVA was experimentally proved; while addition of sodium salts exhibited a slight pro-oxidant effect at specific concentrations. In this part we tried to find out if the oxidative modification of the parental lignite could cause any significant changes in antioxidant efficiency of extracted humic acids.

Stability of PVA/RHA blends was assessed and compared using so-called induction period (IP) measurement. The principle of this approach is given in the Experimental part. Application of Arrhenius equation as the temperature function has been demonstrated to be rather complicated due to *(i)* problems with calculation of temperature integral, *(ii)* problems associated with obtaining of unrealistic

values of induction periods and moreover *(iii)* adjustable parameters cannot be considered to have a physical meaning. On the other hand, such approach can still be used to model the kinetics of the process although without a deeper insight into its mechanism[4]. A better estimation of stabilizing effect can be obtained using the ratio of the lengths of induction periods of treated (stabilized) and nontreated material[5] so-called protection factor (PF).
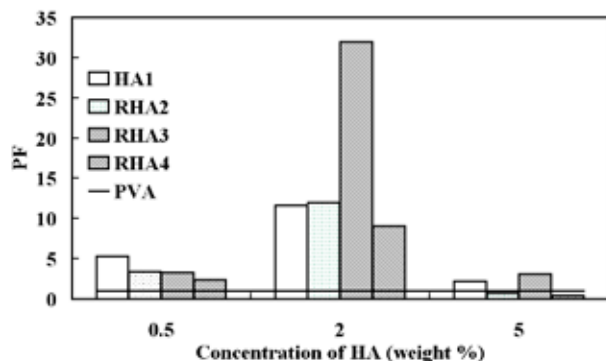

Fig. 2. **Protection factor determined by Arrhenius kinetic**

From results reported in Fig. 2., it seems that the most efficient concentration was 2 %. In this concentration RHA 3 showed the highest efficiency to increase the stability of PVA. Further, results obtained using Eq. 1 showed, that RHA 2 and RHA 3 in concentration 2 % have higher stabilizing effect than nontreated humic acid. Stabilizing effect increases in sequence HA 4, RHA 1, RHA 2 and RHA 3. Concentration 0.5 % of humic acids also stabilizes PVA. In contrast, 5% addition of regenerated humic acids did not bring a significant change in thermo-oxidative stability.

Conclusions

Thermal stability expressed as the length of IP of PVA with addition of humic acids was assessed by means of thermogravimetry and using a mathematical apparatus of isoconversional method. For the calculation of the induction period, Arrhenius temperature function was used.

Stabilities of PVA enriched with 3 regenerated humic acids were compared with PVA blend mixed with humic acid extracted from non-pretreated lignite. Obtained results showed, that almost all regenerated humic acids had greater stabilizing effect than humic acid extracted form paternal lignite.

REFERENCES

1. Berkowitz N.: *In The chemistry of coal,* Elsevier, Amsterdam, 1985.
2. Rausa R., Girardi E., Calemma V.: *Humic acids from coal. Production, characterization and utilization. In Humic Substances in the Global Environment and Implications on Human Health,* Elsevier Amsterdam, , pp. 1225–1244, (1994).
3. Kučerík J., Bakajová B., Pekař M.: Environ. Chem. Lett. DOI: 10.1007/s10311–007–0129, (2008).
4. Šimon P.: J. Therm. Anal. Calorim., *76*, 123 (2004).
5. Šimon P.: J. Therm. Anal. Calorim., *84*, 263 (2006).

P02 DETERMINATION OF PARTICLE SHAPE AND SIZE DISTRIBUTION

EDITA BRETŠNAJDROVÁ[a], LADISLAV SVOBODA[a] and JIŘÍ ZELENKA[b]

[a]*University of Pardubice, Faculty of Chemical Technology, nam. Cs. Legii 565, 532 10 Pardubice,*
[b]*Synpo, a.s., S.K.Neumanna 1316, 532 07 Pardubice, Czech Republic,*
edita.bretsnajdrova@student.upce.cz

Introduction

At present great attention is given to study of preparation and properties of various nanomaterials usable in many applications. They are utilized in varied fields of human activity – e.g. in electronics, medicine, paint industry etc. Except detailed chemical structure, such nanoparticle properties as shape and size distribution are fundamental to the given application. To measure these parameters various methods are used, e.g. transmission electron microscopy (TEM), atomic force microscopy (AFM), acoustic spectrometry and methods based on the light scattering.

All above-mentioned methods were used in this work to characterize particles of two selected model types of nanomaterials – colloidal silica and sodium montmorillonite. Silica represents a material with spherical particles; tabular shapes are typical for montmorillonite materials.

Experiments proved that methods used to measure particle size distribution and based on the light scattering require very diluted dispersions to meet the needs of them. But, on the other hand, these conditions can affect the particle size distribution due to agglomeration or deagglomeration of them. For these reasons methods working with concentrated suspensions, without dilution, are more suitable to get correct results for such colloidal systems, for example acoustic spectrometry. To obtain information on the shape of particles studied TEM and AFM methods were used.

Merits and limitations of the individual methods used to evaluation of nanoparticles of various types are discussed in the work.

Experimental

D y n a m i c   L i g h t   S c a t t e r i n g

Particle size distribution measurement was carried out by dynamic light scattering using Mastersizer 2000 MU.

U l t r a s o u n d   S p e c t r o s c o p y

The ultrasound-based technique is suitable for characterizing heterogeneous solid-in-liquid or liquid in liquid colloidal systems. This method is suitable for concentrated solutions; it is reliable in range from 5 % to 50 %. We have used equipment DT–1 200 (Dispersion technology, USA) and as standard we have used Silica Ludox with nominal particle size approx. 22 nm.

A F M

A Solver Pro M Atomic Force Microscope (NT-MDT; Russia) was used in tapping mode (semi-contact) to produce three-dimensional images of the surface. High-resolution "Golden" silicon cantilevers NSG–1 0 (Au coating, curvature radius 10 nm and cone angle less than 22°°) were used for all measurements. Set point was adjusted on 50 % of a free oscillation. Scan sizes required to evaluate the distribution of particles was 500×500 nm to several microns depending on variation of particles' sizes.

T E M

A drop of the water-diluted suspension was put on a microscopic grid covered by ultra thin carbon film and observed directly with TEM Tecnai G2 Spirit Twin (FEI).

Materials

S i l i c a s

Bindzil CC30
Eka Chemicals AB, Sweden
Dispersion of silica nanoparticles
30% solution in water
Particle size 7 nm

Bindzil 30/360
Eka Chemicals AB, Sweden
Dispersion of silica nanoparticles
30% solution in water
Particle size 7 nm

M o n t m o r i l l o n i t e

Cloisite Na$^+$
Southern Clay
Powder
CEC 90 meq 100 g^{-1}

Results

S i l i c a s

Two types of commercial silicas wear tested (Bindzil cc30 and Bindzil 30/360). These silicas are stabilized different way. While Bindzil cc30 is sterically stabilized, Bindzil 30/360 is stabilized electrostaticaly. The effect of silica concentration on zeta potential and particle size was studied for both type of stabilization. The variety of silica concentrations were prepared by dilution of original samples. Type of stabilization has crucial effect on silica concentration dependence of zeta potential (Fig. 1.).

The concentration of silica has effect on particle size and particle size distribution. Example for Bindzil cc30 is in Fig. 2.

Original sample of Bindzil cc30 has relatively broad particle size distribution. Mean value of particle size is about 40 nm. Measured value is higher than value cited by producer. Presence of bigger formations was confirmed by transmition electron microscopy (Fig. 3.).
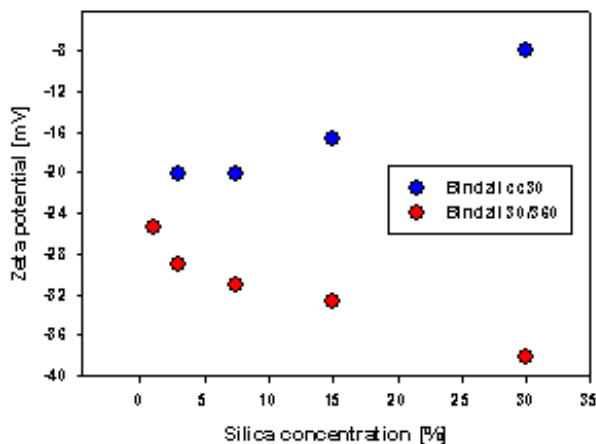
Fig. 1. **Dependence of zeta potential on silica concentration**

Bigger formations are aggregated smaller particles (Fig. 3.). These aggregates are broken up by dilution of original samples (Fig. 2.). The same conclusions can be done from AFM analysis.
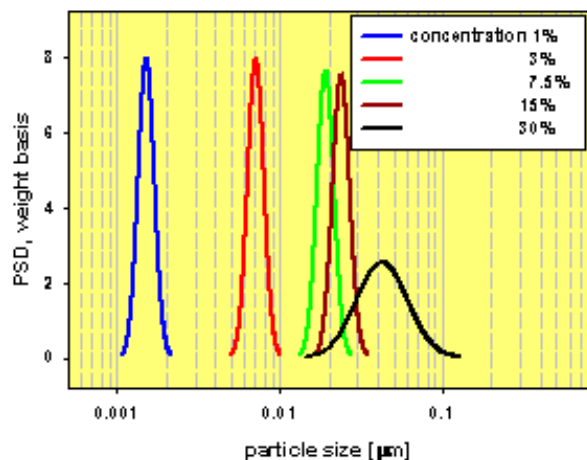

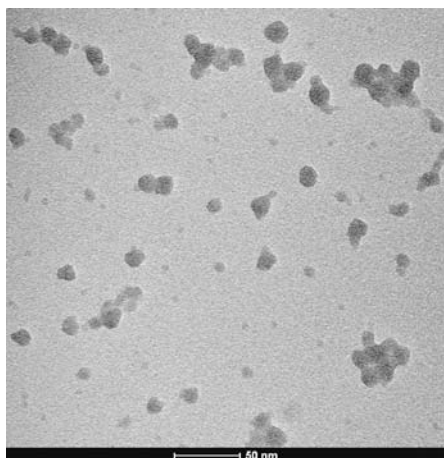Fig. 2. **Particle size distribution on silica concentration**

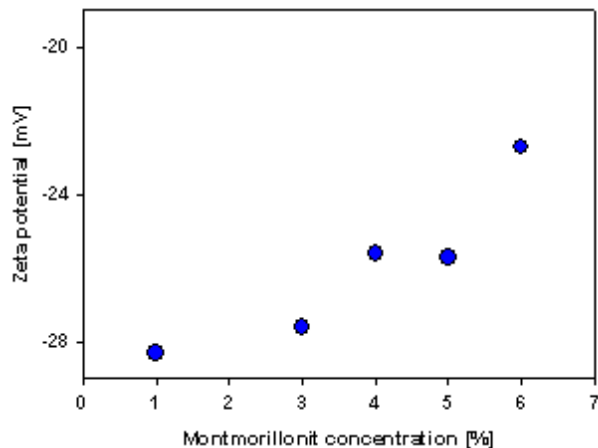Fig. 3. **TEM photo of original sample Bindzil cc 30**

Fig. 4. **Dependence of zeta potential on montmorillonite concentration**

M o n t m o r i l l o n i t e

Zeta potential of water-based dispersion of sodium montmorillonite was influenced by filler concentration (Fig. 4.).

The particles with different shape and dimension were observed by means of different techniques (TEM, AFM). Results from AFM are in Fig 5.
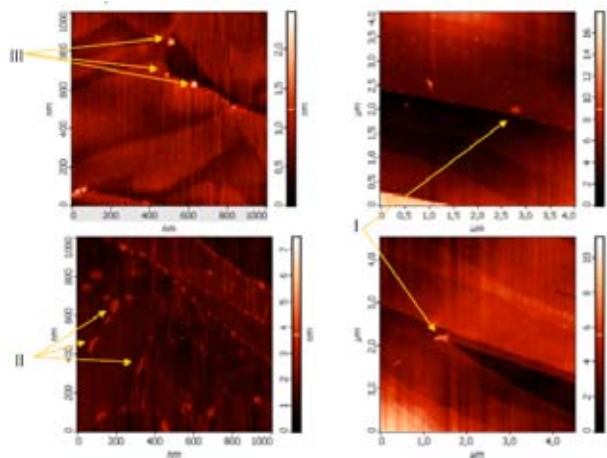

Fig. 5. **AFM photo of sodium montmorillonite sample**

Pentagon particles with particle size about 200 nm can be observed in section I of Fig. 5. Lengthwise formation with highest dimension 100 nm can be seen in part II of Fig. 5. Round particles with diameter 30 nm are in part III. Thickness of all studied particles is practically the same – about 1 nm.

Conclusions

Type of silica particle stabilization influenced behavior of colloidal solutions during dilution (particle size and zeta potential changes). All used methods (AFM, TEM and ultrasound spectroscopy) give similar results. Bigger particles (aggregates primary particles) were observed by means of AFM and TEM. These aggregates were broken up by dilution of original samples.

Commercial sodium montmorillonite is compound from elements different shapes and sizes. There are lengthwise formations, circular and pentagonal particles.

REFERENCES

1. Kosmulski M., Dahlsten P.: Colloids Surf., A *291*, 212 (2006).
2. Pierre A. C., Ma K.: J. Mater. Sci. *32*, 2937 (1997).
3. Yukselen Y., Kaya A.: Water Air Soil Pollut. *145*, 155 (2003).

P03 HYDRATION OF REGENERATED HUMIC SUBSTANCES

PETRA BURSÁKOVÁ, ZOJA VLČKOVÁ, ZDENĚK CIHLÁŘ and JIŘÍ KUČERÍK

Brno University of Technology, Faculty of Chemistry, Institute of Applied and Physical Chemistry, Purkyňova 118, 612 00 Brno, Czech Republic,
xcbursakova@fch.vutbr.cz

Introduction

Humic substances (HS) have a profound effect in many processes including cell biology of living organisms. As they are both hydrophobic and hydrophilic in nature, their function is closely related to the properties of water shell intimately bound on humic molecules and consequently on humic aggregates. A strong affinity of water molecules to stick to each other via H-bonds and formation of specific clusters is a driving force assembling humic molecules into complicated organizations.

The differences in properties of water surrounding HS can be recognized and enumerated using differential scanning calorimetry (DSC). Phase transition behaviour of sorbed water in HS-water systems was investigated as a function of water content. Three types of water can be distinguished: free water whose melting temperature and enthalpy are not significantly different from those of normal (bulk) water, those water species exhibiting large differences in transition enthalpies and temperatures (freezing-bound water), or those for which no phase transition can be observed calorimetrically, known as non-freezing water[1].

The aim of this work was to shed light on properties of hydration water in systems water/regenerated humic acids (RHA). DSC represents a technique which can help to recognize the differences in properties of water surrounding humic matter. The enumeration of water molecules is crucial in order to understand how biomolecular processes work.

Experimental

Material

The line of 8 HA was used. All of them were extracted from pretreated South Moravian lignite by standard alkaline method, purified, and freeze-dried. During the pretreatment procedure the lignite samples were soaked in solutions of either 5%, 10%, 20% nitric acid, 2%, 5% hydrogen peroxide, 20% acetic acid or 20% citric acid.

DSC Measurements

A sample was placed in an aluminum pan (~ 5 mg) and excess water was added. Surplus water was allowed to evaporate slowly at room temperature until the desired water content was obtained. Subsequently, the pans were hermetically sealed and left to equilibrate at room temperature overnight. DSC was performed by using the TA Instruments Q200 to measure phase transition of sorbed water. The measurements were conducted ranging from 40 to –90 °C and then from –90 to 30 °C at 3 °C min⁻¹ under the flow of nitrogen (50 ml min⁻¹).

Water Content Determination

The thermogravimetry analysis (TGA TA Instruments Q 5000) was used to measure water content of original samples to obtain the real concentration of water (W_c). The W_c was defined as follows:

$$W_c = \frac{\text{grams of water}}{\text{grams of dry sample}} \text{ (g/g)} . \tag{1}$$

The obtained W_c were in range from 0.1 to 1.5 g g⁻¹. Assuming both melting enthalpies for freezing-bound water (W_{fb}) and free water (W_f) to be 334 J g⁻¹ water, weights of W_{fb} and W_f (g water g⁻¹ RHA) could be calculated from the endothermic heating transitions. The weight of non-freezing water (W_{nf}) was obtained using the expression:

$$W_{nf} = W_c - \left(W_{fb} + W_f \right). \tag{2}$$

Results

RHA samples with W_c 0.1–1.5 g g⁻¹ were measured. At higher water content there could be observed a large heating endotherm in the region of 0 °C whose enthalpy of transition was close to that of bulk water (334 J g⁻¹). This endotherm was ascribed to the melting of the freezing water in the hydrated RHA-water system. Some samples also showed another endothermic transition below 0 °C when the system was heated. This endothermic peak indicated the presence of freezing-bound water in a humic sample, i.e. water which is already affected by the interaction with humic molecules. Its clusters structure differs from those of bulk water and is physically recognizable by shifted temperature of melting. In fact, the enthalpy of melting differs from that ice which was attributed to the freezing water. Due to the different structure of ice such enthalpy can drop down to 312 J g⁻¹ (ref.[2]). At very low water content nearly all water molecules are present in the form of non-freezing water in this system, and a slight amount of water molecules are present in the form of freezing-bound water which caused the observed endothermic fusion peak below 0 °C. Some samples showed more distinct endothermic fusion peak on heating curves. Shoulders which can be identified in this peak are possibly caused by the overlapping of different peaks which reflects the presence of several different types of freezing-bound water. Since cubic structure of freezing-bound water is thermodynamically metastable[3] such assumption is highly probable.

Representative DSC heating curve of RHA6 with water content W_c 0.7 is given in Fig. 1. where various endothermic transitions at different temperatures, attributed to the melting of different types of ice, can be observed.

The total amount of freezing water in RHA samples was calculated from the area of endothermic melting peak as follows: obtained heat of ice melting (ΔH) calculated from DSC heating curves was normalized dividing by the weight

of the dry RHA. A plot of the enthalpy change, normalized to the RHA weight, as a function of the total water content of the sample will yield the enthalpy change for the free water as a slope (Fig. 2.). The x-intercept is the point at which the total water content is equal to the amount of non-freezing water, and zero enthalpy change is observed[1].
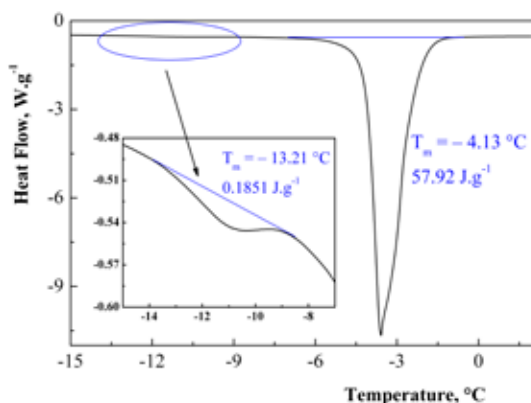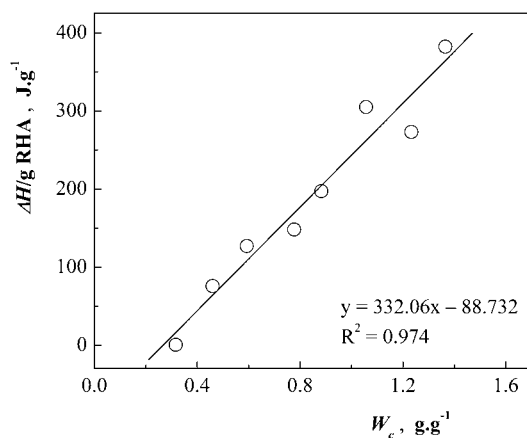

Fig. 1.   **DSC heating curve for RHA6 with W$_c$ 0.7**

Fig. 2.   **Normalized melting enthalpy versus W$_c$ for HA1**

Table I
The content of non-freezing and freezing-bound water

Sample	Pretreatment agent	W_{nf} [g g^{-1}]	W_{fb} [g g^{-1}]	W_{nf+fb} [g g^{-1}]
HA1	–	0.267	n.d.	n.d.
RHA2	5% HNO$_3$	0.223	0.190	0.413
RHA3	10% HNO$_3$	0.081	0.219	0.300
RHA4	20% HNO$_3$	0.245	0.055	0.300
RHA5	2% H$_2$O$_2$	0.187	0.291	0.478
RHA6	5% H$_2$O$_2$	0.035	0.374	0.409
RHA7	20% acetic acid	0.238	0.142	0.380
RHA8	20% citric acid	0.078	0.218	0.296

Table I reports the content of non-freezing and freezing-bound water calculated from DSC experiments. The highest modification efficiency regarding hydration properties of HS was reached using H$_2$O$_2$ (RHA5, RHA6), 5% HNO$_3$ (RHA2) and 20% acetic acid (RHA7) as the pretreatment agents while other samples showed lower water retention capacity.

Conclusions

DSC measurements of RHA showed dependency on both concentration and used modifier. The enthalpy change of melting increased with decreasing concentration of RHA. Using of different pretreatment agents plays a significant role since some modifications can enhance hydration properties of HS. Therefore, this method can bring new information considering the function of HS in biological processes.

REFERENCES
1. Liu J., Cowman M. K.: J. Therm. Anal. Cal. *59*, 547 (2000).
2. Hatakeyama H., Hatakeyama T.: Thermochim. Acta *308*, 3 (1998).
3. Yoshida H., Hatakeyama T., Hatakeyama H.: J. Therm. Anal. Cal. *40*, 483 (1993).

P04　EVALUATION OF SORPTION ABILITIES OF NATURAL LIGNITE FOR ORGANIC SUBSTANCES

PETRA BUŠINOVÁ and MILOSLAV PEKAŘ

Brno University of Technology, Faculty of Chemistry, Institute of Physical and Applied Chemistry, Purkyňova 118, 612 00 Brno, Czech Republic,
businova@fch.vutbr.cz

Introduction

In recent years, possibilities of lignite utilization in various non-fuel applications have been investigated. Lignite as the youngest brown coal has a low degree of coalification which gives it unique chemical composition and specific properties. Therefore, lignite can be used as an interesting and versatile material in several application fields.

Studies on sorption properties have been continuously published for lignite or coals in general. Lignite, even in its natural state, is reported to have significant sorption affinity for metal ions[1,2] as well as for organic molecules, e.g. dyes[3,4].

In our laboratory, sorption properties of lignite mined in the region of South Moravia (Czech Republic) are studied. Affinity of this material for fluoride ion has previously been published[5]. This paper introduces preliminary results on a sorption of basic textile dyes and petroleum products (gasoline, diesel fuel, oils) on the natural South Moravian lignite.

Experimental

Sorption tests were performed using lignite mined in the South Moravia, Mikulčice locality. Its detailed characterization is published elsewhere[6,7]. Fraction of lignite particles smaller than 0.2 mm was used and the sample was dried at 105 °C in an oven for 24 hours. Dried product was consequently left to moisture re-equilibration at ambient atmospheric conditions in laboratory and final moisture content was about 7 %.

Six basic dyes (see Table I) have been studied. Deionized water was used to prepare the dyes solutions. UV-VIS spectroscopy (Hitachi U3300 spectrometer) was used for the determination of a dye concentration in a solution. The wave lengths of the absorption maxima of all dyes are given in Table I. In adsorption experiments, a change in the intensity of these maxima has been used in order to characterize the removal of a dye from solutions.

Sorption of dyes were carried out for four different amounts of lignite: 0.1 g, 0.2 g, 0.5 g and 1 g. Lignite was mixed with 10 ml of a dye solution with dye concentration of 1,000 mg dm^{-3} in 50 ml screw capped plastic centrifuge tubes with conical bottom and mixtures were stirred on a rotary shaker for 24 hours. After this time period, samples were centrifugated at 4,000 rpm and 15 °C for necessary time. The supernatant solutions were pipetted out and intensity of absorption maxima were determined instantaneously using UV-VIS spectrometer.

Table I
The wave lengths of the absorption maxima of used dyes

Dye	λ_{max} [nm]
Astrazon blue 3GL (AB)	593
Maxilon yellow M-3RL (MY)	422
Maxilon red M-4GL (MR)	505
Bezacryl blue FBS (BB)	598
Bezacryl golden yellow GL 200 % (BY)	437
Bezacryl red GRL 180 % (BR)	529

Similarly, sorption tests were performed for gasoline and diesel fuel. 0.5 g of lignite was mixed with 10 ml of adsorbate in screw capped glass test tubes and rotated for 24 hours. Then a liquid portion was poured off and lignite was weighted. Consequently, it was dried at 105 °C in an oven for 24 hours and weighted again. Variation in weight was observed.

Adsorption of oils (motor and gear) was studied according to the reference[8] with slight correction. 2.5 g of lignite were weighted and evenly spread on a filter paper placed into a round stainless steel dish with a wire mesh (2 mm^2) bottom (7 cm in diameter). The dish with lignite was then placed into a square glass dish (12 × 12 × 6 cm) with 60 ml of an oil.

Table II
Residual dye concentration and percentage of dye removed from dye solution after 24 hours

Dye	Lignite amount [g]	C_R [mg dm^{-3}]	Removing [%]
AB	0.1	151.403	84.87
	0.2	–	100
	0.5	–	100
	1	–	100
MY	0.1	3.067	99.69
	0.2	–	100
	0.5	–	100
	1	–	100
MR	0.1	3.067	99.69
	0.2	1.087	99.89
	0.5	–	100
	1	–	100
BB	0.1	9.505	99.05
	0.2	0.869	99.91
	0.5	0.283	99.97
	1	–	100
BY	0.1	3.969	99.60
	0.2	1.844	99.82
	0.5	–	100
	1	–	100
BR	0.1	6.537	99.35
	0.2	0.623	99.94
	0.5	0.163	99.98
	1	–	100

– below detection limit

Table III
Amount of petroleum products sorbed on 1 g of lignite after 24 hours of drying

Petroleum product	Sorbed amount [mg]
gasoline	1425
diesel fuel	579
motor oil	350
gear oil	726

Lignite was left in contact with oil for 30 min. The stainless steel dish with sample was then removed and left to drain until the oil layer disappeared (2 hours). Then lignite was weighted. The weighting was repeated after 22 hours and obtained weights were compared.

All experimental sorption studies were performed at laboratory temperature (25 ± 2 °C).

Results

Sorption abilities of the South Moravian lignite for organic substaces were investigated. Decolorization of a single dye solution was observed, residual dye concentration in solution and corresponding percentage removal of a dye were determined. Effect of lignite to solution ratio was studied. Results are given in Table II and clearly confirm sorption ability of lignite for selected dyes. These results are also guiding for further experiments. Proper ratio between amount of lignite and volume and concentration of a solution has to be found prior for determination of sorption isotherms and kinetics.

The results of sorption tests using petroleum products, summarized in Table III, show the sorption ability of lignite towards them. Further experiments are necessary for the investigation of lignite as a suitable sorbent for removing oil spills.

Conclusions

Sorption abilities of the natural South Moravian lignite for organic substances were investigated. Obtained results show that lignite can be used as an effective sorbent for various textile dyes and that it has a positive sorption ability for petroleum products too.

REFERENCES

1. Pehlivan E., Arslan G.: Fuel Process. Tech. *88*, 99 (2007).
2. Mizera J., Mizerová G., Machovič V., Borecká L.: Water Res. *41*, 620 (2007).
3. Mohan S. V., Rao N. C., Karthikeyan J.: J. Hazard. Mater. *90*, 189 (2002).
4. Allen S. J., McKay G., Khader K. Y. H.: J. Chem. Tech. Biotechnol. *45*, 291 (1998).
5. Pekař M.: Petrol. Coal *3*, 1 (2007).
6. Kučerík J., Pekař M., Klučáková M.: Petrol. Coal *45*, 58 (2003).
7. Pekař M.; Sýkorová I.; Koutník I.: *Proc. Int. Conf. Twenty-Fourth Annual International Pittsburgh Coal Conference*, p.1. 2007.
8. Carmody O., Frost R., Xi Y., Kokot S.: J. Colloid Interface Sci. *305*, 17 (2007).

P05 MAXIMUM BUBBLE PRESSURE AND THE DU NOÜY PLATINUM RING METHOD OF SURFACE TENSION MEASUREMENTS OF SODIUM DODECYL SULFATE AND SODIUM HYALURONATE

MARTIN CHYTIL, JITKA KROUSKÁ, PAVLÍNA KULILOVÁ and MILOSLAV PEKAŘ

Institute of Physical and Applied Chemistry, Faculty of Chemistry, Brno University of Technology, Purkyňova 118, 612 00 Brno, Czech Republic,
chytil@fch.vutbr.cz

Introduction

The measurement of surface tension is a fundamental method in physical or colloidal and interfacial chemistry, assessing important parameter of liquids, surface tension (γ), surface activity of molecules in a medium, detecting *critical micelles concentration* (CMC) etc, which is very important for processing and industrial applications of given substances.

The Maximum Bubble Pressure (MBP) method is a dynamic method of measuring surface tension of liquids. Using this method, a maximum pressure inside the gas bubble, forming at the end of the capillary with a defined radius, is measured at an accurately defined rate of the bubble formation. When the pressure reaches its maximum, the bubble radius is exactly equal to that of the capillary, and the time of this point is designated as the bubble life-time[1]. For the formation of the bubble in the liquid, the surface energy must be overcome. From the surface energy, the surface tension of the liquid is calculated using the Laplace-Young equation, $\gamma = f \cdot P_{max}/2$, where f is the correction factor[2].

The Du Noüy Ring method (DNR) is a static method of surface tension measurement. The surface tension, by this method, is determined from the maximum force of lifting the, usually Pt, ring off the liquid surface just before the rupture of the liquid film having been formed on the ring surface[3].

Sodium hyaluronate (NaHA), widely known as hyaluronic acid or hyaluronan, is a naturally occurred linear polysaccharide composed of repeating disaccharide units of *D-glucuronic* acid and N-acetyl-D-glucosamine alternatively linked by β-(1 → 3) and β-(1 → 4) glycosidic bonds. Due to the presence of carboxyl groups HA is a polyelectrolyte found namely in connective tissues of vertebrate and also as a fermentation product of some *Streptococci* bacteria strains[4,5]. For its numerous unique properties, HA is used in medicine, pharmacy, cosmetics[4–6] etc. Surface tension is an important parameter for processes and applications such as formation of nanofibres from biopolymers, scaffolds in tissue engineering, drug delivery, etc. There have been only few papers reporting about HA surface activity[7], using namely static methods, e.g. pendant drop method. The purpose of this contribution was to compare the MBP and the DNR method of surface tension measurement on measurement series of aqueous solutions of a classical surfactant sodium dodecylsulfate (SDS), to man-age the data proceedings, mainly from the MBP method, and apply particularly the MBP method for the series of HA aqueous solutions. Discussion of the effect of the HA molar mass and the presence of NaCl has been also involved.

Experimental

Materials

- The bacterially produced HA of cosmetic quality with the molar masses of 4.6×10^5 and 1.69×10^6 g mol^{-1} provided by the Contipro, spol. s.r.o.
- SDS, p.a. and NaCl, p.a. by Sigma Aldrich
- Water for injection by Verkon s.r.o.

Preparation of Samples

A desired amount of dry HA was firstly stepwise sprinkled into a desired volume of water upon gently stirring and then let stirred for ca 24 h at room temperature in order to achieve a well homogenized stock solution. Afterwards, the stock solution was diluted into the series of solutions with the water or NaCl solution up to a desired concentration and ionic strength and then the series were vigorously agitated for at least 2 h. The series of SDS solutions were prepared in the same way except the long stirring of the stock solution, which lasted only 2 h in this case.

Methods

The maximum bubble pressure tensiometer BPA-800P from KSV Instruments (Finland) and KSV Sigma 701 tensiometer with the Pt ring were employed. The series of the solutions were measured at room temperature (MBP) or 25 °C (DNR). Between the measurements of each sample by the DNR method, the Pt ring was cleaned in the flame of a burner with occasional immersing into 6% (v/v) HCl. From the MBP method, the dependence of γ on the bubble life-time (t_{life}) is obtained. The measurements were performed in two different modes (Standard and Increasing Flow Rate); the results compared and final calculations were done as the average of those two measurements. By the DNR method, each sample was measured in time until it was stabilized, or for at least 40min. As a result, the plot of γ vs. time of measurement (t_{meas}) was gotten. The measurements were tripled and the other calculations were made from the mean value of all replicates.

Results and Discussions

Comparison of the MBP and the DNR Method

From the MBP method we obtained the plot of dynamic surf. tension, γ_{dyn}, against the bubble life-time, t_{life}. To determine the equilibrium surface tension, γ_{eq}, of a sample, we arranged the plot as $\gamma_{dyn} = f(1/\sqrt{t_{life}})$ (Fig. 1.) and γ_{eq} was assessed from the following equation for $t_{life} \rightarrow \infty$

$$\gamma_{dyn} = \gamma_{eq} + s_\gamma/(a_\gamma + t_{life}^{1/2}), \qquad (1)$$

where the parameters s_γ and a_γ result from the adsorption of the surfactant molecules at the solution/air bubble interface, as described elsewhere[8]. This model fitted relatively well the

data for both SDS and HA. Fig. 1 shows relatively high values of γ_{dyn} of the HA solutions even at higher concentrations (>1 g dm^{-3}), where they began to be quite viscous, comparing to the gradually decreasing γ_{dyn} of SDS solutions with SDS concentration.

Using the DNR method the dependence of γ on the time of measurement, t_{life}, was gained and the γ_{eq} from the DNR measurements was determined as the mean of the values from the last 10 min of the measurement. Another method of γ_{eq} assessment can be the extrapolation of the γ data as a function of $1/\sqrt{t_{meas}}$, to $t_{meas} \to \infty$; nevertheless the data are theoretical and were comparable with the previous ones only except the first very diluted solutions that need more time to be stabilized.
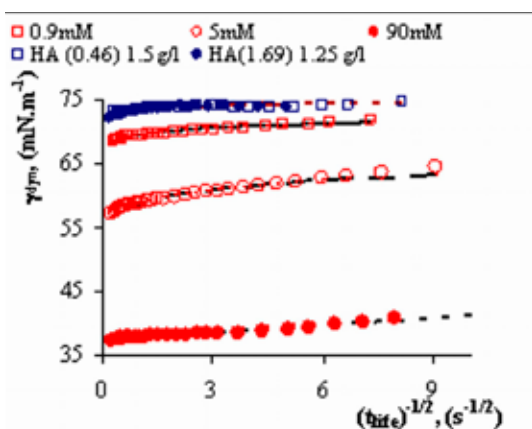
Fig. 1.   **The dynamic surface tension as a function of the square-root of bubble life-time for solutions of SDS (red symbols) and HA (navy symbols) in water; the figures in the brackets refer to the molar mass of the HA in 10^6 g mol^{-1}. The lines represent the model fitted to the experimental data (see in the text)**

From the comparison of the two methods, performed on measurements of mainly SDS solutions (Fig. 2.), a clear difference can be seen. The values of γ from the MBP were higher at lower concentrations of SDS than those of the DNR method; however, they later overlapped with each other behind the CMC of SDS. The onset of γ decrease before the CMC began also at higher concentration for the MBP measurement as well as the slope of the decline was steeper for this method. From the slope, the maximum concentration of a surfactant at the air/solution interface, Γ_{max}, and other parameters can be calculated using the simplified Gibbs adsorption equation[9]:

$$d\gamma = -2.303 \cdot RT \cdot \Gamma \cdot d\log C, \qquad (2)$$

where R is the gas constant, T absolute temperature, and C molar concentration of a surfactant. The values of Γ_{max} calculated from the MBP method were thus larger than those from the DNR method and the CMC of SDS was also determined at higher surfactant concentration using the MBP method than from the DNR in water and 0.15 M NaCl as well. All the parameters are listed in Table I.

Table I
The CMC and Γ_{max} of SDS in water and 0.15M NaCl calculated from the MBP and the DNR method

	CMC [10^3 mol dm^{-3}]	Γ_{max} [10^6 mol m^{-2}]
MBP		
Water	9.8	5.5
0.15 M NaCl	1.4	5.0
DNR		
Water	5.8	3.9
0.15 M NaCl	0.9	3.3

These results clearly demonstrate a different dynamics of these two kinds of adsorption which, in fact, compete with each other and one must note more complicating dynamic balance between these two kinds of adsorption and also micellization taking place in the system during the MBP measurement. It might be suggested a higher affinity of the surfactant molecules to the flat air/solution interface than to the bubble/solution interface considering earlier onset of the decrease of γ with SDS concentration and lower CMC, which induces more negative change of free energy of micellization, $\Delta G°_{mic}$. Nevertheless, as the surface tension drops, this decrease is more rapid for the MBP method and Γ_{max} is attained at a narrower range of SDS concentration resulting in its larger values, and thus more surfactant molecules adsorb at the bubble/solution interface.
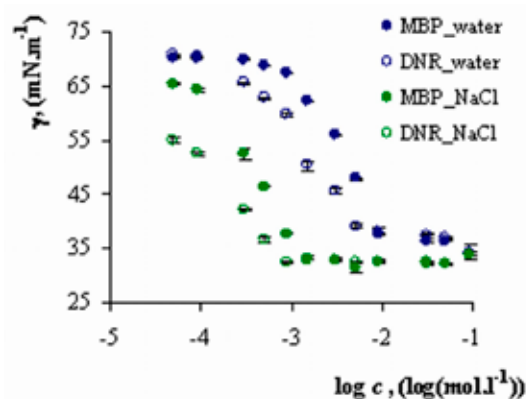

Fig. 2.   **Comparison of surface tension of SDS from the MBP (full circles) and the DNR (empty circles) method in water (navy) and 0.15M NaCl (green) as a function of SDS concentration**

Surface Tension of HA Aqueous Solutions

Figs. 3. and 4. show the surface tension of HA solutions from the DNR and MBP method, respectively. A general result is that the solutions of HA exhibited the values of γ only very moderately different from those of the appropriate solvent, being mostly lower. The values γ of the HA solutions had an oscillation trend with increasing HA concentration. No particular difference between the high-molecular weight and low-molecular weight HA was observed from the
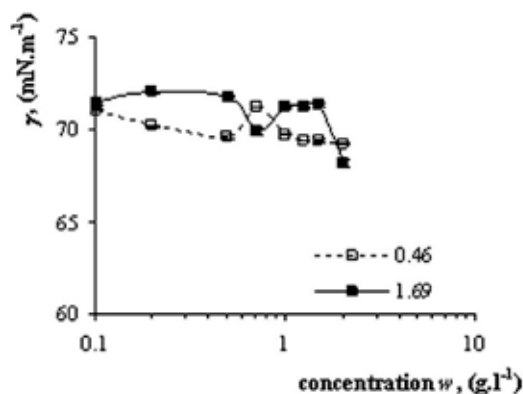
Fig. 3. **Surface tension of HA solutions in water as a function of HA concentration and molar mass from DNR method; the figures in the legend represent the molar mass of the HA in 10^6 g mol^{-1}**
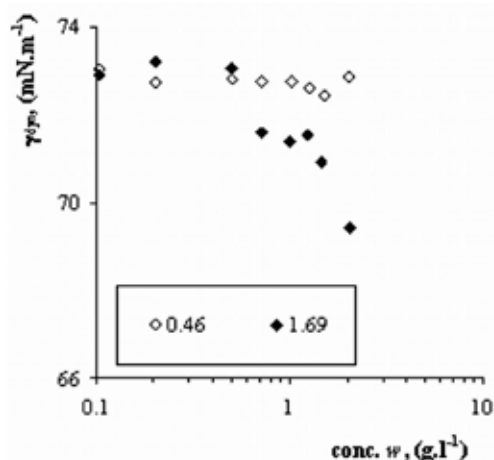

Fig. 4. **The dynamic surface tension (MBP) of HA solutions in water as a function of HA concentration and molar mass**

DNR measurements, only at low concentrations in 0.15 M NaCl, the high-molecular sample displayed slightly lower values of γ.

The similar result was obtained from the MBP measurements; however, the γ values were rather unstable. On the other hand, the opposite result to that from the DNR was observed in water, i.e. the higher-molecular weight HA displayed moderate decline of γ values with its concentration (Fig. 4.). All the samples, nevertheless, displayed a bit higher values of γ in 0.15 M NaCl than in water for both the methods. However, the differences are very small. These data are not in accordance with those found in the literature[7], in which the authors observed a decrease of γ with HA concentration

relating it to viscoelasticity of HA solutions; however, they used different method for surface tension measurement than us, i.e. the pendant drop method.

Conclusions

The comparison of two different methods of surface tension measurement, the MBP and the DNR, has been discussed on the measurements of series of SDS solutions and solutions of HA, varying in molar masses, in water and 0.15 M NaCl. Clear difference between the two methods has been seen, suggesting different dynamics and thermodynamics of adsorption of molecules at the curved air bubble surface. Although the adsorption of SDS at the bubble/solution interface occurred later than at the flat interface, the maximum concentration of the surfactant at the bubble/solution interface was larger than at the flat interface.

The HA solutions studied exhibited weak surface activity and oscillation trend in the change of γ with HA concentration. Only small difference in the behavior of the samples, due to different molar masses of the HA, has been observed, and also the presence of NaCl did not significantly alter the behavior of the HA, but the values of γ were generally a bit higher in the presence of salt. Some difference between MPB and the DNR methods has been observed during the measurement of HA in water, when higher-molar mass HA displayed slightly larger surface activity.

REFERENCES

1. *KSV BPA 800P Manual*. KSV Instruments, 48p, Finland, 2004.
2. Fainerman V. B., Mys V. D., Makievski A. V., Miller R.: J. of Coll. And Inter. Sci. *304*, 222 (2006).
3. Krouská J.: *Diploma Thesis*. Brno University of Technology, Faculty of Chemistry, Brno, Czech Republic, 2008.
4. Lapčík L. jr., Lapčík L., De Smedt S., Demeester, J., Chabreček P.: Chem. Rev. *98*, 2663 (1998).
5. Cowman M. K., Matsuoka S.: Carbohydr. Res. *340*, 791 (2005).
6. Prehm P. in: Bipolymers, *Polysaccharides I: Polysaccharides from prokaryotes* (Vandomme E. J., De Baets S., Steinbückel A. ed.), chapter 15 *Hyaluronan*, p. 379. Weinheim: Wiley-VCH 2002.
7. Ribeiro W., Mata J. L., Saramago B.: Langmuir *23*, 7014 (2007).
8. Christov N. C., Danov K. D., Kralchevsky P. A., Ananthapadmanabhan K. P., Lips A.: Langmuir *22*, 7528 (2006).
9. Zhang T., Marchant R. E.: J. of Col. And Inter. Sci., *177*, 419 (1996).

P06 SURFACE TENSION OF REGENERATED HUMIC ACIDS SALTS

ANNA ČTVRTNÍČKOVÁ, MARTIN DRASTÍK, ZOJA VLČKOVÁ AND JIŘÍ KUČERÍK

Faculty of Chemistry, Brno University of Technology, Purkyňova 118, 612 00 Brno, Czech Republic,
kucerik@fch.vutbr.cz

Introduction

The soil remediation technologies emphasize the transformation and detoxification of pollutants. For example bioremediation enables permanent elimination of pollutants by in situ remediation at low cost, however, is limited by many factors.[1] In contrast remediation using natural surfactants is gaining growing interest. Humic acids (HA) – naturally occurring surfactants are recognized to be a possible aid in soil bioremediation techniques. For example, the bioavailability of polychlorinated biphenyls (PCB) and polycyclic aromatic hydrocarbons (PAH) appeared to be increased by addition of oxygenous HA to contaminated soils[1].

Lignite represents the youngest type of coal with the age belonging between peat and brown coal. One of the most attractive ways of lignite exploitation is their use as a source of HA[2].

The aim of the work was to increase the surface activity of HA by modification of parental lignite and to find technologically appropriate composition of humic acids useful for washing technology of highly polluted soils (i.e. remediation).

Experimental

R e g e n e r a t e d   H u m i c   A c i d

The South Moravian lignite (Mír mine, Mikulčice, Czech Republic) was used as a source of HA. The samples of "regenerated" HA were obtained from the fraction of lignite by its oxidation reaction with two oxidizers (HNO_3, H_2O_2) and two other agents (acetic and citric acids, respectively) according to following procedure: 20 g of raw lignite was mixed with 200 ml of appropriate modifier and stirrred 30 min, washed until agent-free. Procedure was followed by standard alkali extraction according to ref.[2]. The list of studied samples is shown in Table I.

A part of RHA samples was titrated by 0.1 M NaOH to get water-soluble sodium humate (NaRHA) and the second half remained in the protonated form. The protonated form of RHA was used for Elemental Analysis (EA). Details of the EA are given in Table II.

S u r f a c e   T e n s i o n   M e a s u r e m e n t

For surface tension (ST) measurements Sigma 700 tensiometer (KSV Instruments Ltd.) using a 19mm-diameter platinum-iridium (Pt-Ir) ring was employed.

13 samples with concentrations from 0.001 to 10 $g\,dm^{-3}$ of individual NaRHA were prepared by diluting humic solutions one day before measurement. Before experiment each

Table I
The list of the studied samples

Sample	Modifier	Sample	Modifier
HA	–	RHA4	2% H_2O_2
RHA1	5% HNO_3	RHA5	5% H_2O_2
RHA2	10% HNO_3	RHA6	20% acetic acid
RHA3	20% HNO_3	RHA7	20% citric acid

Table II
Elemental analysis of HA and RHAs [% wt.]

Sample	C [%]	H [%]	N [%]	O [%]	C/O	C/H
HA	58.1	4.44	1.53	35.9	1.62	13.1
RHA1	58.5	3.46	2.01	36.1	1.62	16.9
RHA2	58.2	3.55	2.32	35.9	1.62	16.4
RHA3	56.5	4.16	3.38	35.9	1.57	13.6
RHA4	58.0	3.62	2.15	36.2	1.60	16.0
RHA5	58.5	4.25	1.47	35.8	1.63	13.8
RHA6	58.0	3.75	2.06	36.2	1.60	15.5
RHA7	58.2	3.75	2.30	35.8	1.63	15.5

solution was stirred for 5 min in a shallow glass measuring dish. The experiment was carried out after 10 min sample repose drawing the Pt-Ir ring on the solution surface. The time of measurement was 12 hours. Obtained data were fitted by Szyszkowski equation:

$$\gamma_0 - \gamma = a \log(1 + bc), \qquad (1)$$

a and b are empirical parameters of Szyszkowski equations dependence on the structure of dissolved matter, parameter a reflects the nature of surface active substances and has a constant value for the surface active moieties of one type of molecule, parameter b is different for different molecules and characterizes the efficiency of the absorbed molecules to decrease ST, and also describes the surface activity. γ_0 is the ST of the solvent (water at 25 °C: $\gamma_0 = 72.1$ mN m^{-1}), γ is the ST of the solution and c is the concentration of the solute. For the maximal surface saturation by adsorbed molecules following equation was derived[3]:

$$\Gamma_{max} = a/2.303\,RT, \qquad (2)$$

where Γ_{max} is the maximal Gibbs surface excess quantity. For predicted surface excess quantity by monomolecular layer, the area of one molecule at the surface is:

$$s = 1/\Gamma_{max} \cdot N_A, \qquad (3)$$

where N_A is Avogadro's number ($N_A = 6.023 \times 10^{23}$)ref.[3].

Results and Discussion

The surface tension of NaHA and NaRHAs was measured as a function of their concentration and time. In fact,

with increasing concentration of the humic samples the ST progressively decreased and equilibrium, i.e. the constant value of ST, was reached after 10 hours. Since the sorption of amphiphilic humic molecules in the surface layer is a dynamic process governed both thermodynamically and kinetically, it is likely that simultaneously desorption processes occurred. Obtained data of ST in this time were subtracted from the surface tension of the solvent (water), the results were plotted versus respective concentrations and fitted Szyszkowski equation (2) (Fig. 1.).
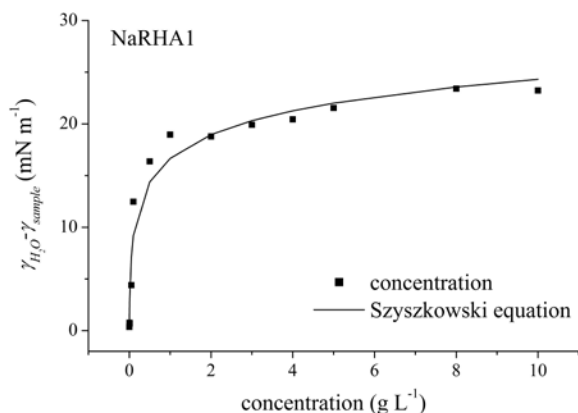
Fig. 1. Dependence of surface tension obtained after 10 hours of the measurement of different concentrated humic samples, fitted by Szyszkowski equation

Basically, the Szyszkowski equation was derived for water solutions of fatty acids and aliphatic alcohols[3]. We assumed that it could be used also for fitting of humic acids solutions ST measurement because the molecules adsorbed in the surface were predominantly aliphatic. The justification of this opinion is based on chemical character of HS since aliphatic molecules in humic acids are mainly lipids and alcohols. From the chemical point of view, those are amphiphiles; hence they are very likely to be excluded from bulk of water to the surface. Parameters obtained from Szyszkowski equation fitting are listed in Table III. There it can be seen almost the same value of parameter a for NaRHA1, NaRHA2, NaRHA3 and NaRHA4 which means that these samples include more or less the same type of molecules adsorbed at the surface. To the other group belong NaHA and NaRHA6. In the last group is NaRHA5. For example for fatty acids the value of a parametr is reported 12.97 $mN\,m^{-1}$.ref.[3]. Therefore, data reported in Table III are in a good agreement with this value and confirms our hypothesis.

Table III
Parameters obtained from Szyszkowski equation

Sample	a $[mN\,m^{-1}]$	b $[dm^3\,mol^{-1}]$	Γ_{max} $[10^{-3}\,mol\,m^{-2}]$	s $[10^{-21}\,m^2]$
NaHA	9.70	41.9	1.70	0.98
NaRHA1	7.67	147.9	1.34	1.24
NaRHA2	7.32	243.2	1.28	1.29
NaRHA3	7.97	169.7	1.40	1.19
NaRHA4	7.77	99.7	1.36	1.22
NaRHA5	8.71	382.2	1.53	1.09
NaRHA6	9.10	88.6	1.59	1.04
NaRHA7	8.25	342.2	1.45	1.15

The parameter b shows significantly high value 382.2 ± 274 for NaRHA5 in comparison with lower NaHA 41.9 ± 19.6. Therefore, it can be seen that the modification of parental lignite lead to production of humic acids with high surface activity. Comparison with literature data[3] shows that efficiency of NaHA sample falls between C4 (butyric) and C5 (valeric) acids (19.6 and 68.5, respectively) whereas sample NaRHA5 falls between C6 (caproic) and C7 (enanthic) acids (233 and 555, respectively).

The parameters obtained from Szyszkowski equation for all studied samples were correlated with C/O and C/H ratios from EA by Pearson correlation coefficient. The significantly high negative correlation was between the a-parameter and C/H ratio, the value was –0.68. It means that there was a close relationship between the type of molecule and aromaticity/aliphaticity of the sample. In fact, the larger value of a-parameter indicates higher aliphaticity of the sample. Positive weak relationship was between b-parameter and C/O ratio, the correlation value was 0.47. That reflects that with higher surface activity the oxidation degree of the samples decreases.

REFERENCES

1. Conte P., Agretto A., Spaccini R., Piccolo A.: Environ. Pollut. *135*, 515 (2005).
2. Kučerík J., Pekař M., Klučáková M.: Petrol. Coal *45*, 58 (2003).
3. Bartovská L., Šišková M. in: *Fyzikální chemie povrchů a koloidních soustav.* VŠCHT v Praze, Praha 2002.

P07 IMMOBILIZATION OF LIGNITE INTO PVAL SPONGES

PETR DZIK, VÁCLAV MACH and MICHAL VESELÝ

Faculty of Chemistry, Brno Universityof Technology, Purky-ňova 118, 612 00 Brno, Czech Republic
petr@dzik.cz

Introduction

Lignite is from geological point of view the youngest form of fossil fuels. Therefore its energy content is rather low. However, much attention has been paid to non-energetic applications of lignite recently[1]. Apart from other interesting way of utilization, lignite proved to be an efficient sorbent for a number of pollutants.

Although loose finely groung lignite can be used on its own, it might be beneficial for a number of industrial application to use some immobilised form of lignite, for example for water purification. Therefore some process for lignite immobilization has to be found.

Poly(vinyl alcohol), PVAl, is a common vinyl polymer with some very special properties. It is highly hydrophilic and well soluble in polar solvents including water. Moreover, it is absolutely non toxic, biocompatible and biodegradable[2]. The reactive secondary hydroxyl groups can be used for further modification[3]. Crossliking is easily performed by a vast array of crosslinking agents[4]. Resulting hydrophilic gels are have very interesting properties and various applications, many of which include the immobilization of other active component (enzymes[5], living cells[6], heterogeneous catalyst particles[7] etc.)

Experimental

Our experiments were decicated to the preparation and study of open-pore hydrophilic sponges with immobilised lignite as sorbent. Such articles might be useful e. g. for water treatment where some immobilised form of sorbent is always preferred.

In a typical example, 10 g of 20 % wt. aqueous solution of PVAl (Mowiol 18-88, Fluka) was mixed with *A* grams of aluminum (fine powder, Fluka). After thorough mixing, 10 ml of hardener solution was added. The hardener solution consisted of two components in variable ratios: Component *B* was a solution of paraformaldehyde in sulphuric acid (10 g of paraformaldehyde was dissolved in 100 ml of 60 % wt. sulphuric acid). Component *C* was 60 % wt. sulphuric acid. After complete mixing, D grams of groung lignite was dispersed into the composition. Individual samples were then given a code (A–B/C–D) fully identifying their composition. For example, sample 0,05–7/3–2 was produced using 9 g PVAl solution + 0,05 g Al + hardener mixture made of 7 ml paraformaldehyde solution and 3 ml 60% H_2SO_4 + 2 g lignite.

After thorough mixing, the composition was transferred into PE form with perforated lid, where it was left to react for 24 hours at room temperature. During this time, formaldehyde reacted with PVAl and formalised, partially crosslinked copolymer was produced – poly(vinyl alcohol-co-vinyl acetate-co-vinyl formal).

At the same time, aluminum powder slowly reacted with sulphuric acid and hydrogen gas evolved. As the volume of hydrogen grew, the mixture was slowly foamed up and its volume increased 3–15 times, depending on the amount of aluminum added. During this process, a solid hydrophilic open-cell sponge was created.
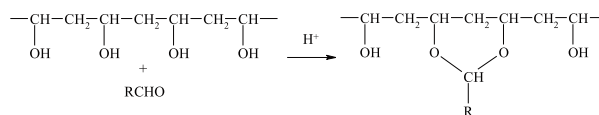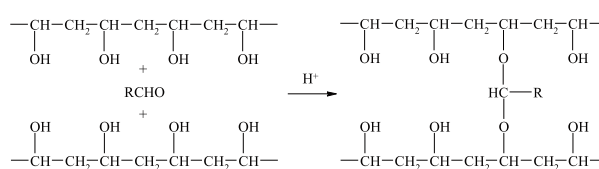

Fig. 1.　**Intramolecular acetalization**

Fig. 2.　**Intermolecular acetalization**

After the reaction, the form was open and the cured sponge was repeatedly washed with running tap water to remove reaction byproducts. After complete washing, the spopnges were stored soaked in 0,001 % wt. aqueous SEPTONEX solution to protect then against microbial contamination.

Table I
Composition and sample naming of PVAl sponges

Al [g]	Hardener composition [B + C, ml]	Lignite [g]	Sample code
0.05	5.5 + 4.5	2	0.05–5.5/4.5–2
		4	0.05–5.5/4.5–4
		6	0.05–5.5/4.5–6
		8	0.05–5.5/4.5–8

Adorption efficiency was studied by measuring the adsorption of Cu^{2+} ions onto pure sponge and lignite-containing sponge samples. Copper concentration was determined vy UV-VIS spectrometry by measuring the absorbance at 808 nm and the amount of of adsorbed copper was expressed as mg of copper per gram of sorbent (i.e. per total weight of sponge). The sorption capacity of lignite depends on the pH and the optimum region is 3.9–5.5. Therefore the samples were immersed in acetate buffer solution of pH = 4.5.

Results

Optical images of sponge crossection were recorded using Nickon Eclipse E200 microscope and Nikon D200 digital camera. FTIR spectra were recorded on NICOLET® Impact 400 spectrophotometer. Samples of sponges
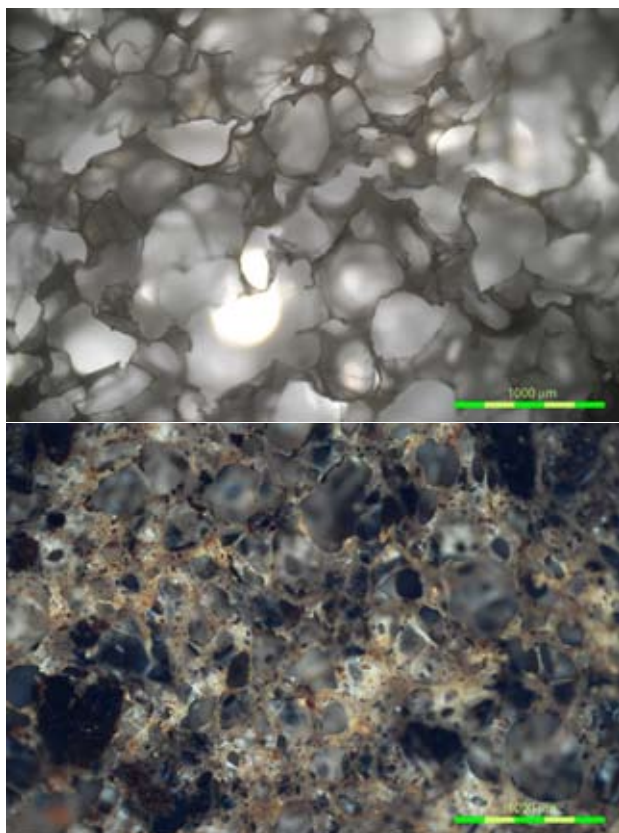
Fig. 3.   **Samples 0.05–5.5/4.5 and 0.05–5.5/4.5–6**

Fig. 4.   **FT-IR spectra of raw and acetalised PVAl**

Table II
Sorprion performance

Sample	m_{Cu} [mg g^{-1}]	
	pH ~ 2,4	pH ~ 4
0.05–5.5/4.5–2	0.13	6.15
0.05–5.5/4.5–4	0.69	11.36
0.05–5.5/4.5–6	1.24	12.03
0.05–5.5/4.5–8	2.36	13.10
Lignite	*	14.43
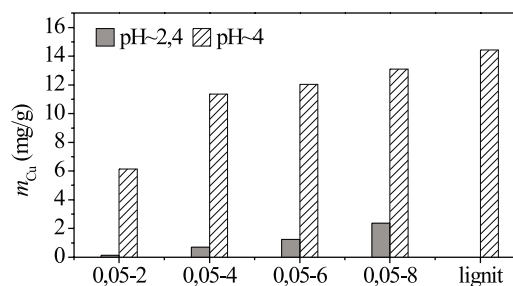
Fig. 5.   **Sorption performance**

were finely ground to very small flakes and pressed to standard KBr tablets.

The recorded IR spectra clearly account for the reactions taking place during curing process:
- The strongly acidic environment resulting from the hardener composition yields complete hydrolysis of residual acetate groups on PVAl macromolecule. This is accompanied by total disappearance of the 1,735 cm^{-1} peak corresponding to ester vibration.
- The decreasing peak at 3,340 cm^{-1} proves the consumption of secondary hydroxyl groups for acetalization.
- C–H vibrations characteristic for formal group appeared at 2,870 and 2,790 cm^{-1} and showed increaseing intesity with increasing amount of hardener.
- Peaks at 1,189, 1,143, 1,076 a 1,033 cm^{-1} are associated with valence vibrations of $=C-O-C-$ groups and account for the formation of formal.
- Peaks at 2,360 cm^{-1} prove the presence of carbon dioxide in the tablets.

The adsorption of copper prooved to be dependent on the pH of the environment. Singe the sponges originated at highly acidic conditions, they tend to release acidity over a long period of time. Therefor the pH value had to be adjusted by the acetate buffer. Results are summarized in the following tables and figures.

Conclusions

Our work was dedicated to the immobilization of lignite into highly porous hydrophilic sponges made of acetalized PVAl. These sponges were prepared by acidic formalization of aqueous solution of PVAl. Pores were formed by gaseous H_2, which originated from the reaction of powder aluminum with acid. Resulting sponges were of open-cell structure, were highly hydrophilic and had variable porosities depending on the amount of blowing agent (aluminum).

A set of sponge samples with varying lignite content was prepared and the properties of resulting sponges were studied. We also studied the sorption capacity of lignite-containing sponges on model pollutants (Cu(II) ions).

REFERENCES

 1. Pekař M., Klučáková M.: CHEMagazín *13*, 8, (2003).
 2. *Mowiol Polyvinyl Alcohol.* Sulzbach/Hessen: Clariant GmbH, 105 p. (1999).
 3. Mleziva J., Šňupárek J.: *Polymery: výroba, struktura, vlastnosti a použití.* Praha: Sobotáles, (2000).
 4. Mark H. F. *Encyklopedia of Polymer Science and Technology: Semicrystalline Polymers to Ziegler-Natta Catalysts.* 3rd ed., New Jersey: John Wiley & Sons, Inc., 2003.
 5. Pourciel M. L., et al. Sens. Actuators, B 94, 330 (2003).
 6. Schmedlenetal R. H.: Biomater. 23, 4325, (2002).
 7. He C.-H., Gong J.: Polym. Degrad. Stab. 81, 117 (2003).

P08   FTIR AND SFS SPECTRA OF HUMIC ACIDS ISOLATED FROM LIGNITE AND CHERNOZEM

NADĚŽDA FASUROVÁ[a], ĽUBICA POSPÍŠILOVÁ[b] and EDUARD POKORNÝ[b]

[a]*University of Technology Brno,Faculty of Chemistry, Institute of Physical and Applied Chemistry, Purkyňova 118, 612 00 Brno, Czech Republic,*
[b]*Mendel University of Agriculture and Forestry, Institute of Agrochemistry, Soil Science, Microbiology and Plant Nutrition,Zemědělská 1, 613 00 Brno, Czech Republic*
fasurova@fch.vutbr.cz

Introduction

In this paper comparison of chemical structure and optical properties of humic acids (HA) isolated from various sources are presented.

Excellent sorption properties of HA are well known to depend on their chemical structure and composition.

Therefore HA isolated from different matrices (soil, lignite) were studied using FTIR and synchronous fluorescence spectroscopy (SFS) in emmision mode. FTIR spectra contributed to authentic knowing of functional groups in HA molecule. The inherent fluorescence of humic acids is an extremely sensitive measure, which allows for non-destructive analyses of samples[1,2,3]. Object of our study were HA isolated from lignite (locality Mikulčice, Czech Rep.) and Modal Chernozem (locality Bratčice, Czech Rep.).

Experimental

- HA from soil were isolated according to the international standard method IHSS[4]. HA from coal were isolated according to the Czech standard on determination of HS content in coal.
- FTIR spectra were measured using KBr technique with Nicolet Impact 400 spectrometer.
- Humic acids were dissolved in 0.5M NaOH and SFS spectra were measured by Spectrofluorimeter Aminco Bowman Series 2 within the range 320–620 nm (at $\Delta\lambda = 20$ nm and temperature 20 °C).
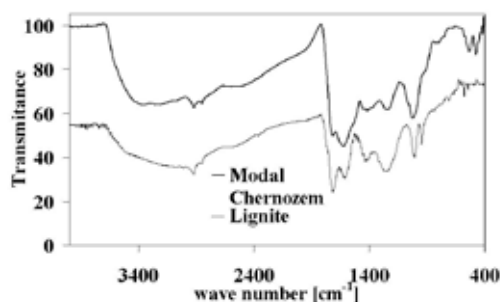

Fig. 1.   **FTIR spectra of HA isolated from Lignite and Modal Chernozem**

Results

F T I R   S p e c t r a

Results showed that the main peaks observed in infrared spectra were similar for both samples (Fig. 1.). There are evident following peaks: small peaks at 3,300–3,400 cm^{-1} (OH groups, H-bonds), two small but distinct peaks at 2,930–2,850 cm^{-1} (asymmetric C of CH$_2$), sharp peak at 1,700–1,720 cm^{-1} (C= of COOH), peak at 1,650–1,655 cm^{-1} (carboxylate and amido groups), peak about 1,620 cm^{-1} (C=C in aromatic structures, C−O stretch), composed band in 1,000–1,220 cm^{-1} (aliphatic C−O stretch, OH groups and polysaccharides).

S F S   S p e c t r a

In SFS spectral range (Fig. 2.) four main fluorophore peaks were identified: at 488, 502, 470, 512 nm (at $\Delta\lambda = 20$ nm). SFS spectra of Modal Chernozem sample showed further peak at about 359 nm. The peak determined at emission 488 nm corresponded with excitation at 468 nm. This value of wavelength was more intensive then others. Maximum fluorescence intensity was shifted from shorter to longer wavelength caused by an increasing number of aromatic compounds in HA molecule. Relative fluorescence indexes (RFI) were calculated as ratio I_{488}/I_{502}. The fluorescence indexes it is supossed to be closely connected with humification degree. Higher RFI index was found in Modal Chernozem humic acid (1.13). RFI index of Lignite humic acid was lower (1.02). So we suggested higher humification degree in Modal Chernozem humic acid. These values could be also related with samples origin (mean residual time and geological age).
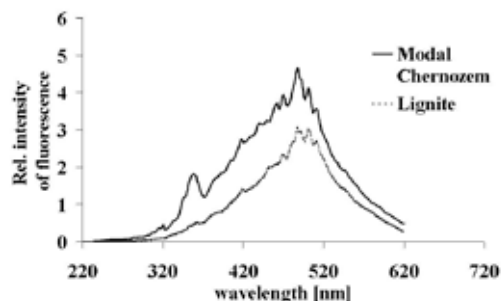

Fig. 2.   **Synchronous fluorescence spectra of Lignite and Modal Chernozem humic acids at $\Delta\lambda = 20$ nm**

Fluorescence of studied samples was compared with fluorescence behaviour of Leonardite humic acid standard (IHSS). According to the literature, studied samples were included into the second group of humic substances[2]. HA in this group had two closely – spaced main excitation peaks at 450, 465 nm and emission maximum about 500–520 nm.

Conclusions

We can conclude that HA isolated from different matrices had both FTIR and SFS spectra very similar except lower wave numbers and wavelengths. Lignite and Modal

Chernozem humic acids contained the same type of fluorophore groups. More intensive fluorescence behaviour gave sample of Modal Chernozem HA. Differences in position of fluorophore peaks were not established.

REFERENCES

1. Chen J., LeBoeuf E. J., Dai S., Gu B.: Chemosphere *50,* 639 (2003).
2. Senesi N., Miano T. M., Provenzano M. R, Brunetti G.: Soil Sci. *152,* 259 (1991).
3. Senesi N., Miano T. M.: Sci. of the Total Environ. *117/118*, 41 (1992).
4. Hayes M. H. B., Wilson W. S.: R. Soc. Chem. *1997*, 83.

P09 ENHANCEMENT OF NORTHERN SOFTWOOD BLEACHED KRAFT PULP ACCESSIBILITY AND ACID HYDROLYSIS BY MEANS OF ULTRASONIC IRRADIATION

MICHAL JABLONSKÝ[a], ŠTEFAN ŠUTÝ[a] and BRANISLAV ŠVEHLA[b]

[a]Department of Chemical Technology of Wood, Pulp and Paper, Faculty of Chemical and Food Technology, Slovak University of Technology in Bratislava, Radlinského 9, 812 37 Bratislava, Slovak Republic,
[b]ECOSON s.r.o., Trencianska 17, 915 01 Nove Mesto n. Vahom, Slovak Republic,
michal.jablonsky@stuba.sk

Introduction

In the past decades, the increase in the world population and economy has resulted in a raising demand for various raw materials for industries such as raw materials for pulp and papermaking[1–4]. Many researchers have investigated the effects of the application of ultrasonic energy to pulp[1,3], recycled fiber[4], enhancement isolation of different compounds and component of wood or straw materials such as lignin[2,5,6], carbohydrate such as cellulose and hemicellulose[7,8]. The of review Willems (1962)[9] describes the use of ultrasound in pulp and paper technology for various processes like debarking, defibration, beating, impregnation and penetration, pulping, bleaching, stock preparation and grafting. The use of the ultrasound produce has evidenced their major potencial in the process of decreases or partial replacement of hazardous chlorine compounds during pulp bleaching alternative chemicals. Hemicellulases have been used to increase lignin extractability by partial degradation of the lignin-hemicellulose complex in the fiber, thus to improve the bleachability of pulp.[1,3,10–12]

Experimental
Raw Material

NIST standard reference material 8495 Northern Softwood Bleached Kraft Pulp was used in this study.

Ultrasonic Treatment

Sonications were carried out at 25, 40 and 80 kHz. For the ultrasonic treatment, 1 g portions of pulp (o.d.) were sonicated in 1L water using an ultrasonic generator (Model ECOSON).

Water Retention Value (WRV)

0.5 g of wet sample was swollen in 22 cm^3 deionized water for 6 hours, After this results treatment, the samples was centrifuged at 2,200 rpm. for 12 min. The dewarted sample was dried to a constant weight at 105 °C.

DRIFT FTIR Spectra

DRIFT FTIR spectra were obtained by means of a Digilab Excalibur FTS 3000MX FTIR spectrometer. Finely divided 13 mg samples of the material surface were grounded and dispersed in a KBr (260 mg). The DRIFT FTIR spectra were recorded with the nominal resolution of 4 cm^{-1} using DRIFT FTIR technique. Spectra were recorded over the range 400–4,000 cm^{-1}. Each spectrum is the average of 30 individual scans. The experimental DRIFT spectra were mathematically evaluated using OMNIC (Thermo Nicolet Corp.) and MicroCal Origin software.

Acid Hydrolysis

The resulting suspensions were then hydrolysed into microcrystals by refluxing for 5 h in 3.5M HCl.

Then the mixture was filtrated and 5 ml filtrate was added to solution of 1M NaOH buffer with pH = 7. Felingh solution I (10 ml) and Felingh solution II (10 ml) was added. This solution was warmed up to boiling point in 3 min. and following the reflux for 2 min. After heating to this sample was cooled and filtrated. Precipitated compound CuO_2 was dissolved in 20 ml 1M HCl and solution was neautralized to pH 8. Finally, this solution was titrated with the chelatone II (c = 0,01 M) using indicator murexid.

Results

The water retention value (WRV) has been extensively used to study several properties of cellulose materials. The accessibility of the cellulose material for swelling depends on several factors. The essential factors limiting the access of swelling of the fibres are: macro and microstructure of the fibres and and, in this manner, on the internal structure of cellulose and other factors such as capillary system and lumen expansion[3]. The mechanical effects of ultrasound provide a greater penetration of solvent into cellular materials and improves mass transfer[11]. The development of irradiation during ultrasonic treatment of softwood kraft pulp and different frequency 25, 40 and 80 kHz on the change of the WRV is shown on Fig. 1. On the basis of obtained results it might be said that increasing frekvence from 25 to 80 kHz in time up to 10 min. affect WRV insignificantly.With the longer
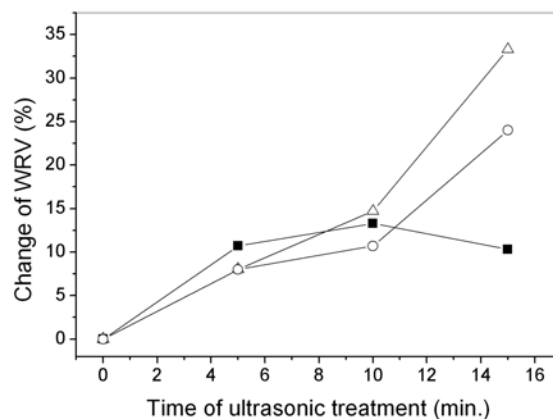

Fig. 1. **The influence of the ultrasonic treatment with the different frequency 25, 40 a 80 kHz on the change of the water retention value (WRV). -■- 25 kHz; -○- 40 kHz; -Δ- 80 kHz**

time of ultrasonic treatment (15 min) was found increase of WRV at 40 and 80 kHz. At 25 kHz was value of WRV didn't change. This effect of ultrasonic treatment is also confirmed by another work Wojcak and Pekarovicova, 2001[3].

The effect of the ultrasonic treatment on the pulp relates to the changes in the porosity of irradiated pulp[3]. These results were investigated in the work Laine and Goring (1977)[1] by the solute exclusion technique. They suggested that the effect of ultrasonic seems to be caused by transformation of the fibres small pores into larger ones. According to Wojcak and Pekarovicova (2001)[3] was observed that ultrasonic treatment increases the porosity of pulp. Several attempts have been made to characterize and quantify the degree of crystallinity of pure celluloses using intensities of certain bands in the infrared spectra.[13–15]
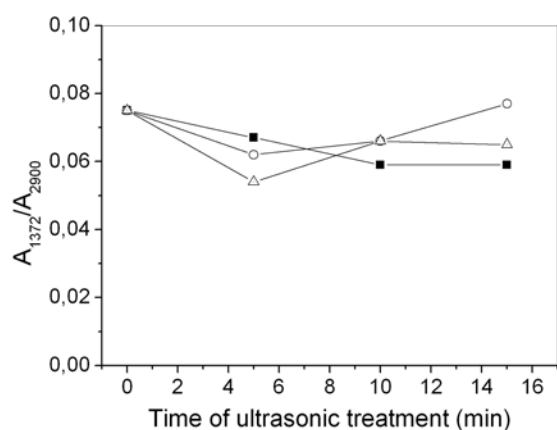
Fig. 2. **The change of the area ratio 1,372 cm^{-1} to 2,900 cm^{-1} (A1372/A2900) during the ultrasonic treatment with different frequency 80, 40 and 25 kHz. -■- 25 kHz; -○- 40 kHz; -△- 80 kHz**

The ratios of bands-heights at 1,429 and 894 cm^{-1}, at 1,372 and 2,900 cm^{-1} have been used as relative measures of cellulose crystallinites. The change in overall crystallinity has been studied by the determination of the absorbance area ratio 1,372/2,900 cm^{-1} (Fig. 2.). For the area of the band at 2,900 cm^{-1}, the baseline was drawn between the shoulders at 3,005 cm^{-1} and 2,590 cm^{-1} while for the area of the band at 1,372 cm^{-1}, the intensity of shoulder at 1,392 cm^{-1} and maximum at 1,350 cm^{-1} were used giving a common baseline for the group of bands, which occur close together in this region. The differences in the absorbane ratio of up to 0.022 units are insignificant for different frequencies which were used for ultrasonic treatment at 25, 40 and 80 kHz.

On the Fig. 3., there is shown the course of acid hydrolysis during the ultrasonic treatment with different frequency 80, 40 and 25 kHz. Samples of ultrasonification in water have exhibited higher acid hydrolysability than untreated ones. During the ultrasonic treatment increase of total content of saccharides at all frequencies was observed. The prolonged ultrasonification up to 15 minutes caused significant increase in hydrolysability. At the frequency 40 kHz was achieved significant increase of total content of saccharides at time
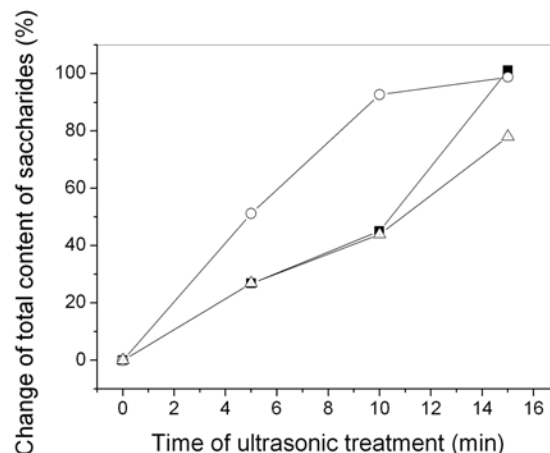

Fig. 3. **Effect of ultrasonic treatment with different frequency 80, 40 and 25 kHz on the total content of saccharides; -■- 25 kHz; -○- 40 kHz; -△- 80 kHz**

of 5 and 10 minutes of ultrasonic treatment comparing sonication at frequencies 25 and 80 kHz. At the time of 5 minutes the increase of total content of saccharides was about 90 % higher comparing to ultrasonic treatment at 25 and 80 kHz and about 106 % higher at 10 minutes of ultrasonic treatment.

Conclusions

Suspensions of northern softwood bleached kraft pulp were subjected to ultrasonic treatment at different ultrasonic frequencies 25, 40 and 80 kHz. Results revealed an increase in cellulose's accessibility in terms of water retention value (WRV) with increasing ultrasonic treatment time with the different frequency 25, 40 and 80 kHz of ultrasonic treatment. Furthermore, the acid hydrolysis of cellulose has been also successfully improved by the ultrasonic treatment. However, no significant changes in crystallinity of cellulose were noted after ultrasonic treatment which was characterized by means of FTIR.

REFERENCES

1. Laine J. E., Goring D. A. I.: Cell. Chem. Tech. *11*, 561 (1977).
2. Sun R.C, Tomkinson J. C.: Ultrason. Sonochem. *9*, 85 (2002).
3. Wojcak A., Pekarovicova A.: Cell. Chem. Tech. *3–4*, 361 (2001).
4. Tatsumi D., Higashihara T., Kawamura S., Matsumoto T.: J. Wood Sci. *46*, 405 (2000).
5. Sun R., Sun X. F. Xu X. P.: J. Appl. Polym. Sci. *84*, 2512 (2002).
6. Gadhe J. B., Gupta R. M., Elder T.: Cellulose *13*, 9 (2006).

7. Hromadkova Z, Ebringerova A., Malovikova A.: Macromolecular Symposia *232*, 19 (2006).

8. Ebringerova A., Hromadkova Z.: Ultrason. Sonochem. *9*, 225 (2002).

9. Willems P.: Pulp & Paper Magaz. Canada *63*, T455 (1962).

10. Manson T. J., Lorimer J. P.: Sonochemistry: *Theory, Applications and users of ultrasound in chemistry*, Ellis Horwood, Chichester, UK, 1988.

11. Mason T. J., Paniwnyk L., Lorimer J. P.: Ultrason. Sonochem. *3*, 253 (1996).

12. Wiikari L., Tenkanen M., Buchert J., Ratto M., Bailey M., Siikaaho M., Linko M.: *Bioconserversion of forest and agricultural residues*. (Saddler J., eds.) p.131, CAB international, Wallingford, UK 1993.

13. Fengel, D.: Holzforshung *46*, 283 (1992).

14. Evans R., Newman R. H., Roick U. C., Suckling I. D., Wallis A. F. A.: Holzforshung *49*, 498 (1995).

15. Schwanninger M., Rodrigues J. C., Pereira H., Hinterstoisser B.: Vib. Spectro. *36*, 23 (2004).

P10　MODELLING OF COMPLEXATION OF HEAVY METALS AND HUMIC ACIDS WITH UTILIZATION OF HIGH RESOLUTION ULTRASOUND SPECTROSCOPY

MARTINA KLUČÁKOVÁ, JIŘÍ KUČERÍK and MILOSLAV PEKAŘ

Institute of Physical and Applied Chemistry, Faculty of Chemistry, Brno University of Technology, Purkyňova 118, 612 00 Brno, Czech Republic,
klucakova@fch.vutbr.cz

Introduction

The high affinity of humic acids (HA) to transition metals is caused by large amount of binding sites in their structure. There is a large number of various coordination sites that are able to bind transition metals by various strengths. The most important functional groups are the carboxylic and phenolic ones. Copper was used as a model metal for experiments due to high affinity to HA and stability of formed complexes.

In previous works, quantum chemical calculations of interaction enthalpies[1] and also measurement of complexation kinetic[2,3] were carried out. On the basis of obtained results the following models have been chosen for this study: citric acid, hydroquinone, pyrocatechol, salicylic acid and EDTA. New band in UV/VIS spectra was detected as a result of complex formation for hydroquinone and pyrocatechol. Others were chosen mainly for their high affinity to metal ions, e.g. salicylic acid is frequently considered as the most suitable coordination site in structure of humic acids, which has been confirmed also by quantum chemical calculations in our works[1,3].

Experimental

Ultrasonic spectrometer with high resolution HR-US 102 (Ultrasonic Scientific, Ireland), was utilized for measurement of basic ultrasonic parameters. The device consists of two independent cells tempered at 25 °C. Both cells were filled by the same model compound (e. g. hydroquinone) and then 1.25M $CuCl_2$ (20 μl) was added into one cell. Velocity (U) and attenuation (N) in both cells was measured, the resulting differences between both cells ($U12$ and $N12$) were computed.

UV/VIS spectra were measured by means of U–3300 Hitachi spectrophotometer.

Results

Time dependencies of *U12* for all used model are shown at Figs. 1 and 2. We can see that hydroquinone and pyrocatechol (Fig. 1.) need relatively long time for stabilization ofter addition of $CuCl_2$ than others.

Pyrocatechol, which has very strong new band in its UV/VIS spectrum after $CuCl_2$ addition, has minimum on its time-curve much higher not only than models without new band in spectra (citric and salicylic acid, EDTA – Fig. 2.) but also than hydroquinone. It seems, that relatively strong complex
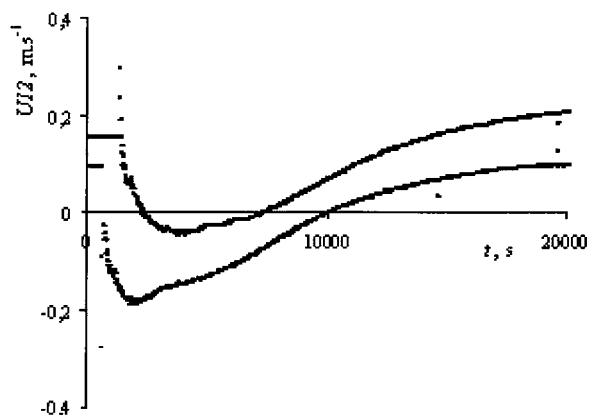

Fig. 1. **The time dependence of U12 for pyrocatechol (upper) hydroquinone after addition of $CuCl_2$**
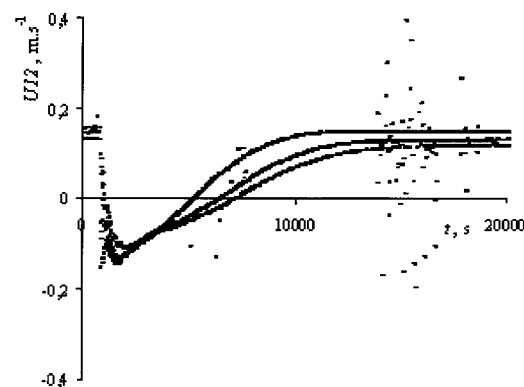

Fig. 2. **The time dependence of U12 for citric acid (upper), salicylic acid (middle) and EDTA after addition of $CuCl_2$**

is formed in this case, but the affinity of Cu^{2+} ions to this model is not too high, which corresponds with lower rate of the process.

On the other hand, high velocity and short time measured for salicylic acid (Fig. 2.) confirmed high ability of this structure to bind cupric ions in stable complexes. Quantum chemical calculations of interaction enthalpies[1] resulted in model of salicylic acid as a most attractive for complexation of metal ions. It is not surprising that complexation of cupric ions gives similar or better results, before its functional groups give possible similar chelating effect. In the case of EDTA is complexation rate probably influenced by molecule sizes and steric effects. But comparison with pzrocatechol and hzdroquinone shows that also this structure is more preferable. High affinity of cupric ions to these three structures probably causes that their interactions are faster than others.

Conclusions

Preliminary results of high resolution ultrasound spectroscopy are presented in this contribution. Obtained data correspond with conclusions in our previous works.[1–3] Salicylic acid, as well as citric acid and EDTA, seem to be attractive coordination sites for complexation of cupric ions.

On the hand very interesting results were obtained for hydroquinone and pyrocatechol Even though, their interaction enthalpies computed in ref.[1] are much lower than values determined for others, these structures contribute also to complexation capacity of humic acids. It corresponds with experimentally measured interaction enthalpy oh humic acids[3], which is approximately three times lower that that of salycilic acid, and EPR and FT-IR spectra of formed complexes discussed in our work[4].

REFERENCES

1. Klučáková M., Pelikán P., Lapčík L., Lapčíková B., Kučerík J., Kaláb M.: J. Polym. Mater. *17*, 337 (2000).
2. Klučáková M., Válková D., Pekař M.: *Proc. 9th International Conference on Environment and Mineral Processing* (Fečko P., Čablík V., eds.), p. 31. Ostrava, 2005.
3. Klučáková M., Pekař M., Válková D *Proceedings of the 13th Meeting of the International Humic Substances Society,* Vol. 45-I I (Frimmel F.H., Abbt-Braun G., eds.) , p. 893. Karlsruhe, 2006.
4. Čechová E., Klučáková M., Krčma F., Majzlík P., Vrajová J.: *ISPC XVIII – book of abstracts*, p. 745. Kjoto 2007.

P11 KINETICS OF SORPTION OF METAL IONS ON LIGNITIC HUMIC ACIDS

MARTINA KLUČÁKOVÁ

Institute of Physical and Applied Chemistry, Faculty of Chemistry, Brno University of Technology, Purkyňova 118, 612 00 Brno, Czech Republic,
klucakova@fch.vutbr.cz

Introduction

High sorption ability of humic acids (HA) is well known. Many authors[1–4] use Langmuir model for mathematical description of adsorption and computing HA sorption capacity. Even thought this model is in relatively good agreement with experimental data, its utilization is connected with some inaccuracies in this case, because it does not take into account the production of hydrogen ions during reactions of metal ions with acidic functional groups on the surface of humic particles. Therefore the new type of adsorption isotherm, respecting the nature of surface chemical interactions, was proposed for adsorption of metal ions on solid humic acids and proved experimentally in previous work[5].

Experimental

HA were obtained from South-Moravia lignite by means of the alkaline extraction[5–6] and characterized in[7].

The ratio 1 g of HA and 50 cm^3 of the Co^{2+} (or Ni^{2+}) salt solution was employed for the sorption experiments. The quantity of adsorbed metal ions was calculated on the basis of the decrease of absorbance (Hitachi U–3300 spectrometer) and calibration curves. The amount of liberated H$^+$ ions was measured using pH-meter Sentron Titan K185-016.

Results

The model was derived for bivalent cations and proved experimentally for sorption of cupric ions. This work deals with kinetics of sorption of cobalt and nickel ions on HA to prove above mentioned new model for metal ions with lower affinity to HA. Following equation was derived for description of adsorption kinetics for binding sites unable splitting of H$^+$ ions:

$$\rho = \ln \frac{c + c_{eq} + \frac{f_0 - c_0 + 1}{b_L}}{c - c_{eq}} = s\,t + const \ , \tag{1}$$

where

$$s = k_{ads} \sqrt{\left(\frac{f_0 - c_0 + 1}{b_L}\right)^2 + 4\frac{c_0}{b_L}} \ , \tag{2}$$

c is concentration of metal ions in given time, c_0 is their initial concentration and c_{eq} is their concentration in equilibrium; f_0 is the initial concentration of free binding sites (adsorption capacity), b_L is adsorption coefficient determined on the basis of adsorption isotherm and t is time. Because equations (1) and (2) are valid for constant pH-value, only data for $t \geq 60$ min (after pH stabilization) were used for computing values of k_{ads}. Obtained results in comparison with those published in ref.[7] for Cu^{2+} ions are listed in Table I.

Table I
Adsorption rate constants

T [°C]	k_{ads} (Co^{2+}) [dm^3 mol^{-1} s^{-1}]	k_{ads} (Cu^{2+}) [dm^3 mol^{-1} s^{-1}]	k_{ads} (Ni^{2+}) [dm^3 mol^{-1} s^{-1}]
30	1.44×10^{-6}	3.55×10^{-5}	6.57×10^{-6}
50	3.62×10^{-6}	6.28×10^{-5}	8.02×10^{-6}
70	1.17×10^{-5}	1.05×10^{-4}	9.67×10^{-6}

We can see that values obtained for Co^{2+} and Ni^{2+} ions are lower comparing with those of Cu^{2+} ions. It is caused by lower HA affinity to these metals and therefore slower adsorption. However, experimental data are in very good agreement with (1) and (2) (see Fig. 1.) and the dependence of kads on temperature can be described by Arrhenius equation similarly as in the case of Cu^{2+} ions. It confirms that developed model can be used also for adsorption of metal ions with lower affinity to HA and chemical bonds are formed in this process.
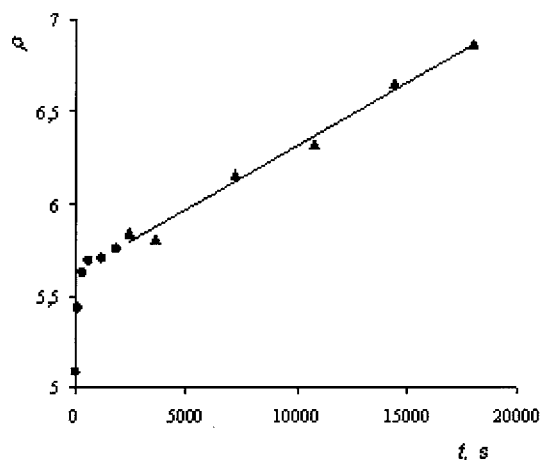

Fig. 1.   **Example of experimental data obtained for adsorption of Ni^{2+} ions at 50 °C fitted by eq. 1 (circles – H$^+$ ions are splittin off, triangles – no changes of pH)**

Conclusions

The new model published in[7] devises binding sites in humic acids into two parts: acidic functional groups, which split of hydrogen ions during surface reaction in adsorption and other binding sites as e.g. aromatic structures, which are not able to change pH value in system. One of the most important advantages of the model is that computed adsorption coefficients are not dependent on pH value as well as adsorption and desorption rate constants obtained from kinetic equation. We are able to determine directly only rate constants for adsorption and desorption, which does not cause splitting of H$^+$ ions.

REFERENCES

1. Ghabbour E. A., Davies G., Ghali N. K., Mulligan M. D.: Can. J. Soil Sci. *81*, 331 (2001).
2. Ho Y. S., McKay G.: Water Air Soil Poll. *158*, 77 (2004).
3. Mesquita M. E., Silva J.: Geoderma *106*, 219 (2002).
4. Prado A. G. S., Airoldi C.: Thermochim. Acta *405*, 287 (2003).
5. Klučáková M., Kaláb M., Pekař M., Lapčík L.: J. Polym. Mater. *19*, 287 (2002).
6. Klučáková M., Pekař M.: Colloid Surface A *252*, 157 (2005).
7. Klučáková M., Pekař M.: Colloid Surface A *286*, 126 (2006).

P12 ACID-BASE PROPERTIES OF FRACTIONATED HUMIC ACIDS

MARTINA KLUČÁKOVÁ and ONDŘEJ PILNÝ

Institute of Physical and Applied Chemistry, Faculty of Chemistry, Brno University of Technology, Purkyňova 118, 612 00 Brno, Czech Republic,
klucakova@fch.vutbr.cz

Introduction

Solid humic acids (HA) are traditionally defined according to their solubility. They are usually considered to be only partially soluble in water. The dependence of their solubility on pH-value is motivation for further fractionation. Preliminary results of the fractionation by HA dissolving in buffers with various pH values were published in ref.[1].

The same method is utilized also in this work. Acid-base properties of obtained HA fractions as well as their solubility in water are studied and compared with behaviour of original HA.

Experimental

HA were obtained from South-Moravia lignite by means of the alkaline extraction[2–3] and characterized in[4].

Batch method of fractionation using universal buffer solution ($NaOH-H_3PO_4-CH_3COOH-H_3BO_3$) of different pH values (4–12). Finely grounded HA (1 g) were mixed with buffer solution (50 cm^3) and stirred for 24 h. Insoluble residue was separated by vacuum filtration and concentrated HCl solution was added to the filtrate (up to pH = 1) in order to precipitate soluble HA fraction. The precipitate was washed by deionized water to remove chloride ions and dried at 50 °C.

Obtained fractions were characterized by UV/VIS (Hitachi U–3300) and FT-IR spectroscopy (Nicolet Impact 400). Content of COOH was determined by standard acetate method[5]. Acid-base properties of individual fractions as well as undissolved residues were studied by dissolving in deionized water (4–40 $g\,dm^{-3}$)[3,6].

Results

HA fractionation and study of behaviour of obtained samples showed many interesting results. While pH-values of buffers, which were before fractionation acidic decreased (up to 3.5), others were after fractionation approximately neutral, even thought dissolved HA amount was much higher. It was found that contain of acidic groups in majority of individual fractions is higher than the content of original HA samples (see Table I). Our hypothesis is that HA structure is changed during fractionation. HA can interact with individual components of buffer and re-arranged their structure, which results in apparently higher acidity of obtained fractions. The re-arrangement of HA structure probably causes, that some acidic groups inside HA aggregates, which are not able dissociate in original HA sample, can contribute to measured acidity in individual fractions.

Table I
Content of COOH groups in individual samples

Sample (fraction)	Initial pH-value	COOH [$mmol\,g^{-1}$]
original HA	–	3.3
undissolved	4	4.2
undissolved	6	3.6
undissolved	8	3.5
undissolved	10	4.2
undissolved	12	2.0
dissolved	8	6.3
dissolved	10	7.5
dissolved	12	5.3

An exception is undissolved HA residue (initial pH = 12), which has lower acidity that original HA. Surprising is that this fraction (after "exhaustion" of the largest amount of HA fraction) has several times higher solubility in water as others. Extracts had to be 30-times dissolved in order to measure UV/VIS spectra. Contradictory results were obtained in measurement of pH and conductivity. Extracts of fraction undissolved at pH = 12 had lower conductivity and very high pH values in comparison of other fractions as well as original HA sample. On the other hand, this fact corresponds with our hypothesis of re-arrangement and possible interactions with buffer, because the most "aggressive" buffer caused the most marked changes in HA properties.
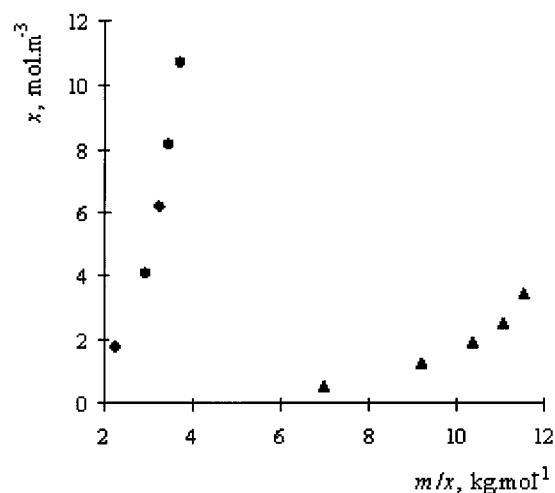

Fig. 1. **Experimental data obtained for initial pH = 6 (triangles) and 10 (circles)**

In previous works[3,6], has been deduced model of HA behaviour in water and aqueous solutions, which included dissociation both dissolved HA and undissolved solid particles. We applied this model of obtained undissolved residues, but their dissolving is different probably as a result of structural changes caused by fractionation (see above). It was derived that equilibrium constant K between dissolved and dissociated HA is

$$K = \frac{x^2}{k.m - x}, \qquad (1)$$

which can be linearized as

$$x = K.k\frac{m}{x} - K, \qquad (2)$$

where x is concentration of H^+ ions, m is content of HA in initial suspension and k is constant. While data measured for original HA agree with (2) very well and they give strong line[3], dependencies obtained for our fraction are curved and curvature increases with decreasing initial pH-value. It is other confirmation of structural changes in HA and also different behaviour of individual samples.

Conclusions

Acid-base properties of HA fractions obtained by means of extraction in buffers with various initial pH-values are studied in this work. It was found that re-arrangement and changes of HA structure are caused by this way of fractio-nation. It results in higher acidity both dissolved and undissolved fractions in comparison with original HA sample and very high solubility of the last residue (initial pH = 12) with lowest conductivity and acidity of its extract in water.

REFERENCES

1. Klučáková M.: *Proceeding of the International Conference Humic Substances in Ecosystems 5* (Gonet S.S, Zaujec A., eds.), p. 39. Bydgoszcz, 2003.
2. Klučáková M., Kaláb M., Pekař M., Lapčík L.: J. Polym. Mater. *19*, 287 (2002).
3. Klučáková M., Pekař M.: Colloid Surface A *252*, 157 (2005).
4. Klučáková M., Pekař M.: Colloid Surface A *286*, 126 (2006).
5. Stevenson F. J.: Humus Chemistry: *Genesis, Composition, Reactions.* Wiley, New York, 1994.
6. Klučáková M., Pekař M.: Colloid Surface A *318*, 106 (2008).

P14　COMPARISON OF VARIOUS PLASMACHEMICAL PROCESSES WITH RESPECT TO THE GAS TEMPERATURE

LUKÁŠ LAZAR[a], PETR SYNEK[a], MONIKA KARÁSKOVÁ[a], MAREK ELIÁŠ[a], ONDŘEJ JAŠEK[a], LUKÁŠ KELAR[a], VILMA BURŠÍKOVÁ[a], PAVEL KONUPČÍK[b] and LENKA ZAJÍČKOVÁ[a]

[a]Department of Physical Electronics, Faculty of Science, Masaryk University,Kotlářská 2, 611 37 Brno, Czech Republic,
[b]Department of Didactic Technology, Faculty of Education, Masaryk University, Poříčí 7, 603 00 Brno, Czech Republic, lucasl@physics.muni.cz

Introduction

Plasma technologies have been already established a key role in many industrial products such as microelectronic devices, solar cells, protective or anticorrosion coatings on machining tools or automobile parts. However, they are still extensively studied as a tool for deposition of new materials and for better understanding of the existing processes.

Using high temperature methods, carbon nanotubes (CNTs) can be produced from carbon vapours generated by an arc discharge or by laser ablation of graphite. Alternative methods are covered by the term chemical vapour deposition (CVD). CVD offers some advantages over other mechanisms particularly in allowing synthesis on specialized surfaces and substrates. By this method, nanotubes can be produced with high purity and in well-ordered arrays of relatively uniform geometry. The CVD group can be further divided into thermal CVD processes and processes utilizing plasma discharges, the so called plasma enhanced CVD (PECVD). The PECVD technique employes combination of physical and chemical processes and is based on the molecule dissociation in the gas phase by impact of energetic electrons and atoms in metastable states followed by chemical reactions of gas radicals. PECVD technique is also one of suitable methods for the deposition of diamond-like carbon (DLC) and crystalline diamond thin films. The PECVD method enables to adjust the film properties and composition by choosing the right deposition parameters and hence make them convenient for a wide variety of applications.

Optical emission spectroscopy (OES) analysis is relatively simple tool for the investigation of plasma used for the deposition or synthesis. Among others, it can be used for the determination of neutral gastranslational temperature that is one of the important factors of the CVD processes. Hence, the OES together with numerical treatment of measured spectra was applied in this work to determine the gas temperature of different plasma processes.

Description of Plasma Processes Studied

Optical emission spectra were measured in the three types of experiments:

- atmospheric pressure microwave (mw) torch used for the synthesis of carbon nanotubes
- low pressure mw ASTeX-type discharge used for the deposition of ultrananocrystalline diamond (UNCD) films
- low pressure r.f. capacitive discharge used for the deposition of nanocomposite diamond-like carbon films

MW Torch for Synthesis of CNTs

The microwave (mw) plasma torch at atmospheric pressure has been sucessfully used for carbon nanotube (CNT) synthesis[1,2]. The whole experimental set-up (see Fig. 1.) used for the synthesis of CNTs and plasma diagnostics is described below. Microwave power is supplied by a 2.45 GHz, 2 kW generator via a standard rectangular waveguide. At the end of the waveguide there is a broadband transition to a coaxial line realized by means of a ridge waveguide. The inner conductor of the coaxial line is hollow double-walled tube accommodating a dual gas flow. A conical hollow nozzle electrode is fixed to its top. The nozzle is made of iron with a central gas flow channel. A set of holes in the outer tube wall allows for separate gas feeding by an outer channel. The central conductor is held in place by boron nitride ceramics. The outer conductor of the coaxial line is terminated by a flange.

The plasma expands from the central nozzle forming a torch discharge. A quartz tube separates the discharge from surrounding atmosphere. At the bottom it is sealed by a teflon piece to the flange of the outer coaxial conductor. At the top it is closed by an upper flange with an exhaust tube and a sealed feedthrough for a substrate holder. The substrate holder is another quartz tube fixed at the upper flange. This tube is closed at its top by a quartz window. At the opposite side, i.e. close to the discharge nozzle, two slits are cut through the tube. Substrates for the deposition (15×10 mm^2) are inserted into these 1 mm wide slits and pressed down slightly by the weight of a 20 mm piece of a narrower quartz tube.

For the CNT deposition 1,500 sccm of argon was flowing through the centre of the nozzle and an H_2/CH_4 mixture was added from the outer channel. The mw power was fixed at 400 W. The deposition of CNTs was carried out at atmospheric pressure on the silicon substrates (10–15 mm) with silicon oxide layer covered by iron (Fe) catalytic thin film.

The silicon oxide was prepared by PECVD in r.f. capacitively coupled low pressure glow discharge from the hexamethyldisiloxane/oxygen mixture and subsequently annealed at 970 K for 30 min. An iron film, 2.5–1 5 nm in thickness, was vacuum evaporated on the top of the silicon oxide

Optical emission spectra were recorded by means of the Jobin-Yvon TRIAX 320 spectrometer with a fibre optics and CCD detector. The fibre was fixed at different distances from the nozzle along the discharge axis in order to study spatial changes in the plasma emission. The measurement spot integrated by the optics was 10 mm. Appropriately, the spatial profiles were carried out with the same step.

Fig. 1.   **Microwave torch used for synthesis of carbon nanotubes**

Fig. 2.   **Microwave ASTeX-type reactor used for UNCD deposition**

M W   A S T e X - t y p e   D i s c h a r g e   f o r
U N C D   D e p o s i t i o n

The bell-jar microwave plasma CVD reactor for UNCD deposition[3] is shown in Fig. 2. The basic features of this reactor included a 10 cm in diameter silica bell-jar, that confines the plasma discharge, and 5 cm diameter substrate holder. The microwave generator (Muegge) used a magnetron to generate 2.45 GHz microwave radiation that was directed by a rectangular air filled metallic waveguide. A circulator allowed the microwave radiation to travel towards the CVD reaction chamber, but redirected any reflected microwaves into a water-cooled dummy load. In this way, any excess energy was dissipated, thus preventing damage to the magnetron. An antenna coupled the energy from the waveguide into the reactor, which was cylindrical in shape. The position of the plasma ball could be changed by bottom matching piston. The substrate was heated by the discharge.The gas mixture and the pressure range utilized were CH_4/H_2 and 4–25 kPa, respectively. The power range was typically 0.5–2 kW.

Continuous nucleation of diamond nanocrystals was achieved by capacitive coupling of r.f. power (35 W, 13.56 MHz) to the central graphite plate of the substrate holder. The outer graphite ring served as a grounded electrode. Due to different mobility of electrons and ions this resulted in a generation of dc self-bias accelerating the ions across the sheath adjacent to the graphite plate, i. e. to the substrate.

R F   C a p a c i t i v e   D i s c h a r g e   f o r
D e p o s i t i o n   o f   N a n o c o m p o s i t e   D L C
F i l m s

The DLC films with various SiO_x content were prepared in r.f. capacitive discharges at low pressures (8–11 Pa) from a mixture of methane (CH_4) and hexamethyldisiloxane (HMDSO)[4]. This basic mixture was used either without any additional gas or with an admixture of argon, hydrogen or nitrogen. The reactor was a glass cylinder with two inner parallel plate electrodes made of graphite. The bottom electrode, with the diameter of 150 mm, was coupled to the r.f. generator (13.56 MHz) via a blocking capacitor. The substrates (silicon single-crystal, glass, steel and polycarbonate) were placed on the r.f. electrode, the r.f. voltage of which was superimposed with a negative d.c. self-bias. The r.f. power was in the range 50 to 350 W. The corresponding self-bias voltage varied from –250 V to –600 V depending on the gas mixture, applied power and deposition pressure. The CH_4 flow rate was varied in the range from 1.4 sccm to 2.85 sccm. The HMDSO flow rate varied from 0 to 0.87 sccm. The flow rate of admixed gas (Ar, H_2 or N_2) ranged from 0.35 sccm to 7 sccm.

Optical emission spectra were recorded by means of the Jobin-Yvon TRIAX 550 spectrometer. Spectrum of N_2^+ (first negative system) was studied for the determination of rotational temperature.

Calculation of Rotational Temperature from Optical Emission Spectra

We have developed the program DMESS[5] for the determination of rotational temperature of diatomic molecules that is based on the least square method in which the difference between the measured and simulated data is minimized.

Nowadays, the program can be used for following vibrational transitions: N_2^+ (first negative system), CN (violet), N_2 (second positive system) and C_2 (Swan system). The line positions of the molecular spectra are calculated either using equilibrium constants that determine the vibrational and rotational constants for the particular electronic transition or, in case of N_2^+, CN and C_2 molecules, from tabulated spectroscopic constants for each vibrational level. The latter approach allows more accurate determination of the energies, i.e. the line positions, of the specific vibration levels. The intensities are convoluted with Lorentzian, Gaussian or triangular lineshapes. The program uses following fitting parameters: rotational temperature, line broadening, spectral shift of measured data and background intensity. In general, the broadening corresponds to the sum of the broadening determined by the resolution of the spectrometer, i.e. apparatus function, and the broadenings caused by physical processes. Two methods can be used for the fitting of spectra within the program, the Nelder-Mead method (known as downhill simplex method) and the Levenberg-Marquardt algorithm. The fast Nelder-Mead method starts the fitting with the user estimated values of the parameters in order to find approximately the position of the global minimum. Then, the more sophisticated Levenberg-Marquardt algorithm can be used for finding more precise parameter values.

Results and Discussion

For the mw torch discharges the gas temperature in the case of deposition mixtures was estimated as the rotational temperature from the (0,0) rotational emission band of the C_2 Swan system.

Dependence of the rotational temperature on the position of the optical fibre with respect to the nozzle electrode was measured. The calculated rotational temperatures by program DMESS show the increase of temperature approximately to position 10 mm above the nozzle electrode, where is the temperature $4{,}200 \pm 70$ K, and the subsequent decrease, 30 mm above the nozzle temperature is $3{,}100 \pm 70$ K. The comparison of measured and simulated rotational structures of C_2 (0,0) is shown in Fig. 3.
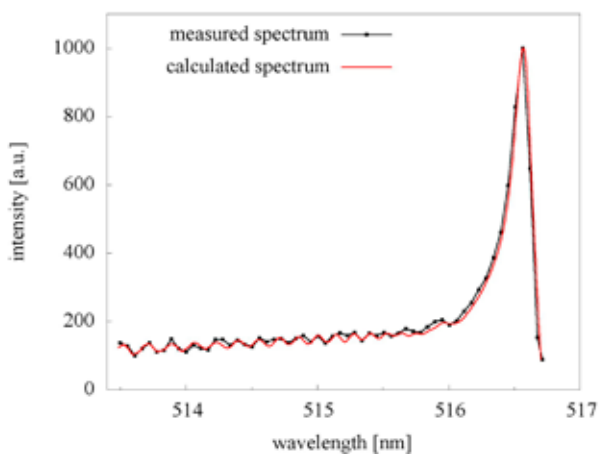

Fig. 4. **A comparison of measured and calculated spectra of C_2 (0,0) Swan system in ASTeX-type discharge used for UNCD deposition. Total line broadening was 0.12 nm**

Similary, for the ASTeX-type discharge the temperature was determined from C_2 (0,0), $T = 2{,}700 \pm 150$ K, but in this case only at one position of optical fibre. The total broadening of spectral lines affected the determination of rotational temperature. The estimated error was higher in less resolved spectrum of ASTeX-type discharge (Fig. 4.) then in micro-
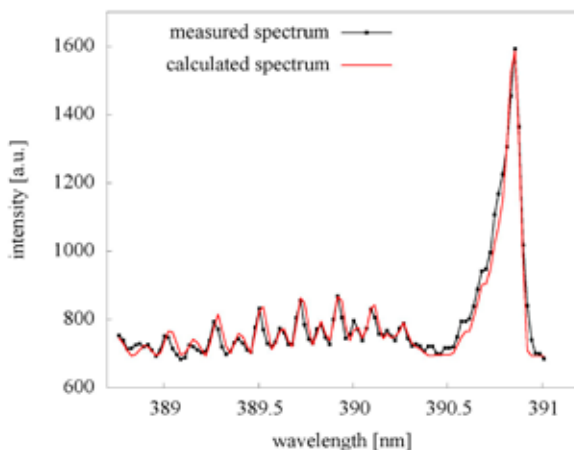

Fig. 3. **Measured spectrum of C_2 (0,0) rotational band of the Swan system is compared with simulation in case of mw torch used for the synthesis of CNTs. The total line broadening was 0.07 nm**

Fig. 5. **A comparison of measured and calculated spectra of N_2^+ (0,0) first negative system in the r.f. capacitive discharge used for deposition of nanocomposite nitrogen-containing DLC films. Ttotal line broadening was 0.06 nm**

wave torch discharge (Fig. 3.). Total broadening in mw torch was about 0.07 nm and in ASTeX-type discharge 0.12 nm.

The rotational temperature in case of r.f. capacitive discharge used for the deposition of nanocomposite DLC films was estimated using the N_2^+ (0,0), first negative system (Fig. 5.) if a small amount of nitrogen was added to HMDSO/CH_4. The calculated temperature was $T = 320 \pm 20$ K, total broadening 0.06 nm.

Conclusions

Rotational temperatures for several types of discharges were determined from optical emission spectra by program DMESS. In the case of mw torch used for synthesis of CNTs and ASTeX-type discharge used for UNCD deposition the temperatures were estimated from the rotational emission band of the C_2 (0,0) Swan system. In the case of r.f. capacitive discharge used for the deposition of nanocomposite nitrogen-containing DLC films the N_2^+ (0,0) first negative system was employed.

REFERENCES

1. Zajíčková L., Eliáš M., Jašek O., Kudrle V., Frgala Z., Matějková J., Buršík J., Kadlečíková M.: Plasma Phys. Control. Fusion *47*, 655 (2005).
2. Jašek O., Eliáš M., Zajíčková L., Kudrle V., Bublan M., Matějková J., Rek A., Buršík J., Kadlečíková M.: Mater. Sci. Eng. C *26*, 1189 (2006).
3. Frgala Z., Jašek O., Karásková M., Zajíčková L., Buršíková V., Franta D., Matějková J., Rek A., Klapetek P., Buršík J.: Czech J. Phys. *56*, 1218 (2006).
4. Buršíková V., Dvořák P., Zajíčková L., Franta D., Janča J., Buršík J., Sobota J., Klapetek P., Bláhová O., Peřina V.: Optoel. Adv. Mater. Comm. *1*, 491 (2007).
5. Lazar L.: *Diploma thesis*. Masaryk University, Brno, Czech Republic, 2005.

P15 EPR STUDY OF NITROXIDE RADICALS GENERATED FROM SOME SECONDARY ALKYL-ARYL AND ARYL-ARYL AMINES

PETR MAJZLÍK[a], LADISLAV OMELKA[a], JAN SVĚTLÍK[b] and PETER RAPTA[c]

[a]*Brno University of Technology, Faculty of Chemistry, Institute of Physical and Applied Chemistry, Purkyňova 464/118, 612 00 Brno, Czech Republic,*
[b]*Faculty of Pharmacy, Department of Pharmaceutical Analysis and Nuclear Pharmacy, Odborárov 10, 835 32 Bratislava, Slovak Republic,*
[c]*Slovak University of Technology, Faculty of Chemical and Food Technology, Department of Physical Chemistry, Radlínského 9, 812 37 Bratislava, Slovak Republic,*
majzlik@fch.vutbr.cz

Introduction

Generally, secondary alkyl-aryl and aryl-aryl amines represent the group of very effective antioxidants. Their action is based on the reaction either with $RO_2^•$ radicals or peroxy compounds, leading to the corresponding nitroxyl radicals[1,2]. By the reaction with peroxides the intermediary formed cation radicals are involved into reaction mechanism[3]. Nitroxyl radicals, generated by both methods can be directly detected by the EPR spectroscopy. In the framework of this paper the radical products of the oxidation of some secondary amines containing one or two -NH- group in the molecule are reported.

Experimental

Within the paper the following secondary amines were studied:
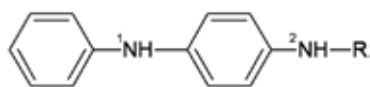
1	
1a	$R = CH(CH_3)_2$
1b	$R = CH(CH_3)-CH_2-CH(CH_3)_2$
1c	$R = CH(CH_3)-C_6H_5$
1d	$R = C_6H_5$
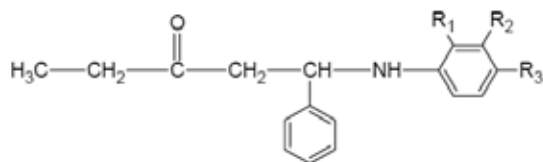
2	
2a	$R_1 = R_2 = R_3 = H$
2b	$R_1 = R_2 = H, R_3 = CH_3$
2c	$R_1 = CH_3, R_2 = R_3 = H$
2d	$R_1 = R_2 = H, R_3 = Cl$
2e	$R_1 = R_3 = H, R_2 = Cl$

### Oxidation of Amines with 3-Chloroperbenzoic Acid

In 10^{-2}M benzene or chloroform solution of 3-chloroperbenzoic acid (3-ClPBA), secondary amines **1**, **2** were dissolved (molar ratio 3-ClPBA: amine = 1 : 1) under stirring for 2 min. 0.5 ml of the solution was placed into the EPR cell and bubbled with nitrogen to remove the dissolved oxygen.

EPR spectra were recorded at the laboratory temperature using an EPR spectrometer SpectraNova. The simulation of the experimental EPR spectra was carried out using the simulation program Simphonia.

Results and Discussion

Within the investigation of antioxidative properties the reaction of amines **1a–1c** with 3-chloroperbenzoic acid was examined. In this way the high concentration of corresponding nitroxile radicals was obtained.

The fundamental problem, accompanying the interpretation of experimental EPR spectra, obtained by the oxidation of **1a–1c** is the attribution of generated nitroxide radicals to the structure **3** or **4** (1).

(1)
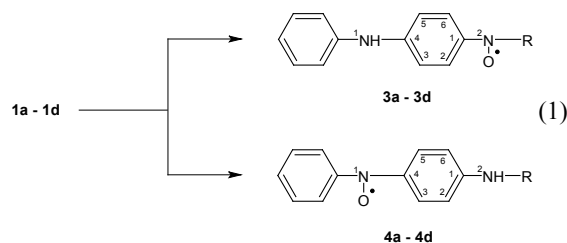
The analysis using spectral simulation has unambiguously shown that the structure **3** is responsible for the nitroxide radicals observed by the oxidation of amines **1a–1b** (structures **3** and **4** are identical in the case of **1d**). This conclusion is supported by the fact that besides the basic nitrogen splitting only the splitting constants from two hydrogen atoms in ortho position of the phenyl ring and one hydrogen atom in $-CH(CH_3)-$ group dominate in EPR spectra of **3a–3b** in benzene solution (Table I). In the case of amine **1c**, containing α-methylbenzyl substituent R, the dependence of the structure of generated nitroxide radical (**3c** *vs.* **4c**) on the solvent is documented. While in benzene the EPR spectrum of **4c** was observed, in chloroform the oxidation evidently proceeds on $-^1NH-$ group, as follows from the splitting constants of **4c**: $a_N(NO) = 1.020$ mT, $5 \times a_H(o,p) = 0.180$ mT, $4 \times a_H(m) = 0.090$ mT, $a_N(NH) = 0.045$ mT.

Characteristic feature of secondary amines **2a–2e** is the presence of only one –NH– group in the molecule. By their oxidation using 3-ClPBA the EPR spectra of generated nitroxyl radicals **5** were registered (2).

(2)

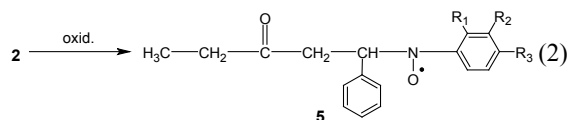Table I

The EPR parameters of nitroxide radicals **3a**–**3d** prepared by the oxidation of amines **1a**–**1d** with 3 chloroperbenzoic acid in benzene (**3a**–**3d**) and chloroform (**3a**–**3b**) solution

Radical	$a_N(NO)$ [mT]	$a_N(NH)$ [mT]	Splitting constants $2a_H(2.6)$ [mT]	$2a_H(3.5)$ [mT]	$a_H(R)$ [mT]	Solvent
3a	1.137	0.045	0.260	0.090	0.316	chloroform
	1.078	–	0.240	–	0.380	benzene
3b	1.127	0.045	0.216	0.085	0.336	chloroform
	1.078	–	0.225	–	0.306	benzene
3c	1.080	–	0.269	–	0.500	benzene
3d[a]	0.960	–	0.182	0.074	0.182 (3H) 0.074 (2H)	benzene

[a]splitting constants taken from ref.[4]

Table II

EPR parameters of nitroxyl radicals **5a**–**5e** generated by the oxidation of secondary amines **2a**–**2e** in toluene solution

Radical	a_N (NO) [mT]	a_H (o,p) [mT]	Splitting constants a_H (m) [mT]	a_H (CH) [mT]	a_H (CH2) [mT]
5a	1.1050	0.2730	0.0900	0.5460	0.0600 (1H) 0.0350 (1H)
5b	1.1225	0.2770 (2H) 0.2970 (3H)	0.0900 0.0350 (1H)	0.5760	0.0600 (1H)
5c	1.2000	0.1500 (2H) 0.1500 (3H)	0.0800	0.4800	–
5d	1.1000	0.2850 (2H) 0.0250 (3H)	0.0950	0.5700	0.0400 (1H) 0.0650 (1H)
5e	1.0500	0.2800	0.0820 (1H)	0.5600	0.0570 (1H) 0.0220 (1H)

In EPR sectrum of **5a**, besides the basic nitrogen splitting, the splittings from protons of phenyl ring and one hydrogen atom of –CH(Ph) were proved. Moreover, the small splitting constants from protons of –CH$_2$– group were extracted. By the introduction of other substituents into *para* and *meta* position of phenyl ring (**2b**, **2d**, **2e**) does not bring any principal changes in spin density distribution. The only exception is represented by the nitroxyl radical **5c**. In this case, very strong *ortho* effect of methyl group, leading to the distortion of the phenyl ring from the plane of –NO˙– fragment is observed. Consequently, the delocalization of spin density into this ring is reduced. The decrease of splitting constants attributed to the protons of phenyl ring is compensated by the increase of basic nitrogen splitting (Table II).

Conclusions

New types of secondary amines were subjected to the oxidation with 3-chloroperbenzoic acid in non-polar sol-

vents. EPR spectroscopy confirmed the formation of nitroxyl radicals, the only radical products observed. Their EPR data were determined using the spectral simulation.

REFERENCES

1. Pospíšil J., Advan. Polym.Sci. *124*, 89 (1995).
2. Thomas J., J. Am. Chem. Soc. *82*, 5955 (1960).
3. Toda T., Mori E., Murayama K., Bull. Chem. Soc. Jpn, *45*, 1904 (1972).
4. Burian M., Omelka L., Ondrášová S., Brezová V., Monatsh. Chem. *134*, 501 (2003).

P16 ROUGHNESS OF PLASMA TREATED PAPERS AND FOILS AND CONDUCTIVITY OF PRINTED STRUCTURE

MILAN MIKULA, ZUZANA POBUDOVÁ and ADAM GILAN

Faculty of Chemical and Food Technology STU, Radlinského 9, 812 37 Bratislava, Slovak Republic, milan.mikula@stuba.sk

Introduction

Printed electronics based on solution-processable organic inks have attracted considerable attention. It has big potential to decrease the cost of electric circuits fabrication, especially when using roll-to-roll printing[1,2]. Principal advantages are mass or large area production, low cost, flexibility of substrates and production variability. Supposed low-cost mass application includes RFID chips, flat OLEDs lightings, flexible displays and solar sells, intelligent packaging and papers etc.

Inkjet printing is applicable to print all required materials (conductors, semiconductors and dielectrics) including OLEDs and TFTs[3,4]. Inkjet was used to print conducting links based on nanosilver colloid[5] and conductive/semiconductive structures based especially on conjugated polymer chain poly(3,4 ethylenedioxythiophene) in complex with poly(styrene sulfonate), PEDOT:PSS, to create conductive links or OLED[6,7]. Conductivity of this system was increased adding organic solvents like dimethyl sulfoxide (DMSO), tetrahydrofuran[8]. The dielectric properties, wetability and roughness of printed substrates are also key parameters of resulted quality.

In this work, N_2 plasma treated coated papers and plastic foils were inkjet printed by water-based PEDOT:PSS and different solvent additives to get high conductivity structures. The influence of substrate roughness, plasma treatment and ink formulation are discussed.

Experimental

Two plastic foils: polyethylenetherephtalate (PET, 120 g m^{-2}) for laser printers and ethylene-tetrafluorethylene copolymer coated by thin 70 nm silicon oxide (ETFE/SiO$_x$, 150 g m^{-2}), and three coated paper sheets: 120 g m^{-2} (glossy varnish, Huber 10L9500, "L1"), 150 g m^{-2} (matt varnish,

Table I
PEDOT ink formulations, η – viscosity, γ – surface energy

PEDOT/ PPS	Water	IPA	DMSO	Designation	η [mPa s^{-1}]	γ [mJ m^{-2}]
1	0	0	0	PEDOT	58.5	68.1
1	0	1/2	+5 %	IPA	–	–
1	1/2	0	+5 %	4 : 2 (5D)	21.1	67.6
1	1/4	1/4	+5 %	4 : 1 : 1 (5D)	17.5	62.4
1	1	1	+5 %	1 : 1 : 1 (5D)	16.5	45.9
1	1/2	0	+10 %	4 : 2 (10D)	20.1	68.4
1	0.3	0	0.2	4 : 1 (15D)	22.4	65.3

Huber 10L9320, "L2") and 120 g m^{-2} copy paper (Xerox Colotech, smooth, white, "CP") were used as substrates for printing.

Standard dielectric barrier discharge (DBD, 15 kV, 5 kHz) was used for plasma treatment of substrates (30 W cm^{-2}) in N_2 at atmospheric pressure (at flow rate of $10 \text{ dm}^3 \text{ min}^{-1}$).

The commercial conductive polymer PEDOT:PSS, 1.3 % wt. in water from Aldrich (hereafter PEDOT) was diluted by water, isopropanol (IPA) or DMSO in several combinations (Table I) and used as ink in inkjet printer EPSON Stylus Photo R360.

Different lines, points and full areas were printed onto all substrates, original and plasma treated, by inkjet printer in slow mode (Fig. 1.).
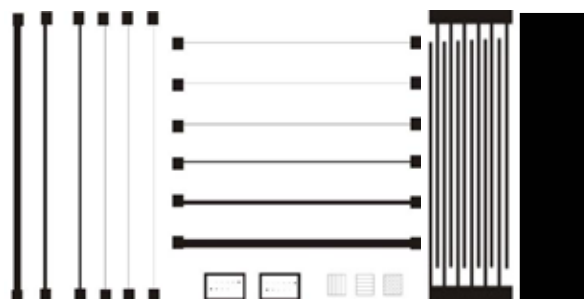

Fig. 1. **Inkjet printed figures**

Ink formulations were characterized by viscosity and surface energy, the substrates by ink wetability and AFM topography including RMS roughness and printed structures by electric conductivity and topography, using the equipments: capillary viscometer UNITEX, contact angle goniometer (SEE, MU Brno), optical and atomic force microscopy CP II, Veeco and LCR Digibridge Quadtech 1715.

Results

Addition of DMSO increased considerably the conductivity of layers (Fig. 2.). Reverse temperature dependences indicate semiconductor character of layers without DMSO and quasi-metal character of layers with DMSO.

Original high viscosity PEDOT could not be inkjet printed. It had to be diluted. Because of high dilution the coatings were very thin, so to get stable results, lines had to be printed several times on each other (more than 4) that caused misregistration problems.

Surface conductivity of printed lines depends on roughness, ink wetability and imbibition. RMS roughness of the substrates are indicated inside the legends of the Fig. 3.a and b. Conductivities on smooth foils are much higher than on papers. Specific conductivity ought to be independent on line thickness, however lines thinner than 0.5 mm are discontinuous.
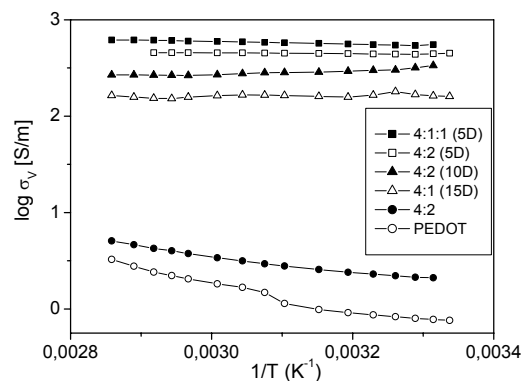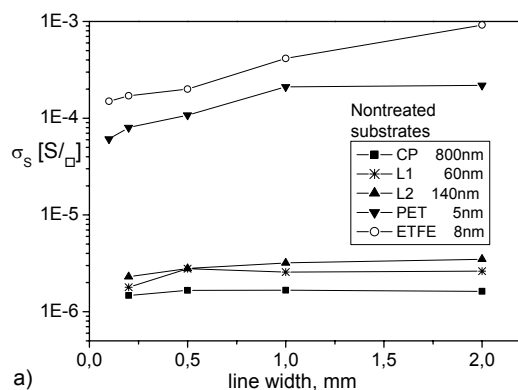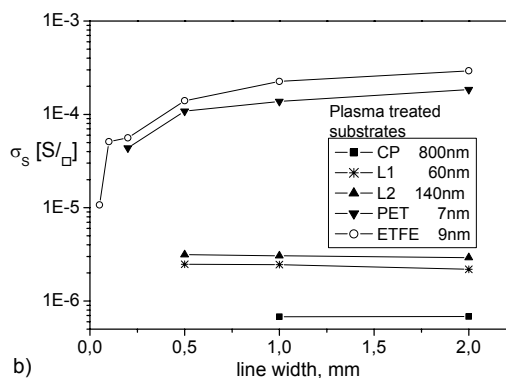
Fig. 2. Specific volume electric conductivity of dry ink layers on clean glass substrates

a)

b)

Fig. 3. Specific surface conductivities of lines 10 times printed by 4:2(5D) ink onto original (a) and plasma treated (b) surfaces

Plasma treatment enhanced the printability of foils (conductivity results were more stable), however it increased the imbibition of copy paper resulting in conductivity decrease (Fig. 3.b).

The ink formulation 4:2 (5D) was found as the most effective considering overall topography and conductivities, but the interval allowed for dilution of PEDOT is narrow so more experiments must be done to find optimal formulation.

Conclusions

Coated and plasma treated papers and plastic foils were inkjet printed by water-based conductive inks (commercial PEDOT:PSS with additives, water, IPA and DMSO.

Addition of DMSO and water improved printability and increased conductivity of lines and full areas. Surface roughness, wetting and imbibition were key factors of features quality.

Sufficient and continuous coating and desired conductivities of lines and areas were achieved just by repeated printing (up to 10 times), so the misregistration was the limiting factor of print quality of lines and dots.

REFERENCES

1. Kallberg E.: *Inteligent Papers*, PhD. thesis, Univ. of Jyvaskyla, Finland, 2006.
2. Mäkelä, T., Jussila, S., Kosonen, H., Bäcklund, T. G., Sandberg, H. G. O., Stubb, H. Synth. Met. *153,* 285 (2005).
3. Yoshioka Y., Jabbour G. E.: *Inkjet Printing and Patterning of PEDOT-PSS*, in Conjugated Polymers, Processing and Application, eds. T. A. Skotheim, J. Reynolds, CRC Press 2006.
4. Svanholm E.: *Printability and Ink-Coating Interactions in Inkjet Printing,* PhD. thesis, Fac. of Technology and Science, Karlstad Univ. 2007, Sweden.
5. Lee H. H., Chou K. S. and Huang K.C. Nanatechnol. *16,* 2436 (2005).
6. Soltman D., Subramanian V.: Langmuir *24*, 2224 (2008).
7. Zmeškal O., Veselý M., Martin V., Bednář P., Bžatek T.: Proc. 8th Seminar in Graphic Arts, Sept.07, Pardubice, Czech Rep., . 131-7, Univ. Pardubice 2007.
8. Kim J.Y., Jung J.H., Lee D.E. Joo J. Synth. Met. *126,* 311 (2002).

P17　INFLUENCE OF DYE STRUCTURE ON ITS DECOMPOSITION BY ELECTRIC DISCHARGE IN WATER SOLUTIONS

JANA PAJURKOVÁ, ZDENKA STARÁ and FRANTIŠEK KRČMA

Brno University of Technology, Faculty of Chemistry, Purkyňova 118, 612 00 Brno, Czech Republic,
xcpajurkova@fch.vutbr.cz

Introduction

During last ten years, electrical discharges generated in water have been widely studied with a great focus on the application in water treatment. Besides classical biological, physical and chemical methods, so-called Advanced Oxidation Processes (AOP's) have been applied in removal of various pollutants. Especially degradation of phenol and some organic dyes by pulsed discharges in point-to-plane geometry have been studied by many authors, for example refs.[1–3].

Applying high energy field into water solution, various physical and chemical processes are initiated. Generation of UV light and shock waves belong to the physical processes while formation of various reactive species is the most important chemical phenomenon. Especially radicals ($\cdot$OH, $\cdot$H, $\cdot$O), ions (O_2^-) and molecules (H_2O_2) are responsible for chemical reactions and degradation processes in water treatment. As these species have high oxidation potential they can very easily attack other molecules contained in water and caused their decomposition.

Diaphragm discharge presented in this paper belongs to the discharge configurations suitable for the purpose of water treatment, too. Its generation starts in the small orifice in the dielectric barrier separating two electrode spaces. If DC high voltage is applied, different kinds of plasma channels propagate from the orifice towards electrodes. Diversity of streamers is not only in their shape but mainly in their energy dissipation substantially influencing subsequent processes in water solution[4].

This paper presents results obtained from the treatment of solutions containing selected organic dyes. Decomposition of these model compounds was investigated from the viewpoint of diaphragm discharge conditions (electrode polarity, input power) as well as of the dye molecular structure.

Experimental

Diaphragm discharge studied in this work was generated in a batch reactor[4] using constant high voltage from the DC source that gave the input power up to 250 W (see Fig. 1.). Two planar electrodes made of stainless steel were separated by the dielectric barrier. Both electrode spaces were connected by only a small pin-hole (initial diameter of 0.25 mm) in this diaphragm. Discharge breakdown appeared just in this orifice and plasma channels propagated from this spot towards electrodes.

Each part of the reactor contained 2 litres of treated solution. Water solutions contained selected dye (initial concent-

Fig. 1. **Photograph of diaphragm discharge reactor used for decomposition of organic dyes dissolved in water**

Table I
List of used organic dyes and their characteristics

Dye	Molecular weight [g mol^{-1}]	Characteristic absorption wavelength [nm]
Direct Red 79	1,048.872	508
Direct Blue 106	741.487	608
Acid Yellow 23	534.366	428
Acid Blue 74	466.350	596

ration of ca 20 mg dm^{-3}) and a definite amount of supported electrolyte providing particular solution conductivity (initial value of 400 µS cm^{-1}). In this study, NaCl electrolyte was used for all experiments (concentration of 4 mmol dm^{-3}). Solution pH was primary adjusted by the electrolyte kind (approximately neutral in NaCl) and it was not specially modified during the experiment. Selected dyes belonged mostly to the group of azo-dyes and they could have been classified into Direct and Acid dyes. From the first group, Direct Red 79 (DR79) and Direct Blue 106 (DB106) were decomposed while Acid Yellow 23 (AY23) and Acid Blue 74 (AB74) were chosen from the second group. Their structural formulas are given below. Samples of treated solution were taken away from both electrode spaces every 5 minute and total treatment time was 40 minutes. Estimation of dye concentration was carried out by absorption spectroscopy (spectrometer Helios alfa) in the visible region (300–700 nm). Dye concentration was determined from the absorption intensity obtained at wavelength characteristic for each dye (see Table I). Decomposition rate α was calculated from the relative concentration decrease for each dye:
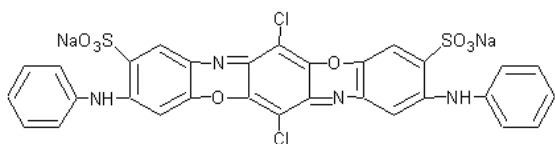
$$\alpha = \frac{c_0 - c}{c_0} \tag{1}$$

where c_0 means initial dye concentration and c is dye concentration determined during the treatment.

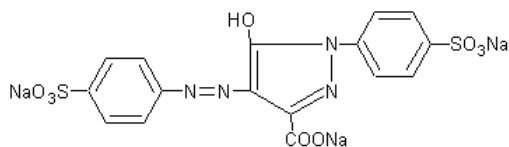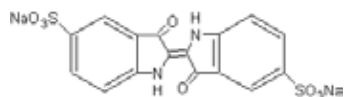Structural formulas of selected organic dyes are as follows:

Direct Red 79
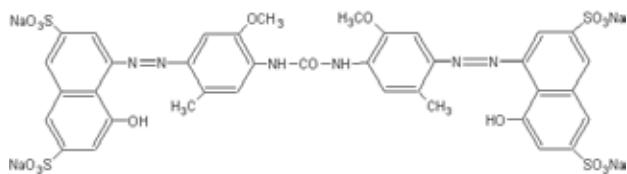
Direct Blue 106

Acid Yellow 23

Acid Blue 74

Results

General Aspects of Dye Decomposition

Decomposition of all tested dyes was observed in both electrode spaces of the discharge reactor. However, removal efficiency was significantly higher in the anode space. Fig. 2. demonstrates results obtained in DB106 solution. Relative dye concentration exponentially decreased in the anode space and reached the value of less than 40 % of the initial DB106 concentration. In the cathode space, decoloration went slowly and almost linearly and final concentration dropped just below 90 %, only. Possible reasons of diverse process evaluation were assumed to be the different shape of plasma streamers (influencing different volume of treated liquid) and substantial effect of electrochemical reactions on the anode due to the application of constant DC high voltage on the electrodes[4]. Moreover, significant change of solution pH was observed during the discharge in both electrode spaces. While in the cathode space pH increased from initially neutral values of NaCl electrolyte to basic medium, situation in the anode space evaluated on the contrary, e.g. to the lower pH values and therefore remarkably acidic conditions. We expect that stronger acidic medium stimulated the degradation process of treated dyes[4]. However, clarifying of this phenomenon will be an object of our further study.

Analyses of treated dye solutions were carried out by absorption spectroscopy over visible region and recorded
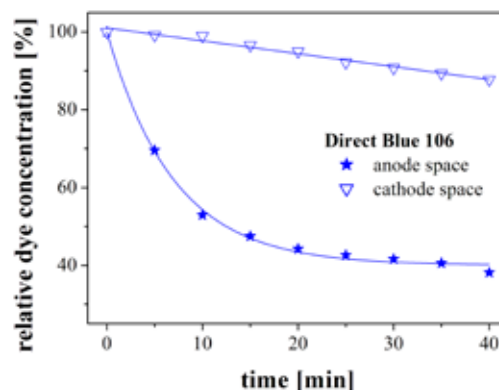

Fig. 2.　**Direct Blue 106 decomposition represented by relative concentration during the diaphragm discharge in the anode and cathode space (input power of 170 W, 4mM NaCl solution)**
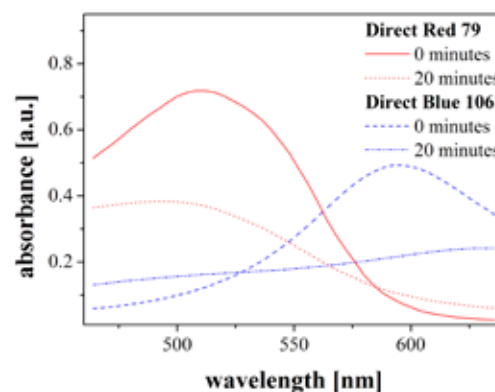

Fig. 3.　**Absorption spectra of two dyes (DR79 and DB106) before and after 20 minutes in diaphragm discharge (anode space, input power of 170 W, 4mM NaCl solution)**

spectra were compared with original non-treated samples. Fig. 3. compares spectra obtained for two azo-dyes (DR79 and DB106) before and after 20 minutes of discharge treatment in the anode space. Besides remarkable decrease of absorption intensity at characteristic wavelength, certain shift of maximal absorption position could be seen. In the case of the red dye (DR79), this shift directed to shorter wavelengths while in the blue dye (DB106) the position of maximal absorption indicated its movement to longer wavelengths. We have assumed that origin of the shift in absorption came from the formation of various by-products when dye molecule was decomposed and these compounds absorbed radiation of slightly different wavelength than the original dye molecule. Determination of final products and by-products is an object of our intensive research.

Influence of Dye Structure

Effect of different molecule structure on the dye decolorization was studied for two compounds belonging to the group of Direct dyes (DR79 and DB106) and for two Acid dyes (AY23 and AB74). Evaluations of decomposition rates
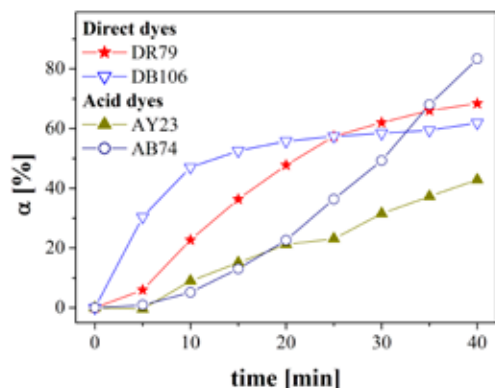
Fig. 4. **Comparison of decomposition rates obtained during diaphragm discharge in the anode space for selected dyes: Direct Red 79, Direct Blue 106, Acid Yellow 23 and Acid Blue 74 (input power of 170 W, 4mM NaCl solution)**
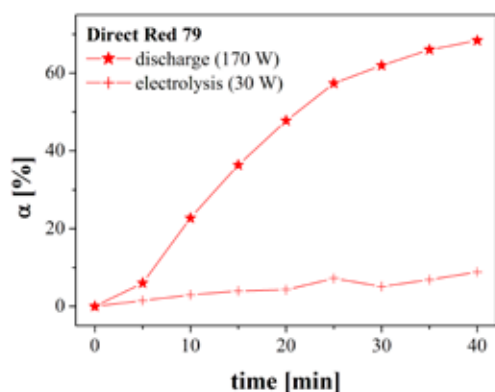

Fig. 5. **Comparison of DR79 decomposition rates obtained during diaphragm discharge (input power of 170 W) and pure electrolysis (30 W) in the anode space (4mM NaCl solution)**

determined during diaphragm discharge in the anode space are shown in Fig. 4. It was observed that removal process in direct dyes had exponential evaluation while it was linear in acid dyes. Moreover, exponential decolorization of direct dyes revealed particular residual concentration of decomposed dye. The best removal efficiency after 40 minutes of the treatment was achieved in AB74 dye (more than 80 %) which structure was on an indigoid base. The other dyes containing azo groups reached 60 % (DR79, DB106) or hardly 40 % (AY23), respectively.

Obtained results were probably caused by different mechanism of ·OH attack (or ·Cl radical coming from supported electrolyte NaCl) on the particular dye molecule, according to its size, number and kind of substitutes (see molecular structures in Experimental). The first impact of radical probably led on the azo-bond –N=N– when azo-dye is decomposed. Subsequently, this bond breaks and nitrogen is released. This reaction should be fast and its effect could explain the rapid decrease of DB106 or DR79 concenration at the beginning of the experiment.

Concerning different dye structure, molecules of acid dyes are smaller (with molecular weigth until ca 600 g·mol^{-1}) and contain lower amount of substitutes than direct dyes. Higher number of substitutes is one of the factors influencing final dye colour. Direct dyes containing more of such functional groups can be attack by active radicals from the discharge in these spots and their detachment can lead to faster decoloration of direct dyes.

On the other hand, indigo molecule (AB74) is relatively small with no substantial substitutes. And moreover, it does not contain an azo-group in its chain. Thus the degradation mechanism probably runs by different reactions and it depends on moment when the aromatic ring is finally opened.

Influence of Input Power and Electrochemical Aspects

Firstly, influence of input power applied from the DC source into the reactor on dye removal was studied for four different power magnitudes (65, 100, 130 and 170 W). From the comparison of DB106 decomposition rates obtained in both electrode spaces it was determined that increasing input power enhanced dye decomposition. Effect of power was more or less linear and with the same intensity in both electrode spaces.

More interesting results were achieved when dye decomposition by diaphragm discharge was compared with dye removal by pure electrolysis. We included this experiment into our study because we had expected a substantial effect of electrochemical reactions due to the application of constant voltage. In such case, especially electrochemical oxidation on the anode takes place and thus this reaction can be one of the factors leading to the dye decomposition.

Effect of electrolytical degradation was studied in the similar device consiting of dielectric diaphragm with one pin-hole (initial diameter of 0.25 mm), stainless steel electrodes on each side and containing electrolyte solution (NaCl) of total volume of 3 litres. Constant voltage from the same DC source was applied on the electrodes. Its magnitude was adjusted on the level at which only electrolysis was kept in the reactor and the discharge was not created in the pin-hole. In that case, total power supplied into the reactor was 30 W (compared to 170 W applied during the discharge). Next procedure was carried out in the same way as the dye degradation by the diaphragm discharge.

Two dyes were selected for the comparison of degradation effect of the discharge and pure electrolysis – Direct Red 79 and Direct Blue 106. Obtained results represented as the evaluation of decomposition rates are demonstrated in Figs. 5. (for DR79) and 6. (for DB106), respectively. Results were achieved in the anode space of the reactor.

Comparison of electrolytic effect during treatment of two dyes surprisingly revealed contrary results. In DR79 solution, electrolysis had only a weak effect on the dye removal. On the other hand, DB106 dye was decomposed by both discharge and electrolysis with almost the same effect (more than 50 % of the initial dye was removed). Based on these
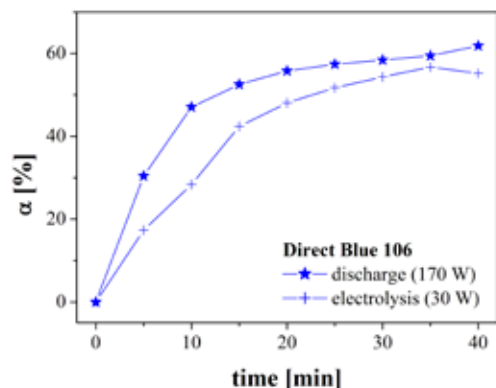
Fig. 6. **Comparison of DB106 decomposition rates obtained during diaphragm discharge (input power of 170 W) and pure electrolysis (30 W) in the anode space (4mM NaCl solution)**

results we have assumed different degradation mechanism of both dye molecules.

To compare energetic efficiency of the discharge and electrolytic treatment in the relevant criterion, efficiency η was calculated according to the following formula:

$$\eta = \frac{RDR \cdot V}{60 \cdot P} \cdot 3,600,000 , \qquad (2)$$

where RDR means the rate of dye removal in $mg\,dm^{-3}\,min^{-1}$, V is volume of the treated solution in dm^3 and P is input power in Watts (170 W for the discharge, 30 W for the electrolysis). Subsequently, efficiency was obtained in $mg\,kWh^{-1}$ and it represented amount of decomposed dye (in mg) per an energetic unit. Calculated efficiency values are given in Table II for both treated dyes.

Concerning DR79, calculated results confirmed remarkably higher efficiency when the dye was decomposed by the discharge. On the other hand, destruction of DB106 showed much higher efficiency of electrolysis (almost $1.7\,g\,kWh^{-1}$) because substantially lower power was needed for the same decomposition rate as in the discharge. We can assume that for removal of relatively larger molecules like DR79 substantially higher power is necessary to be applied while for destruction of simple molecule (DB106), electrolytic reactions initiated by lower power are sufficient.

Conclusions

Water solutions of selected organic dyes from two specific groups (Direct and Acid) were treated by diaphragm discharge generated using constant DC high voltage. Discharge reactor was divided by the dielectric barrier into two electrode spaces and the discharge itself was created in the small orifice in this barrier. Decrease of dye concentration was observed in both electrode spaces by the absorption

Table II
Energetic efficiency of dye decomposition by diaphragm discharge and electrolysis

Dye	Efficiency of diaphragm discharge – anode space $[mg\,kWh^{-1}]$	Efficiency of electrolysis – anode space $[mg\,kWh^{-1}]$
Direct Red 79	644	236
Direct Blue 106	477	1,686

spectroscopy. Study of dye removal as a function of discharge conditions gave following conclusions:

- All tested dyes were decomposed with significantly higher efficiency in the anode space than in the cathode one. The explanation could be in the different kinetic energy of electrons in plasma channels on both sides of the diaphragm as well as in the acidic conditions forming in the anode space during the discharge.
- Absorption spectra of treated solutions were recorded over the visible region. Besides decreasing absorption intensity, a remarkable shift of the position of maximal absorption was observed. Moreover, this shift was different for tested dyes. This phenomenon was probably caused by the formation of various by-products during the dye decomposition.
- Comparing molecular structure of selected dyes, significant influence of molecule size and degree of substitution was assumed as the main reason of different evaluation of dye decomposition by the diaphragm discharge.
- Increasing input power more or less linearly enhanced degradation process in both electrode spaces.

Substantial effect of electrolysis was observed during decomposition of DB106 while this effect was only negligible in DR79. Higher energetic efficiency was achieved by electrolysis in DB106 removal ($1.7\,g\,kWh^{-1}$).

REFERENCES

1. Sun B., Sato M., Clements J.S.: Environ. Sci. Technol. *34*, 509 (2000).
2. Lukeš P., Člupek M., Šunka P., Peterka F., Sano T., Negishi N., Matsuzawa S., Takeuchi K.: Res. Chem. Intermed. *31*, 285 (2005).
3. Njatawidjaja E., Sugiarto A.T., Ohsima T., Sato M.: J. Electrostatics *63*, 353 (2005).
4. Stará Z., Krčma F., Nejezchleb M., Skalný J.D.: J. Adv. Oxid. Technol. *11*, 155 (2008).

P18   NEUTRALIZATION OF MODELS OF HISTORICAL DOCUMENTS WITH MMMK

MIROSLAVA PETROVIČOVÁ[a], HANA PAULUSOVÁ[b], MICHAL ĎUROVIČ[b] and BOHUSLAVA HAVLÍNOVÁ[a]

[a]*Department of Printing Arts Technology and Photochemistry IPM of Chemical and Food Technology SUT,Radlinského 9, 812 37 Bratislava, Slovak Republic,*
[b]*National Archive in Prague, Archivní 4, 149 01 Prague 4, Czech Republic,*
miroslava.petrovicova@stuba.sk

Introduction

The corrosion of iron-gall inks is a result of their composition and is represented by two main degradation processes. On one hand, it is the hydrolytic decomposition of the paper support catalysed by acids which were added to inks during their preparation or released by a chemical reaction in the course of formation of ink colour component. The other mechanism of paper support degradation is cellulose oxidation catalysed by transitional metals, presented in iron-gall inks (Fe, Cu). Because of the presence of reductive substances, the ink lines contain ferrous ions even after centuries[2].

In the world several deacidification methods are used. These methods can be classified into water-based and non-aqueous processes. These processes make use of different combination of solvents, and they are suitable for different types of paper[1].

This work deals with the application of neutralization reagent MMMK (Methoxy magnesium methyl carbonate) and also antioxidant BHT 2,6-ditercbutyl-4-methylphenol on documents containing iron-gall inks and its influence on document properties after stabilization.

MMMK belongs to compounds suitable for deacidification of heavily damaged manuscripts. MMMK doesn't wash out iron-gall inks from substrate hence ink fixation isn't needed prior to its application.

MMMK is an organo-metallic compound which is used as a deacidification agent at Wei T'O non-aqueous process of book deacidification. It is possible to place magnesium in this form into paper structure using non-aqueous system from fluid gas[3].

BHT belongs to the group of synthetic antioxidants produced commercially, and it is also present as a natural substance in plants, e.g. in rosemary. BHT is a white powder that is used in the food industry, pharmacology, medicine for its anti-cancer effect and it is also known in the rubber industry. BHT belongs to the group of sterically hindered phenols and it had been recently introduced as a paper stabilization agent. Its effect as "chain-breaking" antioxidant is presented by deactivation of alkylperoxyle radicals[2,4].

Experimental

The experiments were performed on paper substrate using whatman No. 1 (Cat. No. 10001917) filter paper. This paper represented pure cellulose paper without any additi-

ves. The set of the paper squares (8 × 12 cm) was immersed in a 1% gelatine solution and 5% solution of aluminium sulphate for 5 minutes.

The iron-gall ink was composed of $FeSO_4 \cdot 7H_2O$, tannin acid and gum Arabic, resulting in a molar ratio of iron and tannin acid was 5.5 : 1.

These samples were placed into a climatic chamber for 3 hours at 50 °C, and then samples were immersed in 6% solution of methoxy magnesium methyl carbonate.

Antioxidant BHT was prepared in two concentrations (0.1% and 0.01% solution in ethanol), and samples were immersed in these solutions for 10 seconds.

One part of the samples was artificially aged in an OMT OVEN for 1 day to 24 days at 80 °C and 50 % RH. Second part of the samples was aged in the chamber APT Line Series FED for 1day to 24 days at 105 °C.

The folding endurance of paper was determined using normalized folding endurance tester Schopper according to standard ISO 5626 for the folding endurance of paper.

The changes in chemical structure of iron gall ink and iron gall ink with neutralization reagent MMMK during artificially aged was estimated by FTIR spectroscopy. FTIR spectra were recorded on a spectrophotometer Excalibur Series using transmission method by KBr pellet.

Results and Discussion

M e c h a n i c a l   T e s t

Inked samples showed low mechanical paper properties affected by artificial ageing in both cases – dry and wet ageing. Deacidification of inked samples caused retardation in decrease of mechanical properties (Figs. 1., 2.) hence it was possible to assume that also degradation of cellulose was decelerated.

In Fig. 1. obvious increase in folding endurance from 0 to 65 after neutralization of inked samples with MMMK solution was observed. However after 3 days this value decreased rapidly. Antioxidant BHT improved mechanical properties
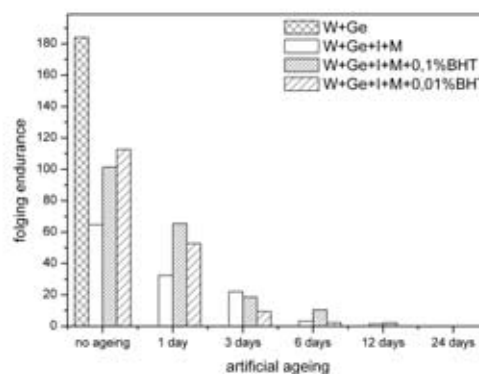

Fig. 1.   **Changes of folding endurance during artificially ageing at 80 °C and 50 % RH. (W + Ge-Whatman paper modified with gelatine and sulphate, I-application of iron gall ink, M-treatment with neutralization reagent MMMK, BHT-treatment with BHT antioxidant)**
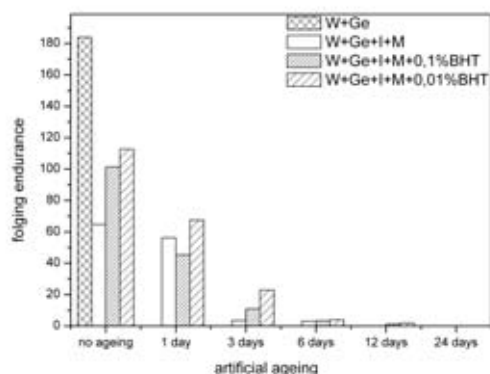
Fig. 2. **Changes of folding endurance during artificially ageing at 105 °C. (W + Ge-Whatman paper modified with gelatine and sulphate, I-application of iron gall ink, M-treatment with neutralization reagent MMMK, BHT-treatment with BHT antioxidant)**

only for unaged samples and samples 1 day aged. If we compared the sample without neutralization and antioxidant (that means only inked paper substrate) with 0 folding endurance even at the beginning, after neutralization with MMMK solution and subsequent stabilization with BHT antioxidant sample remained minimal mechanical properties even after 12 days of artificial ageing.

F T I R   M e a s u r e m e n t s

Fig. 3. represented comparison of FTIR spectra unaged ink and unaged neutralized ink measured in pellet. Ink neutralization with 6% solution of MMMK caused peak decrease at 1,093 cm^{-1} which is characteristic for C-O bond. Next change caused by ink neutralization was formation of new peak at 1,429 cm^{-1} which belongs to vibration of magnesium carbonate.
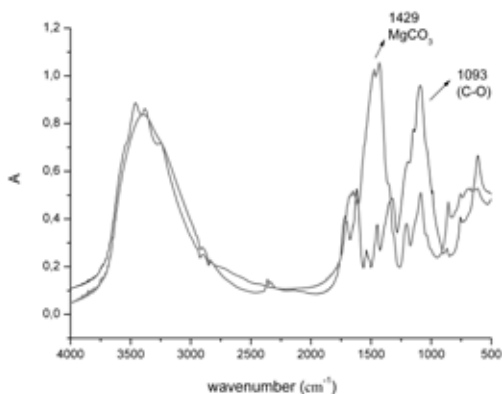

Fig. 3. **FTIR spectra of iron gall ink (black line) and iron gall ink with MMMK (gray line) in pellet**

Magnesium carbonate forms alkaline reserve in deacidified paper just because alkaline reserve is important from the
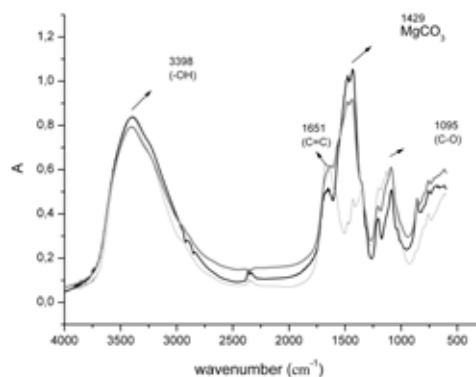

Fig. 4. **FTIR spectra of iron gall ink with MMMK in pellet. Black line: no ageing, gray line: aged 3 days, light gray line: aged 12 days**

viewpoint of paper substrate stabilization, the peak characteristic for magnesium carbonate during ageing was observed. Fig. 4. demonstrated decrease of peak relating to vibration of magnesium carbonate (1,429 cm^{-1}) after 3 days of ageing.

FTIR spectra in Fig. 4. showed that after 12 days of ageing peak at 1,429 cm^{-1} vanished and we assumed depletion of alkaline reserve.

Conclusion

The obtained experimental results showed that neutralization of inked samples with 6% solution of methoxy magnesium methyl carbonatu (MMMK) caused considerable improvement of optical and mechemical properties for unaged and aged inked samples. FTIR measurements confirmed the formation of alkaline reserve in neutralized ink. According to these results we could support stabilizing effect of paper neutralization with MMMK solution. However this alkaline reserve after 12 days of artificial ageing exhausted. Subsequent usage of antioxidant 2,6-ditercbutyl-4-4methylphenolu (BHT) for neutralized samples improved studied properties of unaged paper samples, nevertheless after artificial ageing stabilization effect of antioxidant wasn't approved.

REFERENCES

1. Ďurovič M.: *Research reports*. National Archive, Prague, 2000.
2. Havlínová B., Mináriková J., Hanus J., Janočovičová V., Szabóová Z. Restaurator *28*, 112 (2007).
3. Paulusová H., Novotná M.: X. Seminář restaurátorů a historiků, Litomyšl *1997*, 222.
4. Strlič M., Kolar J., Malešič J.: National and University Library, Ljubljana *2005*, 181.

P19 INFLUENCE OF BOOKSAVER DEACIDIFICATION PROCESS ON STABILITY OF ARYLMETHANE DYES ON PAPER.

BOHUSLAVA HAVLÍNOVÁ[a], MICHAL ĎUROVIČ[b], VIERA JANČOVIČOVÁ[a] and MIROSLAVA PETROVIČOVÁ[a]

[a]*Department of Printing Arts Technology and Photochemistry IPM, Faculty of Chemical and Food Technology SUT, Radlinského 9, 812 37,Bratislava, Slovak Republic,* [b]*National Archive in Prague, Archivní 4, 149 01 Prague 4, Czech Republic,*
miroslava.petrovicova@stuba.sk

Introduction

Even after long period of time historical documents should have the ability to list in, read or possibly interpose other type of cultural experience. For population it is important for its irreplaceableness, uniqueness and attractiveness of literary works, manuscripts or paintings. Thanks to these works our history, customs and thinking could be kept. In presence problems with preservation and conservation methods of cultureal heritage have occurred[1].

Big amount of materials written in last 130 years on acid wooden papers have suffered with continuous damage process which can lead to total lost of printed or written text. The reason for this is the instability of paper substrate and meantime low chemical and light stability of dyes which represent the main component of modern inks. The most proper method against destruction of paper substrate appears to be neutralization hence formation of sufficient alkaline reserve preserving paper during ageing against acid products formed by oxidation and followed by fibre decomposition. Various deacidification methods based on waterborne and non-aqueous treatments have been developed that utilize different solvents and their combinations convenient for different types of papers.

Increase in pH value of paper substrate extends the lifetime but can damage written records mainly at unsuitable climatic conditions at deposit. The aim of this study was to investigate the influence of relative humidity and pH of paper substrate on dyes. For deacidifacation process non-aqueous deacidification was used hence no fixation was necessary[2,3].

Experimental

In this work acid, partially wooden paper with no fillers, sizes nor optical brightening agent made in Slavošovské papierne was used. Part of samples was prepared on original (acid) paper and other part on neutralized paper deacidified by Booksaver PAL method in Preservation Academy in Leipzig. Its initial properties and properties after deacidification process are listed in Table I. Samples 5×5 cm were prepared from unmodified acid paper and also from deacidified paper substrate and were treated with several dye solutions.
- Several dyes for treatment were prepared: Acid Green and Basic Red – 0.1% solutions in ethanol and Methy-

Table I
Initial properties and properties after deacidification process of paper

Property	Acid paper	Paper after deacidification
Brightness [%]	76.40	74.37
Opacity [%]	96.70	97.12
CIE L*	91.14	94.80
CIE a*	−1.07	−0.70
CIE b*	3.41	2.04
pH	4.40	6.94
Alkaline reserve [%]	–	0.67

lene Blue – 0.2% solution in ethanol and water (1:1). Papers were treated with 1 ml of prepared dyes solutions and dried out on air.
- Prepared samples were treated by wet accelerated ageing in climatic chamber SANYO Gallenkamp PLC (Great Britain) at 80 °C and 3 different values of RH: 65%, 50% and 40% for 0, 1, 3, 7, 10, 18 a 30 days.

Non-aqueous deacidification (CSC) Book Saver is a method which uses carbonated magnesium propylate dissolved in n-propanol as a neutralize agent and as a carrier
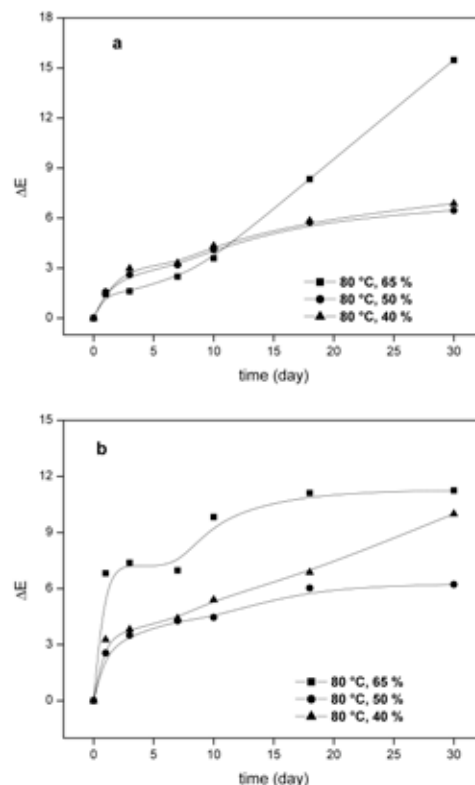

Fig. 1. **Comparison of 3 dependeces of ΔE* of Acid Green dye on 3 different types of ageing; (a) – layered on acid paper substrat, (b) – layered on deacidified paper substrate**
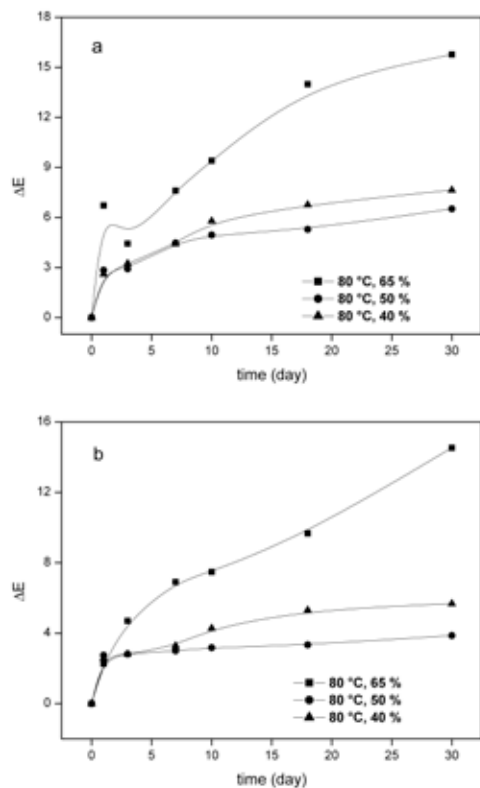
Fig. 2.   Comparison of 3 dependeces of ΔE* of Methylene Blue dye on 3 different types of ageing; (a) – layered on acid paper substrate, (b) – layered on deacidified paper substrate

is 1,1,1,2,3,3,3- heptafluoropropane (HFC 227) chosen for both mass and individual deacidification and is supplied as a spray.

Carbonated magnesium propylate is soluble in non-aqueous n-propanol and solution contains approximately 32 % of carbonate and 68 % of propanol. The composition of deacidification solutiou is: 1.06 kg of carbonated magnesium propylate, 2.25 kg of n-propanol and 190 kg of HFC 227. Neutralization agent further reacts with moisture in paper and produce alkaline reserve in the form of alkaline magnesium carbonate.

Documents were frozen to –20 °C prior to treatment. This method is convenient also for sensitive materials (parchment, leather and moreover immobilize soluble dyes and inks.

The properties of the paper samples were measured according to the Slovak Technical Standards (STN) and STN ISO Standards.

Results

Fig. 1.a showed that the lowest value of colour difference for sample Acid Green 16 on acid paper substrate was in the case of wet ageing at conditions of RH 50 % (6.46), 40 % (6.87) however for RH 65 % it was 15.48. This could be explained by axis a^* which moved by $\Delta a^* = 12.97$ from negative to zero area that means from green to grey. Fig. 1b represented Acid Green 16 on neutralized paper and the least
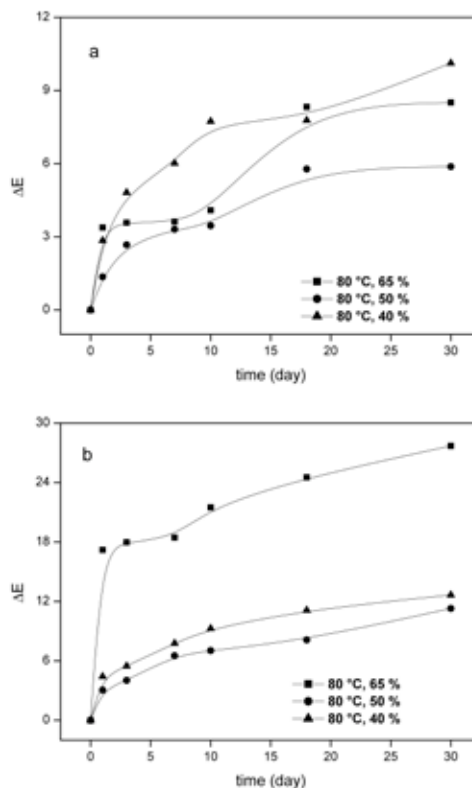
Fig. 3.   Comparison of 3 dependeces of ΔE* of Basic Red 9 dye on 3 different types of ageing; (a) – layered on acid paper substrate, (b) – layered on deacidified paper substrate

noticeable influence on ΔE^* colour difference had ageing at 50% RH (6.22) and for other 2 ageing types final colour difference value was measured 2 times higher.

Fig. 2.a represented Methylene Blue on acid paper substrate and the highest value of colour difference ΔE^* was monitored for wet ageing with RH 65 % (15.77). The most considerable influence on total value of ΔE^* showed axis L^* and b^* that represented significant bleaching of samples and shift of blue colour shade to grey. For ageing at RH 50 % and 40 % much lower values of ΔE^* were measured exactly $\Delta E^* = 6.52$ and $\Delta E^* = 7.64$. Similar behavior was noticed also for Methylene Blue on neutralized paper sample but after ageing the values of ΔE^* were lower (Fig. 2.b). For RH 65 % maximum value of ΔE^* was 14.53, for RH 50 % was ΔE^* 3.87 and for 40 % ΔE^* 5.68.

Fig. 3.a monitored the influence of particular ageing condition on Basic Red 9 dye layered on acid paper. The highest value of colour difference ΔE^* was measured for ageing at RH 40 % ($\Delta E^* = 10.13$) and for RH 65 % ΔE^* 8.51. The lowest value of $\Delta E^* = 5.88$ was obtained at RH 50 %. The sample Basic Red 9 layered on neutralized paper (Fig. 3.b) showed less stability compared to sample layered on acid paper. The most obvious instability was noticed for ageing at RH 65% where ΔE^* was 27.71 which represented the highest value for colour difference. The biggest contribution on total

value of colour difference had the colour axis $a^*(\Delta a^* = 26.88)$ that moved from positive value to zero which means shift from red to grey colour. For ageing condition RH 40 % and 50 % the lowest values of colour difference ($\Delta E^* = 12.66$ and 11.29) were measured.

Conclusions

This study investigated the influence of relative humidity (40 %, 50 % a 65 % at 80 °C) and pH (acid and deacidified paper substrate) on optical properties of several arylmethane dyes (acid Acid Green 16 and alkaline Methylene Blue and Basic Red 9. ΔE^* caused by ageing was measured. The stability of arylmethane dyes on acid and deacidified paper with Booksaver method was compared.

Comparison of optical properties of acid and alkaline dye pigments showed higher stability of acid dye Acid Green 16 layered on acid as well as deacidified substrates. Lower values of RH (40–50 %) caused higher light stability and

ageing at 65 % RH influenced optical properties the most negatively. Deacidification of paper improved optical properties for all 3 types of ageing and dyes particularly Methylene Blue. However even after deacidification ageing at lower RH (40–50%) showed more sufficient.

REFERENCES
1. Zollinger H.: *Color chemistry*, Weinheim. 1991.
2. Havlínová B., Mináriková J., Švorcová L., Hanus J., Brezová V.: Restaurator *16*, 1 (2005).
3. Lewis M. L., Indig G. L.: Dyes Pigm. *46*, 145 (2000).

P20　EFFECT OF ACCELERATED AGEING PROPERTIES OF PARCHMENT

BOHUSLAVA HAVLÍNOVÁ[a], MARTINA OHLÍDALOVÁ[b], MIROSLAVA PETROVIČOVÁ[a] and BOŽENA MARUŠICOVÁ[a]

[a]*Department of Printing Arts Technology and Photochemistry IPM of Chemical and Food Technology SUT, Radlinského 9, 812 37 Bratislava, Slovak Republic,*
[b]*Institute of Chemical Technology Prague, Technická 3, 166 28 Prague 6, Czech Republic,*
miroslava.petrovicova@stuba.sk

Introduction

Parchment is a specially treated form of leather that is soft and durable, making it an excellent writing material. High quality parchment is sometimes referred to as vellum. It is known that parchment was as a writing material as early as the Ptolemaic era, and it was in fact preferred over papyrus in northern regions, where the climate can be unfavorable for papyrus, and also in Near Estern regions. Parchment as a writing material antedates aper by possibly 1500 years, although the name is derived from Pergamum, an ancient city in Asia Minor where its discovery is usally credited to King Eumenes II, in the second century 225–160[1,2].

The use of parchment for book printing in Europe continued even after the advent of prinzing from wood-blocks and moveable type, but did not survive to any extent beyond the year 1500, although for purpose of calligraphy and for printing documents a diplomas, this durable material is in demand to the present day. It was paper, however, that gave printing its real impetus, for had the expensive parchment been the only material available craft of printing could never have developed. At the process of restoration and conservation of parchment it is usually necessary to investigate the degree of parchment damage because it determines the conservation method and conservation agents. We suggest the detection method of parchment shrinking temperature[3,4].

Experimental

The aim of this study was to investigate the influence of 2 types of accelerated ageing on parchment properties.

The effects of accelerated ageing on properties of 2 different samples of parchment – goat leather (bothside grounded) and calf leather (bleached) – were investigated. The samples of parchment were cutinto squares 4×4 cm. According to norm ISO 5630/1 dry ageing at 105 °C was used during 0, 24, 72, 168 and 240 hours. The artificial ageing was performed in a multifunctional oven APT Line Series FED with the regulation R 3.1 by Fisher Scientific (Czech Republic). Second type of accelerated ageing used was wet ageing at 30 °C and 75% RH during 0, 24, 72, 168 and 240 hours according to norm ISO 5630/3. This type of wet ageing was performed in a climatic chamber Heraeus VOTSCH (Germany) situated in Slovak National Archives in Bratislava.

Measurement of Shrinking Temperature

Decay of naturally damaged skin is caused by acid hydrolytic and oxidative scission. Both processes are competitive, simultaneous and interactive. The shrinking temperature effectively reflects changes in separation of aminoacids caused by oxidation, chemical scission of tannic acids, the presence of soluble sulfates and hydrogen ions that are attached to hydrolytic scission. According to norm CSN 79 38 414 the standard measurement of shrinking temperature indicated that the initial shrinking temperature is very important for durability and speed of parchment damage. Higher initial shrinking temperature signifies higher chemical and physical stability and hence higher preservation against material damage. The disadvantage of this method is high disposal of sample material. For this reason we used microscopis method for determination of shrinking temperature.

The thermosystem FP90 Mettler Toledo with measurement chamber FP82HT was used for experiment. This device consisted of microscope with electronically heated table, concave and cover glass, scalpel, preparative needle and as a solution water was used. Few fibres (0.3 g) of parchment sample were removed using scalpel, placed on concave glass with couple drops of water and covered with glass. This way prepared sample was placed on the heated table under the microscope. The table was heated at the rate of 2 °C min^{-1} in the range of 25–80 °C. Shrinking was observed at magnification $40 \times$. Studying samples with microscope temperature T_s or temperature interval were determined when fibres started to shrink. Individual measurements were repeated at least two times.

Shrinking Process

During heating of collagen fibres in water in certain temperature interval deformation occurs. The deformation consists of fibres shrinking and depends on strength, quality and degradation degree of collagen material. This method is a measurement of combined chemical and physical material stability. The shrinking process of parchment fibres can be described in 3 temperature intervals[4].

- Interval A_1/A_2 – temperature range when fibre shrinking occurs,
- Interval – B_1/B_2 shrinking of a fibre is immediately followed by shrinking of next fibre,
- Interval C – temperature range where fibres shrink simultaneously and continuously. Initial temperature of this main interval relates to shrinking temperature T_s. The process describes following equation:

$$\Delta T = T_e - T_s, \tag{1}$$

where T_e is ending/final temperature of interval C. Shrinking process stabilizes during the intervals B_2 and A_2, however for historical parchment non of mentioned intervals can be observed. Fibres of new parchment in relation to temperature proceed following changes:
no fibre acitivity – A_1–B_1–C–B_2–A_2 – total fibre shrinking.

In practice some intervals could absent at temperature lower 40 °C and intervals B and C could not be observed when fibres lost cohesion. Final value of microscopic determination of shrinking temperature depends on the type of skin, sample preparation and subjective evaluation.

Results

Measurements of shrinking temperature for samples of goat and calf parchment indicated that dry ageing at 105 °C caused considerable damage of parchment. Ending/final shrinking temperature of both parchment samples was lower than 40 °C which indicated high degree of damage.

Fig. 1. represents dependency of shrinking temperature on time of artificial ageing of goat and calf parchment exposed to dry ageing at 105 °C during 0, 24, 72, 168 and 240 hours. Shrinking temperature decreased after 240 hours of dry ageing by 19 °C for calf skin parchment indeed only by 12 °C for goat skin parchment. However for both samples decrease of temperature below 40 °C was recorded, total degration occurred for both samples.
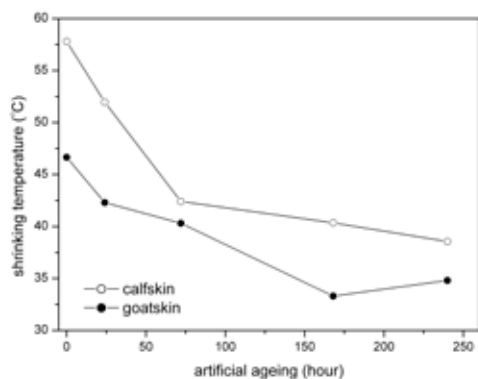

Fig. 1. Dependency of shrinking temperature on artificial ageing of goat and calf parchment exposed to dry ageing at 105 °C durings 0, 24, 72, 166, 240 hours
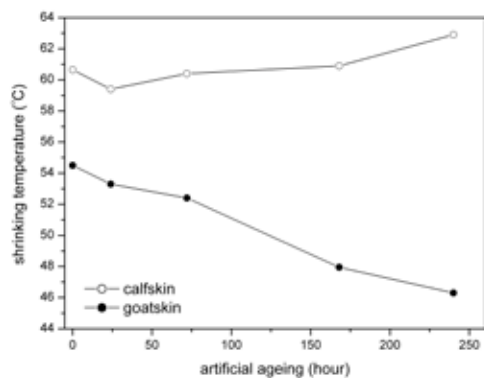

Fig. 2. Dependency of shrinking temperature on artificial ageing of goat and calf parchment exposed to wet ageing at 30 °C and relative humidity 75 % during 0, 24, 72, 168, 240 hours

Table I

Shrinking temperatures of goat and calf parchment for dry ageing at 105 °C

Artificial ageing [h]	Calf skin T_s [°C]	Goat skin T_s [°C]	Interval of shrinking [°C] Calf skin	Goat skin
0	57.8	46.8	57.8–66.1	46.8–52.7
24	51.9	42.3	51.9–59.7	42.3–48.6
72	42.4	40.3	42.4–52.2	40.3–46.9
168	40.4	33.3	40.4–49.2	33.3–37.9
240	38.6	34.8	38.6–43.4	34.8–40.4

Table II

Shrinking temperatures of goat and calf parchment for wet ageing at 30 °C a 75 % RH

Artificial ageing [h]	Calf skin T_s [°C]	Goat skin T_s [°C]	Interval of shrinking [°C] Calf skin	Goat skin
0	60.7	54.5	60.7–64.8	54.5–58.9
24	59.4	53.3	59.4–65.3	53.3–58.6
72	60.4	52.4	60.4–66.1	52.4–58.3
168	60.9	47.9	60.9–69.0	47.9–55.2
240	62.9	46.3	62.9–68.4	46.3–53.9

Fig. 2. indicates dependency for wet ageing at 30 °C and 75 % RH where calf skin parchment didn't show any damage not even after final ageing. The value T_s after final ageing was 63 °C and even higher compare to initial value which could correspond to measurement error or the sample was prepared from different part of skin. For goat skin parchment the value decreased after final wet ageing approximately by 8 °C hence certain damage of parchment occurred. Experimental values and their comparison indicated that wet ageing for both parchments was less drastic and total degradation didn't occur, just damage.

Conclusions

Changes of shrinking temperature reflected changes in collagen structure, agents, pH and overall storage conditions.

Initial shrinking temperature appeared to be suitable indicator of parchment durability. We could assume that higher shrinking temperature higher relative durability.

Since shrinking temperature reflects parchment's bulk condition we can recommend microscopic determination of shrinking temperature as a method for testing the damage of historical documents made of parchment and also for parchment designated for restauration.

REFERENCES

1. Ďurovič M.: *Restaurování a konzervování archiválií a knih,* Paseka 2002.
2. Larsen R., Vest M., Nielsen K. J. Leather Technol. Assoc. *77*, 154 (2006).
3. Abdel-Maksoud G., Marcinkowska E.: Restaurator *21*, 3 (2000).
4. Larsen R., Dorte V., Poulusen and Marie Vest.: Microanal. of Parchment *2002*, 55.

P21 QUALITY OF SOIL HUMIC SUBSTANCES BY SFS AND UV-VIS SPECTROSCOPY

ĽUBICA POSPÍŠILOVÁ[a] and NADĚŽDA FASUROVÁ[b]

[a]*Mendel University of Agriculture and Forestry, Institute of Agrochemistry, Soil Science, Microbiology and Plant Nutrition, Zemědělská 1, 613 00 Brno, Czech Republic,*
[b]*University of Technology Brno, Faculty of Chemistry, Institute of Physical and Applied Chemistry, Purkyňova 118, 612 00 Brno, Czech Republic,*
pospisi1@mendelu.cz

Introduction

In this paper we followed UV-VIS, SFS spectra and chemical properties of different origin soil humic subctances (HS). We selected HS from following soil types – Modal Cambisol, Litic Cambisol, Modal Chernozem, Modal Rendzina and Modal Pararendzina (Czech soil samples).

Soil quality is closely connected with HS character and chemical properties. Humic substances fractionation is contributed to specific amount of humic acids (HA) and fulvic acids (FA). Ratio HA/FA is one of the important criteria for soil quality and health. Optical curves and indexes in UV-VIS and SFS ranges indicate chemical properties and structure of HS.

Experimental

- Fractional composition of HS was made by short fractionation method according to Podlešáková et al. (1992).
- UV-VIS spectra were measured using Varian Cary 50 Probe with optical fiber within the range 300–700 nm.
- HS were dissolved in mixture of 0.1M sodium pyrophosphate and 0.1M NaOH. SFS spectra were measured after dilution (10 times) using Spectrofluorimeter Aminco Bowman Series 2 within the range 220–620 nm (at $\Delta\lambda = 20$ nm and temperature 20 °C, scan rate: 60 nm min^{-1}).
- Notes to Fig. s: Modal Cambisol (1), Litic Cambisol (2), Modal Chernozem (3), Modal Rendzina (4), Modal Pararendzina (5).
-

F r a c t i o n a l   C o m p o s i t i o n   o f   H S

HS fractional composition showed high FA amount in all samples.except Modal Pararendzina. HA/FA ratio was <1 in all samples except Modal Chernozem (HA/FA = 3). Humification degree varied from middle to low as follows: Modal Chernozem (Hrušovany)>Modal Rendzina (Sloup)>Modal Pararendzina (Pouzdřany)>Modal Cambisol (Náměšť nad Oslavou)>Litic Cambisol (Ocmanice).

U V - V I S   S p e c t r a

Absorbance in UV-VIS range was the highest in Modal Chernozem (Fig. 1.). Optical indexes increased in following order: Modal Chernozem<Modal Cambisol<Modal Rendzina<Modal Pararendzina<Litic Cambisol. Practically the same sequence was found for HA/FA ratio. Increrasing of $Q_{4/6}$

indicated decreasing of HS quality. Very similar were optical indexes ($Q_{4/6}$) for Modal Rendzina, Modal Pararendzina and Modal Cambisol (about 6). Only modal Chernozem had $Q_{4/6} < 4$ which indicated high HS quality. Very high index $Q_{4/6}$ was found for Litic Cambisol (>10) and indicated high amount of FK.
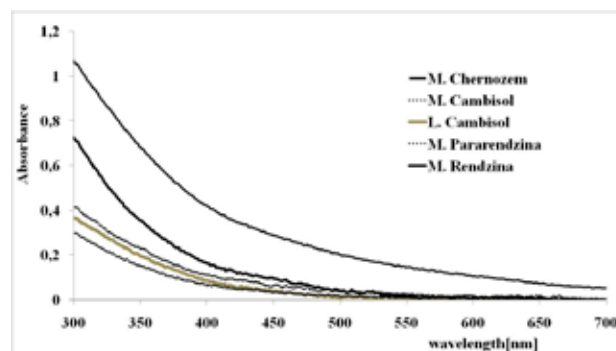

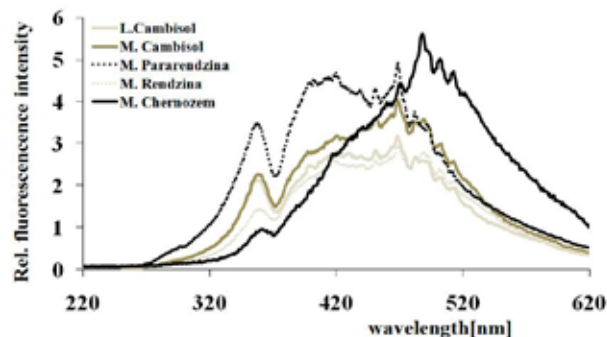Fig. 1. **UV-VIS spectra of HA isolated from different soil types**

Fig. 2. **Synchronous fluorescence spectra of HA isolated from different soil types**

S F S   S p e c t r a

In SFS spectral range (Fig. 2) five main fluorophore peaks were identified: at 359, 450, 469, 489, 501 nm. Some of them gave another two peaks at 420, 513 nm (at $\Delta\lambda = 20$ nm). All samples had maximum fluorescence intensity shifted from shorter to longer wavelength and maximum at 469 or 489 nm. According to Senesi et al. (1991) there are some samples with more intensive emission (at $\Delta\lambda = 20$ nm $= (\lambda_{em.} - \lambda_{ex.})$ at 470 and others with more intensive emission at 488 nm. The last is caused by contain of aromatic compounds in HA molecule. Modal Chernozem SFS spectra showed the main peak at 489 nm and the highest relaive fluorescence to compare to others. Modal Pararendzina and Litic Cambisol contained much more aliphatic compounds and fulvic acids indicated by peaks at lower wavelegth 359 a 420 nm. Modal Cambisol had no peak at 420 nm.

Relative fluorescence indexes (F) were calculated as ratio I_{469}/I_{452}. The lowest index (F) was found for Modal Chernozem and the highest for Modal Pararendzina. The fluorescence indexes it is supossed to be closely connected with HS humification degree.

Results

In Modal Chernozem highest HA amount was found. Fulvic acids highest amount was found in both Cambisols. HA/FA ratio indicated decreasing HS quality in order: Modal Chernozem < Modal Rendzina < Modal Pararendzina < Modal Cambisol < Litic Cambisol. Linear correlation between $Q_{4/6}$ and HA sum was found.

UV-VIS spectra showed the highest absorbance in Modal Chernozem. Optical indexes $Q_{4/6}$ indicated high HS quality in Modal Chernozem and low in Litic Cambisol.

Fluorescence of studied samples was compared with literature data and/or with standard. Samples contained substitued naphtalene and coumarine derivates. Samples had similar fluorescence behaviour as Elliot soil humic acid standard (IHSS) and all samples indicated two main excitation peaks at 450, 468 nm.

Low relative fluorescence index (F) was found in Modal Cambisol (0.73). Highest index F was in Modal Pararendzina (1.16). From SFS spectra we can also suggested highest intensity of fluorescence in Modal Chernozem. These results were confirmed by HS fractionation but maximum F index in Modal Chernozem was not determined.

Conclusions

We can conclude that HS of different origin had very similar SFS and UV-VIS spectra except lower wavelengths and wave numbers. But some differences were observed in Modal Chernozem. The last had main fluorophore peak at 489 nm. Other samples contained main peak at 469 nm. UV-VIS spectra were mostly influenced by fractional composition (HA, FA content). Samples origin was therefore an important factor influencing HS quality.

REFERENCES

1. Podlešáková E. et al.: *Rozbory půd, vod a rostlin, VUMOP* , Praha, pp. 259 (1992).
2. Sierra M. M. D., Giovanela M.,Parlanti E., Soriano-Sierra E.J.: Chemosphere *58*, 715 (2005).
3. Senesi N., Miano T. M., Provenzano M. R., Brunetti G.: Soil Science *152*, 259 (1991).
4. Senesi N.: R. Soc. Chem. *1993*, 73.

P22　SENSORIC PROPERTIES OF AROMATIC AND HETEROCYCLIC COMPOUNDS WITH CONJUGATED BONDS

OTA SALYK[a], PAVEL BEDNÁŘ[a], MARTIN VALA[a] and JAN VYŇUCHAL[b]

[a]*Brno University of Technology, Faculty of Chemistry Purkyňova 118, 612 00 Brno,* [b]*Research Institute of Organic Syntheses, Rybitvi 296, Rybitvi, 533 54, Czech Republic,* salyk@fch.vutbr.cz

Introduction

For expected future hydrogen economy is expected vast need of hydrogen operating devices including new sensors, while nowadays sensors need extra power for hydrogen dissociation[1]. There exist a range of organic molecules with three valent nitrogen atom with high proton affinity. I case of diketopyrrolopyrrole derivatives with pyridyl, piperidyl or morpholinyl ring we obtain a pigment with potential color change while protonated. These materials are also semiconductive, so protonation can influence their conductivity. It was already observed in case of pyridyl derivative[2]. The protonation itself is tested in acids vapour so because in acid water solvent the shielding effect of water molecules prevent in proton penetration to the active centres in rhe DPP film. Protonation in real hydrogen gas is possible only after the hydrogen molecule dissociation. It proceeds on catalyzer surface of noble metal as platinum or palladium[3]. The presence of electric field supports the hydrogen dissociation, so the cluster non-conductive catalyzer layer between gap electrodes has to be obtained. It can be sputtered, evaporated or galvanically electrodeposited using anodic alumina templates[4]
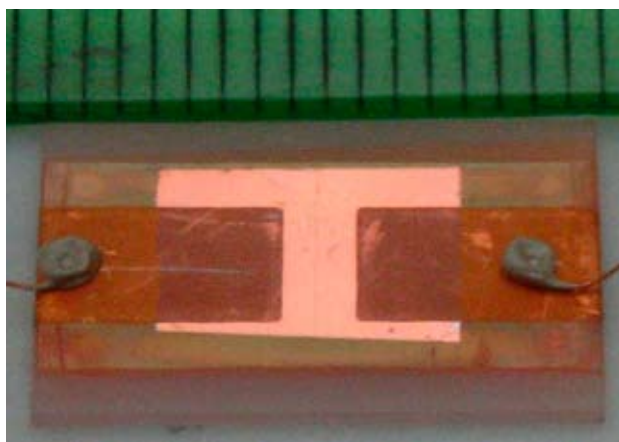

Fig. 1.　**Samples of DPP gap structure (10 μm) on glazed alumina plate with aluminium deposited contacts**

Experimental

Thin films of DPP derivative materials were prepared by vacuum evaporation method. Substances composed from heterocyclic rings appeared only poor solubility in organic solvents in case of no alkyl chain bonded to the molecule.

Table I
Series of discussed compounds with melting points T_m [°C]

U14　　　　U15　　　　U16
$T_m > 300$ °C　$T_m > 300$ °C　$T_m > 300$ °C

U34　　　　U35
$T_m > 300$ °C　$T_m > 300$ °C
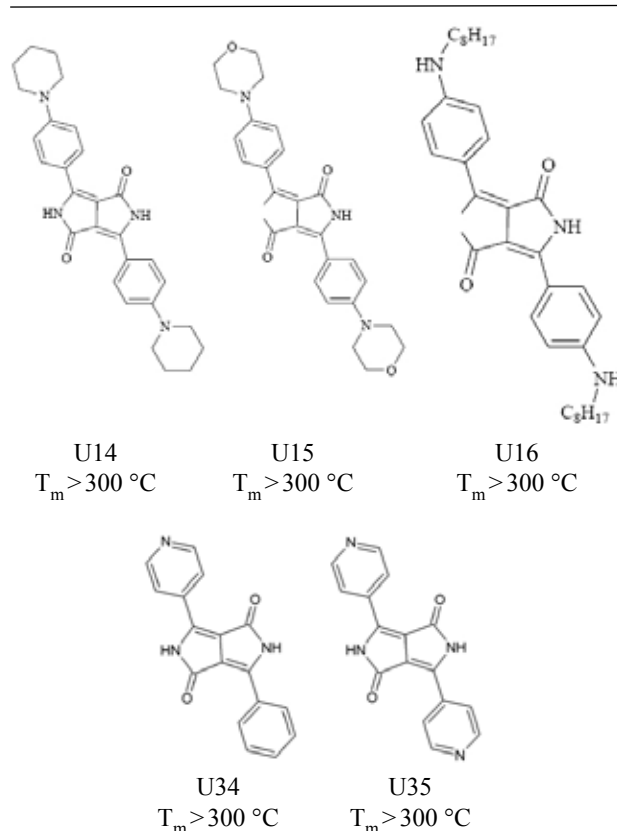
Substrates were used according to following investigation; low resistivity silicon wafers both for scanning electron microscopy (SEM) and atomic force microscopy (AFM) were used besides indium tin oxide (ITO) coated low alkali Corning glass for electro-optical testing, quartz glass for optical measurement and gap arrangement on glassed alumina plates.

The deposition of the active DPP layer was carried out in the vacuum coating facility B.55.3 HV Dresden with ultimate pressure 1×10^{-4} Pa pumped by diffusion oil pump. The crystal thin film thickness monitor was used for deposition monitoring. Thin films of thickness 200 nm were deposited on standard substrates. The material was pressed into pellets 6 mm in diameter and about 1 mm high, usually about 30 mg of mass, which was the proper dose for 200–300 nm thick layer without wasting. The sophisticated shape of the boat prevented direct radiation of the deposited layer and also focused the irradiation onto the pellet, so it decreased required heating power. This procedure allowed steady sublimation and deposition rate without sputtering of bigger clusters or drops and material melting. It also improved easy manipulation and cleanness preservation – no powder was sputtered into vacuum chamber.

The thickness measured by elipsometry typically 40–100 nm resulted. The deposition rate was typically

0.2 to 0.5 nm s^{-1}. The 10 μm gap was created by aluminium evaporation through a 10 μm tungsten wire mask.

The samples were than investigated on scanning electron microscope (SEM) FEI QUANTA 200. No grain structure in scale of 50 nm resolution was observed, so the surface appeared uniform.

The samples were than situated into quartz cell and measured on absorption on Varian UV-VIS-NIR spectrometer in hydrochloric acid solution and nitric acid vapours.

Results

Samples from Table I were investigated by acid vapour and acid solution effect on colour variation. Thin film samples U14, 15 and 16 react on HNO$_3$ vapour presence in etching dish by changing their colour from vivid violet to orange; samples U34 and U35 exhibit a colour shift from vivid red to violet at the same conditions. Similar reaction was observed in other acid vapours. Organic simple acids as formic or acetic vapours brought dissolving and destruction of the thin film.
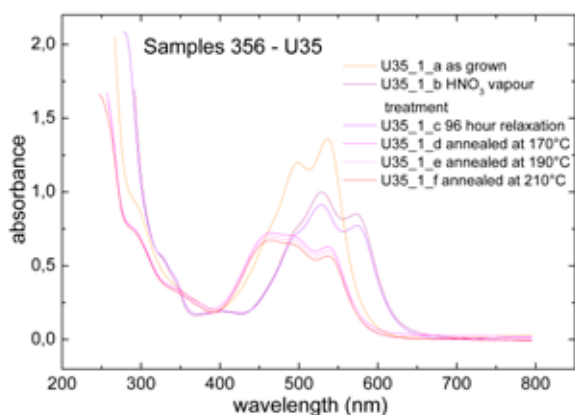

Fig. 2.　**Sample U35 – Absorption changes affected by nitric acid vapour treatment and subsequent annealing**

The attempt with water acid solution of various pH did not bring any change for samples U14, U15 and 16 and only a weak spectral shift in case of samples U34 and U35. It is explained by water molecules shielding of protons that cannot penetrate into active centres of the thin film.

Absorbance spectra in UV VIS region were scanned systematically for thin film samples U34 and U35 on quartz glass substrates. The results are presented in Fig. 2., Fig. 3. and Fig. 4. The nitric acid vapour treatment causes spectrum change, which is steady according to relaxation on air for four days. Annealing to temperature above 160 °C returned the spectrum back, but not exactly to initial shape. The change in relative intensity of the vibronic structure indicates reorganisation of the molecules geometry. The absorbance decrease is also considered as it returned to c-curve after repeated HNO$_3$. Both quantitative and qualitative reversible changes are well apparent and give an evidence of structure change. The reversibility of the spectral change was observed also
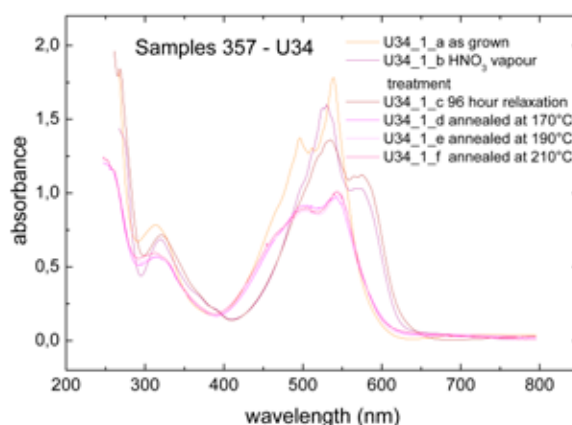

Fig. 3.　**Sample U34 – Absorption changes affected b nitric acid vapour treatment and subsewquent annealing**
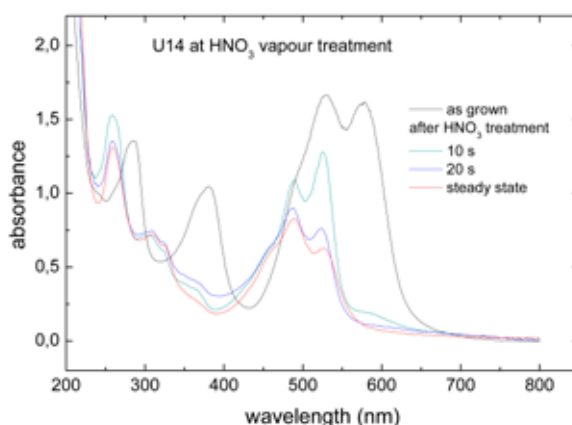

Fig. 4.　**Sample U14 – Absorption changes affected by nitric acid vapour treatment**

at U14 sample after annealing at 200 °C but already at room temperature within 5 days appeared remarkable initial state regeneration.

The spectral variation has following explanation[3]: Hydrogen ion from the acid is captured on nitrogen atom in the pyridyl ring and the complex salt $(R-N-H)^+(NO_3)^-$ resulted into colour and structure change. The evolution of NO_2 and O_2 is possible as well while the free electron remains in the material. In case of dissociated hydrogen is presumed reaction, where instead of $(NO_3)^-$ ion free electron is created, which contributes to material conductivity.

However, the behaviour of the U14–U16 derivatives differs from the U34 and U35. Since the absorption spectrum of the latter derivatives undergo bathochromic shift the former derivatives shows large hypsochromic shift. The central part of the DPP unit acts as electron acceptor. Substitution of the electron donating groups (U14–U16) leads to an increase of the absorption coefficient and cause a bathochromic shift. The treatment of the derivatives under acid vapour cancelled the electron donating character of the substituents and therefore caused shift back to the absorption of non-substituted diketo-pyrrolo-pyrrole.
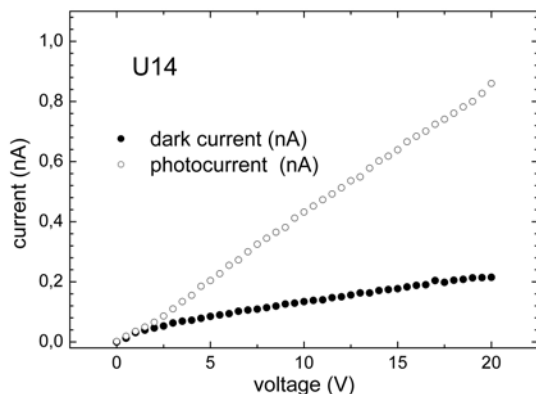
Fig. 5. **V-A characteristics of U14 as grown sample in gap structure**

The conductivity and photoconductivity of the thin film was tested as well and its changes with acid vapour treatment is also expected (Fig. 5)

Conclusions

Set of thin film samples of DPP derivatives thin films prepared by evaporating and spin coating methods were investigated by absorption spectra measurements at HNO_3 vapour treatment. The nature of electron donating groups was changed by nitric ion and absorption spectra shift was observed. Similar behaviour exhibited also other acids. This affected also conductivity. The effect was reversible. It is believed that it can be exploited for new sensing material development, especially hydrogen sensing.

REFERENCES

1. Seisler M. J.: *World Forum for Harmonization of Vehikle Regulationa (WP. 29)*, United Nations, Ženeva, March 10, 2004.
2. Mizuguchi J., Tomohiko I., Takahashi H., Yamamaki H.: Dyes Pigm. *68*, 47 (2006).
3. Takahashi H., Mizuguchi J.: J. Appl. Phys. *100*, 034908 (2006).
4. Klosová K., Hubálek J.: Phys. Stat. Sol. (a)*1–4* (2008)/ DOI 10.1002/pssa.20078169.

P23 STRUCTURE AND MORPHOLOGY OF SOME DIPHENYL-DIKETO-PYRROLO-PYRROLE DERIVATIVES PIGMENTS

OTA SALYK[a], MARTIN WEITER[a] and JAN VYŇUCHAL[b]

[a]*Brno University of Technology, Faculty of Chemistry Purkyňova 118, 612 00 Brno, Czech republic*
[b]*Research Institute of Organic Syntheses, Rybitvi 296, Rybitvi, 533 54, Czech Republic,*
salyk@fch.vutbr.cz

Introduction

After more than 15 years of academic and industrial research worldwide, the class of organic materials, conjugated polymers and organic molecular systems, has reached very high level of outstanding material properties and the potential for different industrial applications is now emerging. Resistors, capacitors, diodes, photodiodes, organic light-emitting diodes (OLED), field-effect transistors and optically pumped solid-state lasers can be fabricated by different methods and integrated into electronic and optoelectronic circuits[1].

In this study, a group of several derivatives of 3,6-diphenyl-2,5-dihydro-pyrrolo[3,4-c]pyrrole-1,4 dione, also known as DPP (see Table I) were investigated. DPP derivatives are mainly used as high performance pigments and are valued for their fatigue resistance; nevertheless some of their physical properties make them as potential candidates for OLED applications[2].
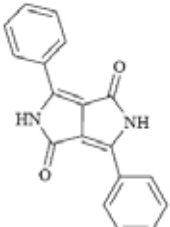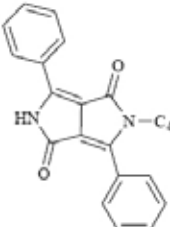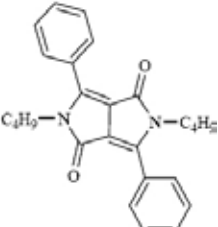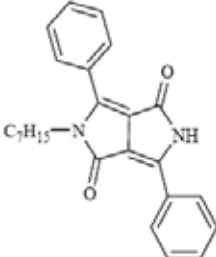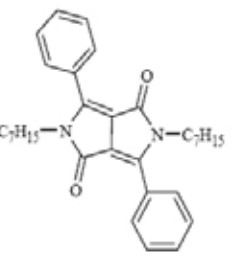
Molecular OLED devices are generally fabricated by sublimation under vacuum of successive layers of electron- and hole transporting materials. In contrast, low-cost solution-based processing techniques are usually requested for industrial production. Therefore four different derivatives of diphenyl-diketo-pyrrolopyrrole (DPP) with alkyl side groups were synthesized to increase their solubility (see Table I) and the question of relation between the chemical structure and morphology of prepared thin films were addressed.

Experimental

Thin films of DPP materials were prepared by spin coating method and by vacuum evaporation method. Low resistivity silicon substrates were used for scanning electron microscopy (SEM) and atomic force microscopy (AFM), whereas indium tin oxide (ITO) coated low alkali Corning glass were used for electro-optical and quartz glass for optical characterization, respectively. Thin layers spin-casted from chloroform-toluene solution (7:3) were typically 100–200 nm thick as measured by elipsometry.

The vacuum deposition of the active DPP layer was carried out in the vacuum coating facility B.55.3 HV Dresden with ultimate pressure 1×10^{-4} Pa pumped by diffusion oil pump. The crystal thin film thickness monitor was used for deposition monitoring. Thin films of thickness 200 nm were deposited on standard substrates. The material was pressed into pellets 6 mm in diameter and about 1 mm high, usually

Table II
Series of discussed compounds with melting points T_m [°C]

U4	U9	U10
$T_m > 300$	$T_m = 248–252$	$T_m = 118–120$

U11	U12
$T_m = 211–213$	$T_m = 109–213$

about 30 mg, which was the proper dose for 200–300 nm thick layer without wasting. The sophisticated shape of the boat prevented direct radiation of the deposited layer and also focused the irradiation onto the pellet, so it decreased required heating power. This procedure allowed steady sublimation and deposition rate without sputtering of bigger clusters or drops and material melting. It also improved easy manipulation and cleanness preservation – no powder was sputtered into vacuum chamber.

The deposition rate was typically 0.2 to 0.5 nm s^{-1}. Some samples were deposited at higher temperature, so the heated sample holder with six positions was used in order to enable preparing a series of samples at different substrate temperature. For lower than room temperature the water cooled holder combined with Peltier cell was designed. The substrate temperature –20 °C was achieved with water cooling measured by Pt100 thermometer.

The morphology of the samples was investigated by scanning electron microscope FEI QUANTA 200.
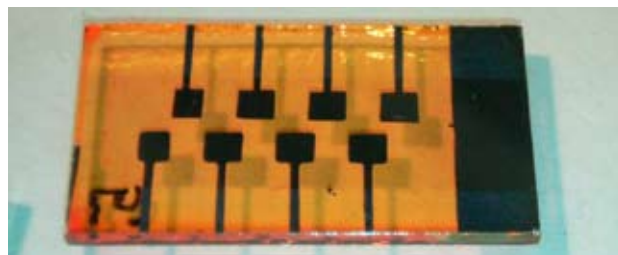

Fig. 1. **Samples of DPP sandwich structure with aluminium deposited contacts**
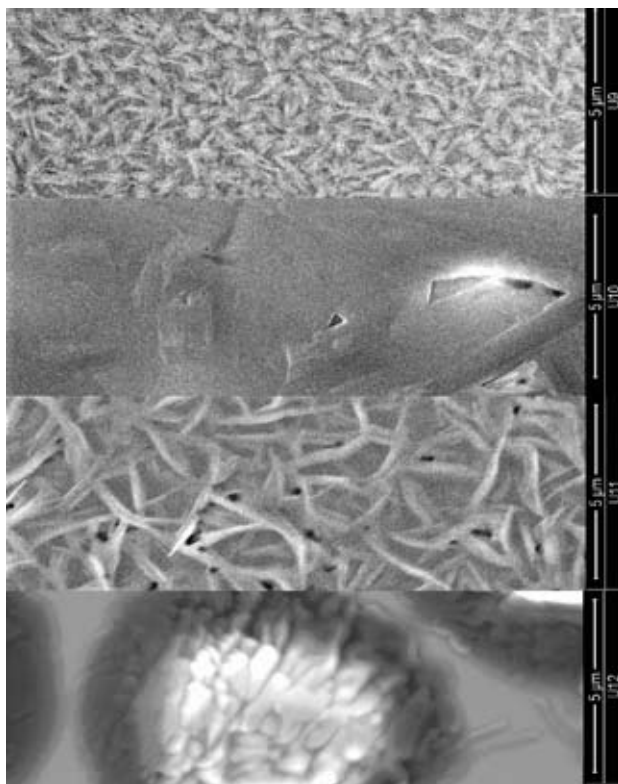
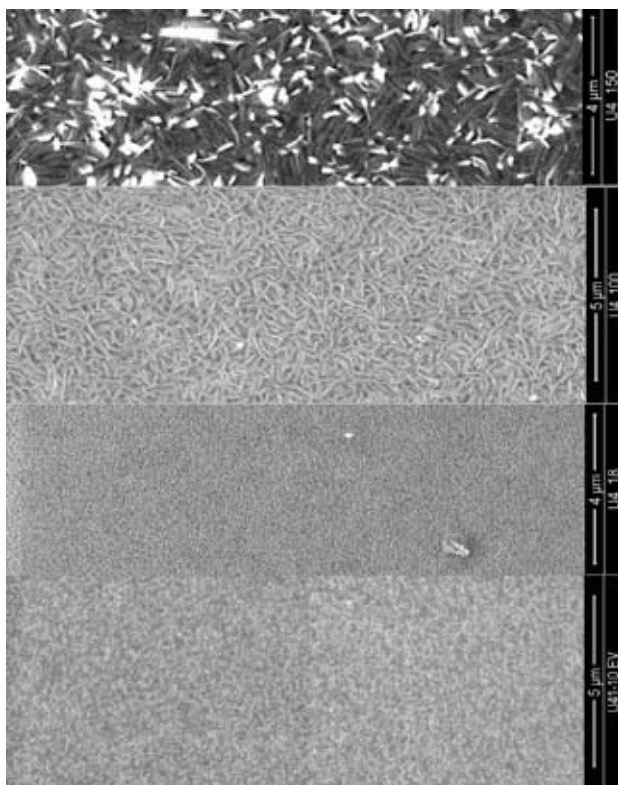Fig. 2.   **Structure of evaporated thin films of materials U9, U10, U11 and U12**

Fig. 3.   **Sample U4 prepared at various substrate temperature – 10 °C, 18 °C, 100 °C and 150 °C**
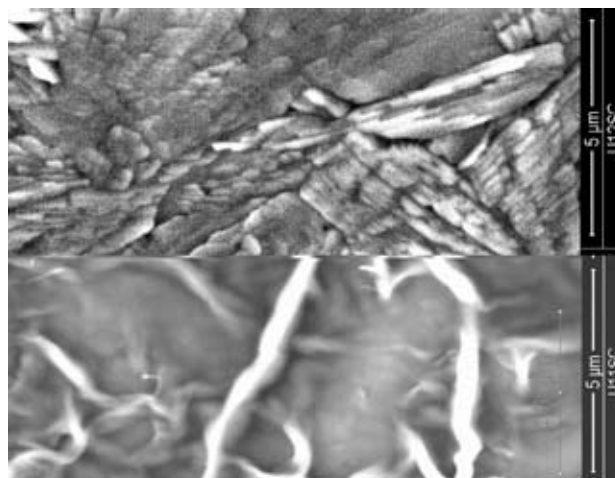

Fig. 4.   **SEM snap of U11SC and U12SC spin coated**

Results

Theory of thin film growth predict that a particle impinged onto the substrate surface can move laterally unless it losses its kinetic energy and finds the energy potential well. It is usually after joining with other particles and this particle – molecules – cluster is the nucleus of future columnar or island structure. Further more crystallization can be in process. Usually the uniform thickness and homogeneous structure is demanded in order to enable electrical thin film device to fabricate. Fig. 2. represents the series of DPP derivatives with alkyl chains symmetrically (U10, 12) and asymmetrically (U9, 11) bonded. The SEM snaps show, that they create crystalline structure with bigger and flat crystals in case of symmetric molecules and smaller and fibre crystals in case of asymmetric molecules. The melting point is lower in case of longer alkyl chain material, so it results in coarse grain structure with no amorphous phase. The island structure occurs with holes causing electrical breakthroughs in sandwich devices. The U12 material is deposited as amorphous islands, but in short time – hours – it crystallises. This effect was observed also at other materials with melting point round 100 °C and lower.

Condensation of evaporated molecules brought also problems with adhesion. The high deposition temperature causes shrinkage while cooling, more for organics than substrates and it resulted into peeling observable especially at U4–150 sample. The free crystal ends in space give high reflection in SEM due to charging and they appeared bright.

How the surface mobility of condensed molecules corresponds to surface temperature explains Fig. 3. The high melting point material was deposited by evaporation and the grain size corresponded the condensing surface temperature. The aim of the attempt should be the uniform structure, although it was achieved in scale of SEM resolution (50 nm), the electrical breakthroughs still appeared.

Samples prepared by spin coating method behave similarly, but the structure is usually continuous – no islands and visible holes m- see Fig. 4. The solvent affects blurred

transition when crystals grow just at solvent evaporation, but in case latter crystallization the grain boundaries appear sharp.

Conclusions

Set of samples of DPP derivatives thin films prepared both by evaporation and spin coating methods were investigated by SEM. Their convenience for sandwich electronic devices was criticized by the morphology appearance. The uniform thin film in scale below 100 nm grain size was not achieved due to crystallization processes. The grain size corresponded to melting point of the materials and did not vary rigorously between evaporating and spin coating method, which one gave better results due to absence of holes and continuous layer creation. Crystallization and non uniform surface appeared as well. Therefore the optimization of the chemical structure and the detail morphology studies should be done to achieve homogeneous stable layers suitable for OLED application.

REFERENCES
1. Harrop P., Das R.: *Organic Electronics: Forecasts, Players & Opportunities 2005–2025*, IDtechEx, New York, 2005.
2. Collona G., Pilati T., Rusconi F., Zecchi G.: Dyes Pigm. *75*, 125 (2007).

P24 THE INFLUENCE OF MECHANICAL ACTIVATION ON THE PRODUCTION OF THE HUMIC ACIDS IN THE BROWN COAL

M. SKYBOVA and L. TURCANIOVA

Institute of Geotechnics, Slovak Academy of Sciences
Watsonova 45, 043 53 Kosice, Slovakia
skybova@saske.sk

Introduction

One of the perspective trends of non-fuel usage of coals is the production of humic preparations on its base, which are to be used in different branches of industry and agriculture[1]. The most suitable raw material for obtaining these products is brown coals[2].

Humic acid is one of the major components of humic substances, which are dark brown and major constituents of soil organic matter humus that contributes to soil chemical and physical quality and are also precursors of some fossil fuels. They can also be found in peat, coal, many upland streams, dystrophic lakes and ocean water[3].

In the studies of Baláž[4,5] was tested the use of mechanical activation, called GACL (Grinding Aqueous Caustic Leaching) procedure which is based on the simultaneous grinding and leaching of coal. In this process of grinding was occurred significant demineralisation and detoxication. The content of humic acids increased by more than 2 times.

Recent studies using pyrolysis-FIMS and -GC/MS, multidimensional NMR and synchrotron-based spectroscopy have shown that humic substances posses both aromatic and aliphatic characteristics. The dominant functional groups, which contribute to surface charge and reactivity of humic substances, are phenolic and carboxylic groups[6].
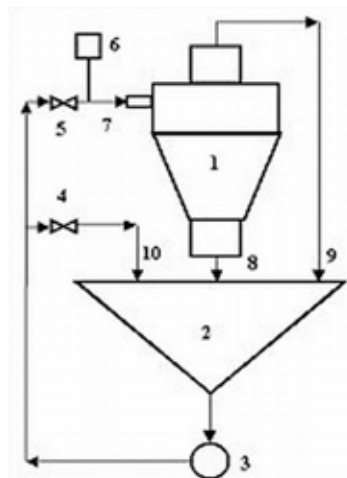

Fig. 1. **Scheme of hydrocyclone station[7]**
1 – hydrocyclone, 2 – agitating tank, 3 – pump, 4 – valve of reverse circuit, 5 – valve for regulation of input press, 6 – pressure gauge, 7 – hydrocyclone input, 8 – heavy product – underflow, 9 – light product – overflow, 10 – circulating charge

Experimental

Hydrocyclone Separation

The steam brown coal from Handlová Colliery (central part of Slovakia) was washed in the WOC (Water-Only Cyclone). During experiments the WOC was installed in hydrocyclone station[7] (Fig. 1.). The WOC can be characterized by the following parameters: the inner diameter of cylindrical part: 150 mm; the height of this part: 200 mm; the diameter of inlet pipe 45 mm. The vortex finder and apex diameters were of 68 mm and 14.6 mm, respectively. The cone consisting of three angles (135 °, 75 ° and 20 °) was applied. The experiments have been carried out at the input pressure of 10 kPa. The concentration of solids was of 100 g dm^{-3}. The basic products of washing were collected using sieves with a mesh size of 0.5 mm. Finally, circulating slurry was collected and included into total material balance. The basic coal sample – feed (F), the obtained treatment products, i.e. washed coal – overflow (O), were dried, ground below 0.1 mm and characterized by standard analytical methods.

Extraction of Humic Acids

The coal samples (F, O) were subject to mechanical activation by the GACL (Grinding Aqueous Caustic Leaching) method in following conditions: made-up: 20 g, volume of leaching agent: 200 ml, concentration of leaching agent: 0.1%; 0.5%; 1% and 2% NaOH, leaching temperature: 60 °C, grinding period: 60 minutes, revolutions: 400 min^{-1}.

Mechanical wet grinding was performed in the attritor Molinex, type 075 Netzch, Germany with a grinding capacity of chamber – 500 ml and the grinder filling, i.e. glass balls with a weight of 685 g and 2 mm in diameter.

After the performance of the grinding test the solid phase was separated from liquid product in the centrifuge (JANETZKI T23). After through washing of the leached coal extraction in distilled water and after its drying there were determine humic acids by standard STN 441347.

^{13}C Nuclear Magnetic Resonance

The solid-state ^{13}C-NMR spectra were obtained on a Bruker Avance 500 WB/US (Karlsruhe, Germany, 2003) spectrometer.

The following experimental conditions were employed: a 4 mm ZrO$_2$ rotor with standard CPMAS pulse program, during the measuring of ^{13}C-NMR signal was applied a bipolar decupling – TPPM (two-pulse phase-modulated), a pulse length of 4.8 μs, angle of phase modulation was 15 °.

Chemical shifts were assigned according to Maciel[8].

SEM Microscopy

Scanning electron microscopy (SEM) of sample of brown coal was performed using microscope type TESLA BS 340.

Micro-shots of samples of the brown coal taken from a screening electronic microscope were enlargement of 2,000 times.

Results

The results of chemical analysis of steam brown coal and of washed WOC products are presented in Table I. It was found that WOC process reduce the amount of ash (the washed coal (O) contains lower amount of ash A^d = 9.01 % in comparison to the basic sample A^d = 36.80 %).

Table I

Characteristics of brown coal samples from Handlová Colliery. Superscripts: d – dry basis, a – analytical specimen, O^d – by difference – according to $100 - (A^d + C^d + H^d + N^d + S^d_{Total})$

Characteristics\Product	Feed	Overflow
Ad [%]	36.80	9.01
Wa [%]	9.02	7.55
Cd [%]	46.11	68.12
Hd [%]	3.04	4.49
Nd [%]	0.32	0.62
Od [%]	11.78	16.03
SiO_2 [%]	20.42	4.14
Al [%]	4.14	1.01
Ca [%]	0.48	0.31
Mg [%]	0.47	0.12
Fe – total [%]	1.49	0.59
S – total [%]	1.76	1.73
As [ppm]	62.00	66.00

Several procedures of preparation of humic acids make use of the traditional method of caustic treatment of brown coal with a relatively higher content of humic acids.

In Table II there is presented the influence of the concentration of leaching agent NaOH during the mechanical processing of coal before and after the WOC by the GACL method.

Table II show that a greater effect of mechanical activation by GACL process is determined by using the samples, which were not washed and which have a higher content of ash. There is the increase 1.5 in average (feed as against overflow).

In the case of mechanical activation of basic sample (after GACL method), the increase of humic acids is 2 times in comparison to the basic sample (HA – 1.62 g) before GACL method and the amount of humic acids is increased with the increase of NaOH concentration.

This same process is observed by using samples after WOC, the amount of humic acids before CACL method is 1.83 g.

The distribution of humic acids into the liquid and solid product is significant in the basic samples (liquid product $HA^{0.5}$ = 4.35 g as against $HA^{0.5}$ = 1.04 g in solid product).

In the samples after WOC, the distribution of the humic acids is relatively equal.

The ^{13}C-NMR spectra of the isolated coal HA are shown in Fig. 2.a), b). The spectra of HA sample were very similar and practically the minimal changes were detected.

TableII

Mechanical activation of coal using GACL process

Characteristic	$HA^{0.1}$ [g]		$HA^{0.5}$ [g]		HA^1 [g]		HA^2 [g]	
F: solid	1.41	3.57	1.04	5.39	1.42	4.72	1.34	6.04
liquid	2.16		4.35		3.30		4.70	
O: solid	1.02	1.94	1.43	2.83	1.92	3.92	1.45	4.85
liquid	0.92		1.40		2.00		3.40	

Concerning that, coal is very complicated nature product; its resolution of nmR spectra is very small for the most part. Inasmuch as, there is possible to estimated only basic, typical fraction of functional groups: area of 190–170 ppm – carboxylic groups or amidic carbonyls, 170–150 ppm – aromatic carbons of phenols and phenolic ester, 150–135 ppm – alcylated aromatic carbons, 135–100 ppm protonised and unprotonised bridgehead aromatic carbons, 108–100 ppm – anomeric CH of cellulose and hemiacetal carbons, 90–70 ppm – resonance area CH secondary alcohols and other carbon atoms binded to oxygen atom., 65–55 ppm – area of resonance of CH_3 group aliphatic and aromatic ethyleters and α-carbons of amino acids, 55–50 ppm – area of resonance of CH_3 group of metylesters of carboxylic groups, 50–35 ppm
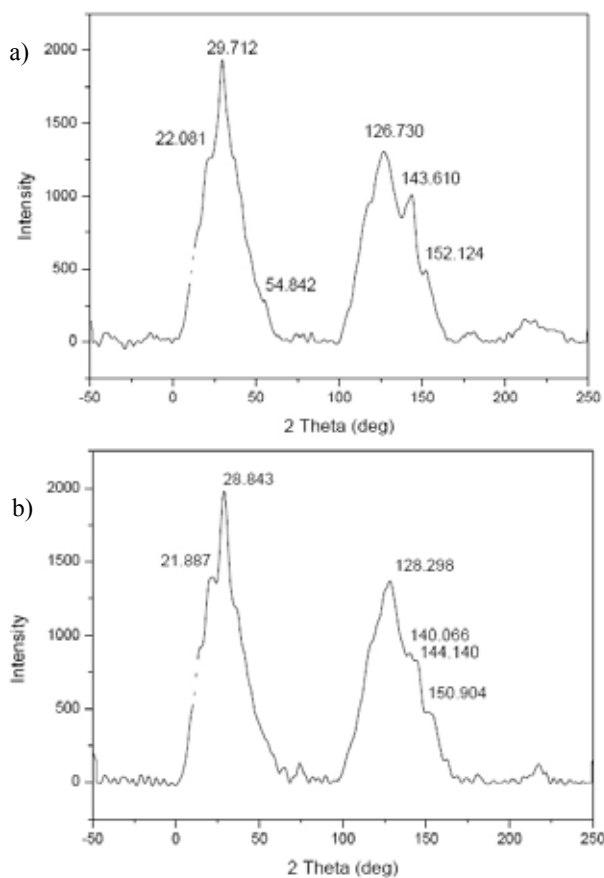

Fig. 2.   **^{13}C – nuclear magnetic resonance spectra of the humic acids – a) Overflow before the GACL process, b) Overflow after the GACL process**

acetylic group, 25–1 0 ppm – area of resonance of alcylic methyls.

Fig. 3.a) and b) show the micro-shots of the grains in mechanically active coal samples after WOC (before and after the GACL method) in the conditions of active grinding time 60 minutes

Comparing the micro-shots it may be clears that in Fig. 3.b), there is obvious aggregation of the grains in the ground stock as against 3.a). The mechanism of aggregation of ultra-fine grains cannot be definitely specified.

Conclusions

From the results presented it follow that a greater effect of mechanical activation by GACL process is determined by using the samples, which were not washed and which have a higher content of ash. In the case of leaching of the basic sample there occurs a significant selective penetration of humic acids into the liquid product. In the samples after WOC, the distribution of the humic acids into liquid and solid product is relatively equal.
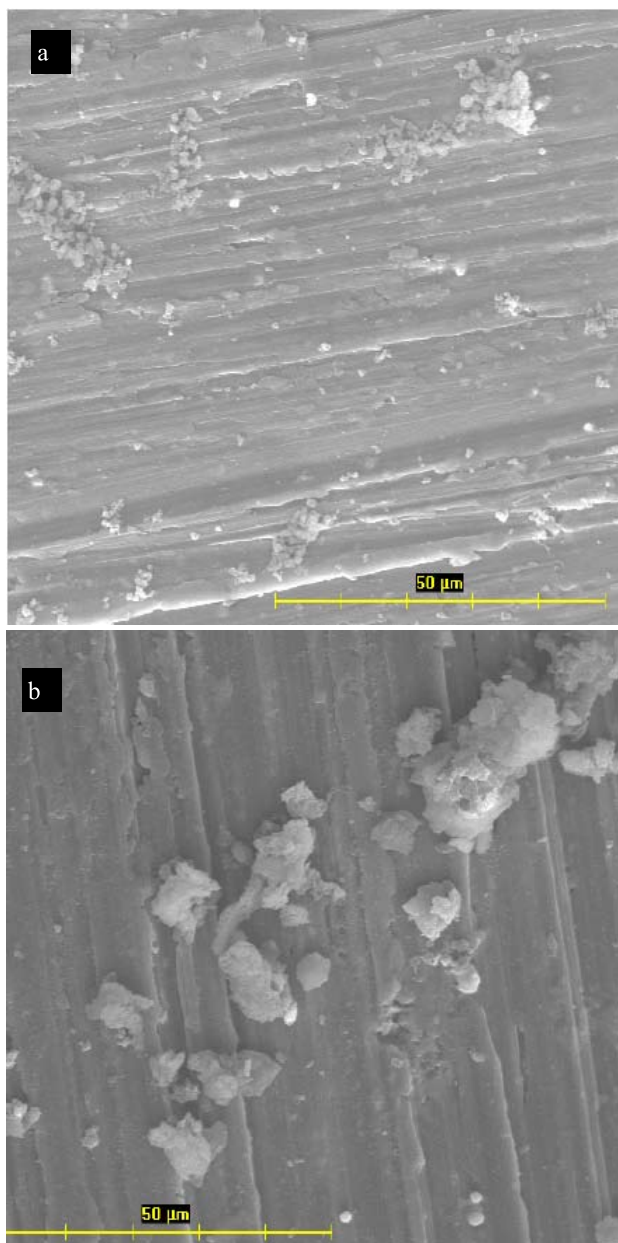
Fig. 3. **Shots of samples of the Slovak brown coal (Handlova) taken from a screening electronic microscope at a enlargement of 2,000 times: a) Overflow before the GACL process, b) Overflow after the GACL process**

– area of resonance of quarternary carbons and CH carbons, 35–25 ppm – area of resonance of CH_2 alcylic group and CH_3

REFERENCES

1. Gorlov E. G., Rodae V. V., Ryzhkov O. G., Koledin D. M.: *XXI International Mineral Processing Congress,* Rome, Italy (2000).
2. Butuzova L., Krzton A.: *European Carbon Conference. The British Carbon Group* (1996).
3. International Humic Substance Society http://www.ihss.gatech.edu/
4. Baláž P., Turčániová Ľ.: Acta Montanistica Slovaca *3*, 348 (1998).
5. Baláž P., La Count R. B., Kern D. G., Turčániová Ľ.: Fuel 80 (2001).
6. Stevenson F. J.: *Humus Chemistry: Genesis, Composition and Reaction.* Wiley, New York, (1994).
7. Jakabský Š, Lovás M., Hredzák S., Turčániová Ľ.: *Proceedings of the Fifteenth Annual International Pittsburgh Coal Conference* (1998).
8. Maciel G. E.: J. Mol. Struct. *550*, 297 (2000).

P25 NUMERIC MODELLING OF V-T PROCESS IN NITROGEN GROUND STATE UNDER POST-DISCHARGE CONDITIONS

I. SOURAL[a], F. KRČMA[a] and V. GUERRA[b]

[a]Faculty of Chemistry, Brno University of Technology, Purkyňova 118, 612 00 Brno, Czech Republic,
[b]Departamento de Física, Instituto Superior Técnico, 1049-001 Lisboa, Portugal,
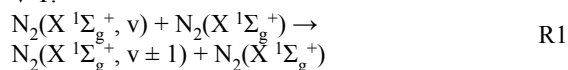xcsoural@fch.vutbr.cz

Introduction

Many scientists have tried to create the kinetic model describing the processes occurred during the nitrogen post-discharge[1,2]. These endeavours are not fully successful up to now because there are many metastable electronic and vibrational states in nitrogen and the bimolecular and trimolecular reactions among these excited states have mainly unknown reaction rate constants[3,4]. If the active discharge turns to the post-discharge period there is about 90 % of total energy in plasma dissipated into vibration at levels states of the ground state[5] and during the consequent reactions (including also the other excited species) this energy changes to the electron excitation, ionization, dissociation and other processes[6]. It means, nearly all the post-discharge kinetics starts by reactions of metastable vibrationally excited nitrogen ground state molecules. This is reason why it is necessary to study vibration distribution function of the ground state in the time evolution. Vibration distribution function is depended on different processes as V-T (Vibration-Translation transition), V-V (Vibration-Vibration transition), electron excitation, ionization and another. V-T and V-V processes are the most important for the evolution of vibration distribution function (VDF). Much work is needed for all calculations. However we have already finished V-T calculations so this work is focused on this only.
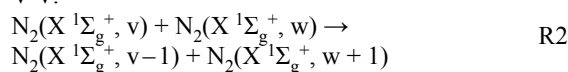
Theoretic Base of Numeric Model

There are two main well known energy transfer processes in the ground state: V-T process[7], i.e. the transfer of vibrational energy into the energy of translational motion of molecule (see R1) and V-V process[7] where the molecules exchange their vibrational excitation energy (see R2).

- V-T:
  $N_2(X\ ^1\Sigma_g^+, v) + N_2(X\ ^1\Sigma_g^+) \rightarrow$
  $N_2(X\ ^1\Sigma_g^+, v \pm 1) + N_2(X\ ^1\Sigma_g^+)$ R1

- V-V:
  $N_2(X\ ^1\Sigma_g^+, v) + N_2(X\ ^1\Sigma_g^+, w) \rightarrow$
  $N_2(X\ ^1\Sigma_g^+, v-1) + N_2(X\ ^1\Sigma_g^+, w + 1)$ R2

Nitrogen molecule in ground state has 60 vibrational levels (from 0th to 59th)[8]. The SSH (Schwartz-Slawsk-Herzfeld) theory was used in the presented model[9], because it is easier than quantum mechanic theory, where calculations are more complicated and need longer computation time than

SSH theory. On the other hand, SSH theory allows calculation of the rate coefficients for the first 46 vibration levels only.

The rate coefficients of all two body collisions must be known for the numeric model of V-T process. 46 different particles with 46 kind of two body reactions are used in SSH theory because the state of the second interacting particle is not resolved. Each particle can transfer its state to any from 45 others but transition with $\Delta v > \pm 1$ have very low probability at temperatures below 1,000 K and thus can be neglected.

This is reason why model calculates and uses only $P_{v,v-1}$ (probability of transition from v to $v-1$) and $P_{v-1,v}$ (probability of transition from $v-1$ to v).

Calculation of Transition

Transitions probabilities for both V-T and V-V processes were calculated using SSH theory for the lowest 46 vibrational levels using the following set of equations.

$$E_v = \hbar\omega\left[\left(v+\frac{1}{2}\right) - \chi_e\left(v+\frac{1}{2}\right)^2\right] \tag{1}$$

$$P_{v,v-1} = Z\frac{v}{1-\chi_e v}\frac{2\mu}{\mu^{A_2}}\frac{kT_g}{\hbar\omega}F\left(Y_{v,v-1}\right) \tag{2}$$

$$Z = \pi d^2\left(8kT_g/\pi\mu\right)^{1/2} \tag{3}$$

$$F(y) \equiv \begin{cases} \frac{1}{2}\left[3 - \exp\left(-\frac{2y}{3}\right)\right]\exp\left(-\frac{2y}{3}\right) & \text{for } 0 \le y \le 20 \\ 8\left(\frac{\pi}{3}\right)^{1/2} y^{7/3}\exp\left(-3y^{2/3}\right) & \text{for } y \rangle 20 \end{cases} \tag{4}$$

$$Y_{v,v-1} = g(1 - 2\chi_e v) \tag{5}$$

$$g = \left(\frac{1}{2}\right)^{3/2}\left(\frac{4\pi^2\varpi^2 L^2\mu}{kT_g}\right)^{1/2} \tag{6}$$

$$P_{v,v-1}^{w-1,w} = Z\frac{v}{1-\chi_e^{A_2}v}\frac{w}{1-\chi_e^{B_2}\varpi}\frac{\mu kT_g}{8L^2\mu^{A_2}\varpi^{A_2}\mu^{B_2}\varpi^{B_2}}F\left(Y_{v,v-1T}^{w-1,w}\right) \tag{7}$$

$$Y_{v,v-1}^{w-1,w} = \frac{\pi L}{\hbar}\left(\frac{\mu}{2kT_g}\right)^{1/2}\left|\Delta E_{v,v-1}^{w-1,w}\right| \tag{8}$$

$$\Delta E_{v,v-1}^{w-1,w} = \hbar\omega^{A_2}\left(1 - 2\chi_e^{A_2}v\right) - \hbar\omega^{B_2}\left(1 - 2\chi_e^{A_2}\varpi\right) \tag{9}$$

$$P_{v-1,v} = P_{v,v-1}\exp\left(-\frac{\hbar\omega}{kT_g}\left(1 - 2\chi_e v\right)\right) \tag{10}$$

$$P_{v-1,v}^{w,w-1} = P_{v,v-1}^{w-1,w}\exp\left(\frac{\Delta E_{v,v-1}^{w-1,w}}{kT_g}\right) \tag{11}$$

$$P_{v,v-1} = v\left(\frac{1-\chi_e}{1-\chi_e v}\right)P_{1,0}\frac{F\left(Y_{v,v-1}\right)}{F\left(Y_{1,0}\right)} \tag{12}$$

$$P_{v,v-1}^{w-1,w} = v\varpi\left(\frac{1-\chi_e^{A_2}}{1-\chi_e^{A_2}v}\right)\left(\frac{1-\chi_e^{B_2}}{1-\chi_e^{B_2}\varpi}\right)P_{1,0}^{0,1}\frac{F\left(Y_{v,v-1}^{w-1,w}\right)}{F\left(Y_{1,0}^{0,1}\right)} \tag{13}$$

$$P_{1,0} = 1{,}07.10^{-12} T_g^{3/2} F(Y_{1,0}) \tag{14}$$

$$P_{v,v-1}[\text{OK}] = \frac{P_{v,v-1}}{\left[a + 35{,}5\left(\dfrac{v-1}{39}\right)^{0,8}\right]} \tag{15}$$

$$a(T_g) = 0{,}2772.T_g - 80{,}32 \tag{16}$$

$$P_{0,1}^{0,1} = 6{,}35.10^{-17}.T_g^{3/2} \tag{17}$$

$$P_v^{N_2-N} = \sum_{w \langle v} P_{v,w}^{N_2-N} \tag{18}$$

Variables	Names of variables
$a(T_g)$	Correction coefficient
d	Particle diameter
$\Delta E_{v,v-1}^{w-1,w}$	Energy difference of simultaneous transfer from level "v" to "$v-1$" and from "$w-1$" to "w"
E_v	Vibration energy
$F(y)$	Adiabatic factor
$F(Y_{1,0})$	Adiabatic factor, for transfer from 1 to 0 level
$F(Y_{0,1})$	Adiabatic factor, for transfer from 0 to 1 level
$F\!\left(Y_{1,0}^{0,1}\right)$	Adiabatic factor, for transfer from 1 to 0 level by first molecule and from 0 to 1 by second molecule
$F(Y_{v,v-1})$	Adiabatic factor for "v" to "$v-1$" transfer
$F\!\left(Y_{v,v-1}^{w-1,w}\right)$	Adiabatic factor, for transfer from "v" to "$v-1$" level by first molecule and from "$w-1$" to "w" by second molecule
g	Factor
$\hbar$	Modified Planck constant
k	Boltzmann constant
L	Parameter characterizing magnitude of repulsion potential
μ	Total reduced mass of both molecules by collision
μ^{A_2}, μ^{B_2}	Reduced mass of molecule A_2 and B_2
$P_{1,0}$	Probabilities of excitation transfer from vibration level 1 to level 0
$P_{0,1}^{0,1}$	Probability of simultaneous transfer from vibration level 1 to level 0 and from level 0 to 1 by second molecule
$P_{v-1,v}$	Probability of transfer from vibration level "$v-1$" to level "v"
$P_{v,v-1}$	Probability of transfer from vibration level "v" to level "$v-1$"
$P_{v,v-1}[\text{OK}]$	Probability of transfer from vibration level with correction (from SSH theory to quantum mechanic theory)
$P_{v,v-1}^{w-1,w}$	Probability of simultaneous transfer from vibration level "v" to level "$v-1$" and "$w-1$" to "w" by second molecule
$P_{v-1,v}^{w,w-1}$	Probability of simultaneous transfer from vibration level "$v-1$" to level "v" and "w" to "$w-1$" by second molecule
T_g	Neutral gas temperature
v	Vibration level

|	
ω	Fundamental vibration frequency (for N_2 ground state $\omega = 4.443 \cdot 1{,}014$ Hz)
$\omega^{A_2}, \omega^{B_2}$	Vibration frequency of A_2 and B_2 molecule
χ_e	Constant of anharmonicity (second virial coefficient)
$\chi_e^{A_2}, \chi_e^{B_2}$	Anharmonicity constant for A_2 and B_2 molecule
y	Distance between molecules A_2 and B_2
$Y_{v,v-1}$	Factor
$Y_{v,v-1}^{w-1,w}$	Factor
Z	Collisions frequency

Our model includes two basis of calculation. The first one is based fully on theory, the second way uses experimental value of $P_{1,0}$ probability and the other probabilities are computed by SSH theory.

In presented schemes 1 and 2 you can see sequence of equations used in numeric model.
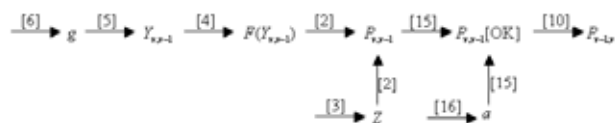
Scheme 1

Equations for calculation of probabilities for vibration-translation transfer $P_{v,v-1}$ and $P_{v-1,v}$ by SSH theory with correction to quantum mechanic theory. This scheme shows calculation of all probabilities from SSH theory.
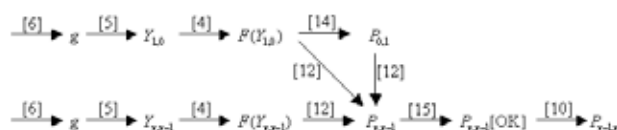
Scheme 2

Equations of calculation probabilities for vibration-translation transfer $P_{v,v-1}$ and $P_{v-1,v}$ by SSH theory with correction to quantum mechanic theory. This scheme shows calculation of probabilities from SSH with used experimentally obtained probability $P_{1,0}$ value.

Results

The gas temperature, pressure and vibrational quantum number are the main parameters of calculation. The calculated rate coefficients are shown in Figs. 1 and 2. The probabilities for the exothermic V-T transfer $P_{v,v-1}$ are higher than probabilities for endothermic V-T transfer $P_{v-1,v}$. Both these probabilities increase with the increase of vibration quantum number because energy difference between neighbour levels decreases with the increase of v according to the anharmonic potential curve of electronic state.

Also it can be seen that probabilities obtained by theory ("TH") are smaller than probabilities from theory with experimental value of $P_{1,0}$ coefficient ("EX"). These figures show the strong dependence of all probabilities on temperature. Temperature increase of about three times evokes the probability increase of about three orders in magnitude.
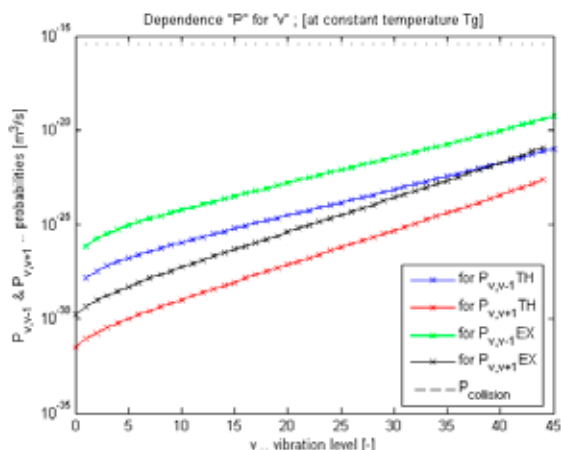
Fig. 1. **Dependence of probabilities for vibration-translation energy transfer $P_{v,v-1}$ and $P_{v-1,v}$ on vibration level at temperature 400 K. Curves "TH"are just from theory SSH with correction, and curves "EX" are from theory with experimental value of $P_{1,0}$ coefficient**
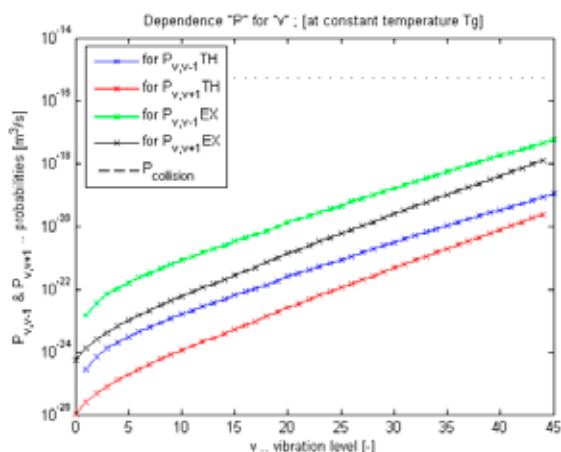

Fig. 2. **Dependence of probabilities for vibration-translation transfer $P_{v,v-1}$ and $P_{v-1,v}$ on vibration level at temperature of 1,000 K. Curves "TH" are just from SSH theory with correction, and curves "EX" are from theory with experimental value of $P_{1,0}$ coefficient**

Vibration Distribution Function

Vibration distribution function (VDF) is time dependent during the post-discharge. The initial VDF is the same as in an active discharge and it can be calculated using active discharge conditions. Fig 4. shows VDF time evaluation at 300 K and pressure of 1,000 Pa.

Evolution of VDF shows decrease of population at the highest vibration levels. The populations at lower levels do not show any significant changes during initial part of post-discharge. As particles at higher vibrational levels have higher V-T probabilities, they are more or less in Boltzmann distribution (see blue line in Fig. 4., particles with v>20), while particles at the lower vibration levels conserve more or less
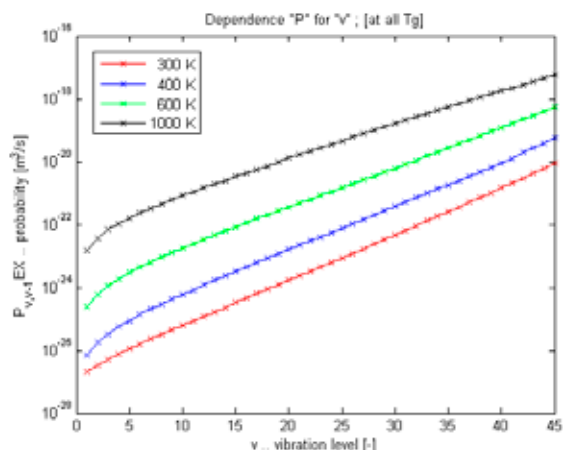
Fig. 3. **Dependence of probabilities $P_{v,v-1}$ (from theory and experimental $P_{1,0}$) under temperature 300 K (red line), 400 K, 600 K and 1,000 K (blue lines) for vibration level**
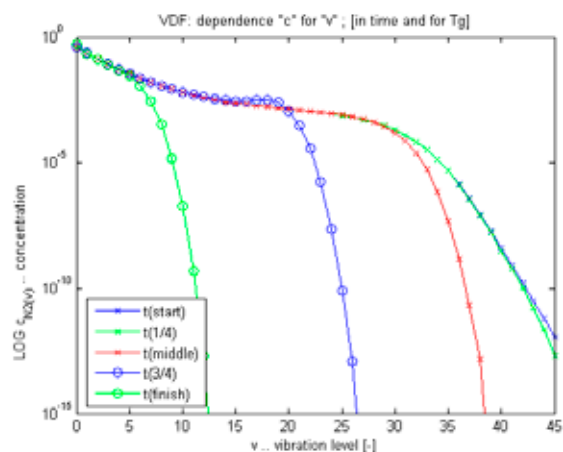
Fig. 4. **Time evaluation of vibration distribution function at 300 K (t(start) is t = 10^{-5} s, t(1/4) is t = 10^{-3} s, t(middle) is t = 10^{-1} s, t(3/4) is t = 10^{1} s, t(finish) is t = 10^{3} s)**
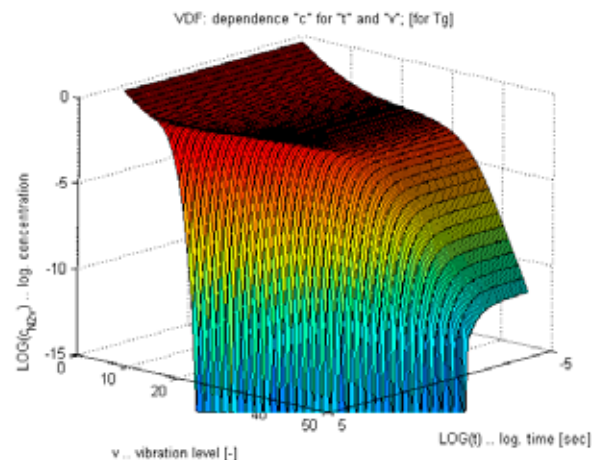
Fig. 5. **3D diagram of vibration distribution function at 600 K**
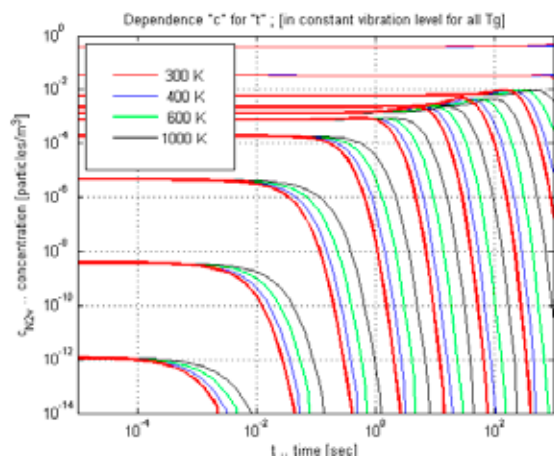
Fig. 6. **Relative populations at selected vibration levels during the post-discharge. Red lines are concentrations at temperature of 300 K and blue lines are concentrations at 400 K, 600 K and 1,000 K**

Fig. 7. **Vibration energy distribution function at 1,000 K, where t(start) is t = 10^{-5} s, t(1/4) is t = 10^{-3} s, t(middle) is t = 10^{-1} s, t(3/4) is t = 10^{1} s, t(finish) is t = 10^{3} s, smooth red line is Boltzmann distribution for infinity time. EvDF is nearly the same as VDF but vibration levels are recalculated to vibration energy**

Fig. 8. **Vibration energy distribution function (EvDF) at 300 K (red lines), 400 K, 600 K and 1,000 K, t(start) is t = 10^{-5} s, t(1/4) is t = 10^{-3} s, t(middle) is t = 10^{-1} s, t(3/4) is t = 10^{1} s, t(finish) is t = 10^{3} s**

post-discharge. As particles at higher vibrational energy have higher V-T probabilities, they are more or less in Boltzmann distribution (see in Fig. 7, particles with $E_v = 0.9 \times 10^{-18}$ J), while parti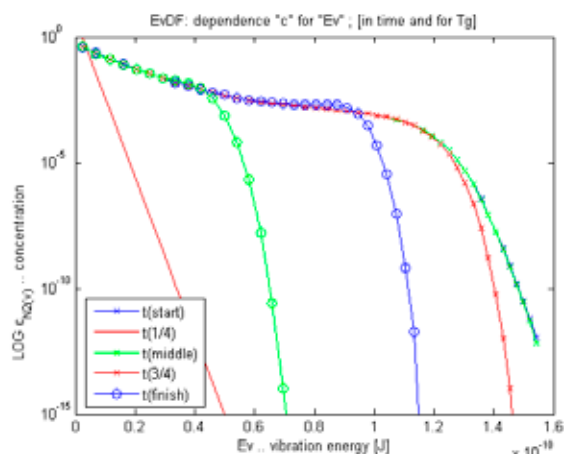cles at the lower vibration energy conserve more or less the initial distribution function. The same situation is described also in Fig. 8 for more temperatures.

The small increase of the population is well visible at the decay time of 10 s originates in the faster decrease of populations at higher levels.

Conclusions

This work was focused on the numeric modelling of V-T energy transfer in nitrogen molecule ground state. This process is one of the main mechanisms during the post-discharge when the systems changes its conditions from an active discharge to the common Boltzmann distribution at given (usually ambient laboratory) temperature.

The calculations were made using two approaches. The SSH theory with correction to the quantum mechanics was used in the first one, the second one was the same with included experimental value of $P_{1,0}$ probability. The V-T probabilities calculated by the first procedure were significantly smaller than that calculated by the other procedure. In both cases, probabilities for the exothermic V-T transfer (change of vibrational level $P_{v,v-1}$) are significantly higher than that for the endothermic (change of vibrational level $P_{v-1,v}$). The V-T transfer probability increased with the increase of vibrational quantum number due to the anharmonic potential curve of the ground electronic state. Due to this fact, the Boltzmann equilibrium distribution was reached at earlier post-discharge times at higher vibrational levels; the highest levels (over 40) were nearly the equilibrium even at begin of calculation.

The temperature had very high effect on the transition probabilities. The temperature increase of about three times evoked the V-T probability increase of three orders independently on vibrational level. On the other hand, the decrease of

the initial distribution function. The same situation is described also in Fig. 7 for higher temperature.

Fig. 6. demonstrates the time evolution of relative vibrational populations. It can be seen that all populations are significantly higher at higher temperatures. It is also evident the populations at higher levels decrease earlier than at lower levels.

Energy vibration distribution function (EvDF) is time dependent during the post-discharge. The initial EvDF is the same as in an active discharge and it can be calculated using active discharge conditions. Fig. 7. shows EvDF time evolution at 1,000 K and pressure of 1,000 Pa.

Evolution of EvDF shows decrease of population at the highest vibration energy. The populations at lower vibrational energy do not show any significant changes during initial part of
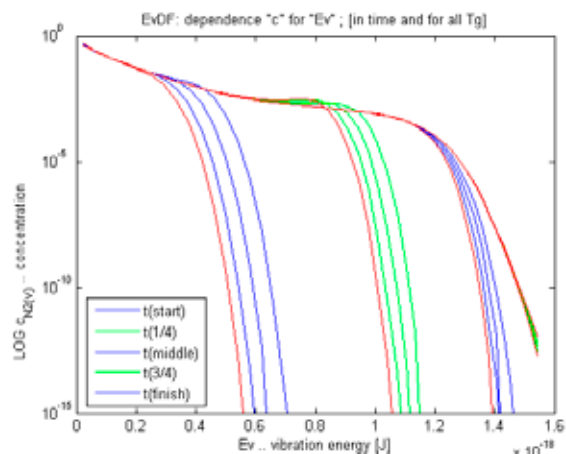
vibrational populations during time is slower at higher temperatures.

The presented model showed evolution of VDF by V-T process. For the description of any real system more other processes (V-V, pooling, step-vise ionization and others) are needed to include and calculation of real system realization needs a lot of hard work and time. Its necessary to know more constants of system, new rate coefficients (that are strongly temperature dependent) and thus it is a really complex task. V-T process simulation was the first step on the way to complex numeric model of the post-discharge phenomenon.

REFERENCES
1. Guerra V., Sa P. A., Loureiro J.: J. Phys. D, Appl. Phys. *34*, 1745 (2001).
2. Guerra V., Sa P. A., Loureiro J.: Europ. Phys. J. Appl. Phys. *28*, 125 (2004).
3. Pintassilgo C. D., Loureiro J., Guerra V.: J. Phys. D, Appl. Phys. *38*, 417 (2005).
4. Krčma F., Mazánková V., Soural I.: Publications of the Astronomical Observatory of Belgrade *82*, 133 (2007).
5. Loureiro J., Ferreira C. M.: J. Phys. D, Appl. Phys. *19*, 17 (1986).
6. Paniccia F., Gorse C., Cacciatore M., Capitelli M.,: J. Appl. Phys. *61*, 3123 (1987).
7. Zelechov A., Rapp D., Sharp T. E.: J. Chem. Phys. *49*,286 (1968).
8. Guerra V.: PhD thesis, Instituto Superior Technico, Lisbon (1998).
9. Guerra V.: *Private communications*, Lisbon, (January-May 2007).
10. Soural I., Diploma thesis, Brno University of Technology, Faculty of Chemistry, (2007).

P26 EVALUATION OF INTAKE CAPPABILITY OF LCM SURFACE BY ADSORPTION DYEDING METHOD AND ITS UTILIZATION FOR EVALUATION OF CHANGES IN SURFACE POLARITY CAUSED BY DCSBD LOW-ENERGY PLASMA

RADOVAN TIŇO, LIVIA BEŇOVÁ and SVETOZÁR KATUŠČÁK

Institute of Polymer Materials, Department of Chem. Technology of Wood,Pulp and Paper, Slovak University of Technology in BratislavaRadlinského 9, 812 37, Bratislava, Slovak Republic,
radovan.tino@stuba.sk

Introduction

Use of the color information for non destructive evaluation of wood has some advantages and drawbacks. Advantages of color information on lignocellulosics: *Visually* evaluated color information are widely used in common praxis and in everyday life for grading, production control, sale, decisions of consumers, aesthetic and economical value evaluation, in utilisation, renovation and recycling of wood materials and products. The quantified color data have shown to be valuable tool in forestry and forest products area, especially in the areas and processes of production of decorative wood[1], storage[2], drying and steaming[3]; veneers production[4], coating[5], testing of ageing[6], aesthetic evaluation[7], pulp and paper production[8], wood pyrolysis[9] tec.

The most widely used in the material engineering area inclusive wood science and technology is the CIE system.

The advantage of usage the color information for evaluation of diferences between controled and plasma modified surfaces colored with standard dyestuff solution in water is the potentialy practical readability of the method and the color information. The method would express more or less directly the water-repellent properties: the less water soluble dyestuff has been adsorbed the higher the water-repellency and the hydrophobicity. It could further correlate with the end-use properties of plasma treated wood surfaces e.g. mantainability and dirtability.

Disadvantages of color information on lignocellulosics: In spite of their value-estimating and industrial meaning analysed in the works cited above, are the color information and another optical properties of wood not so systematically known as the other physical, mechanical and chemical properties.

We have selected CIE $L^*a^*b^*$ – space as the most suitable space for the communication on the color of wood and for systematic presentation of the wood color as well as for monitoring color differences and kinetic changes of lignocellulosic materials[10,11].

For measurement of changes of surface polarity there are used methods and parameters such as: contact angle, surface energie of solid surfaces, spectroscopic methods for measurement of polar and non-polar functional groups and compounds, for an instance after their extraction from the surface of lignocellulosic materials (LCM)[12]. For characterization of LCM surfaces nowadays exists also many spectroscopic methods, which investigate functional groups of the surface, while many of them work at ultra high vacuum.[13] If it comes to the change of LCM surface ad effectum of plasma, change of ability to absorb color substances can occur. For example, when hydrophobization strikes, LCM surface takes less of polar dyeding solution or dyestuff.

Measurement of the change of surface polarity should be in such a case performable also on the basis of change colorability or change of dyestuff adsorption on the unmodified surface as well as on the surface modified with Diffuse surface coplanar barrier discharge (DCSBD).

Experimental

In experimental part was proposed new method for measurement of polarity changes on the LCM surface by means of colorimetry.

Change of colourity can be measured colorimetricaly in whole range by microspectrophotometer, which gives the exact value ΔE^*.

$$\Delta E^* = \sqrt{(\Delta L^*)^2 + (\Delta a^*)^2 + (\Delta b^*)^2} \qquad (1)$$

Value of ΔE^* refered to a plasma untreated dyed LCM surface (control sample). Measurement of color coordinates of surfaces was performed by colorimeter Minolta, CR–200.

Surface analysis offers information about chcemical composition, level of impurity, physical structure or morphology of surface.

By measuring the contact angle it is possible to study effects of wetting. For reproducibility of results of measurement contact angle is necessary to keep constant conditions: quality of testing solution, constant volume and size of drop, quality of surface (homogenity). Direct measurement of contact angle shoul be performed on lighted drop sitting on solid surface.

Contact angle θ by Surface energy evaluation system (SEE System)[14], which captures profile of solid/liquid meniscus of a liquid drop set on a solid surface with build-in camera. Images taken with camera are subsequently transfered into SEE System software, where they are processed for evaluation of surface free energy, it's portions, contact angles etc.

Preparation of Samples

Samples of European spruce (*Picea excelsa*) with dimensions of $8 \times 2.5 \times 0.5$ cm were used during the experiment. The spruce was chosen as a commercially used wood. All samples were air-conditioned prior the treatment in air-conditioned chamber with relative humidity RH = $50 \pm 2\%$ and temperature T = 23 ± 1 °C during at least 4 hours. The surface of samples was sanded by 150-grit paper. After sanding the spruce surface was blasted by air stream to remove attached dust. The spruce surface was air blasted also after the plasma treatment, in order to remove possible low molecular

fragments from the surface. Water droplet contact angle was measured with Surface energy evaluation system (SEE System)[14]. Plasma treatment of wooden samples was done by the Diffuse Coplanar Surface Barrier Discharge (DCSBD) – a planar source of the low-temperature plasma[15]. The DCSBD electrodes, consisting of 15 pairs of silver strip electrode embedded 0.5 mm below the surface of 96% Al_2O_3 ceramics, was supplied by HV generator LIFETECH VF300. The mutual distance of the 200 mm long and 2 mm wide silver strip electrodes was 1 mm. Discharge was supplied by harmonic 1,86 kHz sine high voltage of (100 ± 5) Watt, which gives 0.92 W cm^{-2} of power per treated area of sample.

The electrode was mounted inside the closed reactor chamber equipped with forced air ventilation with air flow 4 dm^3 min^{-1}.

The mutual distance d_{p-w} was adjusted by the stack of 0.13 mm thick microscope cover slips in amount (0–10 pieces) inserted between the surface of plasma electrode and surface of treated wood sample. After the treatment, samples were put again into the air-cond. chamber, where stayed another 24 hours. After this periode they were colored with 10% water solution of stain commercially known as Spoloxyl blue 6. Filter paper previously submerged 10 s in stain solution was put on the sample surface, then was loaded with 3 kg weight during 5 s and on the end, excess of stain was sucked out by clean filter paper loaded with 3 kg weight during 5 s. After this procedure, samples stayed for 4 hours in air-conditioned chamber and after that they were measured by colorimeter Minolta CR–200. Color coordinates of LCM surfaces were measured and color difference ΔE^* was calculated from them.

Measurement of Contact Angle

The thermodynamic properties of spruce wood samples were investigated by means of the sessile drop technique using the Surface Energy Evaluation System (SEE System, http://www.advex-instruments.cz,10.5.2008). The contact angles were measured directly from the images of the solid/liquid meniscus of a liquid drop set on a solid, taken with build in camera. Because the sessile drop gradually spreads over the wood surface, thus reducing its contact angle value, the initial contact angle was taken only.

Measurement of Water Uptake Time

For measurement of water uptake time was used 5-µl droplets of deionized water, which were applied onto spruce surface with Krüss single auto-dosing system D03004. Water uptake time was measured at the same time as the measurement of contact angles. The determination of water uptake time has been done in accordance with[16] in order to mutually compare obtained results. The water uptake time was the time interval from the impact of the droplet to the complete penetration of the droplet into the wood surface (no optical reflection can be seen).
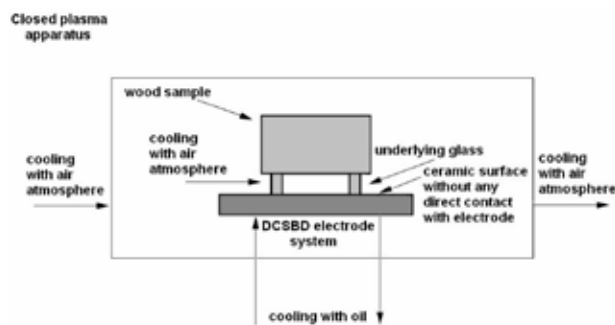
Fig. 1.   **DCSBD plasma system scheme**
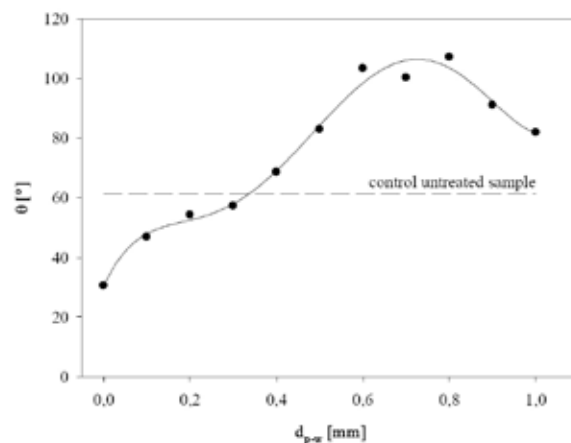
Fig. 2.   **Change of contact angle as a function of different mutual distance dp-w between surface of treated sample and surface of DCSBD plasma electrode. Dashed line represents untreated control sample**

Results

Table I sumarizes results from the measurements of color coordinates, total color difference, surface contact angle and water droplet uptake time as a function of mutual distance of the sample surface and surface of plasma electrode. By having look at color coordinates of plasma treated samples and their comparison with untreated sample is obvious, that plasma causes changes in colorability of plasma treated lignocellulosic surfaces. At the same time it is possible to say, that contact angle of plasma untreatet sample is almost the same as that treated from the distance 0.3–0.4 mm above plasma electrode. The same behaviour was observed in the case of water uptake time.

Fig. 2. shows dependance of contact angle θ on mutual distance d_{p-w} between surface of treated sample and surface of DCSBD plasma electrode. There is also present line representing value of 62 ° which matches with plasma untreated sample (control). At distance between 0.3 and 0.4 mm is contact angle of the plasma treated surface equall 62 °. Plasma makes treated surface hydrophilic (i.e. contact angle is less than 62 °). The generation of plasma at zero distance (i.e. the wood sample lying directly on the DCSBD electrode) was

Table I
Evaluation of color coordinates of stained LCM surfaces treated with DCSBD plasma by CIELab system. DCSBD plasma treated surfaces were colored with 10% water solution of stain commercially known as Spoloxyl blue 6 and are compared with plasma untreated controll sample, where: $d_{p\text{-}w}$ – mutual distance of the surface of sample and surface of plasma electrode, θ – contact angle, τ_w-water uptake time, L^* – lightness, a^* – red-green axis, b^* – yellow-blue axis and ΔE^* – total collor difference

$d_{p\text{-}w}$ [mm]	L^*	a^*	b^*	ΔL^{*2}	Δa^{*2}	Δb^{*2}	ΔE^*	θ [°]	τ_w [s]
Cont.	35.57	−8.22	−27.7	0	0	0	0	62	30
0	37.4	−11.2	−26.3	3.5	9	1.9	3.8	31	4
0.1	41.3	−13.9	−23.3	32.3	32.6	19	9.2	47	10
0.2	41.8	−14.7	−22.1	38.6	41.9	31	10.6	54	14
0.3	40.3	−14.0	−20.5	22.4	33.8	52	10.4	57	16
0.4	41.7	−13.5	−21.4	37.2	27.7	40	10.2	69	45
0.5	42.3	−15.7	−18.6	45.4	55.8	84	13.6	83	450
0.6	48.4	−15.1	−8.2	164.6	47.3	381	24.4	103	630
0.7	44.8	−13.3	−14.5	84.8	26.0	173	16.9	100	550
0.8	52.7	−12.3	−4.5	294.5	16.8	540	29.2	107	870
0.9	49.0	−15.3	−12.3	180.4	50.7	238	21.7	91	510
1	43.2	−14.3	−19.2	57.5	37.2	73	12.9	82	370

allowed due to the natural porosity and roughness of wood sample.

Samples in direct contact with the plasma electrode became more hydrophilic after the treatment which corresponds with significantly higher rate of water uptake as can be seen on Fig. 3. Samples which were more than 0,4 mm over the surface of plasma electrode became after the plasma treatment more hydrophobic which corresponds with longer period of water uptake (Fig. 3.) on their surface as well as with the higher contact angle in comparison to that of control sample.

Fig. 4 shows dependance of the total color difference on ΔE on mutual distance $d_{p\text{-}w}$ between surface of treated spruce sample and surface of DCSBD plasma electrode. There are two peaks. First lays in the range of 0mm up to 0.4 mm. Total

color difference rises from 0 to 10.6 at $d_{p\text{-}w} = 0.2$ mm and then slowly decreases to 10.2 at $d_{p\text{-}w} = 0.4$ mm which corelates with the thickness of plasma layer generated in air with the used experimental setup. By further increasing the mutual distance, ΔE^* starts to rise again and reaches maximum value of 29.2 at $d_{p\text{-}w} = 0{,}8$–$0{,}9$ mm and then starts to decrease. It seems to be, that plasma has two effects. One, when samples are in close distance up to 0.3–0.4 mm, where are treated directly with the generated plasma layer. At distances above 0.4 mm there is no visible generated plasma layer, but there is still area above the layer, which is also active at plasma

Fig. 3.   **Change of water uptake time τ_w as a function of different mutual distance dp-w between surface of treated spruce sample and surface of DCSBD plasma electrode. Dashed line represents untreated control sample**

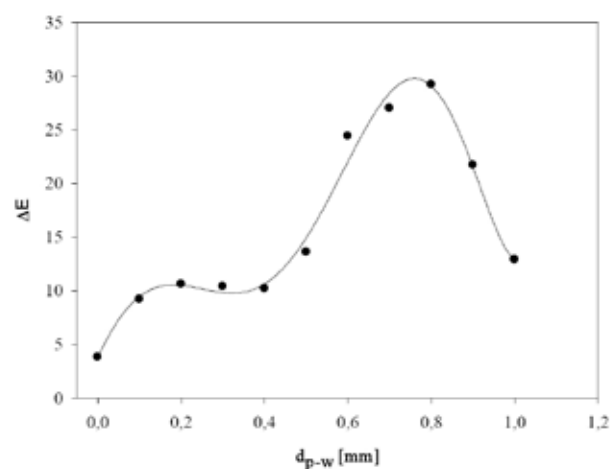Fig. 4.   **Change of total color difference ΔE^* as a function of different mutual distance $d_{p\text{-}w}$ between surface of treated spruce sample and surface of DCSBD plasma electrode. The biggest color difference was obtained when the sample was during the plasma tretment approximately 0.8 mm over the surface of plasma electrode. At this point also the strongest hydrophobization took the effect**

treatment. This area is responsible for hydrophobization of lignocellulosic surfaces, while are bellow 0.3 mm makes surface hydrophilic. However, whole range of distances from 0 mm up to observed 1.17 mm causes changes in colorability

Table II
Order of coefficients of correlation between results from colorimetric measurements (parameters CIELab (ΔE^*, L^*, a^*, b^*, $(\Delta L^*)^2$, $(\Delta a^*)^2$, $(\Delta b^*)^2$) and commonly used parameters describing the polarity of lignocellulosic materials (θ contact angle, τ_w – water uptake time)

| Order | Parameter | Coefficient of corelation R^2 for | |
		Contact angle (θ)	Water uptake time (τ_w)
1	b^*	0.91	0.93
2	ΔE^*	0.90	0.92
3	L^*	0.87	0.89
4	$(\Delta b^*)^2$	0.81	0.89
5	$(\Delta L^*)^2$	0.78	0.87
6	a^*	–0.33	–0.14
7	$(\Delta a^*)^2$	0.31	0.15

Table II shows color parameters measured at samples of spruce treated by DCSBD plasma and their correlations with the contact angle and water uptake time. Individual paramaters are ordered from that with the highest correlation with both above mentioned characteristics of surface polarity, which is parameter b^*. This parameters correlates with contact angle as well as with the water uptake time very well (91and 93 %). Also ΔE^*, L^*,$(\Delta b^*)^2$, $(\Delta L^*)^2$ correlate quite well, so they can be used for evaluation of changes on the lignocellulosic surface caused by DCSBD plasma treatment. Parameters a^* and $(\Delta a^*)^2$ don't correlate with above mentioned characteristics of surface polarity and they are not suitable for evaluation of intake capability of lignocellulosic surfaces by adsorption dydeding method.

Conclusions

　　The particular aim of this paper is to propose and test characteristic color parameters and to correlate them with polarity changes on the wood surface made by DCSBD plasma treatment.

　　The new method for evaluation of changes in polarity of solid lignocellulosic surfaces by measurement of differencies of trichromatic components between untreated and plasma treated surface colored by given standard dye was developed. Measurement was performed in CIE Lab system. It was verified, that by measurement of color difference it is possible

to evaluate polarity of lignocellulosic surfaces, what was confirmed by comparison of this method and other utilized methods for measurement of polarity changes such as measurement of water uptake time and contact angle.

REFERENCES
1. Phelps J. E., Rink G., Workman, E. C. Jr.*: Proceedings from All-Division 5 Conference "Forest Products" Vol2*, p.203, 23.–28. August 1992, Nancy.
2. Kucera L. J., Katuscak S.: *in Weinfelden: Holz-Farbe-Gestaltung, 4.-5. 11. 1992, Lignum Zürich* 1992, pp.43-52.
3. Avramidis S., Ellis S., Liu, J.: *Proceedings from All-Division 5 Conference "Forest Products" Vol.2*, 23–28 August 1992, Nancy.
4. Katuščák S. et al.: Res. Rep. 48/90, State For.Prod.Res. Institute Bratislava 1990.
5. Németh K.: Möbel und Wohnraum, Leipzig *38*, 121 (1985).
6. Plackett D. V., Dunningham E. A., Singh, A. P.: Holz als Roh- und Werkstoff *50*, 135 (1992).
7. Goncales J., Janin G., Keller R.: *Proceedings from "All-Division 5 Conference "Forest Products"*, Vol.1, 245, 23.–28. August 1992, Nancy.
8. Katuscakova G., Katuscak S.: Papir Celuloza *41*,41 (1986)
9. Bourgois J., Janin G., Guyonnet R.: Holzforschung *45*, 377 (1991).
10. Katuščák S., Katuščákova G.: Holzforschung *41*, 315 (1987)
11. Kucera L. J.: Institut für Wald- und Holzforschung ETHZ, Fachbereich Holzkunde und Holztechnologie, Zürich 1986.
12. Nováková E: *Diploma thesis*, STU, Bratislava 2007
13. Sparrow G. R., Mishmash H. E.: *ASTM STP 643, N. S. McIntyre,* Ed., American Society for Testing and Materials, 1978, pp. 164–1 81.
14. Bursikova V., St'ahel P., Navratil Z., Bursik J., Janca J.: *Surface Energy Evaluation of Plasma Treated Materials by Contact Angle Measurement.* Masaryk University, Brno, 2004.
15. Šimor M., Rahel J., Vojtek P., Brablec A., Černák M.: Appl. Phys. Lett. *81*, 2716 (2002)
16. Rehn P., Wolkenhauer A. et al Surf Coat Technol *174–175*, 515 (2003).

P27 EVALUATION OF EFFIENCY, RELEASE AND OXIDATION STABILITY OF SEABUCKTHORN MICROENCAPSULATED OIL USING FOURIER TRANSFORMED INFRARED SPECTROSCOPY

MONICA TRIF and CARMEN SOCACIU

Department of Chemistry and Biochemistry, University of Agricultural Sciences and Veterinary Medicine, Cluj-Napoca, 400372, Romania
monica_trif@hotmail.com

Introduction

Alginate and *k*-carrageenan are seaweed carbohydrate biopolymers commonly used in bioencapsulation.

The high content of polyunsaturated fatty acids, carotenoids and other oxygen sensitive lipid molecules make seabuckthorn oil susceptible to oxidation, limiting its application. This paper examines the microencapsulation efficency, the release and oxidation process of seabuckthorn oil encapsulated in ionotropically crosslinked alginate-carrageenan complex beads, using the Fourier transformed infrared (FTIR) spectroscopy.

Experimental

Sodium alginate (SA) was purchased from Promova, k-carrageenan (k-Car) from Danisco, calcium chloride ($CaCl_2$) from Sigma Aldrich, sea buckthorn oil (SBO) was extracted from the fruits of sea buckthorn, which were collected from Transilvania region, Romania.

Beads Preparation

SA (0.75 %, w/v) and *k*-Car (0.75 %, w/v) were dissolved in de-ionized water and were used to encapsulate the SBO by ionotropically cross-linked gelation. The SBO-SA-*k*-Car emulsion obtained was dropped using a syringe with a needle (0.4×20 mm) into a hardening bath 2% (w/v) solution of $CaCl_2$ in water.

Microscopy

Images of emulsions at magnification $10 \times$ were obtained using an inverted microscope Olympus, with a digital camera.

FTIR-ATR measurements

The FTIR spectra were obtained with a Fourier transform spectrometer (PerkinElmer), equipped with ATR. The oxidation process induced by UV light (254 nm) after 1, 4 and 6 hours was monitored calculating the ratios between absorbance of some relevants spectral bands of free and encapsulated oil.

Encapsulation Efficiency (EE %) of the SBO

EE % was calculated taking into consideration the amount of β-carotene contained by SBO, before and after encapsulation. The amount of β-carotene was assayed spectrophotometrically at 454 nm using tetrahydrofuran (THF) as solvent, and also as a solvent to extract β-carotene from beads. The formulae (1) was used:

$$EE \% = C_1/C_2 \times 100, \qquad (1)$$

where: C_1 = β-carotene concentration content in the SA-*k*-Car beads [mg dm^{-3}] and C_2 = β-carotene concentration in SBO before encapsulation [mg dm^{-3}].

Carotenoids Release Rates Measurement from Beads

Control release of carotenoids contents fom beads in different solvents: methanol, hexane and THF were measured spectrophotometrically. The absorption spectra were obtained with a Jasco UV-VIS spectrometer the range 300–500 nm.

Results

Emulsion stability evaluations. The microscopic imaging of the SBO-SA-*k*-Car emulsion used for encapsulation reveals the presence of polydisperse oil droplets with sizes between 20–50 μm (Fig. 1.a.).

Beads characterization. Orange beads obtained from the emulsion had a diameter between 2–3 mm and spherical shapes were obtained (Fig. 1.b.).

Encapsulation efficiency of the oil. β-carotene content of SBO oil was 1.212 mg dm^{-3}. The β-carotene content in the SA-*k*-Car beads was 1.1964 mg dm^{-3}, showing that the EE% of β-carotene in beads was 98.71 %.

Carotenoid release rates measurement from beads. The carotenoid release rate was substantially slower in hexane than in the case of the methanol and the best release was obtained into THF (Fig. 1. c.). THF was demonstrated to be one of the best solvents to extract carotenoids, as mentioned elsewhere.

FTIR-ATR measurements. FTIR spectra of SBO, SA, *k*-Car and SA-*k*-Car blank beads are shown in Fig. 1.d..

The SA spectrum showed the characteristic peaks at 3242 cm^{-1} (OH$^-$ stretching), 1,596 and 1,407 cm^{-1} (COO$^-$ asymmetric and symmetric stretching), 1,081–1,024 cm^{-1} (C−O−C antisymmetric stretching), and carboxyl and carboxylate at about 1,000 to 1,400 cm^{-1}. The sign of O−H deformation of water is evident near band 1,640 cm^{-1} in all spectra.

FTIR spectrum of *k*-Car powder showed various distinct peaks: 3,514 cm^{-1} due to polyhydroxy (OH)n group; 2,953, 2,911 and 2,894 cm^{-1} due to the C−H stretch; 1,474 and 1,400 cm^{-1} due to C−H deformation; 1,223 cm^{-1} due to the S=O stretch of sulfate ester salt; 1,063 cm^{-1} C−O stretch of cyclic ethers; 924 cm^{-1} due to the C−O stretch of polyhydroxy groups attached to carbons.

In FTIR spectra of SBO some of the most significant bands are the following[1,2] the band at 3,485 cm^{-1} is assigned to the overtone of the glyceride ester carbonyl; band appearing at 3,005 cm^{-1} in the spectrum to the CH stretching of =C−H bonding; the two intensive bands at 2,922 and 2,853 cm^{-1} are assign to the aliphatic CH$_2$ asymmetric and symmetric
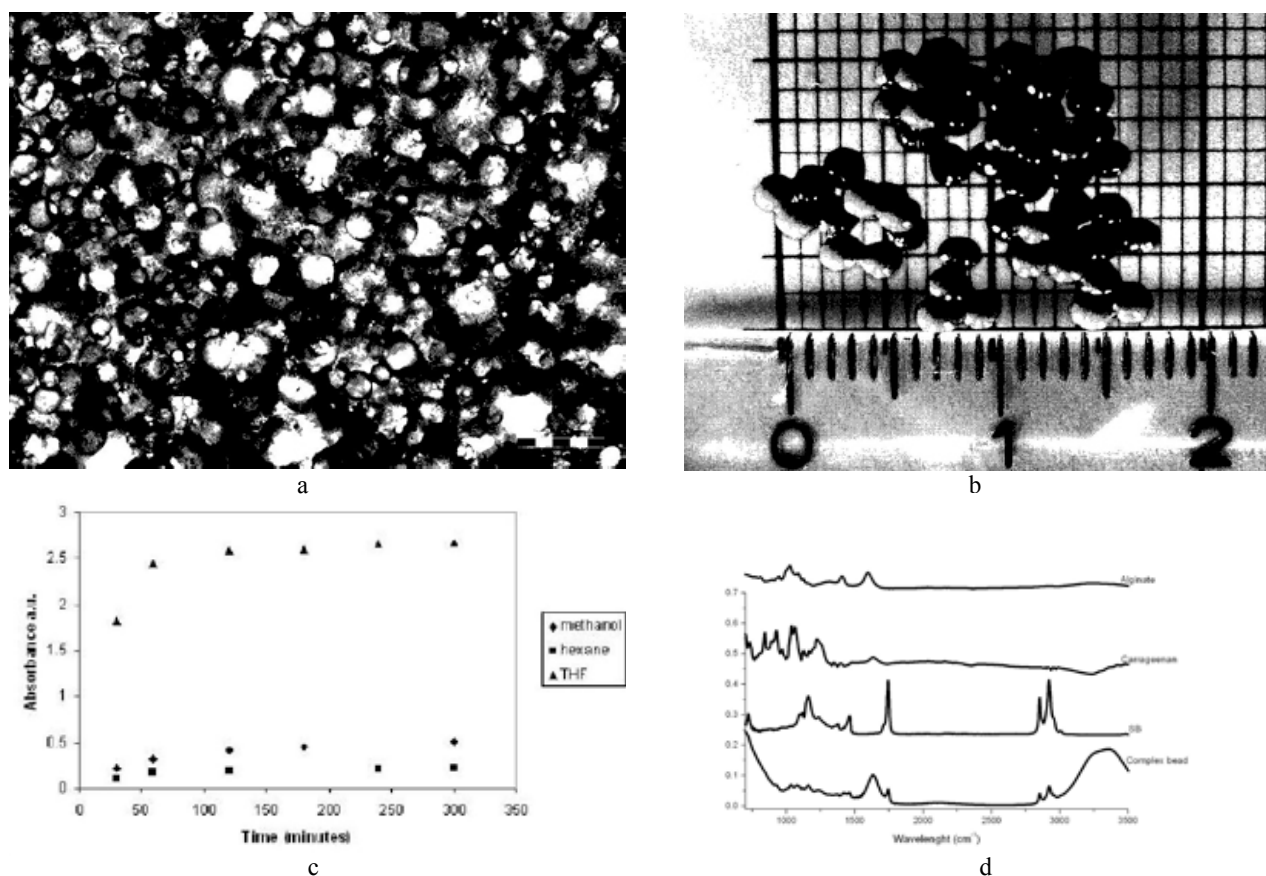
a

b

c

d

Fig. 1.   **a – the microscopic imaging of the SBO-SA-k-Car emulsion, b – SA-k-Car beads with SBO, c – carotenoid release rates measurement from beads, d – FTIR spectra of SBO, SA, k-Car and SA-k-Car blank beads**

stretching vibration, respectively; the band at 1,744 cm^{-1} is assigned to the C=O stretching vibration of the ester carbonyl functional group of the triglycerides; at 1,464 cm^{-1} is observed a band which is assigned to C=H scissors deformation vibration; the band near 1,377 cm^{-1} is assign to the bending vibration of CH$_2$ groups; the bands at 1,160 and 1,236 cm^{-1} are assign to the vibration of the C–O ester groups and CH$_2$ group.

We considered as markers of oxidation processes in SBO, the following ratios between absorbances of these important bands: $A_{2,853}/A_{3,005}$, $A_{2,853}/A_{1,744}$, $A_{2,853}/A_{1,160}$, $A_{1,744}/A_{3,005}$, $A_{1,377}/A_{3,005}$, $A_{1,160}/A_{3,005}$.

According to observations made by Guillen et al.[2], the values of ratios between absorbances of some important bands which are parameters of the oxidation level indicate a second or third stage oxidation of the pure oil comparing with the first stage of oxidation of encapsulated oil.

Conclusions

A good encapsulation efficency of 98.71 % was obtained for SBO in SA-*k*-Car complex, and the best release in THF. Encapsulation in SA-*k*-Car improved SBO stability. The encapsulated oil showed better stability against oxidation, as indicated by FTIR markers.

REFERENCES

1. Guillen M. D.and Cabo N., J. Agric. Food Chem. *47*, 709, (1999).
2. Guillen M. D.and Cabo N., J. Agric. Food Chem. *80*, 2028 (2000).

P28 ^{13}C NMR SPECTROSCOPY OF HUMIC ACIDS ECTRACTED FROM INCUBATED PLANT RESIDUES IN HAPLIC LUVISOL

ANTON ZAUJEC[a], JOZEF ŠIMA[b], JURAJ CHLPÍK[a], NORA SZOMBATHOVÁ[a] and ERIKA TOBIAŠOVÁ[a]

[a]*Department of Pedology and Geology, Agricultural University of Nitra, Tr. A. Hlinku 2, 949 76 Nitra, Slovakia,*
[b]*Department of. Inorganic Chemistry, Slovak Technical University of Bratislava, Radlinskeho 9, 812 37 Bratislava, Slovakia*
Anton.Zaujec@uniag.sk

Introduction

The humic acid (HA) plays an important role in determining soil characteristics by influencing its chemical, physical, and biological properties. Content of soil organic matter in soil is a reflection on the decomposition of existing humus and the formation of new humic substances from plant and animal remains. The chemical composition of post-harvest residues which is very important factor of formation of humic substances, as well as their physico-chemical properties should be taken into account Gonet and Debska[3]. The application of ^{13}C-NMR spectroscopy to the study of humic substances in soils and sediments has been reviewed by Chukov[2]. In this study, the reliability of the analyses was assessed the relative abundance of different HA carbon types, derived from NMR spectra.

Experimental

Post-harvest residues with different chemical composition were used as sources of organic matter in model incubation experiment, at temperature 23–25 °C, in a constant humidity of 60 % for period one years. A laboratory incubation experiment was carried out in pots with and without the soil according to following scheme:

Variant	(symbol) materials
LO	Haplic Luvisol (soil)
WR	Wheat residues (straw and roots, 4 : 1 ratio)
LO+WR	Soil + wheat residues (LO to WR = 10 : 1)
AA	Alfalfa (hay and roots, 1 : 1.5 ratio)
LO+AA	Soil + alfalfa residues (LO to AA = 10 : 1)
MR	Maize (straw and roots, 2 : 1)
LO+MR	Soil + maize residues (LO to MR = 10 : 1)
GM	Green manures residues (oat and vetch, 3 : 1)
LO + GM	Soil + green manures (LO to GM = 10 : 1 ratio)

Humic acids (HA) were extracted, purified and measured ^{13}C-NMR spectra method´s published by Zaujec et al.[6]. The relative carbon distribution was determined by integration of the signal intensity in the different chemical shift regions using an adapted integration routine supplied with the instrument software. For quantification, the spectra were used chemical shift regions described by Knicker and Ludemann[4] and Wilson[5].

Table I
Relative intensities [% of total area] for the ^{13}C NMR signals of humic acids

Spectral region/ samples of HA	Alkyl-C [%]	O-alkyl-C [%]	Aryl-C [%]	Carboxyl-C [%]
LO	17.9	20.3	37.6	24.1
WR	11.3	38.1	40.3	10.3
LO + WR	17.9	27.8	36.3	18.0
AA	17.2	33.5	33.9	15.4
LO + AA	21.6	22.2	33.1	23.1
CM	17.4	33.9	36.5	12.2
LO + MR	20.7	24.7	34.1	20.4
GM	14.2	30.8	38.9	16.1
LO + GM	20.9	26.9	32.9	19.3

Results

The HA chemical composition is evaluated from the intensity distribution among the chemical region of the different functional groups in the NMR spectra. The spectra are dominated by the signal in the chemical shift region (110–160 ppm) of aromatic/olefinic C (32.9–40.3 %) and O/N-alkyl C (20.3–38.1 %) followed by that of carboxyl/amid C (10.3–24.1%) and alkyl C (11.3–21.6 %).

Extracted HA's, called "young", from incubated plant residues are characterised by significantly higher proportions of O-alkyl C (mean content 34.08 ± 3.02 %), mainly derived from hemicellulose and cellulose than HA of variants with soil (25.41 ± 2.48) and Haplic Luvisols (Table I). These data refer to an enrichment of aromaticity of HA from Haplic Luvisol relative to the HA from incubated crop residues with Haplic Luvisol or crop residues, O-Alkyl C has been degraded preferentially. The first finding is in agreement with the lignin results, indicating that crop residues are mainly composed of remaining more resistant plant tissues that have already lost part of their polysaccharide-C structures.

Based on indexes of aromaticity (α) we found Zaujec

Table II
Evaluations parameters of humic acids

Samples of HA	ID (+)	Change of ID	α (++)	alkyl-C+aryl-C/ O-alkyl-C+ carboxyl-C
LO	0.880	100%	49.6	1.249
WR	0.297	33.7	44.9	1.066
LO + WR	0.653	73.1	44.3	1.184
AA	0.513	58.3	40.1	1.045
LO + AA	0.973	110.5	43.1	1.208
CM	0.513	58.3	41.6	1.169
LO + MR	0.938	95.2	42.9	1.216
GM	0.461	52.4	46.4	1.132
LO + GM	0.779	88.5	40.7	1.164

(+) ID = Index of decomposition = (alkyl-C/O-alkyl-C)
(++) α = (aryl-C/alkyl-C + O-alkyl-C + aryl-C).100 (%)

et al.[6] that aromaticity of the HA from incubated crop residues increased as humification progressed. Ratios of alkyl C to O-alkyl C were calculated by Baldock et al.[1] as indicator for decomposition process of organic matter in soils.

The major changes that occur in an NMR spectrum after decomposition of plant residues are a decrease in carbohydrates, an increase in the relative proportion of alkyl (aliphatic chains) and carboxyl C, and partial breakdown of lignins. The relative degree of aromaticity among the HA's appears to vary as a function of the humification process. The carboxyl content and the aromaticity increase with humification. This tendency is also consistent with the nmR results discussed above and with the analytical data.

Conclusions

Comparison of the ^{13}C-NMR spectra of the samples HA extracted from incubated plant residues and organic matter applied to Haplic Luvisols after incubation indicates that those from plant residues show a higher intensity in the aromatic C and O/N-alkyl C regions and a lower proportion of alkyl C and carboxyl C. The nmR spectra show that the aromaticity of humic acids extracted from incubated plant residues slowly increases during the humification process (Table II). New formed HA from humified plant residues, mainly wheat residues, decrease decomposition index and values of ratios alkyl-C + aromatic-C/O-alkyl-C + aromatic-C.

REFERENCES

1. Baldock J. A., Oades J. M., Nelson P. N., Skene T. M., Golchin A., Clarke P.: Australian J. Soil Res. *35*, 1061 (1997).
2. Chukov S. N.: Eur. Soil Sci. *31*, 979 (1998).
3. Gonet S. S., Debska B.: Rostl. Vyr. *45*, 455 (1999).
4. Knicker H., Ludemann H. D.: Org. Geochem. *23*, 329 (1995).
5. Wilson M. A.: *nmR Techniques and Application in Geochemistry and Soil Chemistry.* Pergamon Press, Oxford 1987.
6. Zaujec A., Šíma J., Liptaj T.: Procceedings of 8th Meeting of the Intern. Humic Subst. Soc.: The role of Humic Substances in the Ecosystems and Environmental Protection (Drozd J. et al., eds.), p.207. PTSH Wroclaw 1997.

L18 HS-SPME AND GC-MS AS VALID TOOLS TO ASSESS VOLATILE ORGANIC COMPOUNDS FROM SOIL NATURAL ORGANIC MATTER

C. DE PASQUALE, R. FODALE, M. GIULIVI, P. CONTE and G. ALONZO

ITAF Department – Università di Palermo Ed. 4 viale delle Scienze, 90128, Palermo, Italy
c.depasquale@unipa.it

Introduction

Humic acids (HAs) which are involved in almost all physical, chemical, and biological processes occurring in soil system[1,2] represent the most abundant fraction of soil organic matter. In particular, HAs are well known to be very active in interacting to various extents and modalities with a variety of organic and inorganic chemical contaminants[3]. Knowledge of the composition, structure, and functionalities of HAs is therefore, essential for the understanding of their chemical behavior and reactivity in environmental matrices.

Chemical analyses on HAs are traditionally done by chromatographic and spectroscopic techniques. Recent advances in the chemistry of humic substances, revealed that a detailed characterization can be better achieved when a separation of the different components is obtained[4]. Here we suggest head space solid-phase micro-extraction (HS-SPME) coupled with gas-chromatography/mass spectrometry (GC-MS) as a new analytical tool for the characterization of the volatile components released from humic substances at 80 °C.

Materials and Methods

Soil

Two surface horizons were sampled from the ancient caldera of Vico (nearby Rome) and Monte Faito (Naples) in Italy. Detailed characterization of the two soils are reported elsewhere[5].

HA Extraction

Humic acids (HAs) were extracted by using common procedures[6]. Namely, 100 g of each soil were suspended in 500 ml of 1M NaOH and 0.1M $Na_4P_2O_7$ and centrifuged at 7,000 rpm for 20 min. The supernatant was then treated with 37% HCl until pH 1 was reached to precipitate HAs. Humic acids were purified by a series of dissolutions in 1M NaOH followed by flocculations in 6M HCl. Each HA was then shaken twice in a 0.25M HCl/HF solution for 24 h, dialized agaist distilled water till Cl-free and freeze-dried.

CPMAS ^{13}C-NMR Spectroscopy

CPMAS ^{13}C-NMR experiments were performed on a Bruker Avance 400 spectrometer operating at 100.6 MHz on carbon-13 and equipped with a 4 mm standard bore solid state probe. The rotor spin rate was set at 13,000 Hz. Samples were packed in 4 mm Zirconia rotors with Kel-F caps. A contact time of 1 ms, a recycle delay of 2 s, an acquisition time of 35 ms and a RAMP sequence to account for inhomogeneities of the Hartmann-Hahn condition at high rotor spin rates were used. Spectra acquisition was done with Topspin 2.0, whereas data elaboration was done with Mestre-C 4.9.9.9 by using a line broadening (LB) of 50 Hz and an automatic baseline correction with a 3rd order polynomial and Bernstein algorithm. Semi-quantitative results were obtained by integrating the spectral regions in the intervals 184–159 ppm (COOH), 159–110 ppm (aromatic C), 110−88 ppm (anomeric C), 88–62 ppm (C−O), 62–48 ppm (C−N) and 48–0 ppm (alkyl C). All the areas were normalized to the total spectral areas and content percent was obtained.
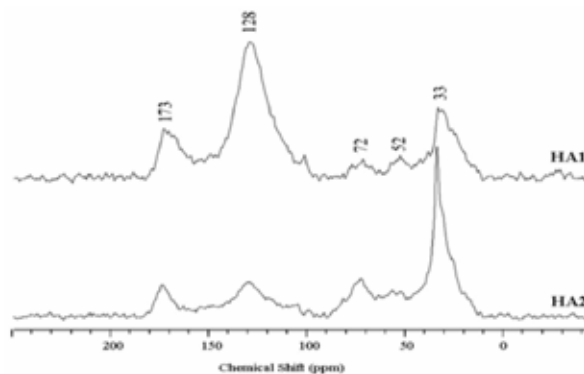

Fig. 1. **CPMAS ^{13}C-NMR spectra of the two humic acids used in the present study**

HS-SPME Extraction

A polydimethylsiloxane fiber (PDMS 100 µm, Supelco, Bellefonte, PA – USA) was used to sample the head space in equilibrium with 20 mg of the two HAs placed in 15 ml glass vials. These were sealed with a poly(tetrafluoroethylene) silicon septum-lined cap (Supelco, Bellefonte, PA, USA) and heaten 30 min at temperatures of 80 °C. The sampling time for was 5 min maintaining the 80 °C temperature.

GC-MS Analysis

The gas-chromatographic analyses were run on a Hewlett-Packard 5890 GC system interfaced with a HP 5973 quadrupole mass spectrometer. A HP5–MS column was used (5% diphenyl − 95% dimethylpolysiloxane 30 m × 0.2 mm, 0.25 µm film, J & W Scientific, Folsom CA, USA). The fibre was manually inserted in a GC inlet port equipped with a specific glass liner for SPME injection (0.75 mm i.d.). Analyses were carried out in splitless mode with helium as carrier gas at 1 ml min$^{−1}$. Chromatographic conditions were: injector temperature 250 °C, oven temperature program: 1 min at 60 °C followed by a linear temperature increase of 5 °C min$^{−1}$ up to 280 °C held for 15 min. The MS full-scan conditions were: source temperature 230 °C, interface temperature 280 °C. The electron impact ionization spectra were obtained at 70 eV, recording mass spectra from m/z 40 to 550.

Results and Discussion

The HS-SPME extraction method allowed the identification of 31 chemical components in each HA. Analyses at different temperatures have been done (data not repoted).

The optimal temperature conditions for the qualitative discrimination of HAs 80 °C giving a relative standard deviation [RSD, %] of ≤10 % for each identified component. Moreover, the amount of volatile components sampled in the head space was significantly representative of the whole HA systems as assessed by analyses with icreasing HA material. Table I reports the class of substances identified over the two solid state humic acids. Eight classes of organic compounds were discriminated. Among those, the largest contribution was from aromatic materials. In fact, HA1 revealed 66.77 % of aromatic moieties in the volatile mixture, whereas HA2 was 81.55 % (Table I). The amount of volatile aromatic molecules in HA1, smaller than in HA2, appears at variance with the content of aromatic systems obtained from CPMAS ^{13}C-NMR spectroscopy (Fig. 1, Table II). The aromatic C content by NMR (159–110 ppm) was the largest in HA1, thereby leading to the hypothesis that such material should produce a larger amount of volatile aromatic components than HA2. The contradictory HS-SPME GC-MS and CPMAS ^{13}C NMR results could be explained by considering the different natures of the soils from which the HAs were extracted. In fact, HA1 was extracted from a buried soil whereas HA2 was obtained from a surface horizon of a different volcanic soil. Organic material in buried conditions undergoes to anaerobic and abiotic degradation. Conversely, aerobic and biotic transformations occur in organic materials placed on surface soil horizons. The abiotic degradation in anaerobic conditions may produce highly condensed aromatic systems. Due to the larger molecular size of the condensed aromatic substances in HA1, these are less available for head space sampling than the corresponding aromatic systems formed in aerobic and biotic transformations. Except for the aromatic moieties which were in disagreement when comparing the gas-chromatographic data with the NMR results, the remaining components be have similarly. In fact, Tables I and II report the same trends for all the relative amounts revealed by the two analytical techniques used in the present study.

Conclusions

In the present study we used a new analytical tool for the characterization of the volatile components in humic substances. Results showed that the amount of volatile aromatic moieties was depending on the nature and genesis of the soils from which the HAs were extracted. Moreover, a number of fatty acids, as well as alkane-systems were also found in the head space in equilibrium with the solid humic substances. The relevant novelty was that we expected fatty acids and hydrophobic alkanes to be confined mainly inside the hydrophobic and chemically protected core of the supramolecular humic acids. For this reason the volatilization to the head space was thought to be difficult. Conversely, our findings appeared to confirm CPMAS ^{13}C NMR results from Conte and Berns (2008)[7] which described the conformation of humic substances as made mainly by a hydrophobic aromatic core surrounded by long carbon chains. The HS-SPME-GC-MS technique appears to be a very promising tool in obtaining relevant information on the lighter fraction of organic components weakly bound to humic materials.

REFERENCES

1. Schulten H.-R.: Fresenius' J. Anal. Chem. *351*, 72 (1995).
2. Shevchenko S. M., Bailey G. W., Akim L. G.: J. Mol. Struct. *460*, 179 (1999).
3. Pignatello J. J.: Adv. Colloid Interface Sci. *76–77*, 445 (1998).
4. Conte P., Spaccini R., Piccolo A.: Anal. Bioanal. Chem. *386*, 382 (2006).
5. Conte, P., Piccolo, A., van Lagen, B., Buurman P., De Jager, A.: Geoderma *80*, 327 (1997).
6. Stevenson, F. J.: *Humus Chemistry: Genesis, Composition, Reactions*, 2nd ed. Wiley, New York, 1994.
7. Conte P., Berns A. E.: Anal. Sci. 2008 accepted.

Table I

Composition of the volatile components released by the two HAs at 80 °C. The compounds were grouped according to their functional groups. The reported correspondent percent amounts [%] of identified compounds are the medium value of three different chromatographic analyses

	Content [%]	
Compounds	HA1	HA2
Acids	18.64	7.30
Aldehydes	3.56	1.19
Ketones	1.36	0.00
Alcohols	0.53	0.40
Amines	0.57	0.40
Olephins	1.21	1.11
Aromatics	66.77	81.55
Alkanes	7.19	8.27

Table II
Content [%] by CPMAS ^{13}C NMR of the different groups in HAs

Soil humic acid	COOH	Aromatic C	Anomeric C	C–O	C–N	Alkyl C
	184–159 ppm	159–110 ppm	110–88 ppm	88–62 ppm	62–48 ppm	48–0 ppm
HA1	12	55	5	4	4	21
HA2	9	21	3	14	8	45